UNIVERSITY OF LIVERPOOL

In-beam Gamma and Electron Spectroscopy of ^{253}No

Thesis submitted in accordance with the requirements of the University of Liverpool for the degree of Doctor in Philosophy

by

Andrew Kishor Mistry

Oliver Lodge Laboratory

2014

Abstract

The (S)ilicon (A)nd (Ge)rmanium (SAGE) spectrometer has been employed, together with the RITU gas-filled separator and the GREAT focal plane spectrometer with Total Data Readout (TDR) at the University of Jyväskylä to analyse the heavy actinide nucleus ^{253}No (Z=102).

Initially, the neutron-deficient odd-A isotope ^{177}Au (Z=79) is studied using the recoil-decay tagging technique, enabling testing and demonstration of γ ray and conversion electron coincidence analysis techniques using SAGE. This has allowed for conversion coefficient measurements on a number of low-lying states.

The main focus of the study is on ^{253}No with combined in-beam γ ray and electron spectroscopy through the recoil-tagging technique. Orbitals emanating from the next shell closure above ^{208}Pb are sensitive to measurement in the deformed heavy midshell region. Thus probing the single-particle structure of regional midshell heavy nuclei allows for exploration of the island of enhanced stability toward the next closed nucleon shells. Using ^{253}No data from SAGE has enabled γ-electron coincidences to be established for level scheme construction with transition energies determined. Recoil-tagged prompt γ ray and internal conversion electron spectra are compared to Monte Carlo simulations to confirm the rotational structure nature of the bands. Internal conversion coefficient measurements establish the multipolarity of transitions within the bands. Measurement of the B(M1+E2')/B(E2) interband-intraband ratio confirms the assignment of the bandhead configuration, with results presented strongly supporting the $9/2^-[734]_\nu$ observed in previous studies. An isomeric state is measured with $T_{1/2}$=28.6±2.3 µs confirmed through a decay via a 167 keV M2 transition resulting from the $5/2^+[622]_\nu$ configuration. A 608±20 µs slower isomer has also been tentatively measured, potentially with decay through a non-yrast structure. Excited ^{249}Fm states following the α-decay of ^{253}No are also measured through the recoil-decay tagging technique.

Acknowledgements

Firstly, a big thank you to my supervisor Prof. Rodi Herzberg for giving me the opportunity to study under his guidance and teaching, and his friendly help and exceptional support throughout my PhD. Special thanks also to Dr. David Joss for his assistance and enlightening discussions about gold. I am grateful to the STFC for providing financial support during my studies. Thanks to all student and staff members of the nuclear group at Liverpool, past and present, for their help and friendship. Chris McPeake (Xmas), Joe Rees, Mark, Revill, Baha, Jamie, Faye, Amina, Alex T and Alex G for physics (and mostly non-physics) stuff. Thanks to Danny, Philippos, Fuad and Andrew W, for making travelling to experiments more interesting and invaluable support with SHEs and SAGE.

I would like to thank collaborators from the University of Jyväskylä, without whose outstanding efforts this research would not have been possible.

Finally thanks to my friends Dan Webster, Rhogan, Will, Felix, Joe Mee, Birley and the rest for giving me a break from the physics and family, especially my Mum, Dad and Brother for their patience and support over the last 26 years.

Contents

Chapter 1

Introduction

One of the key goals in nuclear physics is the study of the heaviest elements. Around Z=100 the repulsive Coulomb potential of the positively charged protons is enough to overcome short range interaction of the nuclear strong force and the nucleus will become unstable. However, the existence of heavier nuclei suggests that something more is at play here. Recent efforts in the field have focussed on uncovering how the heaviest elements form, and the reasons why are they are so stable against decay.

Whilst the atomic system is well understood, the nucleus is an immensely complex many-body quantum system. A number of different models have been theorised in an attempt to gain a comprehensive understanding of the factors that are governing the properties of the nucleus. Two branches of models have emerged: collective motion of the nucleus which involves the bulk properties of the nucleus as a macroscopic approach, and single particle motion which considers the effects of the valence particles on the nucleus as a microscopic approach.

The liquid drop model [1] was a first attempt at a macroscopic approach to model the nucleus, however failed to match experimental stability results with deviations from a smooth nucleon configuration. The shell model [2] remedied this by introducing a quantum shell concept whereby nucleons have a specific arrangement in the nucleus. It was found that the nucleus displays greatly enhanced stability at magic numbers N and Z=2, 8, 20, 28, 50, 82 and N=126 where N and Z are the number of neutrons and protons in the nucleus respectively. Despite these approaches, the location of the region around the next closed shell gap above ^{208}Pb,

known as the 'island of stability,' remains a mystery. Depending on how the model calculation parameters are varied ultimately dictates where this lies in the nuclear chart.

Marrying the macroscopic and microscopic models has proved successful in predicting experimental results. This approach is a combination of the smoothly varying component of the liquid drop model and an oscillatory component from the shell model. A completely separate approach is to use self consistent mean field models [3]. This involves calculating the nuclear wavefunction from a central potential iteratively until the potential and wavefunction converge. From this two approaches are used: the Relativistic Mean Field (RMF) approach [4] and the Skyrme-Hartree-Fock (SkHF) approach. A comparison of the macroscopic-microscopic and SkHF approaches are illustrated in Figure 1.1 with the shell energy as a function of proton and neutron number plotted. For the Wood-Saxon microscopic approach this is the difference between the total binding energy and the liquid-drop part of the macroscopic energy, similarly for the Hartree-Fock approach, the spherical component of the macroscopic energy is subtracted from the ground state energy. This ultimately determines the stabilisation of the nucleus in the region of low shell correction energy.

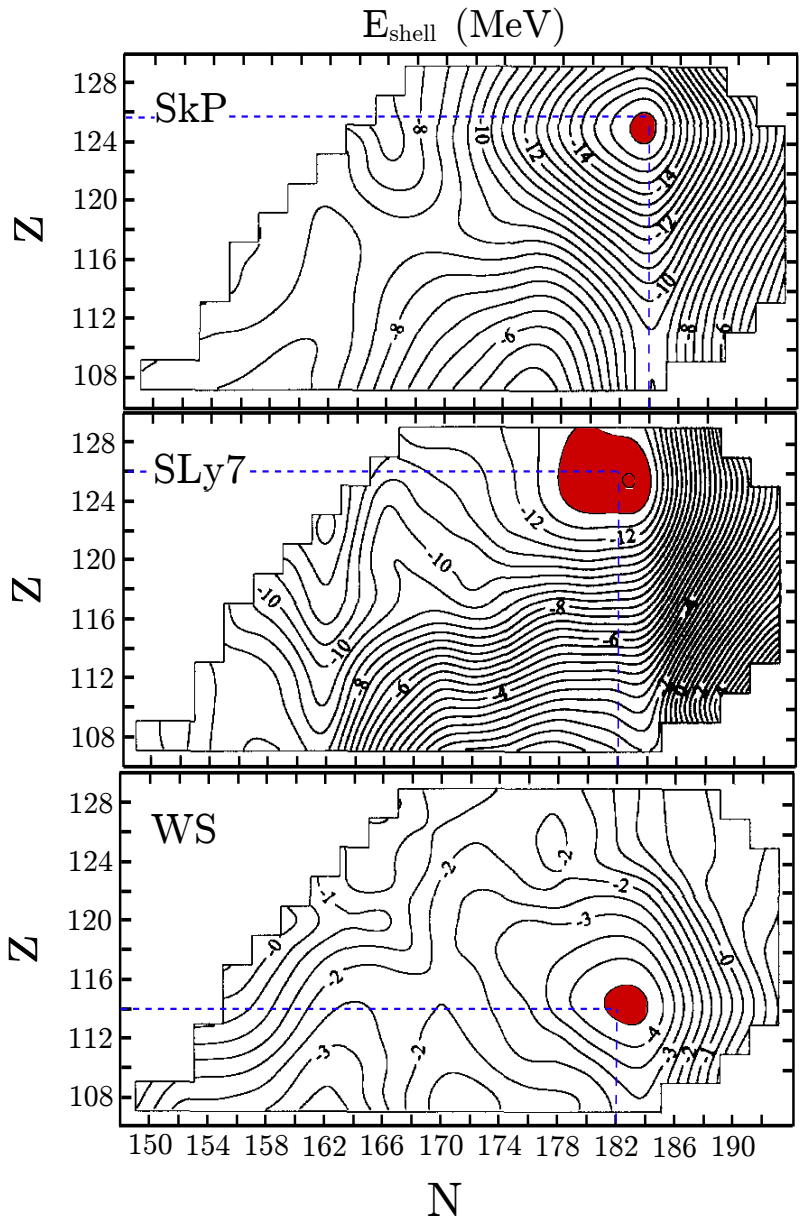

Figure 1.1: *Shell correction energy contour plot (sum of proton and neutron shell corrections in MeV) shown for two parametrisations of the SkHF model (SkP and SLy7) and the Wood-Saxon (WS) microscopic-macroscopic approach. Adopted from [5].*

For the SkHF approaches there are minima around the isotope $^{310}126$ indicating that this is doubly magic for the given models. However for the WS approach the minimum occurs at ^{296}Fl (Z=114), thus both approaches yield markedly different results. Further comparisons have been made within self-consistent approaches between RMF and SkHF basis in the Sn (Z=50) region [6].

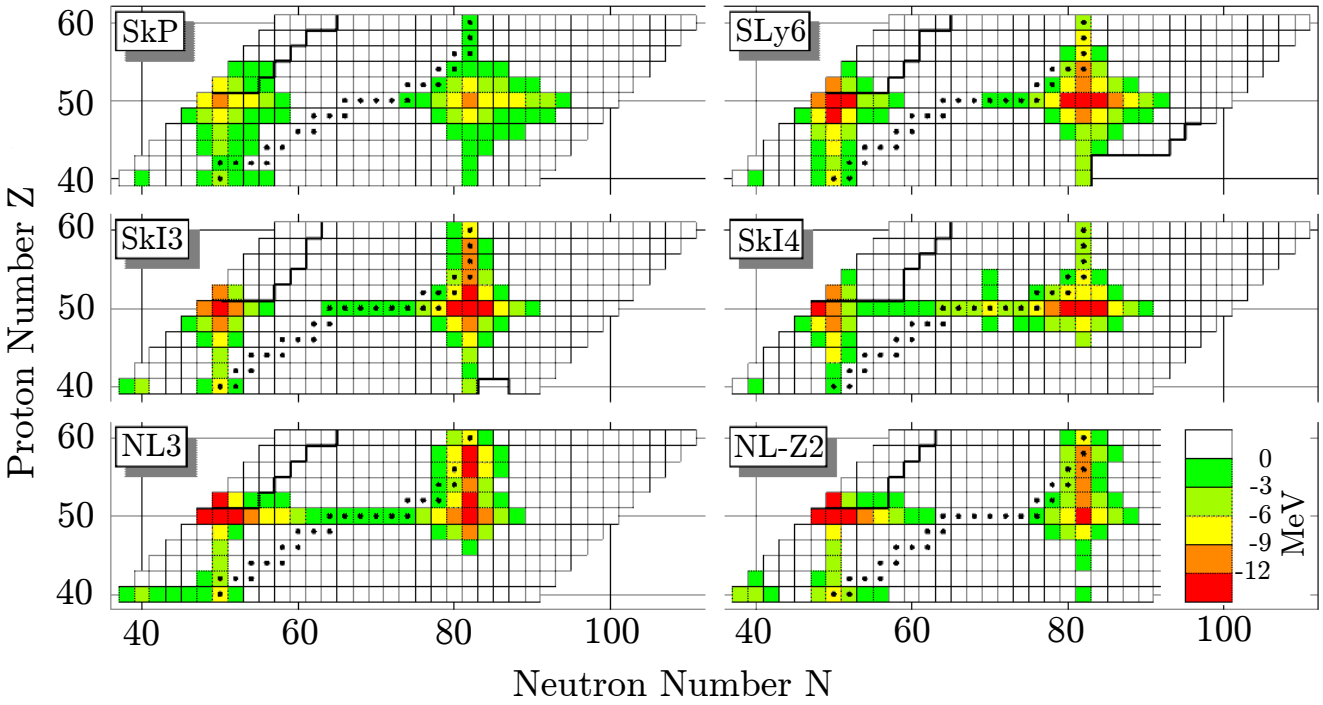

Figure 1.2: *Shell correction energies (in MeV) comparing SkHF parametrizations (SkP, SkI3, SLy6 and SkI4) to RMF models (NL3 and NL-Z2) in the Sn shell stabilised region. Enhanced shell correction energy (in units of MeV) is observed by decreasing green to red [6].*

Well defined regions indicate shell closures around doubly magic ^{100}Sn and ^{132}Sn with both RMF and SkHF models in agreement of the location of this shell gap. Applying these models to the superheavy element region is shown in Figure 1.3

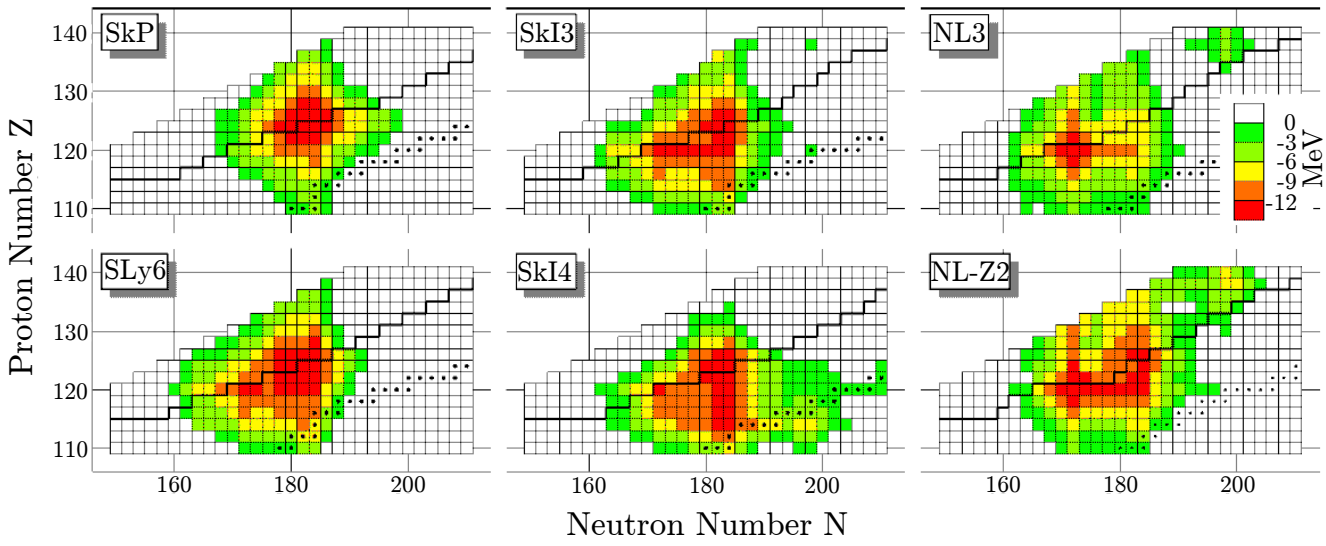

Figure 1.3: *Shell correction energies comparing SkHF parametrizations (SkP, SkI3, SLy6 and SkI4) to RMF models (NL3 and NL-Z2) for heavier Z nuclei. A well defined region is no longer seen with a broad region of shell stabilization evident [6].*

Compared to well defined nucleon shell gaps, here large regions of enhanced shell stabilisation occur as an island of stability. The single-particle level density is larger in the heavier elements at deformation, but around the shell gap, a region of low level density is evident. This, combined with low-j orbitals close to the Fermi surface, is the reason for the increase in shell correction energy and broader stabilised regions. This is shown in Figure 1.4 for protons levels around the Z=50 and Z=126 shell gaps.

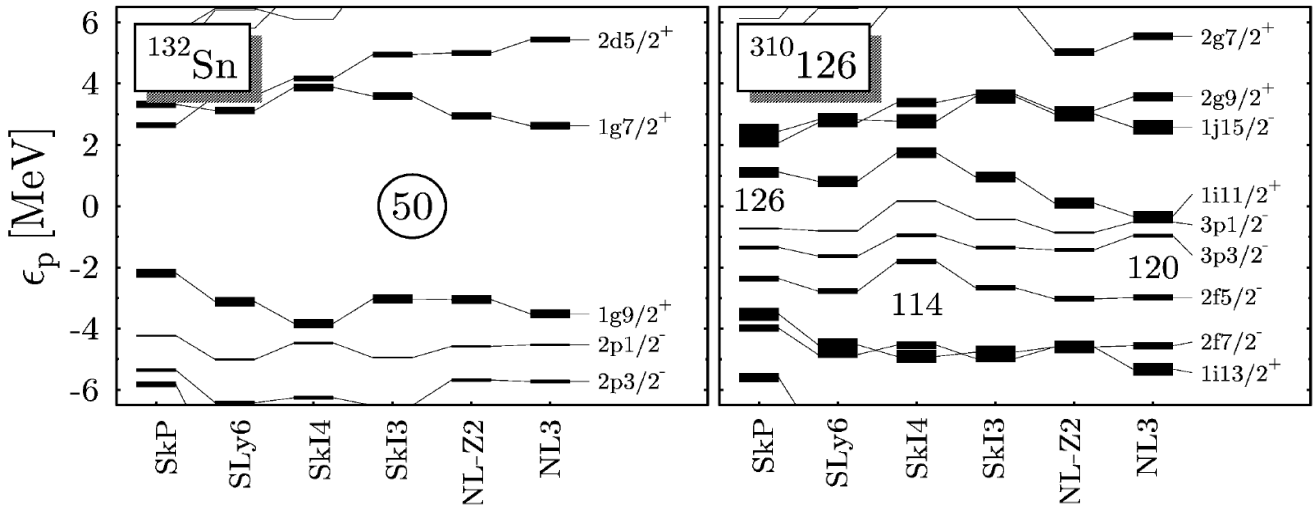

Figure 1.4: *Proton single-particle energy levels relative to the Fermi surface for ^{132}Sn and Z=126. Increased level density is clear for the heavier system, with low-j orbitals near the Fermi surface ($3p_{1/2}$ and $3p_{3/2}$ between Z=120 and 126) [6].*

For the Z=50 region there is a pronounced gap between levels and the level density is lower compared to the high Z region. For the higher Z levels this gap is smaller and lacks definition across each of the models. The different models and parametrizations give different regions for where the increased areas of stability might lie. Experimental studies are therefore key in pinning down this location.

Experimental work has led to the synthesis of the heaviest element to date being Z=118 [7]. Z=115 and 117 have been most recently confirmed [8] [9] with collaboration from members of the Liverpool nuclear structure group during experimental searches for Z=119 and Z=120 in GSI, Germany. These superheavy elements (SHEs) are created in heavy-ion fusion evaporation reactions with very low production cross sections resulting in nuclei closer to the proton dripline. Ideally one would like to examine more neutron rich SHEs, closer to the shell stabilized region, however current experimental techniques limit such studies. Instead, examining neutron deficient nuclei in the heavy actinide region around Z$\sim$100 proves more fruitful. The single-particle orbitals emanating from around Z=120 downslope close to or at the Fermi surface in this deformed mid-shell region. Thus probing the structure of these nuclei is of great value when attempting to determine the location of the island of stability. Further discussion

on the experimental work on the transactinide region can be found in [10] and [11], and an in-depth discussion on the production of the superheavy elements can be found in reference [12].

The isotope ^{253}No was discovered in 1967 by Ghiorso *et al.* [13] and lies in this region of interest. This study aims to explore the single particle orbitals of this nucleus, improving on systematic data in this region, which will in turn assist in the determination of the ordering and energy of levels in the superheavy element region.

Chapter 2

Nuclear Models and Decay Modes

As discussed in the introduction, there are a variety of theoretical approaches made to model the structure of the nucleus. This chapter will outline the basis behind these models and their scope in replicating experimental data. The understanding behind decay modes also proves essential for matching models to data. This will also be discussed.

2.1 Liquid Drop Model

Classically, the nucleus can be considered as a drop of incompressible nuclear matter: a quantum liquid with uniform density. This is known as the **L**iquid **D**rop **M**odel (LDM), a macroscopic approach to explain the collective structure of the nucleus [1]. The volume of the nucleus is considered to be constant with the surface tension holding the nucleus together (as the strong force). While this determines bulk properties such as deformation and rotation well, the model fails when replicating asymmetric fission properties. The binding energy is defined as the energy required to break up the nucleus into its constituent protons and neutrons. This increases rapidly with A until the nuclear force saturates at about A=20 and it becomes approximately constant. To adapt for the shortcomings of the LDM, a semi-empirical approach was taken to fit with experimental data. This is given in the form of the Bethe-Weizsäcker formula [14]

$$B.E. = a_v A - a_s A^{2/3} - a_c Z(Z-1)A^{-1/3} - a_a(N-Z)^2 A^{-1} \pm \delta. \tag{2.1}$$

Z, N and A refer to the proton, neutron and atomic numbers respectively. The volume term, $a_v A$ demonstrates that the binding energy per nucleon is approximately constant and scales with A. However this is a poor approximation since there are less nearest neighbour nucleons at the surface and thus the binding energy is reduced by a factor given by the surface term $a_s A^{2/3}$. The positive electrostatic repulsion of protons results in the Coulomb term $a_c Z(Z-1)A^{-1/3}$ arising from the radial separation of interacting pairs resulting from the nuclear radius being given by $R = R_0 A^{1/3}$. The three terms outlined make up the binding energy based on the LDM. Additional non-classical terms arise from nucleons not moving independently in the nucleus and so a microscopic approach is considered. The asymmetry term $a_a(N-Z)^2 A^{-1}$ is a result of the Pauli exclusion principle. With increasing Z the electrostatic repulsion in the nucleus increases. To compensate for this, more neutrons are required, however this has the effect of the neutrons occupying higher energy levels and thus decreasing the binding energy of the nucleus. The pairing term δ is from pairing of like nucleons with even-even pairing more stable (δ positive) than odd-odd (δ negative) or even-odd (odd-even) (δ zero). With the addition of these two final terms to the LDM, the model becomes a combination of macroscopic and microscopic approaches.

2.1.1 Spontaneous Fission

During fission the nucleus splits into highly energetic fragments. In terms of the process that governs this, only the first three terms (volume, Coulomb and surface) of the LDM contribute to this. One can define the fissility parameter [15]

$$x = \left(\frac{Z^2}{A}\right)\left(\frac{Z^2}{A}\right)^{-1}_{crit}, \tag{2.2}$$

with $(Z^2/A)_{crit}$ being a critical value at which the spherical shape becomes unstable with the Coulomb repulsion counteracting the effect of the surface tension (related to the parameter b_{surf}),

$$\left(\frac{Z^2}{A}\right)_{crit} \propto \frac{b_{surf} r_0}{e^2}. \tag{2.3}$$

The probability for spontaneous fission increases as the fissility parameter increases. For $x \approx 0.88$ and zero angular momentum the liquid drop fission barrier vanishes and the nucleus becomes unstable against spontaneous fission. For $x<1$ the barrier decreases for increasing angular momentum. A plot of the spontaneous fission lifetime against fissility parameter is shown in Figure 2.1.

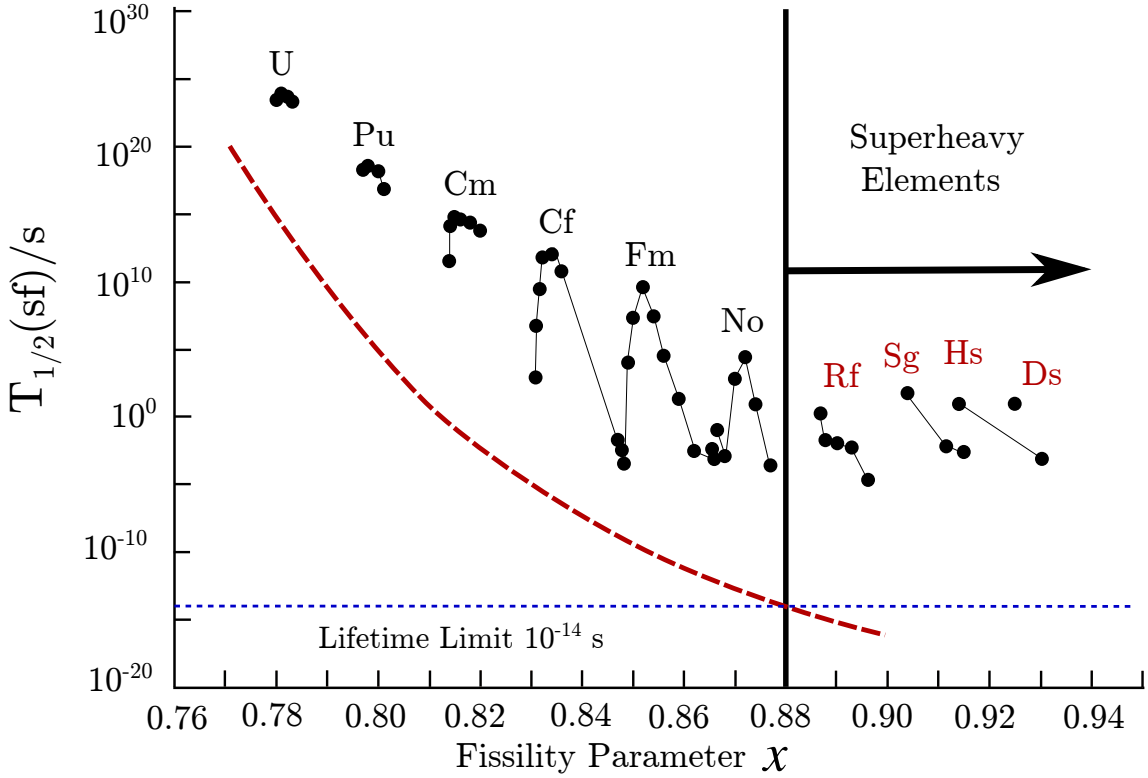

Figure 2.1: *Measured spontaneous fission half-lives for even-even nuclei (circles) as a function of fissility parameter x. The red dashed line represents the fissility parameter in the LDM, while the blue horizontal line shows the minimum time for the formation of a chemical element. Adapted from [16].*

Figure 2.1 shows the limits of the LDM for predicting fission in the heavier element regime. There are clear discrepancies between the LDM fissility and experiment highlighting the impact additional factors dictating stability. Around rutherfordium (Z=104) the LDM predicts spontaneous fission and nuclei should not exist in the measured state that has been experimentally shown. Thus shell effects play the dominant role in the stability of superheavy nuclei.

2.2 The Spherical Shell Model

Experimental evidence for a shell-like structure in nuclei is broad. Examples include [17]:

- Discontinuities of the binding energy at the magic numbers. At the magic numbers, the closure of shells result in large energy separation from the next highest shell.
- The binding energies of the removal of the last pair of nucleons (two nucleon separation energies) is much larger at the magic numbers relative to away from shell closures.
- The first (2^+) excited states in even-even nuclei are much higher in energy relative to the ground state at the shell closures.
- The shape of the nucleus in the form of the quadrupole moment is at a minimum at the magic numbers and thus the nucleus exhibits spherical shape.

To explain the deviations from a macroscopic model, a microscopic shell based model was theorised. The shell model represents an independent particle model whereby all nucleons are independent, and a single nucleon is under the influence of a smoothed out mean field potential created by all other nucleons. The average potential acting on each nucleon is

$$V_a(r_r) = \left\langle \sum_j v(r_{ij}) \right\rangle, \tag{2.4}$$

where $v(r_{ij})$ is the potential between two nucleons.

The Hamiltonian is expressed in the form of kinetic energy plus the potential felt by all nucleons

$$H = \sum_i T_i + \sum_{ij} v(r_{ij}), \tag{2.5}$$

which can be separated into a central component and a residual component

$$H = H_0 + H_{residual} = \sum_i^A \left[\frac{\mathbf{p}_i^2}{2m_i} + V_i(r_i) \right] + \lambda \left[\sum_{ij}^A v(r_{ij}) - \sum_i^A V_i(r_i) \right]. \tag{2.6}$$

Based on the shell model assumption $\lambda \to 0$ hence the central interaction dominates over any residual interactions. Choice of the potential $V_i(r_i)$ requires consideration of a number of differing expressions. The criteria is that the binding increases toward the centre of the nucleus from the surface, and that no net force is applied at the centre. Comparisons are shown in Figure 2.2.

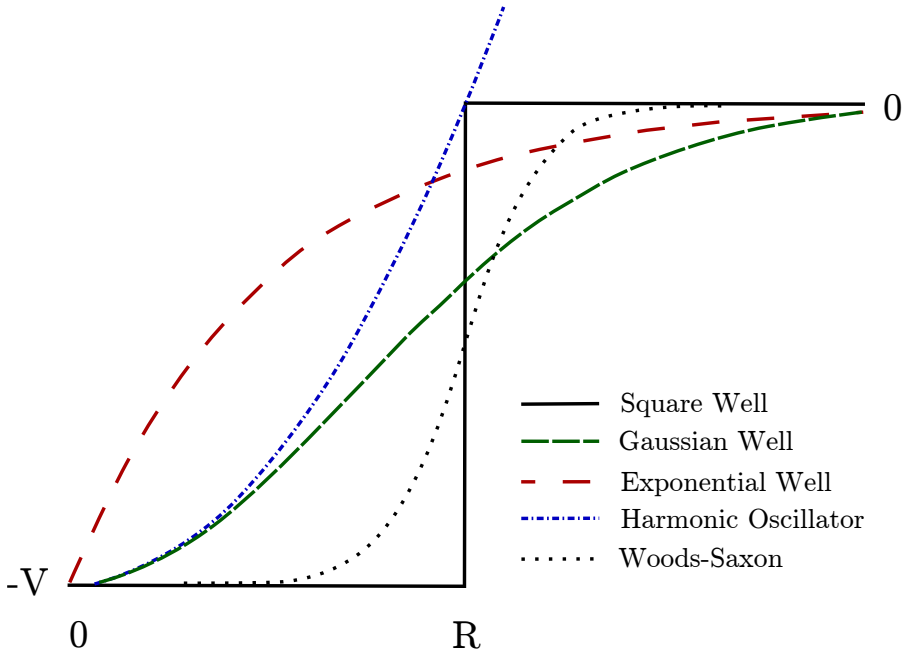

Figure 2.2: *Potential well options to model the central potential in the spherical shell model.*

The square well potential is the simplest case to solve analytically but fails to reproduce magic numbers correctly. For a well depth V_0, nuclear radius R and nuclear surface thickness a, the Woods-Saxon potential of the form

$$V(r) = \frac{-V_0}{\left[1 + e^{\frac{r-R}{a}}\right]}, \tag{2.7}$$

proves the most realistic nuclear potential, however proves more difficult to solve analytically. In order to reproduce the magic numbers, the harmonic oscillator proves a good approximation once additional factors of spin-orbit coupling and an l^2 centrifugal term are included.

2.2.1 Harmonic Oscillator Potential

The spherical harmonic oscillator potential has the form

$$V_{HO}(r) = -V_0 \left[1 - \left(\frac{r}{R}\right)^2\right], \tag{2.8}$$

with

$$V_0 = \frac{m\omega_0^2}{2}, \tag{2.9}$$

as the potential well depth, ω as the nucleon angular frequency, and R as the nuclear radius. The Hamiltonian can be solved to acquire energy eigenvalues,

$$E_N = \hbar\omega_0 \left(N + \frac{3}{2}\right), \tag{2.10}$$

with N as the oscillator shell quantum number such that $N = (2n + l)$ with $n = 0, 1, 2, 3...$ and $l = 0, 1, 2, 3...N$. For each N. degeneracy is introduced by l given by

$$d_N = (N + 1)(N + 2), \tag{2.11}$$

which gives an occupation for the shells filling up with nucleons in accordance with the Pauli exclusion principle to maximum occupancy closed shells. These however still do not match the magic numbers experimental evidence is consistent with. The higher angular momentum nucleons spend more time in the outer radius of the nucleus thus introducing an attractive l^2 centrifugal term represents this effect. This flattens the radial shape of the potential having the effect of creating a potential that is part harmonic oscillator and part square well, similar to the Woods-Saxon potential. Introducing another term to the harmonic oscillator potential; the spin-orbit interaction

$$V_{SO} = f(r)\mathbf{l} \cdot \mathbf{s}, \tag{2.12}$$

with the spin-orbit force given as

$$f(r) = \lambda \frac{1}{r} \frac{dV}{dr}, \tag{2.13}$$

(where λ is a strength parameter) serves to attain more consistent magic numbers. The spin-orbit coupling introduces additional degeneracy by splitting the levels as $j = l \pm \frac{1}{2}$, where j is the total angular momentum of the nucleon. Converse to the atomic spin-orbit interaction, the $j + \frac{1}{2}$ states are lower in energy than the $j - \frac{1}{2}$ as a consequence of the interaction being attractive. A schematic summarising the magic numbers produced is shown in Figure 2.3.

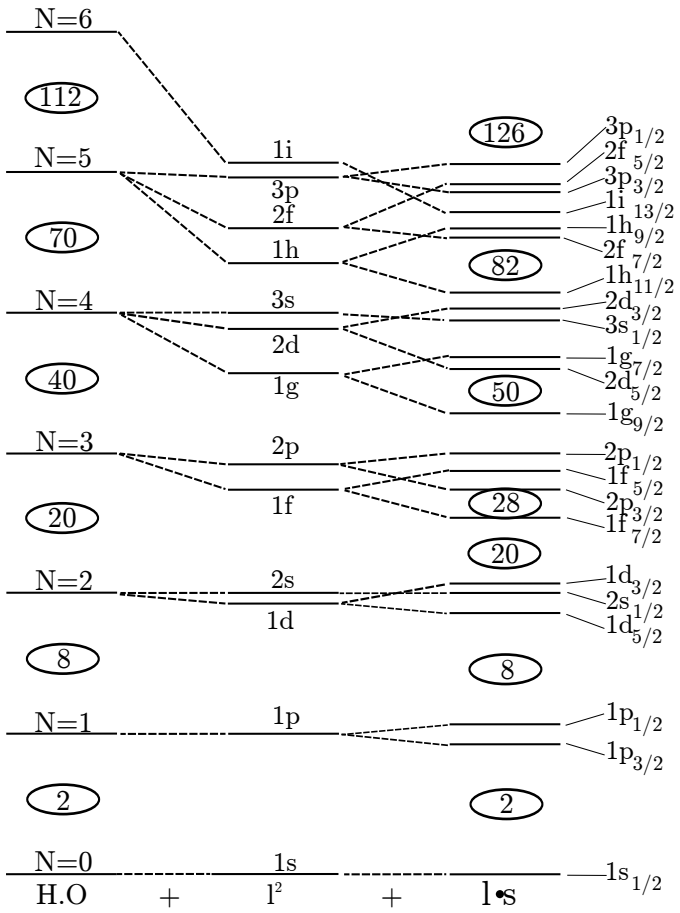

Figure 2.3: *Single-particle states with closed shells indicated by the sum of nucleons in all occupied states. The levels to the left shows the harmonic oscillator (H.O), in the centre is with the addition of the l^2 term and to the right with the spin-orbit interaction addition to form a modified harmonic oscillator potential. The states are labelled by their quantum numbers nl_j. Modified based on [18].*

The harmonic oscillator potential replicates lower energy states but breaks down for higher mass systems. The additions of the l^2 and $\mathbf{l} \cdot \mathbf{s}$ reproduces experimentally measured states

well at the shell closures. Differences between the Wood-Saxon and the modified harmonic oscillator potentials fall under the ordering of certain states. The spherical shell model has proven successful in replicating experimental results near or at closed shells. However away from closed shells the nucleus loses sphericity and so a new approach must be taken.

2.3 The Deformed Shell Model

Large amounts of experimental data point to nuclei having deformation. The existence of rotational bands, large quadrupole deformation away from closed shells, and the existence of single-particle spectra to name a few examples. Away from closed shells, the spherical shell model is no longer valid and adjustments to the model must be made to match shell energies.

2.3.1 Deformation

The shape of the equipotential surface of the nucleus given in a polar coordinate based system $R(\theta, \phi)$ can be expressed in terms of spherical harmonics

$$R(\theta, \phi) = C(\alpha_{\lambda\mu}) R_0 \left[1 + \sum_{\lambda=0}^{\infty} \sum_{\mu=-\lambda}^{\lambda} \alpha_{\lambda\mu} Y_{\lambda}^{\mu}(\theta, \phi) \right], \tag{2.14}$$

with $C(\alpha_{\lambda\mu})$ satisfying conservation of volume, R_0 as the radius of a sphere, $\alpha_{\lambda\mu}$ as coefficients which represent the differences between an equilibrium spherical shape. If one assumes a prolate axially symmetric nucleus, then μ can be assumed to be 0 and λ can be 2 for quadrupole, 3 for octupole, or 4 for hexadecapole deformation. $\alpha_{\lambda\mu}$ can be expressed for quadrupole deformation in terms of 5 coefficients,

$$\alpha_{20} = \beta_2 \cos\gamma,$$

$$\alpha_{21} = \alpha_{2-1} = 0, \tag{2.15}$$

$$\alpha_{22} = \alpha_{2-2} = \frac{1}{\sqrt{2}} \beta_2 \sin\gamma,$$

such that the shape of the nucleus can be expressed in terms of β_2:- the 'amount' of quadrupole deformation and γ:- the degree of axial symmetry. Thus $\alpha_{\lambda 0}$ can be expressed as β_λ and the nuclear surface shape is simplified in terms of Legendre polynomials P_λ in a purely axially symmetric basis

$$R(\theta) = CR_0 \left[1 + \sqrt{\frac{2\lambda+1}{4\pi}} \sum_\lambda \beta_\lambda P_\lambda(\cos\theta)\right], \tag{2.16}$$

$$= CR_0 \left[1 + \overbrace{\sqrt{\frac{5}{4\pi}}\beta_2 P_2(\cos\theta)}^{quadrupole} + \overbrace{\sqrt{\frac{9}{4\pi}}\beta_4 P_4(\cos\theta)}^{hexadecapole}\right],$$

the first Legendre term of which represents an ellipsoid shape and the second a hexadecapole shape via rotation around the symmetry axis with deformation parameters β_λ. The larger the value of β_λ, the greater the degree of deformation.

2.3.2 Anisotropic Harmonic Oscillator

In order to model the states associated with such deformation one can initially consider an anisotropic harmonic oscillator (AHO) with a deformed potential along the z-axis

$$V_{AHO} = \frac{1}{2}m[\omega_\perp^2(x^2+y^2) + \omega_z^2 z^2], \tag{2.17}$$

where $\omega_\perp$ and ω_z are the harmonic oscillator frequencies perpendicular and parallel to the symmetry axis respectively. Energy eigenvalues from solving the AHO problem take the form

$$E_{Nn_z n_\perp} \approx \hbar\omega_0 \left[N + \frac{3}{2}\right] - \frac{1}{3}\delta\hbar\omega_0[2n_z - n_\perp], \tag{2.18}$$

$N = n_z + n_\perp$ and the latter term represents the energies from a spherical based system with a correction term proportional to the deformation subtracted. The eigenstates of the AHO are labelled in the form asymptotic quantum numbers

$$[Nn_z\Lambda]\Omega^\pi, \tag{2.19}$$

for an axially symmetric non-rotating deformed nucleus. N is the number of oscillator quanta, n_z number of oscillator quanta along the symmetry axis, π is the parity given as $\pi = (-1)^N = (-1)^l$, Λ is the projection of the orbital angular momentum l along the symmetry axis, and $\Omega = \Lambda \pm \frac{1}{2}$ is the projection of the total angular momentum onto the symmetry axis. This is shown in Figure 2.4. While the AHO forms a basic case for transforming from a spherically based system to a deformed system, as with the spherical case, a modified anisotropic harmonic oscillator is required to match experimental results.

2.3.3 The Nilsson Model

The Nilsson model represents a shell model for a deformed nucleus [19]. Adding spin-orbit $\mathbf{l} \cdot \mathbf{s}$ and centrifugal $\mathbf{l}^2$ terms to the AHO forms the basis of the Nilsson model. The Nilsson potential is expressed as

$$V_{Nil} = \frac{m}{2}\left[\omega_x^2(x^2+y^2) + \omega_z^2 z^2\right] - \kappa\hbar\omega_0\left[2\mathbf{l}\cdot\mathbf{s} + \mu(\mathbf{l}^2 - \langle\mathbf{l}^2\rangle_N)\right]. \tag{2.20}$$

$\omega_{x,y,z}$ are related to the deformation,

$$\omega_x^2 = \omega_y^2 = \omega_0^2\left(1 + \frac{2}{3}\delta\right), \tag{2.21}$$

and

$$\omega_z^2 = \omega_0^2\left(1 - \frac{4}{3}\delta\right),$$

where ω_0 is the spherical oscillator frequency ($\hbar\omega_0 = 41A^{-\frac{1}{3}}(\text{MeV})$) and $\delta \approx \frac{3}{2}\sqrt{\frac{5}{4\pi}}\beta_2$ thus the first term of Equation 2.20 defines the deformation in terms of the oscillation frequency along a given deformed axis. For prolate shapes $\delta, \beta_2 > 0$ whereas for $\delta, \beta_2 < 0$ an oblate shaped nucleus is defined. The secondary term of Equation 2.20 gives the spin-orbit coupling and centrifugal term (which acts to deepen the effective potential well) with coupling strength parameters κ and μ. The subtraction of $\langle\mathbf{l}^2\rangle_N$ acts to restore the energy spacing of shells below $\hbar\omega_0$. The spin-orbit and centrifugal terms act to lift the degeneracy of the N states to $2(n_\perp + 1)$-fold

with each $[Nn_z\Lambda]\Omega^\pi$ state having only two-fold degeneracy for particles with $\pm\Omega$ (time-reversal degeneracy). A representation of the asymptotic quantum numbers is shown in Figure 2.4

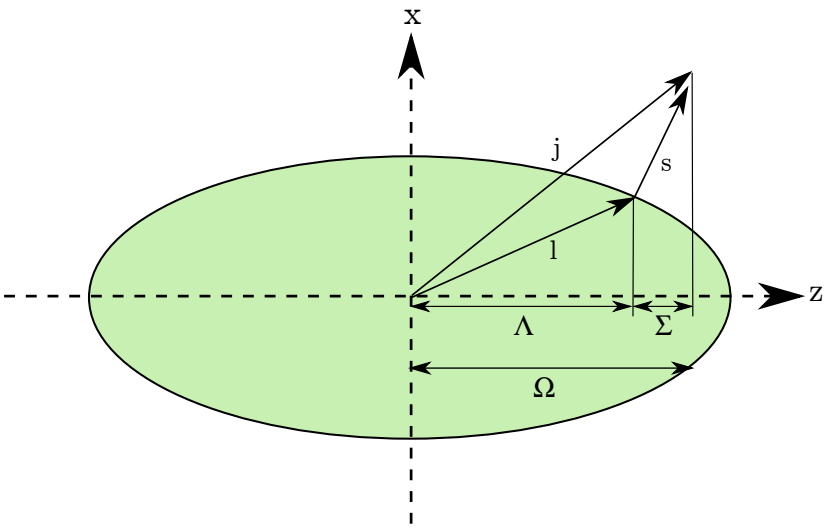

Figure 2.4: *Asymptotic quantum numbers labelled on a prolate ellipsoid deformed about the x-axis.*

Nilsson diagrams demonstrating the single-particle energy levels for proton with Z≥82 (Figure 2.6) and neutrons with N≥126 (Figure 2.5) are shown as a function of deformation parameter ε_2.

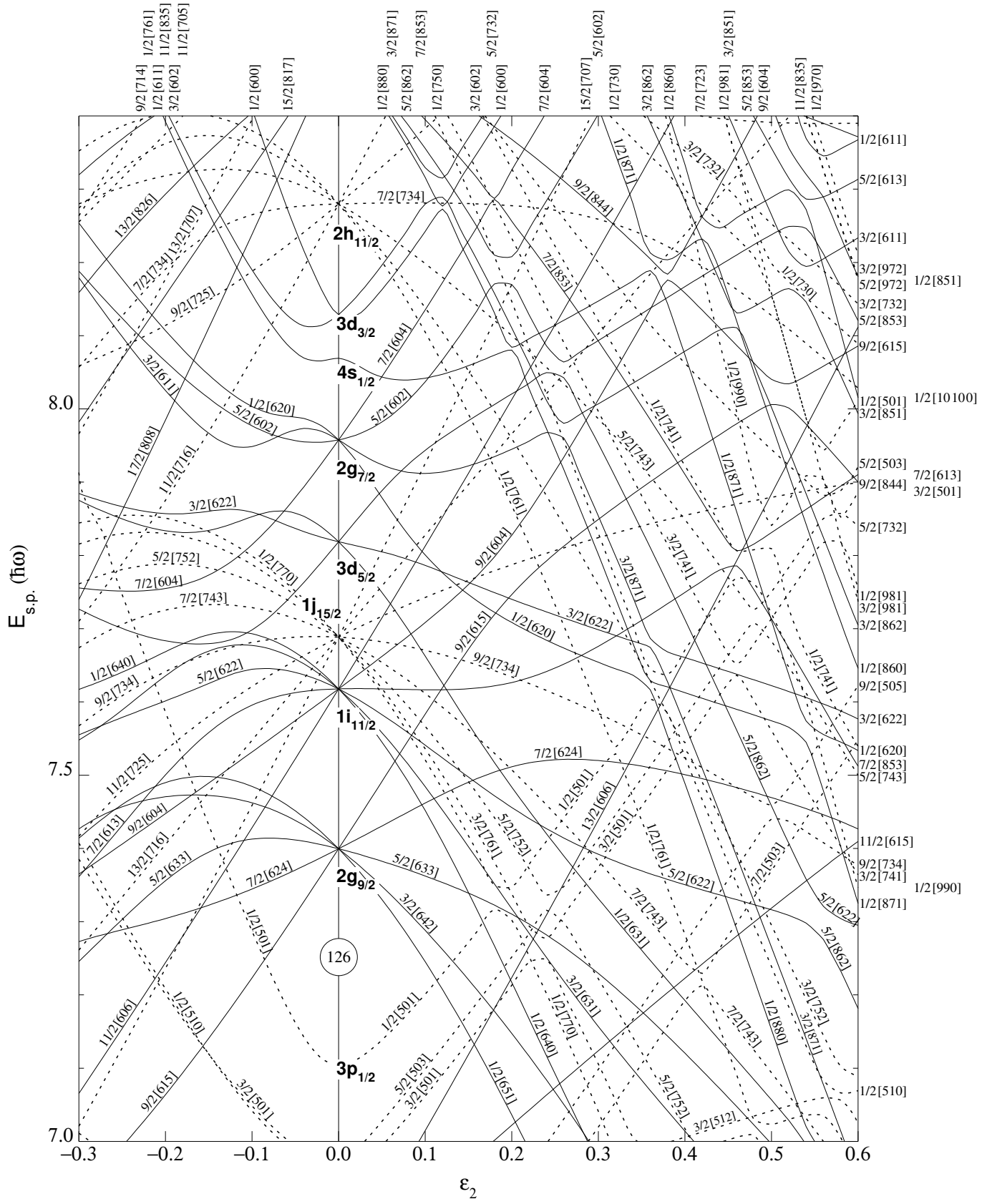

Figure 2.5: *Nilsson diagram for neutrons N≥126. Adopted from [20].*

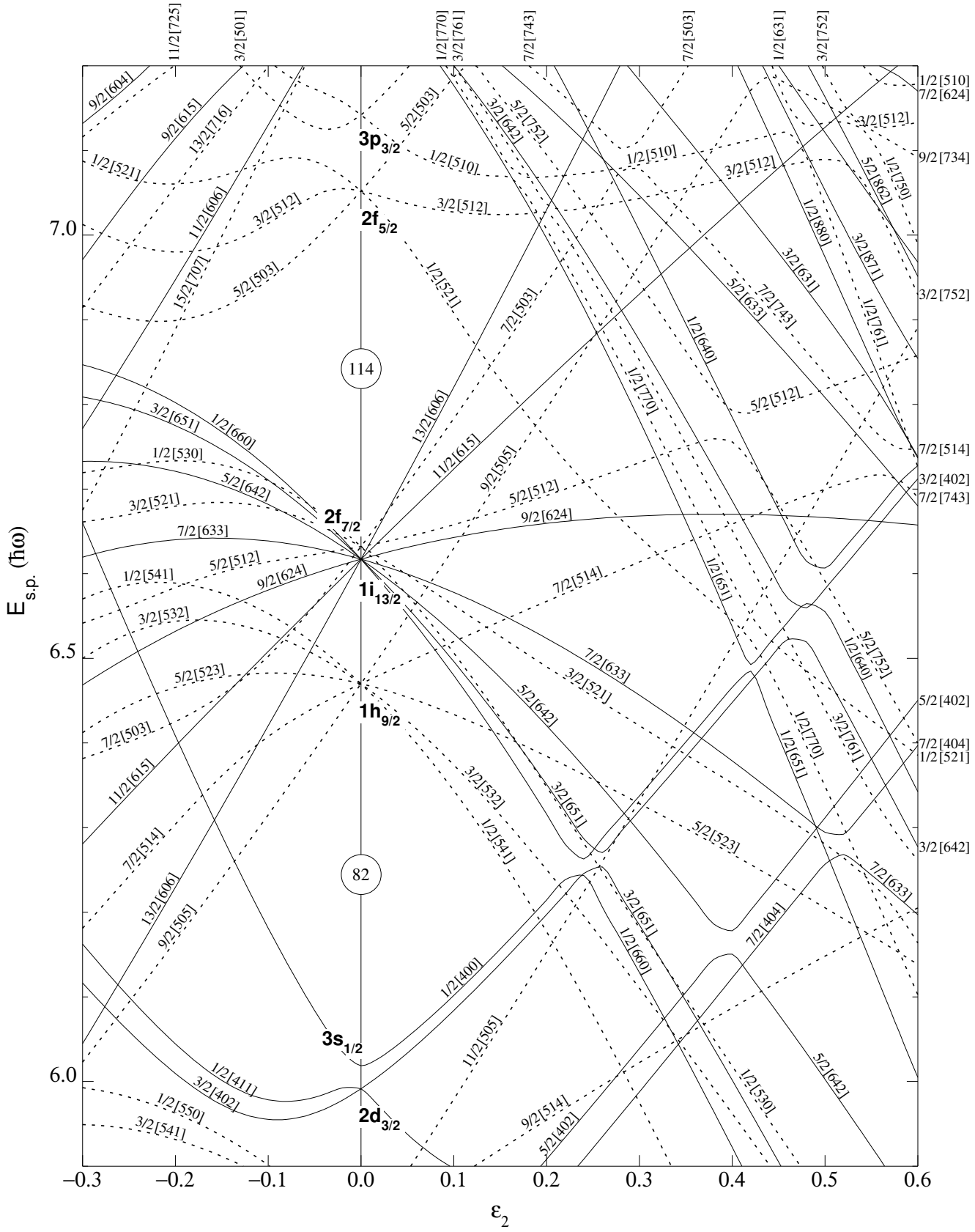

Figure 2.6: *Nilsson diagram for protons Z≥82. Adopted from [20].*

At the magic numbers low level density is evident but increases as deformation increases. Each orbital has its own unique Nilsson quantum numbers with only Ω and π being good quantum numbers. Orbitals with the same Ω cannot cross according to the Pauli principle, but may mix j values of differing energies causing them to change slope and character. The low-Ω orbitals strongly overlap with the prolate core and are thus lowered in energy with increasing deformation (the same for high-Ω and oblate shapes). The concept of intruder orbitals is evident in the deformed mid shell region, as high-j orbitals emanating from the next shell gap downslope towards the Fermi surface thus have increased chances for population by an excited particle over other orbitals in the vicinity.

2.3.4 Strutinsky Shell Correction

The shell model serves as a microscopic approach for understanding the quantum properties of the nucleus but fails to reproduce experimental evidence on the bulk properties of the nucleus, for example nuclear binding energies. Similarly the macroscopic approach is in good agreement with mass number trends, but fails to replicate the quantum nature of the constituent nucleons. To remedy this, Strutinsky [21] developed a macroscopic-microscopic approach with a smooth component of the macroscopic model (such as the LDM) with an oscillatory shell component

$$U = U_{Smooth} + U_{Osc}. \tag{2.22}$$

The binding energy of the nucleus is strongly dependent upon the level density near the Fermi surface. For regions of low level density, the nucleus is more bound than for regions of higher density. The dependence of stability on the level density helps to explain the bound nature of deformed, heavy nuclei. Energy minima can occur for deformed nuclear shapes (deformed shell gaps). The oscillatory component gives level densities at and around the Fermi surface while the smooth component replicates a constant level density. This is demonstrated in Figure 2.7.

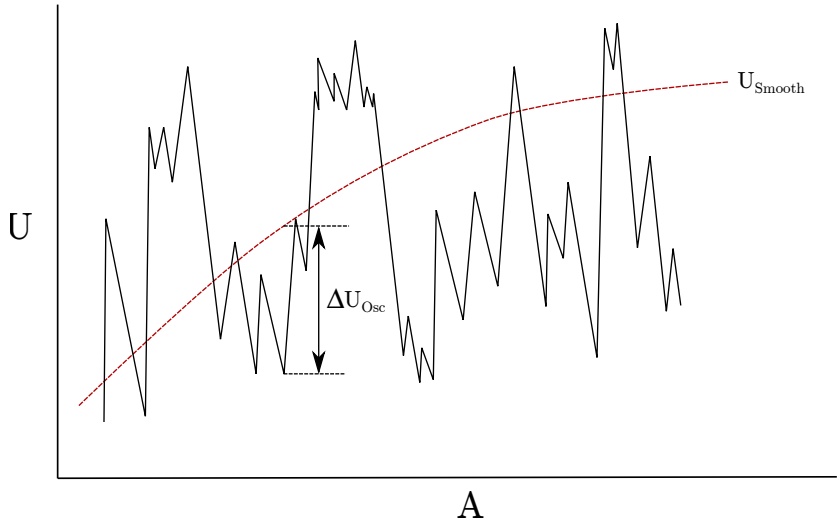

Figure 2.7: *Arbitrary nuclear property U as a function of mass number for a macroscopic-microscopic model with a smooth macroscopic component and an oscillatory single-particle model component.*

For U_{Smooth} the LDM can be used. To obtain the oscillating shell model component $\Delta U_{Osc}(= \Delta U_{Shell})$, the components of the shell model must be separated into the smoothly varying part (which does not replicate bulk nuclear properties) and an oscillatory component. The total shell model component is represented by

$$U_{Shell} = \sum_{i=1}^{A} \varepsilon_i = \bar{U}_{Shell} + \Delta U_{Shell}, \tag{2.23}$$

where ε_i are the single-particle eigenvalues for each individual nucleon. Hence,

$$U = U_{LDM} + [U_{Shell} - \bar{U}_{Shell}], \tag{2.24}$$

with U_{LDM} as the macroscopic component and $[U_{Shell} - \bar{U}_{Shell}]$ as the quantum oscillatory microscopic component.

2.4 Self-Consistent Models

A different approach is to use self-consistent models such as the Hartree-Fock method. This involves assuming a mean-field approximation as for the microscopic approach. An effective interaction is initially suggested and an average potential is identified. Solutions for the eigenstates and eigenvalues are determined which can then be solved again in an iterative process until convergence occurs. An example of the effective interaction that has proven successful in matching experimental results is the Skyrme force which uses a two-body interaction with a number of different parametrisations. A more detailed discussion of these models applied on the heavy element region can be found (for example) in a paper by Bender *et al.* [22].

2.5 Nuclear Rotation

Rotation in a spherical system is forbidden due to invariance of the nuclear wavefunction under rotation. The deformation of the nucleus introduces a new degree of freedom in the form of rotation. This allows for a definition of orientation of the nucleus about an axis. The total angular moment of the system is separated into two components, the collective rotation of the nuclear core **R** plus the contribution to the rotation from the individual nucleons **J**

$$\mathbf{I} = \mathbf{R} + \mathbf{J}, \tag{2.25}$$

with

$$\mathbf{J} = \sum_{i=1}^{A} \mathbf{j}_i, \tag{2.26}$$

as the sum of all individual valence nucleon total angular momenta. The projection of **I** onto the symmetry axis gives the quantum number K analogous to Figure 2.4.

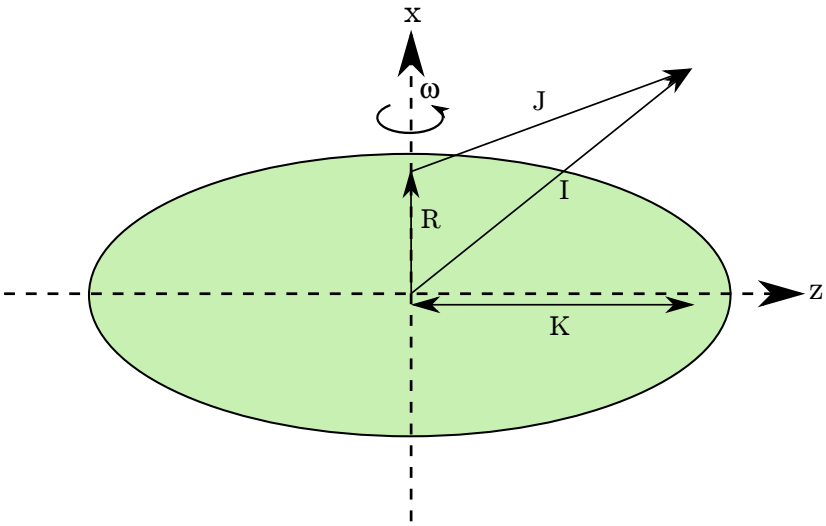

Figure 2.8: *Schematic showing the coupling between the rotating nuclear core* $\boldsymbol{R}$ *the valence nucleons* $\boldsymbol{J}$ *to sum to the total angular momentum* $\boldsymbol{I}$ *of a deformed nucleus rotating perpendicular to the symmetry axis.*

The rotational energy of the nucleus can be expressed as

$$E(I) = \frac{\hbar^2}{2\Im} I(I+1), \tag{2.27}$$

with $\Im$ as the static moment of inertia. The K quantum number is related to **J** but cannot change if **R** is varied. As a result of this a rotational band will consist of a number of states, all with the same K value upon which the band is built. An example of the structure of coupled rotational bands is shown in Figure 2.9.

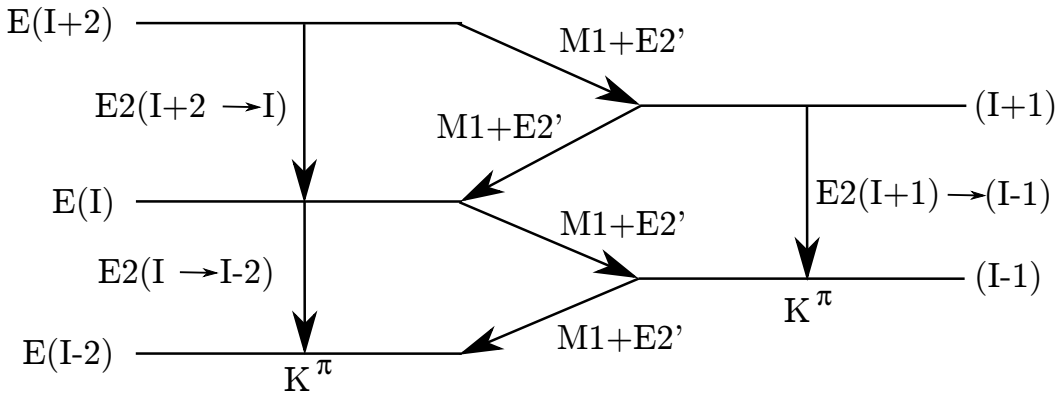

Figure 2.9: *An example of the structure of two coupled rotational bands. Stretched E2 transitions connect levels together while a combination of M1 and E2 transitions link the two bands together.*

See Section 2.8 for details on the multipolarity of the γ ray transitions. Determining the

band head configuration requires measurement of the intensity ratio between the interband and intraband transitions. This will be discussed further in Section 2.7.

2.5.1 Moments of Inertia

Nuclear matter can be modelled as an irrotational superfluid [17]. This can be seen in the definition of the moment of inertia. The moment of inertia of a deformed nucleus varies depending on the spin and can be considered partially rigid body, partially fluid body with a rigid core and a 'fluid' of valence nucleons. In addition the pairing properties of the nucleus further complicate the picture. The collective rotation of the nucleus with rotational frequency ω, can be expressed in the form of the kinematic and dynamic moments of inertia. In a classical rotational model they are expressed as

$$\Im^{(1)} = \left(\frac{2}{\hbar^2}\frac{dE(I)}{dI}\right)^{-1} = \hbar\frac{I}{\omega}, \tag{2.28}$$

for the kinematic moment of inertia and,

$$\Im^{(2)} = \left(\frac{1}{\hbar^2}\frac{d^2E(I)}{dI^2}\right)^{-1} = \hbar\frac{dI}{d\omega}, \tag{2.29}$$

for the dynamic moment of inertia, assuming that the maximum alignment of the total angular momentum is along the symmetry axis ($I_x \sim I$). The two are related to one another through

$$\Im^{(2)} = \Im^{(1)} + \omega\frac{d\Im^{(1)}}{d\omega}. \tag{2.30}$$

In a quantum system the derivatives are replaced by differentiations of quantised variables and their expectation values. In terms of transition energy,

$$\Im^{(1)} = \frac{\hbar^2}{E_\gamma}(2I - 1), \tag{2.31}$$

and,

$$\Im^{(2)} = \frac{4\hbar^2}{E_\gamma(I+2 \to I) - E_\gamma(I \to I-2)}. \tag{2.32}$$

The nucleus also has a fluid rotational component leading to deviations from this form. To match experimental data a more sophisticated approach is required involving a cranked relativistic Hartree-Bogoliubov theory. See [22] and [23] for more details.

Backbending and Alignment

As the rotational frequency of the nucleus increases the first excited band may be lowered in energy closer to the ground state band. This can then become energetically favourable and the bands cross at a critical frequency ω_c. This effect is caused by the Coriolis force acting upon two paired valence nucleons causing them to break and become aligned along the rotational axis. This causes a rapid increase in spin for small increments of rotational frequency evidenced by a 's' shaped backbend in a plot of the rotation against spin (Figure 2.10). A weaker version of a backbend can be observed as an upbend.

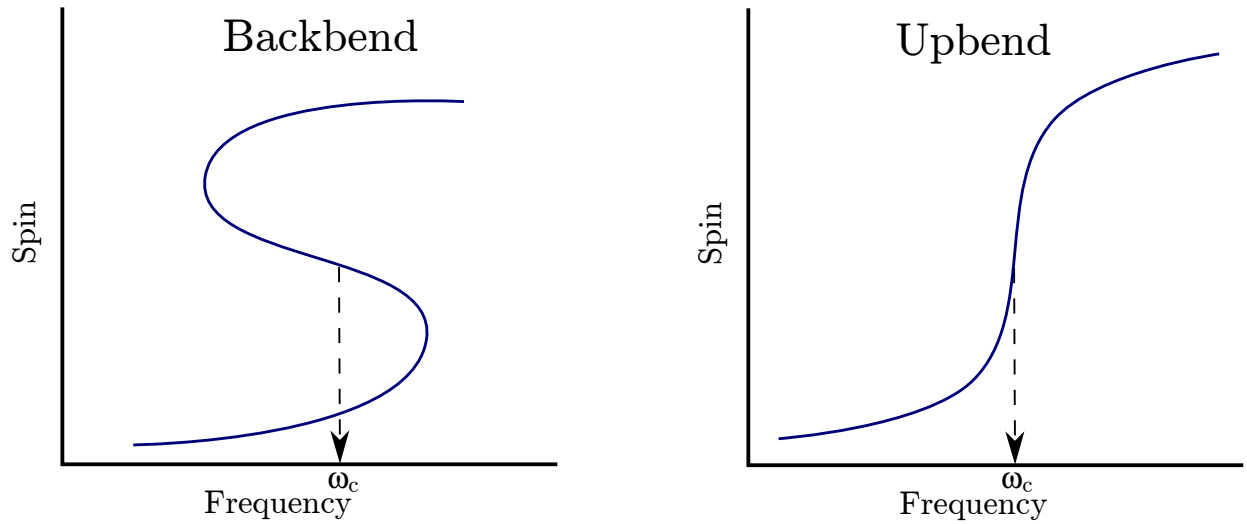

Figure 2.10: *Lowering of the first excited band causing a crossover with the ground state band (GSB) resulting in a backband. An upbend may also be observed as a band crossing with different intrinsic properties.*

2.6 Quasiparticles and Pairing

In the nuclear groundstate, the particles occupy states in accordance with the Pauli principle up to the Fermi surface. Additional excitations may then promote a single nucleon into a higher energy orbit leaving a hole in the initial orbit and thus creating a quasiparticle composed of a particle and a hole. By transforming from the residual interaction in the deformed shell model to a system of non-interacting quasiparticles, the model basis becomes simplified. Assuming a constant potential acting over the nucleus, the pair in a state ν has a potential acting on individual nucleons expressed in terms of creation and annihilation operators [17]

$$V_{pair} = -\Delta \sum_{\nu>0} \left[a^\dagger(\bar{\nu}) a^\dagger(\nu) + a(\nu) a(\bar{\nu}) \right]. \tag{2.33}$$

The creation and annihilation operators a and $a^\dagger$ represent addition and subtraction of a pair of particles to the system. Δ is the gap parameter defined in terms of the sum over two components

$$\Delta = G \sum_{\nu} U_\nu V_\nu, \tag{2.34}$$

with U_ν and V_ν being defined as the emptiness and fullness factors respectively with U_ν as the probability the orbit ν is empty and V_ν is the probability that it is filled (hence $U_\nu^2 + V_\nu^2 = 1$). G is a pairing strength parameter and is smaller for high-j orbitals, being dependent on the spatial overlap of two nucleons and scales with mass. A simple phenomenological description is given

$$G_p = \frac{17}{A}; \qquad G_n = \frac{23}{A}, \tag{2.35}$$

for protons and neutrons respectively.

The Hamiltonian describing nuclear motion is given as

$$H = H_0 + V_{pair} - \lambda \hat{N}, \tag{2.36}$$

with the energy of the individual particles contributing H_0, and with the energy increase to the

system per added particle as the chemical potential λ, thus representing the Fermi level. The λN term compensates for the Bogoliubov transformation (required for pairing) not conserving particle number. A quasiparticle has an energy relative to the ground state

$$E_\nu = \sqrt{(\varepsilon_\nu - \lambda)^2 + \Delta^2}, \tag{2.37}$$

where the energies of the single-particle states is ε_ν. The particle-hole excitation can be described by a two quasiparticle excitation for initial and final state energies given by the sum of the quasiparticle energies [16]

$$\Delta E = E_i + E_f = \sqrt{(\varepsilon_i - \lambda)^2 + \Delta^2} + \sqrt{(\varepsilon_f - \lambda)^2 + \Delta^2} \geq 2\Delta, \tag{2.38}$$

Away from the Fermi level the original particle-hole energy is apparent, but closer to the Fermi surface requires a minimum energy of 2Δ is necessary. The probability of a pair of nucleons occupying a level ε_ν is

$$P_\nu(\varepsilon_\nu) = \frac{1}{2}\left[1 + \frac{\varepsilon_\nu - \lambda}{(\sqrt{(\varepsilon_\nu - \lambda)^2 + \Delta^2})}\right]. \tag{2.39}$$

Nucleons occupying a state act to pair together in time-reversed orbits satisfying the Pauli principle. A vast swathe of experimental evidence exists for this such as the ground state of even-even nuclei having a spin and parity of $I^\pi = 0^+$. This pairing causes a smearing of the Fermi surface from the case when no pairing occurs where V_ν^2 is zero above the Fermi surface. The nucleons can scatter into higher energy orbits creating an occupation probability greater than zero above the Fermi surface.

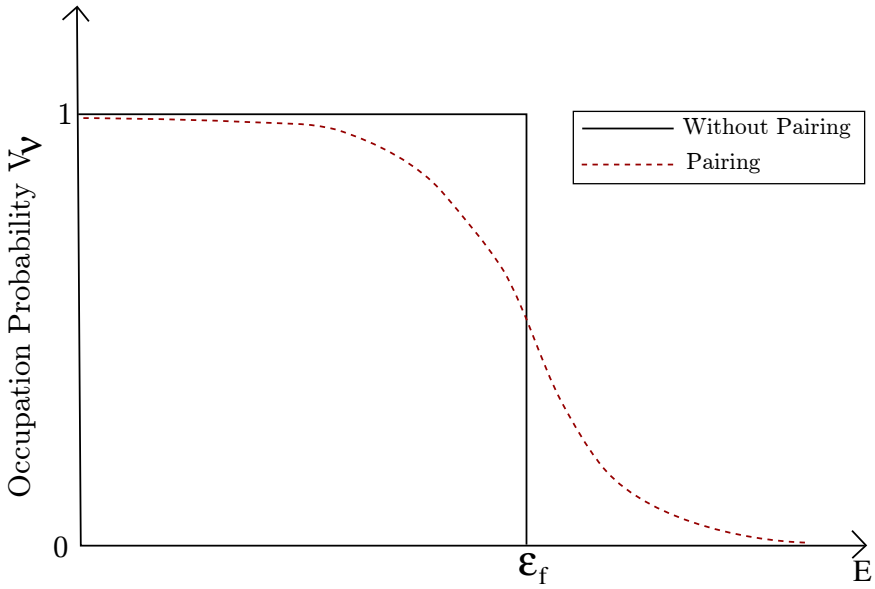

Figure 2.11: *The occupation probability of a particle in the cases of no pairing and pairing. Pairing allows for particles to occupy states above the Fermi surface, ε_f.*

2.7 g-Factors

The nucleus is a deformed rotating charged body, thus a magnetic dipole moment is created by the orbital motion of the protons and the intrinsic spins of all nucleons. This can be expressed in terms of the contribution of the nuclear core and the valence nucleons to the rotation

$$\mu = \left(g_R I + [g_K - g_R] \frac{K^2}{I+1} \right) \mu_N, \tag{2.40}$$

where μ_N is the nuclear magneton ($\mu_N = \frac{e\hbar}{2m_p c}$), g_K is the single valence nucleon's contribution, and g_R is the collective rotational contribution of the nuclear core to the nuclear magnetic moment. This can be approximated as $g_R \approx Z/A$ for a uniformly rotating charged system. The g_R factor has experimentally been shown to have values consistently low across the rare earth mass region such that a quenching factor is appended [24]. However this factor is not known beyond the mass region $140 \leq A \leq 200$ with experimental data limited. Pairing between nuclei simplifies things as the magnetic component is zero for J=0. The unpaired valence nucleon

gyromagnetic factor g_K is given as,

$$g_K = \frac{1}{\Omega} \langle \Omega | \, g_l \mathbf{l} + g_s \mathbf{s} \, | \Omega \rangle \, ; \qquad (K \neq 0), \tag{2.41}$$

$$= g_l \pm \frac{1}{2l+1}[g_l - g_s],$$

where $\mathbf{l}$ is the orbital angular momentum, and $\mathbf{s}$ is the spin and g_l and g_s are their g-factors respectively. Thus the g_K value is dependent upon the coupling between intrinsic spin and orbital angular momentum. The g-factors can be used to determine the single-particle (or multi-particle) configuration of the nucleus. This will be demonstrated in this study.

2.8 Decay Modes of Excited Nuclear States

The modes of de-excitation of the nucleus provides information for the experimentalist on the structure and mechanisms of the nucleus. Of particular importance in this study is the detection of prompt γ ray and internal conversion electron (ICE) emission.

2.8.1 Electromagnetic Decay

After compound nucleus formation, the nucleus de-excites through the emission of E1 multipolarity statistical γ rays following which it decays along the yrast line towards the ground state. The yrast line represents those states with lowest energies for given spins. The decay along the yrast line occurs primarily through γ ray or competing internal conversion electron emission. Measurement of this provides the experimentalist with crucial information on single-particle structure and collective behaviour in the nucleus.

Gamma Decay

One form of de-excitation is via the emission of γ ray photons. Gamma rays remove energy and angular momentum from the nucleus and can cause a change in parity between levels. The

energy of the γ ray is given as the difference between an initial energy state i and a final state f

$$E_\gamma = E_i - E_f. \tag{2.42}$$

The γ rays are characterized by their angular momentum L and parity π and are subject to selection rules.

- Angular momentum is conserved for a decay between states,

$$\boldsymbol{I}_i = \boldsymbol{L} + \boldsymbol{I}_f, \tag{2.43}$$

- The angular momentum selection rules fall within the vector sum interval

$$|I_i - I_f| \leq L \leq |I_i + I_f| \qquad L \neq 0, \tag{2.44}$$

  for states with a total angular momentum I. A transition $0^\pi \rightarrow 0^\pi$ via a monopole $L = 0$ emission cannot proceed through γ ray decay due to the photon having non-zero angular momentum. However this is allowed for conversion electron de-excitations (see page 35).

- Electric transitions have even (positive) parity when $L =$ even whereas magnetic transitions have even parity when $L =$ odd. The parity of the electromagnetic field is expressed as

$$\Delta\pi(EL) = (-1)^L \tag{2.45}$$

$$\Delta\pi(ML) = (-1)^{L+1}$$

  such that E1, M2... are odd and M1, E2... are even parity transitions. Odd parity infers a change in parity whereas parity is retained between states for even γ ray transitions.

The transition probability of a photon of energy $\hbar\omega$ and angular momentum L from an initial state I_i to a final state I_f is expressed as [17]

$$T(\sigma L; I_i \to I_f) = \frac{8\pi(L+1)}{\hbar L[(2L+1)!!]^2}\left(\frac{E_\gamma}{\hbar c}\right)^{2L+1} B(\sigma L; I_i \to I_f), \qquad (s^{-1}) \qquad (2.46)$$

with $B(\sigma L; I_i \to I_f)$ as the reduced transition probability. This is expressed in terms of reduced matrix elements. The reduced elements contain the nuclear structure information and can be deduced to give direct knowledge on the initial and final states. For electric transitions the reduced transition probability is

$$B(EL; I_i \to I_f) = (2I_i+1)^{-1}\left|\left\langle f \left|\left|\hat{M}(EL)\right|\right| i\right\rangle\right|^2, \qquad (2.47)$$

and for magnetic

$$B(ML; I_i \to I_f) = (2I_i+1)^{-1}\left|\left\langle f \left|\left|\hat{M}(ML)\right|\right| i\right\rangle\right|^2, \qquad (2.48)$$

with $\hat{M}(EL)$ and $\hat{M}(ML)$ being the electric and magnetic multipole operators respectively. Based on these, estimates can be made on the transition rates. These are known as the Weisskopf estimates and are listed in Table 2.1 for lower multipole orders [17].

σ L	$T(\sigma L)$ (s^{-1})	$B(\sigma L)$ (W.u.)
E1	$1.59 \times 10^{15} E^3 \cdot B(E1)$	$6.45 \times 10^{-2} A^{2/3}$
E2	$1.22 \times 10^{9} E^5 \cdot B(E2)$	$5.94 \times 10^{-2} A^{4/3}$
E3	$5.70 \times 10^{2} E^7 \cdot B(E3)$	$5.94 \times 10^{-2} A^{2}$
E4	$1.69 \times 10^{-4} E^9 \cdot B(E4)$	$6.29 \times 10^{-2} A^{8/3}$
M1	$1.78 \times 10^{13} E^3 \cdot B(M1)$	1.79
M2	$1.37 \times 10^{7} E^5 \cdot B(M2)$	$1.65 A^{2/3}$
M3	$6.39 E^7 \cdot B(M3)$	$1.65 A^{4/3}$
M4	$1.90 \times 10^{-6} E^9 \cdot B(M4)$	$1.75 A^{2}$

Table 2.1: *Transition probabilities $T(\sigma L)$ and Weisskopf single-particle estimates $B(\sigma L)$. The units for $B(\sigma L)$ are Weisskopf units (W.u.) The energy (E) is in MeV [17].*

It is clear from Table 2.1 that γ rays are most likely to have a lower order multipole with the probability diminishing by orders of magnitude for each increase in angular momentum. One can also see that electric transitions are favoured over magnetic. The reduced transition probability for M1 transitions is related to the g-factors in rotational nuclei

$$B(M1; I \to I-1) = \frac{3}{4\pi}[g_K - g_R]^2 K^2 |\langle IK10|\ (I-1)K\rangle|^2 \qquad (\mu_N)^2, \tag{2.49}$$

but for E2 transitions there is no dependence on the collective or single particle g-factors, with the charge distribution of the nucleus (related to the intrinsic quadrupole moment Q_0) being the determining factor here,

$$B(E2; I \to I-2) = \frac{5}{16\pi} Q_0^2 |\langle IK20|\ (I-2)K\rangle|^2 \qquad (eb)^2. \tag{2.50}$$

Based on this, the ratio of reduced transition probabilities (branching ratio) is sensitive to the squared ratio of the rotational g-factors and the electric quadrupole moment (charge distribu-

tion) of the nucleus,

$$\frac{B(M1)}{B(E2)} \propto \frac{(g_K - g_R)^2}{Q_0^2}, \tag{2.51}$$

As $g_K \to g_R$ the ratio weakens. Thus for a strongly coupled rotational band with interlinking M1 transitions the competition of the flow of intensity between one or two units of spin change is determined by the g_K factor. Note that the interband transitions undergo one unit of spin change and thus can proceed via M1 or E2 transitions. The multipole mixing ratio (δ) gives a measure of the ratio of M1 compared to E2 transitions in this $\Delta I = 1$ transition. Measuring the intensity ratio (λ) between the interband (mixed M1+E2') and intraband (stretched E2) transitions provides information on the single-particle structure the bands are built upon.

Transitions between $0^\pi \to 0^\pi$ states is possible only through E0 transitions. Predominantly this is via conversion electron emission with a single γ ray transition forbidden through angular momentum conservation. Measurement of these electrons provides information on changes of the nuclear surface [25]. For $0^\pi \to 0^\pi$ levels this is predominately through ICE emission. However I→I transitions where I≠0 can be a combination of E0 ICEs and higher order multipolarity γ rays and electrons.

Internal Conversion

The second form of electromagnetic decay is in the form of internal conversion electron emission. The electromagnetic multipole field of the nucleus interacts with the atomic shell electrons, the electron orbitals partly penetrating the nucleus [26] causing them to be ejected with energy

$$E_e = E_\gamma - E_{B\ell}, \tag{2.52}$$

with E_γ being the transition energy and E_{Bl} as the binding energy of the electron in a given atomic shell ℓ (= K, L, M...). The emission of an X-ray photon follows electron ejection with an outer orbiting electron filling the hole left by the ejected electron. The internal conversion coefficient (ICC or α) provides a measure of the ratio between electrons emitted compared to

γ rays for a given decay energy of a transition.

$$\alpha = \frac{\lambda_e}{\lambda_\gamma}. \tag{2.53}$$

Based on this, the total probability of decay, λ can be expressed in terms of the contribution from γ rays plus the contribution from conversion electrons

$$\lambda = \lambda_\gamma(1 + \alpha). \tag{2.54}$$

The total ICC is the sum of all atomic shell components

$$\alpha = \alpha_K + \alpha_L + \alpha_M + ... \tag{2.55}$$

for which each shell component can be expanded into their degenerate substates (for example the L shell ICC is given as $\alpha_L = \alpha_{LI} + \alpha_{LII} + \alpha_{LIII}$). Assuming a simple, non-relativistic picture in which the nucleus is taken to be a point and energies above a certain threshold, the ICCs can be roughly approximated for electric transitions

$$\alpha(EL) \simeq \frac{Z^3}{n^3}\left(\frac{L}{L+1}\right)\left(\frac{e^2}{4\pi\varepsilon_0\hbar c}\right)^4\left(\frac{2m_ec^2}{\hbar\omega}\right)^{L+5/2}, \tag{2.56}$$

and for magnetic,

$$\alpha(ML) \simeq \frac{Z^3}{n^3}\left(\frac{e^2}{4\pi\varepsilon_0\hbar c}\right)^4\left(\frac{2m_ec^2}{\hbar\omega}\right)^{L+3/2}. \tag{2.57}$$

Both schematic equations demonstrate the strong dependence on a number of key factors. Proton number scales cubically such that for heavier elements conversion is dominant at lower transition energies compared to lighter nuclei. Principal quantum number n is inverse to this, and hence higher atomic shell electrons contribute less to conversion. The transition energy dependence $\hbar\omega$ results in lower energy having much larger conversion. While these equations give a reasonable description of the physical properties affecting ICCs values, it is clear in the energy range probed that the assumption of $E_e \ll m_ec^2$ is not valid and more rigorous models

such as the Hartree-Fock approach must be used to attain theoretical coefficients. An online calculator BRICC uses similar advanced models in ICC calculations for a given transition energy and multipolarity [27]. Data obtained from this is plotted in Figure 2.12. A number of relations discussed are demonstrated with calcium and nobelium compared.

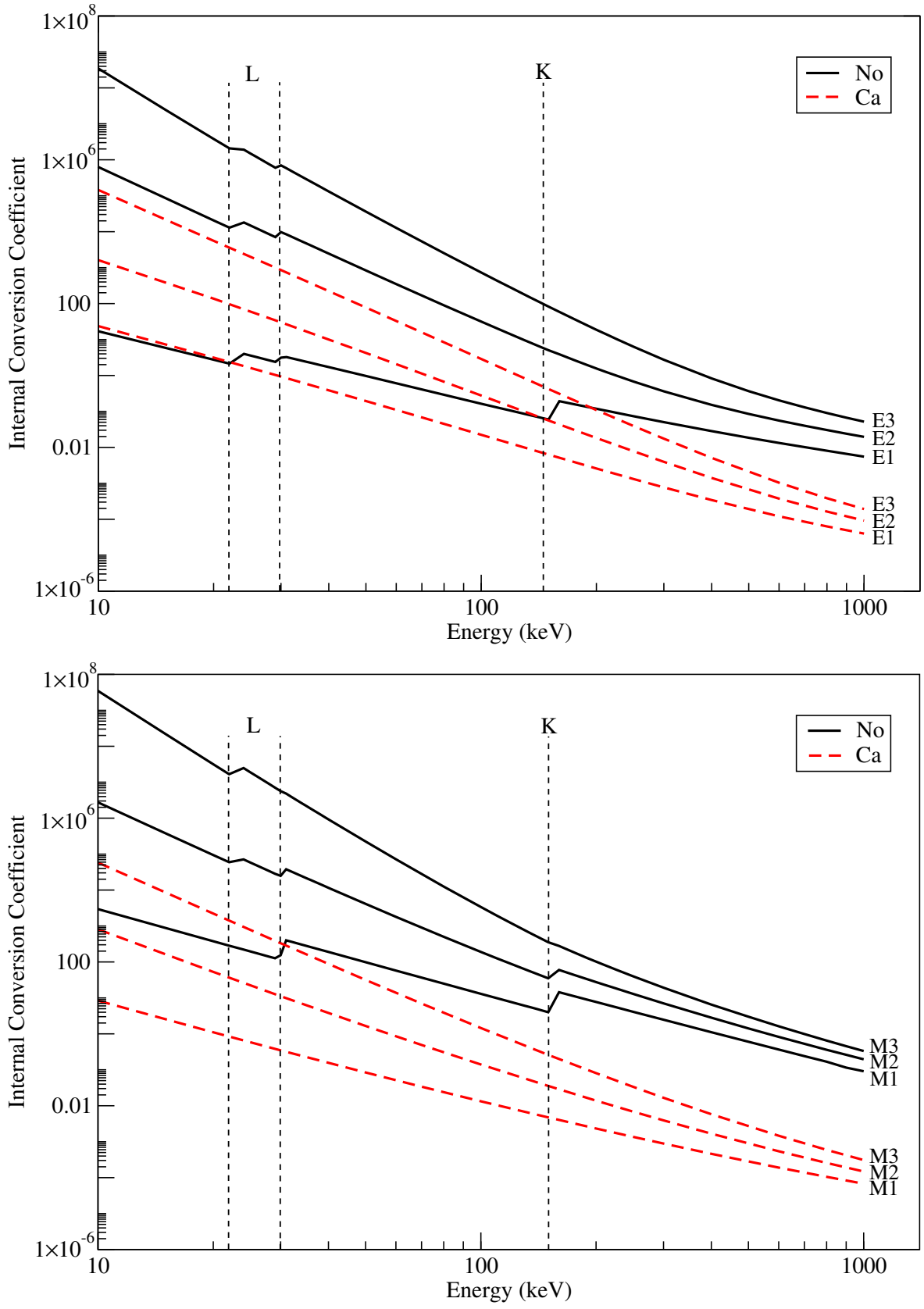

Figure 2.12: *A demonstration of the dependence of the ICC with Z, energy, and lower order multipolarity for electric and magnetic transitions. Calcium (Z=20) and nobelium (Z=102) are compared. The K and L bound shells are labelled for No. All of the Ca and remaining No shell binding energies are below the 10 keV threshold.*

From the plot, one can see that the magnetic multipoles have much larger conversion compared to electric. Furthermore, at lower transitions energies the level of conversion between the two elements differs by several orders of magnitude underlining the importance of electron measurements during the study of the heavier elements.

The ICC is sensitive to the multipolarity and mixing ratios of transitions. Comparisons between measured values and calculations can be useful for testing spin and parity assumptions for given states through determination of the multipolarity.

Due to the complex nature of the overlap of the electron wavefunction with the nuclear wavefunction, at lower energies L_2 shell electron emissions are dominant over L_1 shell emission for E2 transitions. For M1 transitions the K shell dominates providing that it the transition is above the K electron binding energy. This feature varies with energy, at higher energies one shell may become more dominant than others at a lower energy.

The multipole mixing ratio whereby more than one multipole may be possible for a given transition can be determined through ICC measurements. This is a result of the internal conversion coefficient being independent of transition matrix elements (with the exception of monopole E0 transitions) but sensitive to the multipolarity. For example the M1+E2' multipole mixing can be determined using a combination of calculated and measured values

$$\delta^2 = \frac{\alpha_K^t(M1) - \alpha_L^t(M1)\left(\frac{\alpha_K}{\alpha_L}\right)_m}{\alpha_L^t(E2)\left(\frac{\alpha_K}{\alpha_L}\right)_m - \alpha_L^t(E2)}, \tag{2.58}$$

with t representing theoretically calculated values and m the experimentally measured ratio between K- and L- shell electrons.

2.8.2 Alpha Decay

Alpha decay is one of the prominent modes of transmutation in the heavy actinide region. The α particle is a $^4He^{2+}$ nucleus, which is emitted from the mother nucleus with discrete energy E_α. The decay mechanism is given as

$$ {}^{A}_{Z}X_N \rightarrow {}^{A-4}_{Z-2}Y_{N-2} + \alpha, \tag{2.59} $$

for a mother nucleus X (with mass m_X) and a daughter nucleus Y (mass m_Y). Conservation of energy results in the Q-value of the process,

$$ Q = (m_X - m_Y - m_\alpha)c^2 = T_Y + T_\alpha. \tag{2.60} $$

The Q value is the sum of the kinetic energy of the decay fragments, for spontaneous α emission to occur $Q > 0$. The α particle will remove angular momentum from the mother nucleus in the range $|I_i - I_f| < I_\alpha < I_i + I_f$ and may change parity by $(-1)^l_\alpha$. The mechanism behind α decay is described as the ^{4}He nucleus preforming in the nucleus and will have a probability of emission via tunnelling through the Coulomb barrier. The probability of α emission is given as

$$ P_{\alpha-decay} = P_{preform}P_{tunnel}. \tag{2.61} $$

The probability of an α particle preforming is determined by the reduced α decay width

$$ \delta^2 = \frac{\lambda h}{P_{tunnel}}, \tag{2.62} $$

where λ is the partial decay width. Determining this probability can give an insight into the structure of the mother nucleus since the half-life is dependent upon this variable. The tunnelling probability is expressed as

$$ P_{tunnel} = e^{-2G}, \tag{2.63} $$

where G is the Gamow factor which represents the region of barrier that must be penetrated before α emission occurs.

A number of different states in the daughter nucleus may be populated resulting in a fine structure across the α particle energy range. This provides information on the structure of the single-particle levels populated in the daughter nucleus. If a change in angular momentum occurs between the mother and daughter levels populated then the decay may be hindered due to the centrifugal barrier, increasing the half-life. The hindrance factor is given as

$$H.F. = \frac{\delta^2_{g.s.}}{\delta^2_{e.s.}}, \tag{2.64}$$

with $\delta^2_{g.s.}$ as the ground state to ground state and $\delta^2_{e.s}$ as the ground state to excited state reduced α decay widths.

Chapter 3

Experimental Setup and Details

Producing heavy elements for experimental studies provides a number of technical challenges. Low production cross sections and short half-lives require novel experimental apparatus and techniques. The development of multi-detector systems such as SAGE, RITU and GREAT, combined with techniques such as recoil-tagging and recoil-decay tagging have allowed for a full investigation into the heavy actinide region focussed around Z=102. This section contains an overview of the apparatus and techniques used in this experiment.

3.1 Production of ^{253}No

The experiment was performed at the JYFL Accelerator Laboratory at the University of Jyväskylä, Finland. A $^{48}Ca^{10+}$ ion beam is produced in the Electron Cyclotron Resonance Ion Source (ECRIS) and accelerated by the K130 cyclotron to a beam energy of 219 MeV was incident upon a 400 µg/cm^2 ^{207}Pb target in the reaction ^{207}Pb(^{48}Ca, 2n)^{253}No. This results in a fusion-evaporation reaction, a common experimental method in creating heavier nuclei towards the proton dripline.

3.1.1 Heavy-Ion Fusion Evaporation

Fusion-evaporation reactions optimise the production cross sections for heavier elements, as well as populating the high angular momentum states required for this study. The standard reaction can be described as

$$a + X \rightarrow Y^* \rightarrow Z + b \tag{3.1}$$

which represents a light projectile, a incident upon a heavier target X. This creates an excited compound nucleus Y^* which subsequently decays to Z, releasing light evaporation particles b. The lighter projectile (in this experiment ^{48}Ca) requires a sufficient amount of energy to overcome the Coulomb barrier. For a spherical nucleus this is expressed as [28]

$$E_c \propto \frac{Z_p Z_t}{(A_p^{\frac{1}{3}} + A_t^{\frac{1}{3}})}, \tag{3.2}$$

where Z_p and Z_t are the proton numbers and A_p and A_t are the atomic numbers for projectile and target respectively. In order to optimise the production of the ^{253}No the beam energy utilised was 219 MeV. This selection was based upon measurements performed by Oganessian *et al.* [29], which determined the optimal cross section to be approximately 1 µb. The cross sections for ^{48}Ca on various lead isotopes are shown in Figure 3.1. The sequence of events following fusion evaporation are shown in Figure 3.2.

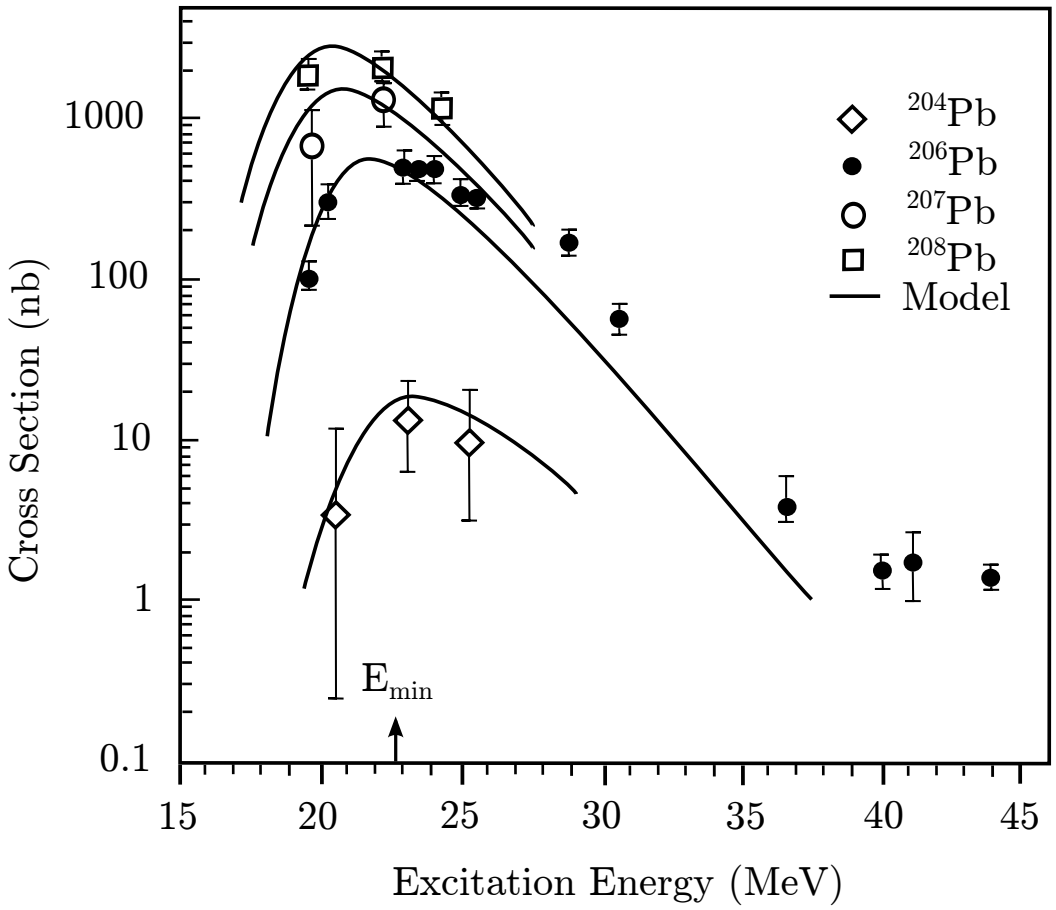

Figure 3.1: *Predicted and measured fusion-evaporation cross sections for ^{48}Ca incident upon Pb isotopes [29]. The arrow (E_{min}) at 22.8 MeV refers to the Bass barrier [30] for a ^{48}Ca projectile on a ^{207}Pb target. The solid lines represent model calculations.*

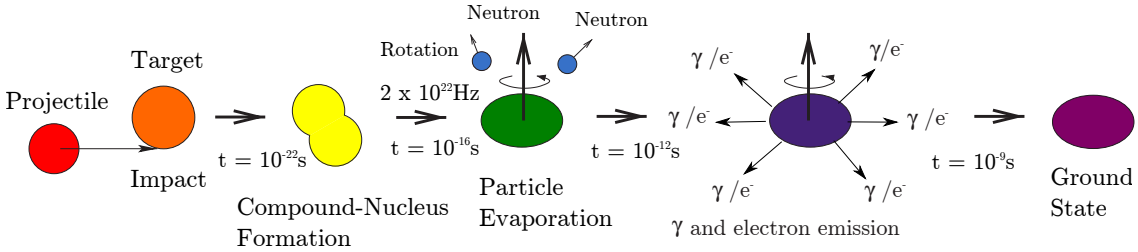

Figure 3.2: *A schematic of the fusion-evaporation reaction. Adapted from [31].*

Around 10^{-22} s after fusion has occurred the sequential emission of lighter particles (evaporation) acts to remove energy from the excited system. Neutrons are typically favoured for this, removing large amounts of energy for small values of angular momentum. The reaction channel studied was two neutron evaporation, which takes approximately 10 MeV of energy

from the excited compound nucleus. Additional energy and angular momentum is then removed via statistical γ rays. These carry large energies for low values of angular momentum but are experimentally unresolvable. Once the yrast line is reached, there is a rapid decrease in angular momentum for smaller energies in the form of γ rays and conversion electrons until the ground state is reached. It is these transitions along the yrast line that are measured in this study.

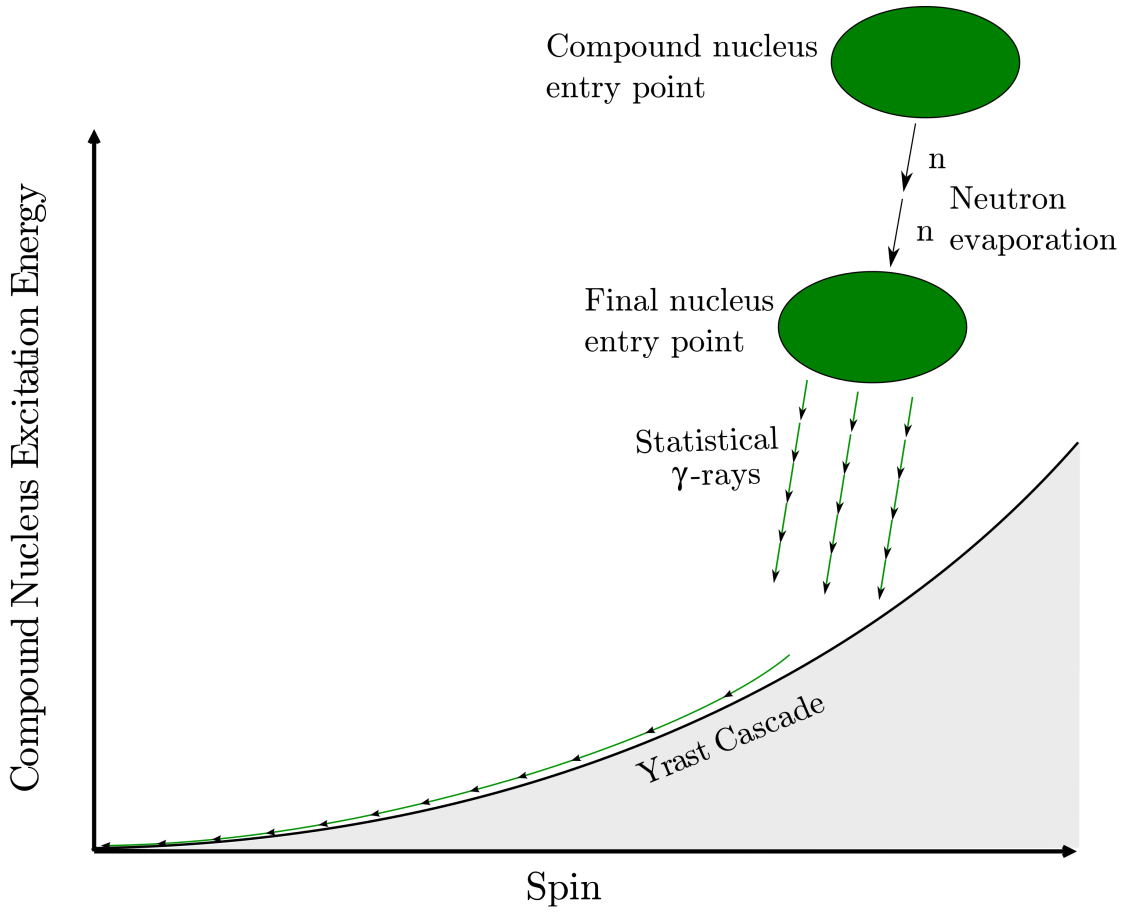

Figure 3.3: *The de-excitation process that occurs during a fusion evaporation reaction after compound nucleus formation.*

3.2 Experimental Apparatus

This experiment used the SAGE-RITU-GREAT setup. Internal Conversion Electrons and γ rays, which are emitted following fusion-evaporation, are detected at the target position by SAGE. Newly created recoil ions pass through the RITU gas-filled separator, filtering out unwanted reaction products, and are implanted in the GREAT focal plane spectrometer. Charged particles and γ rays produced from α and isomeric decays are detected by the array of detectors that GREAT is comprised of, allowing for correlations to be drawn between recoil implantation and prompt emission at the target position.

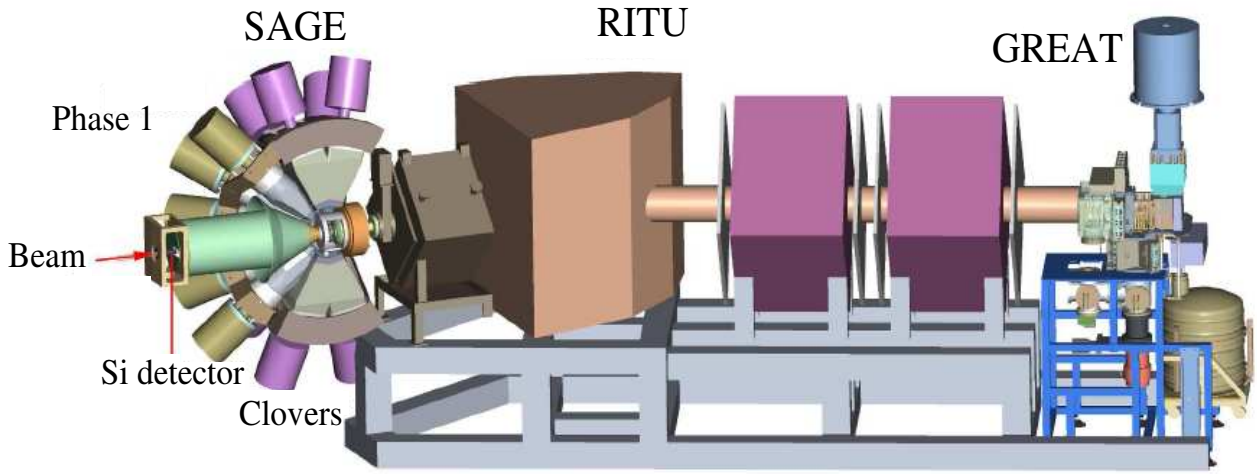

Figure 3.4: *Diagram of the experimental setup [32].*

3.2.1 SAGE

The **S**ilicon **A**nd **Ge**rmanium detector [33] comprises of the JUROGAM II high purity germanium detector array for prompt γ ray detection, and a highly segmented (90 pixel) silicon detector for ICE detection. Figure 3.5 shows a cross sectional diagram of the SAGE spectrometer.

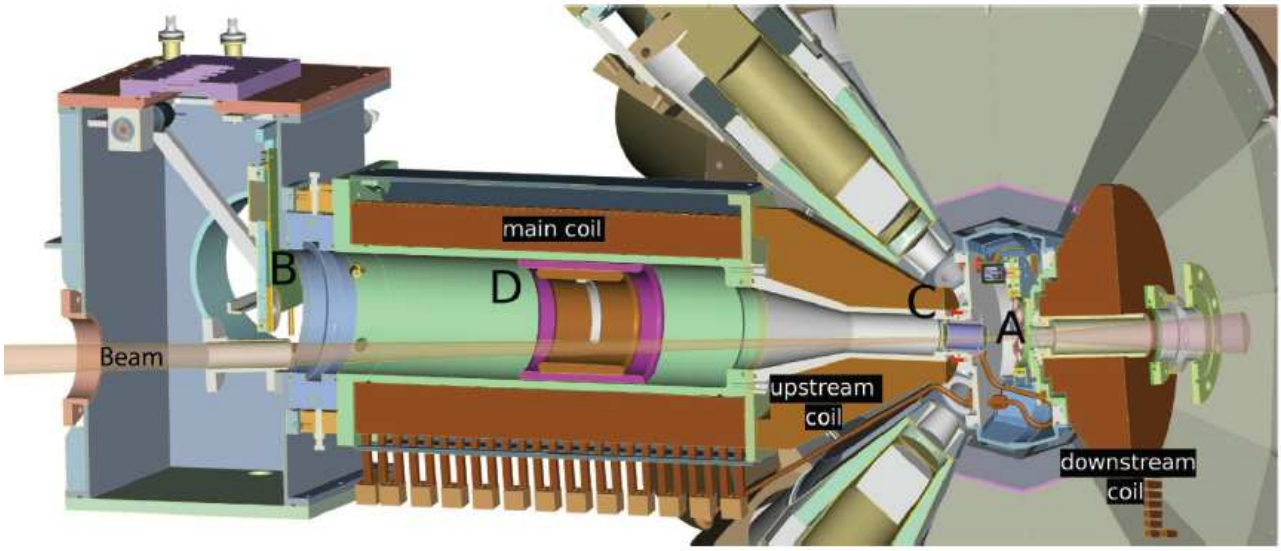

Figure 3.5: *The* SAGE *spectrometer showing: The target position (A), silicon detector (B), carbon foil unit (C) and high voltage barrier (D). Each element is detailed below. The phase one and clover germanium detectors of* JUROGAM II *are also visible surrounding the target position [32].*

Silicon Detector

The electron detector is a 50 mm diameter highly segmented silicon detector organised into a concentric ring structure with 90 segments. It is designed to obtain an even distribution of electron counts across the detector and minimise electron scattering between the segments. Its location at a backwards angle of 3.2° relative to the beam axis aids in the reduction of low energy δ-electrons. The silicon detector is mounted on a printed circuit board (PCB) which also houses the preamplifers and power connection for each of the segments. An ethanol cooling circuit is applied to the casing of the PCB to reduce electronic noise in the detector and prevent overheating.

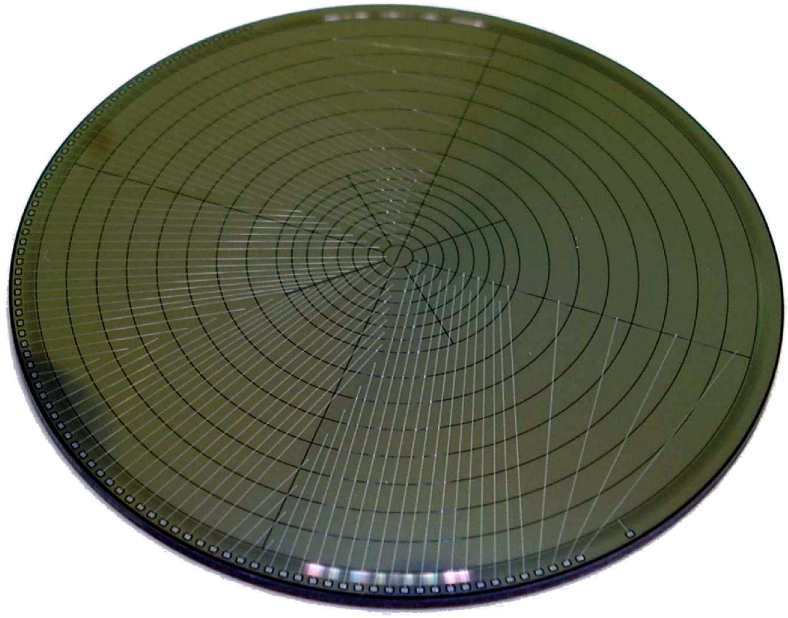

Figure 3.6: *A photograph of the silicon detector used in* SAGE. *The individual pixels and signal wires are visible [32].*

The number of segments increases towards the centre of the detector. The electrons are focussed on this area around the magnetic field axis and so a uniform count rate distribution and optimised efficiency is achieved. Setting a minimum segment size of 1 mm helps to reduce electron scattering between segments, promoting full energy deposition in a given segment.

Magnetic Field

A solenoid coil induces a magnetic field to transport the electrons from the target position to the detector (located upstream from the target). Near collinear geometry between the beam axis and the solenoid axis also helps to reduce Doppler broadening. Three magnets are employed for this. One located downstream helps to compensate for the absence of a magnetic field at the target position which ultimately produces a mirroring effect for electrons emitted in the direction of the target. The upstream and main coils transport the electrons to the detector along the beam axis. A simulation of the magnetic field using the Monte Carlo package SOLENOID [34] (utilised in [35]) is shown in Figure 3.7.

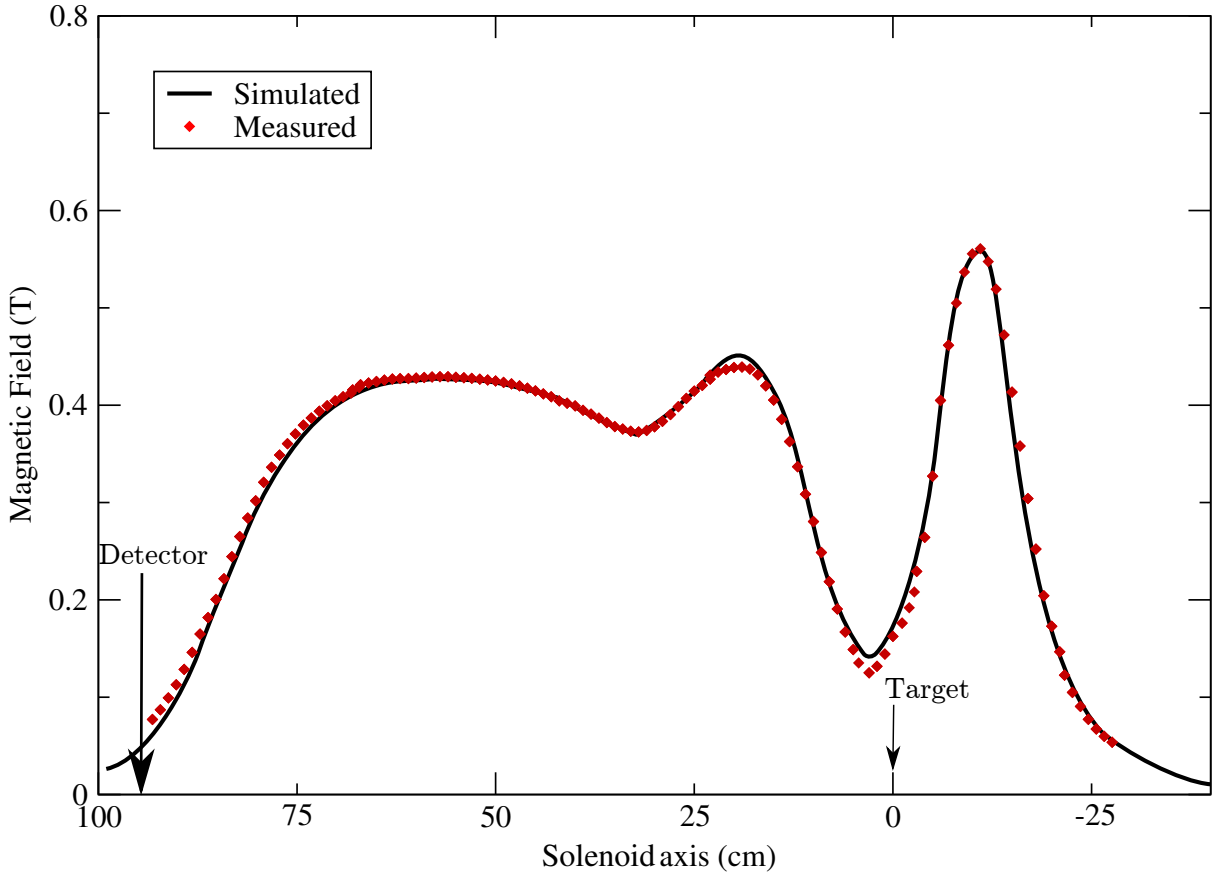

Figure 3.7: SAGE *magnetic field as a function of position parallel to the beamline. Based on a simulation with a solenoid current of I=700 A. Data acquired from [36].*

High Voltage Barrier

A high voltage barrier is situated between the beam and the target. This is in place to drastically reduce the flux of delta electrons. As with all detector systems, there are a number of experimental challenges to overcome in order to optimise the use of the electron spectrometer. One of the issues is the beam and target ionisation producing a flux of low energy electrons (δ-electrons) creating a low energy background in electron spectra. As discussed, the high voltage barrier helps to suppress these electrons, however, not all are stopped. The maximum delta electron energy is given for electrons emitted in a downstream direction by [37]

$$E(\delta) = 4\sqrt{\frac{m_e}{m_p}E_k E_p} + 4\frac{m_e}{m_p}E_p, \tag{3.3}$$

for beam particles of mass m_p, and energy E_p, with E_k as the K-shell electron binding energy, and m_e the electron rest mass. For a ^{48}Ca beam on a Pb target at 219 MeV, the maximum δ-electron energy is 69 keV. However, the majority of the electrons will have a lower energy than this and will contaminate this region. The high voltage barrier was set to -38 kV during the experiment, a compromise between allowing some δ-electron flux without impacting on the energetic region of interest.

Carbon Foil Unit

The setup of SAGE is such that two different pressure regions are required: The high voltage barrier under high vacuum of $\sim 1 \times 10^{-6}$ mbar, and the RITU gas filled separator with 1 mbar of He gas. To separate these two regions, two 50 µg/cm^2 thick C foils are placed in the aperture between the target and the upstream beamline region. This is to ensure there are no losses for recoil transmission into RITU, and to maintain the secondary purpose of the He gas for target cooling. Typical energy loss for electrons as a result of the carbon foil unit was measured to be 0.5 keV for 100 keV electrons [33].

JUROGAM II

The JUROGAM II array consists of 24 high-purity germanium (HPGe) coaxial clover detectors [38], and 15 HPGe Phase 1 detectors [39, 40] designed to measure prompt γ ray emission. The detectors are mounted in a geometry to maximise the solid angle coverage around the target position. When the electron spectrometer is in place, a ring of 5 Phase 1 detectors is removed due to spatial constraints. The details of the physical operation of semiconductor germanium detectors are not discussed here in any detail. Reference [41] is an excellent resource for such information. A diagram of a JUROGAM II clover detector is shown in Figure 3.8.

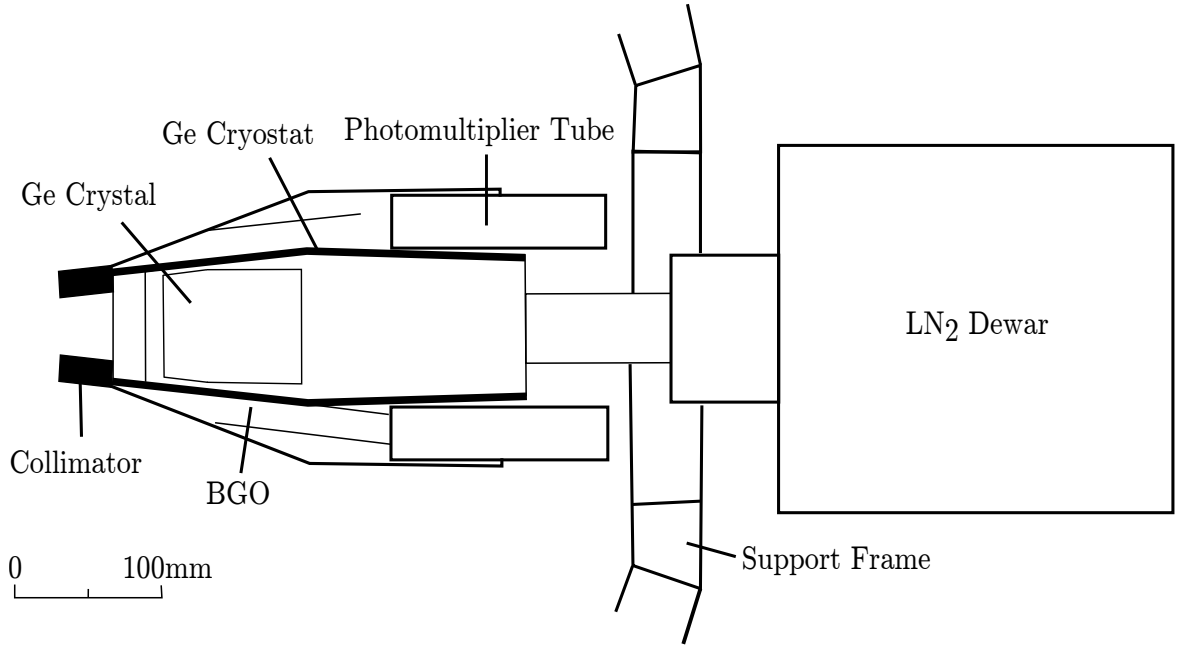

Figure 3.8: *A diagram of a* JUROGAM II *Phase 1 detector. Adapted from [39].*

The HPGe crystals are surrounded by bismuth germanate (BGO) crystals coupled to photomultiplier tubes in order to veto incomplete detection of Compton scatter events in the JUROGAM II germanium detectors, and hence improve the peak to Compton ratio [40]. A collimator reduces the flux of photons that scatter off the frame of the setup into the detector, while an absorber layer on the face of the detector reduces low energy X-rays from the frame. The crystals are cooled using liquid nitrogen to a temperature of 77 K due to the small band gap in Ge at room temperature (0.7 eV), thus minimising the leakage current and reducing electronic noise. The detectors are grouped in rings around the target at angles of 85.8°, 94.2°, 107.9°, 133.6° and 157.6° (removed to accommodate for the magnetic coils) with respect to the beam axis.

3.2.2 RITU

The **R**ecoil **I**on **T**ransport **U**nit [42] is a gas filled separator allowing for the dissociation of recoil ions from scattered products. It consists of 3 quadrupole magnets (Q) and a dipole magnet (D) in the formation Q_V D Q_H Q_V, where Q_V and Q_H refer to vertically and horizontally focussing and defocussing quadrupole magnets respectively. The addition of the focussing quadrupole

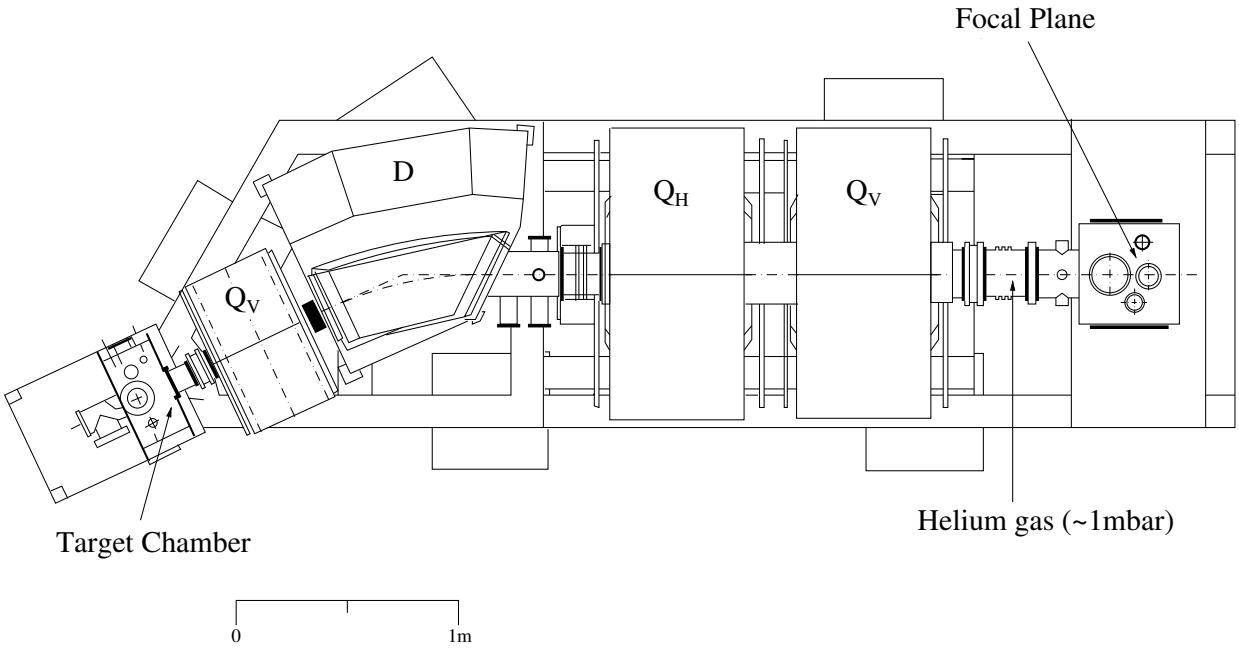

Figure 3.9: *An adapted schematic of the* RITU *separator [42].*

magnet before the dipole magnet helps to improves the angular acceptance as the recoils enter the separator. A diagram of RITU is shown in Figure 3.9.

The separator is filled with 1 mbar of helium gas such that the evaporation residues passing through RITU collide with the He molecules and attain an average charge state. This average charge state can be expressed in the form of the Thomas-Fermi model of the atom

$$q_{ave} = \left(\frac{v}{v_B}\right) eZ^{1/3}, \tag{3.4}$$

where v is the recoil ion velocity, $v_B = (1/137)c$ (the Bohr velocity) and Z is the proton number of the recoil [43][44]. This can be related to the magnetic rigidity [42]

$$B\rho = \frac{p}{q_{ave}} = \frac{p}{(v/v_B)eZ^{1/3}} = \frac{0.0227A}{Z^{1/3}} \qquad [Tm], \tag{3.5}$$

where B is the magnetic field, p is the momentum, ρ is the radius of curvature, v the velocity of the recoil, e the electric charge, q_{ave} the average charge state attained by the recoil and A the mass number of the recoil. Thus the magnetic rigidity is independent of the initial charge state and recoil velocity and the device acts as a mass separator.

In comparison to vacuum separators, gas-filled separators have high transmission efficiencies but low mass resolving powers. This is suitable for heavy elements where recoil production is low, but few reaction channels are open. Distinguishing between different reaction channels relies on the recoil and recoil-decay tagging techniques. The transmission efficiency of RITU for asymmetric reactions in the region of interest is approximately 40%.

3.2.3 GREAT

The focal plane detectors are collectively named **G**amma **R**ecoil **E**lectron **A**lpha **T**agging (GREAT) [45]. Recoils that pass through RITU are implanted into GREAT. Subsequent charged particle and γ ray decays of the recoil are also detected here. A schematic of GREAT is shown in Figure 3.10.

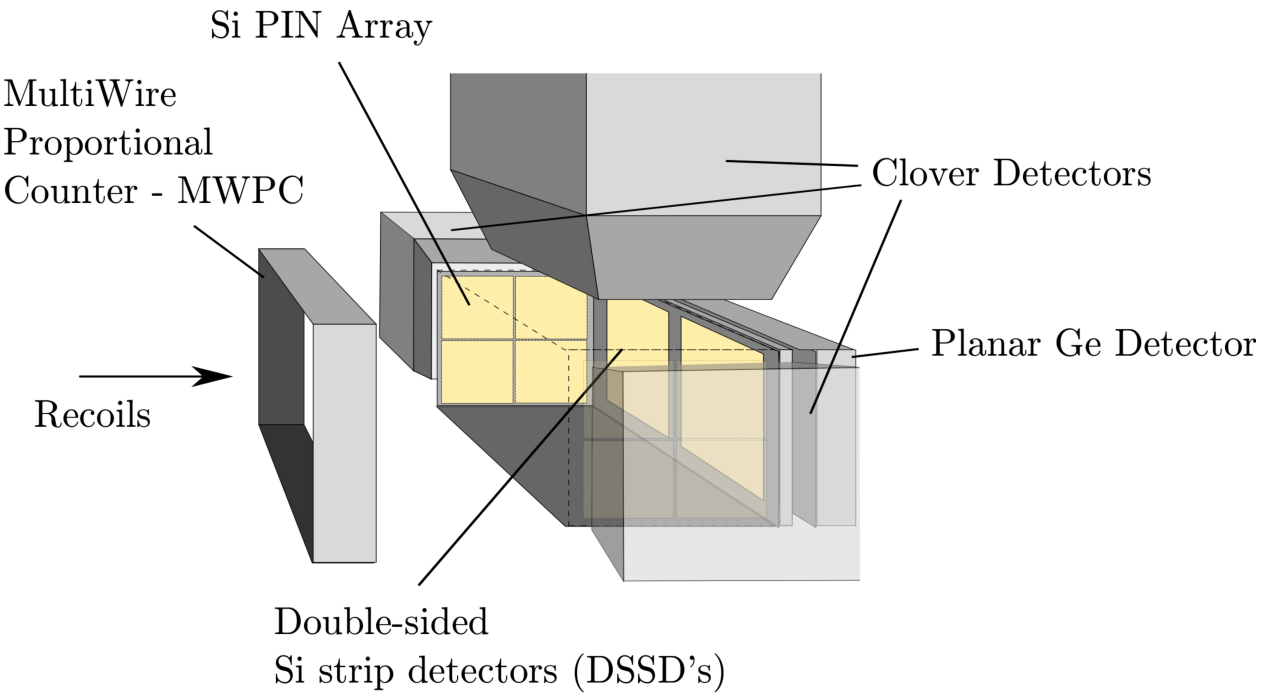

Figure 3.10: *The* GREAT *focal plane spectrometer. The detector elements are labelled.*

The five key detector elements are discussed hence:

- **A Multi-Wire Proportional Counter (MWPC)** in place just after the exit of RITU. This is filled with isobutane gas, which becomes ionised after fragments pass through it.

An electric field applied across the counter allows for charge collection of the ionised gas which is proportional to the energy deposited by the recoil. This allows for energy loss, position and time measurements of the travelling recoils to be performed.

- **Double-Sided Silicon Strip Detectors (DSSDs)** detect recoil implantation and their subsequent α and ICE isomeric decays. They are composed of two silicon detectors adjacent to one another with an area of 60 x 40 mm and perpendicular strips with a pitch of 1 mm in both directions (a total of 4800 pixels). By having two sets of strips (x and y), each side can be separately gain matched allowing for different energy ranges to be probed.

- **PIN diode** (Positive Intrinsic Negative) detectors surround the DSSDs in a box formation and are in place to detect escaped alphas and isomeric conversion electrons. 28 of these diodes are used for this purpose.

- **Planar germanium detector** behind the DSSD box in the beamline direction. This is in place to detect low energy γ rays and X-rays.

- **Clover germanium detectors** perpendicular to the beam axis are placed above and to the sides of the DSSD box. They are in place to detect higher energy γ rays from isomeric decays.

A schematic of some of the decay processes that GREAT can detect are shown in Figure 3.11.

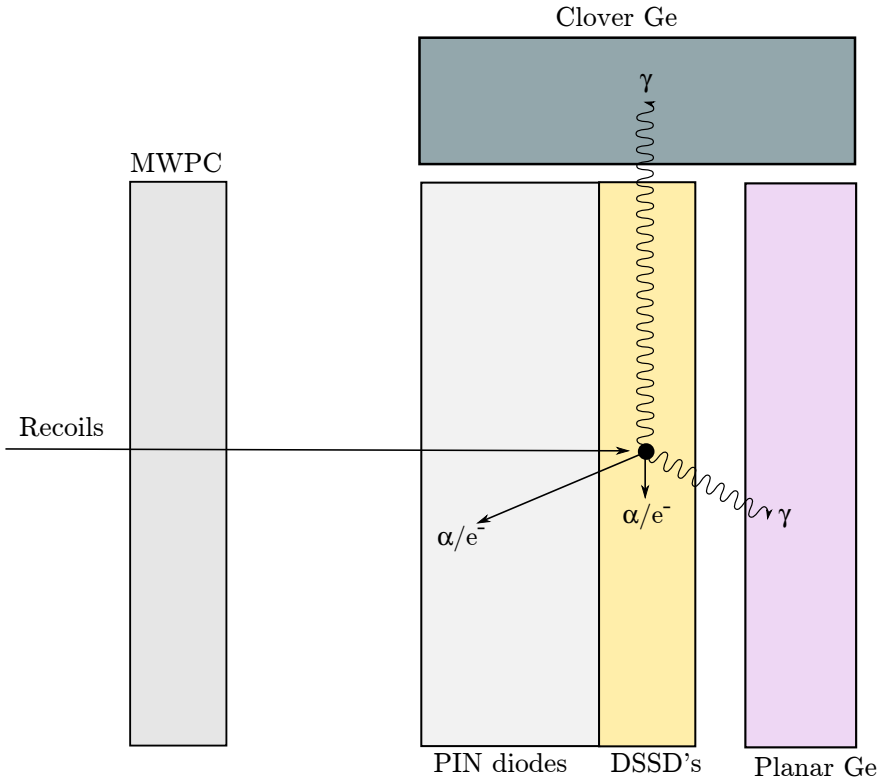

Figure 3.11: *Schematic of* GREAT *and the radiation detection type for each element. Recoils are implanted into the* DSSD*s where they undergo isomeric decays through γ ray and electron cascades which are detected by the* PIN*s, germanium clovers, and planar detectors. The recoil may undergo α decay, which can be detected by the* DSSD*s or* PIN *diodes following an escape. Further isomeric and alpha decays in the decay chain are also detected.*

3.2.4 Data Acquisition and Electronics

The setup uses a Total Data Readout (TDR) technique [46] whereby all the data is time stamped (10 ns) and read out to tape. The data can then be filtered using correlations in an event builder. The TDR data acquisition is triggerless, so when it is used with tagging experiments, minimises the dead time of the system which would be a huge issue for longer lived decays. The lack of a common trigger means dead time is limited to individual detector components.

The SAGE spectrometer uses digital electronics offering high count rate performance (∼30 kHz) in comparison to analogue electronics employed previously for standalone JUROGAM II (10 kHz). The focal plane array uses analogue electronics. A schematic of the TDR electronics is shown in Figure 3.12.

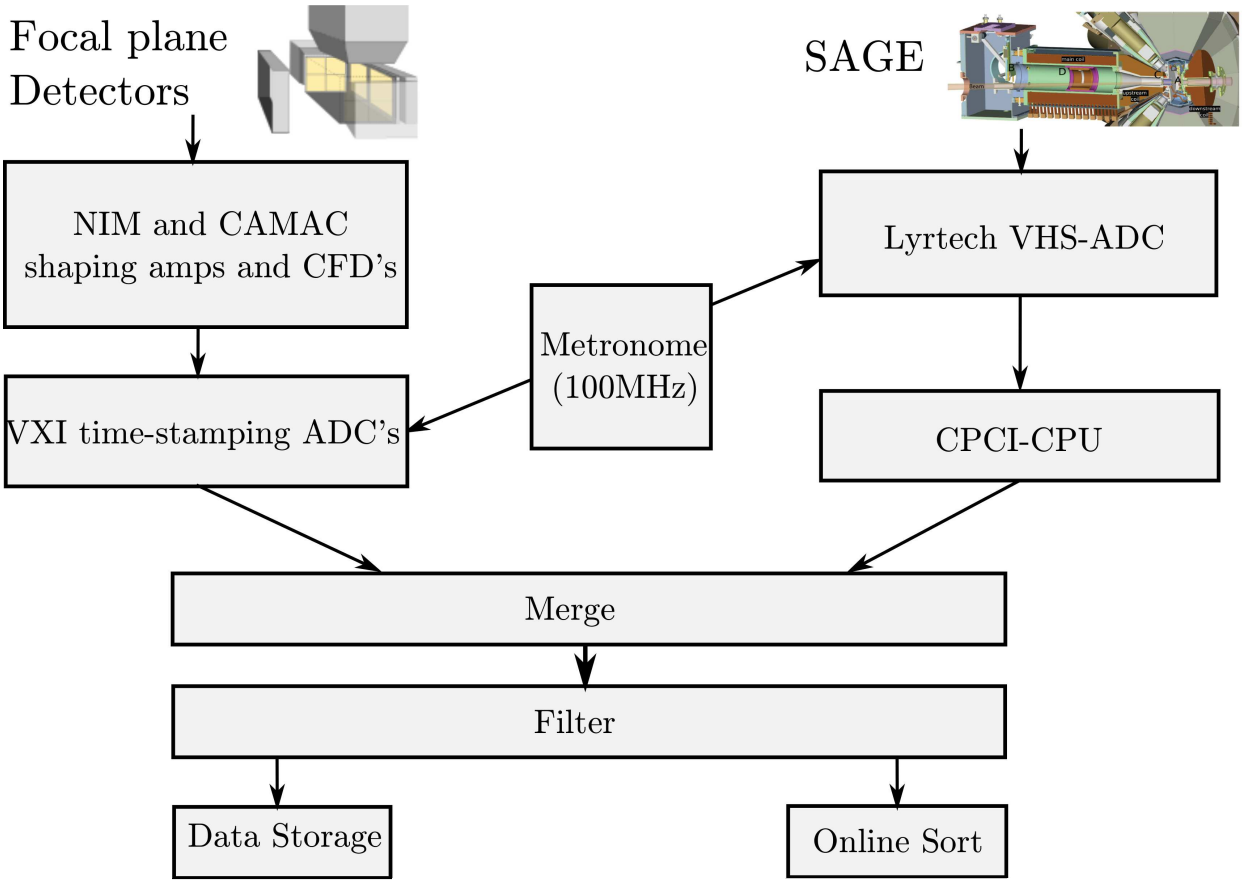

Figure 3.12: *A schematic of the data acquisition system using the TDR method.*

In the focal plane a detected event is fed out through the linear amplifiers to VXI time stamping ADCs. A 100 MHz metronome timestamps the data events individually. The data is then merged with the in-beam events. SAGE events enter into Lyrtech VHS-ADC digitiser cards via (preamplifiers and GO-cards) which are synchronised with the global clock from the metronome. The data is collected using CPCI CPU modules for data readout and control and combined with the focal plane data in the merge. Both focal plane and in-beam data is sent to the filter for data storage or online correlations. The data is sorted using the Java based analysis program GRAIN [47]. The event data comprises a time window (defined by an event width and delay) around a trigger, so any DSSD event can be used as a trigger to correlate data from both the in-beam and focal plane spectrometers. The detector type is determined by the ADC channel assigned. The GRAIN software allows a full coincidence analysis to be performed.

3.2.5 Energy Calibrations

Before observing and measuring the γ ray and ICE data of interest, it is first necessary to calibrate for energy and efficiency and correct for Doppler shift. In the target position the energy calibration is performed for each individual Ge crystal in JUROGAM II using a EuBa source with known γ ray energies. For the electron spectrometer, an open ^{133}Ba source with known electron energies is used, with each pixel element calibrated separately. The peak fitting program *'tv'* [48] is used, allowing for Gaussian (and Poisson if required) distribution fits to the peak of interest, taking into account the background around the region of interest. The calibration coefficients are then calculated through a least squares fitting method.

The energy range and type of radiation to be detected determine the type of calibration performed on the focal plane detectors. The clover and planar germanium detectors are calibrated using a EuBa source, while the PIN diode detectors and the x-strips of the DSSDs use an open ^{133}Ba electron source. The voltage across the y-strips of the DSSDs is set to be sensitive to the α energy region and hence are calibrated using a three line α source composed of ^{239}Pu, ^{241}Am and ^{244}Cm.

3.2.6 Efficiency

In a realistic detector system, the detection efficiency varies as a function of energy and must be measured for each detector system. The activity of the calibration sources is known and so the absolute efficiencies can be determined

$$\varepsilon_{abs} = \frac{N}{A \cdot t \cdot I}, \tag{3.6}$$

where N is the peak area, A is the activity of the source, t is the time the source undergoes detection and I is the intensity of the transition. These transitions are then plotted as a function of energy and a curve is fitted through chi-squared minimisation using

$$\varepsilon_{abs} = K \exp[(A + Bx + Cx^2)^{-G} + (D + Ey + Fy^2)^{-G}]^{-\frac{1}{G}}, \tag{3.7}$$

where

$$x = \ln\left(\frac{E_\gamma}{100}\right) \quad , \quad y = \ln\left(\frac{E_\gamma}{1000}\right),$$

and A, B, C, D, E, F, and K are all constants and are listed in Table 3.1 for both JUROGAM II and the silicon detector.

C.f.	JUROGAM II	Silicon
A	4.9	6.3
B	2.7	2.8
C	0	0
D	4.0	3.4
E	-0.6	-1.1
F	0.05	0.15
G	8.0	3.5
K	5.9×10^{-4}	3.2×10^{-4}

Table 3.1: *Coefficients used in the efficiency fit for* SAGE. *These were applied in Equation 3.7.*

The measured efficiency as a function of energy for JUROGAM II is shown in Figure 3.13. The uncertainties on the efficiency are calculated from a chi-squared minimisation fit using Equation 3.7 to the upper and lower measured uncertainties on the data points. The same method was used to determine the uncertainties on the silicon detector efficiency. This provides the uncertainty on the efficiency for a given energy.

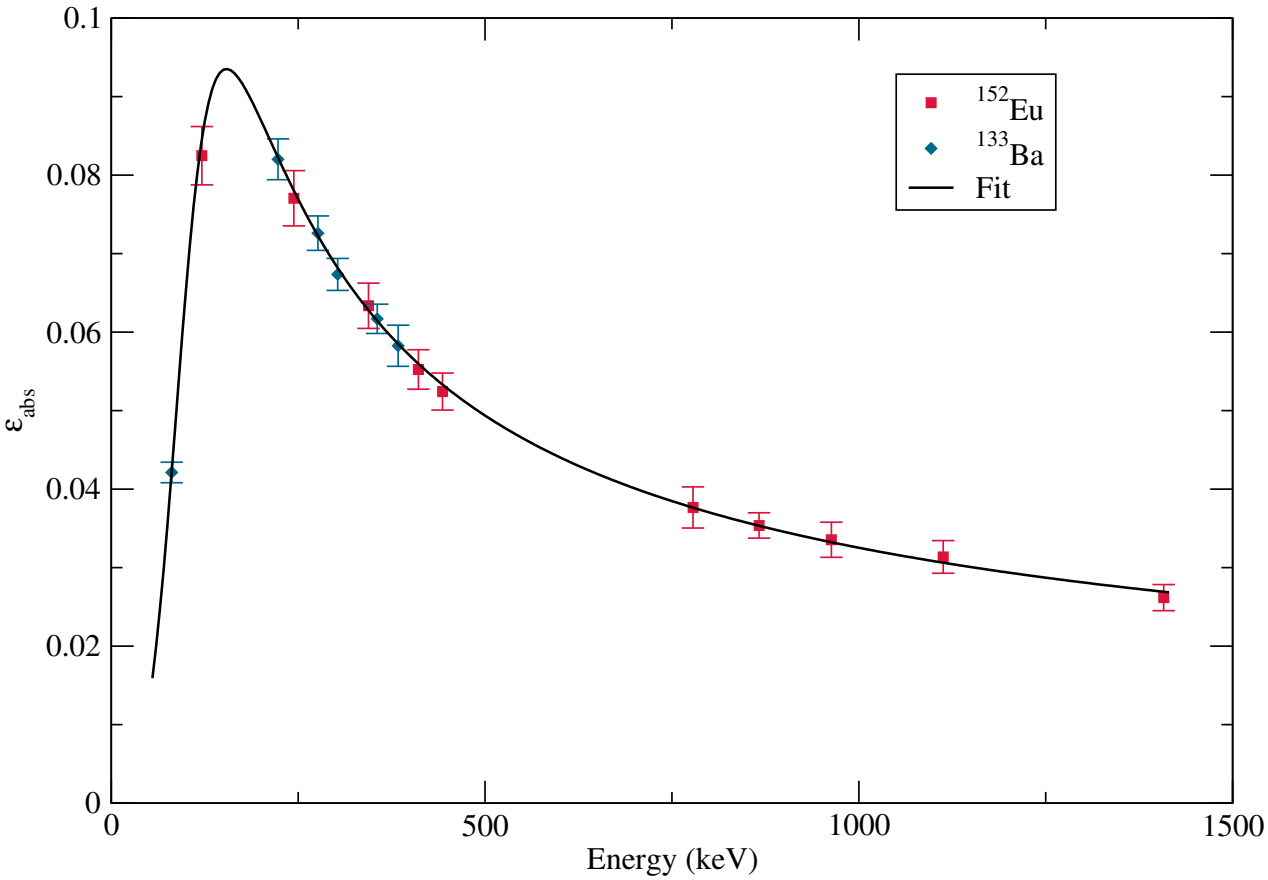

Figure 3.13: *The absolute efficiency for* JUROGAM II *measured using a EuBa source*

Figure 3.14 shows an energy calibrated prompt electron spectra for ^{133}Ba using all pixel elements of the SAGE silicon detector. The magnetic field and HV barrier are activated with the same setting as used during the online experiment. Figure 3.15 shows the γ rays from the same source measured with JUROGAM II.

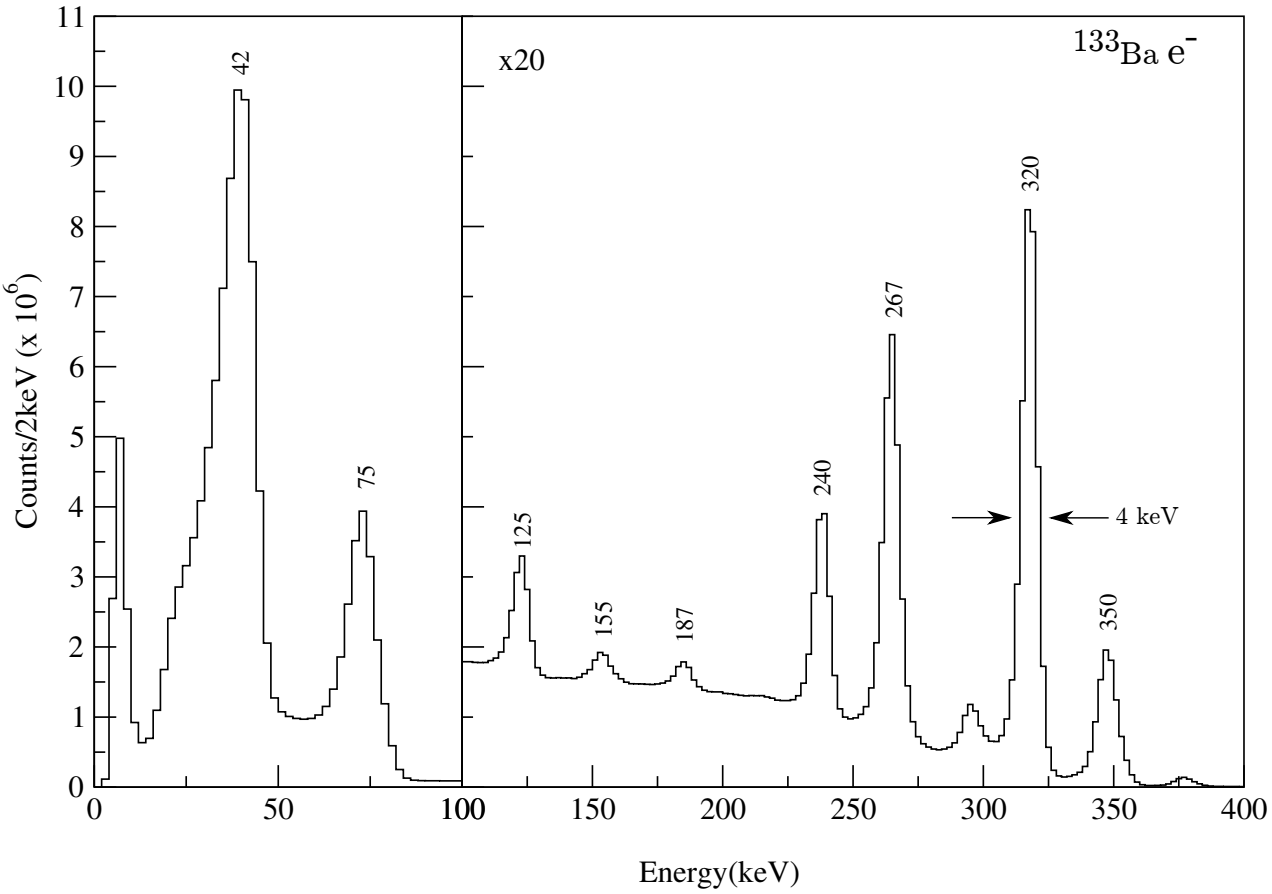

Figure 3.14: *The electron spectrum measured in the silicon detector of* SAGE *from a* ^{133}Ba *source.*

While the resolution (FWHM) for SAGE is 4 keV at 320 keV for a static source, during a fusion evaporation reaction this increases to 8-10 keV due to Doppler broadening [33].

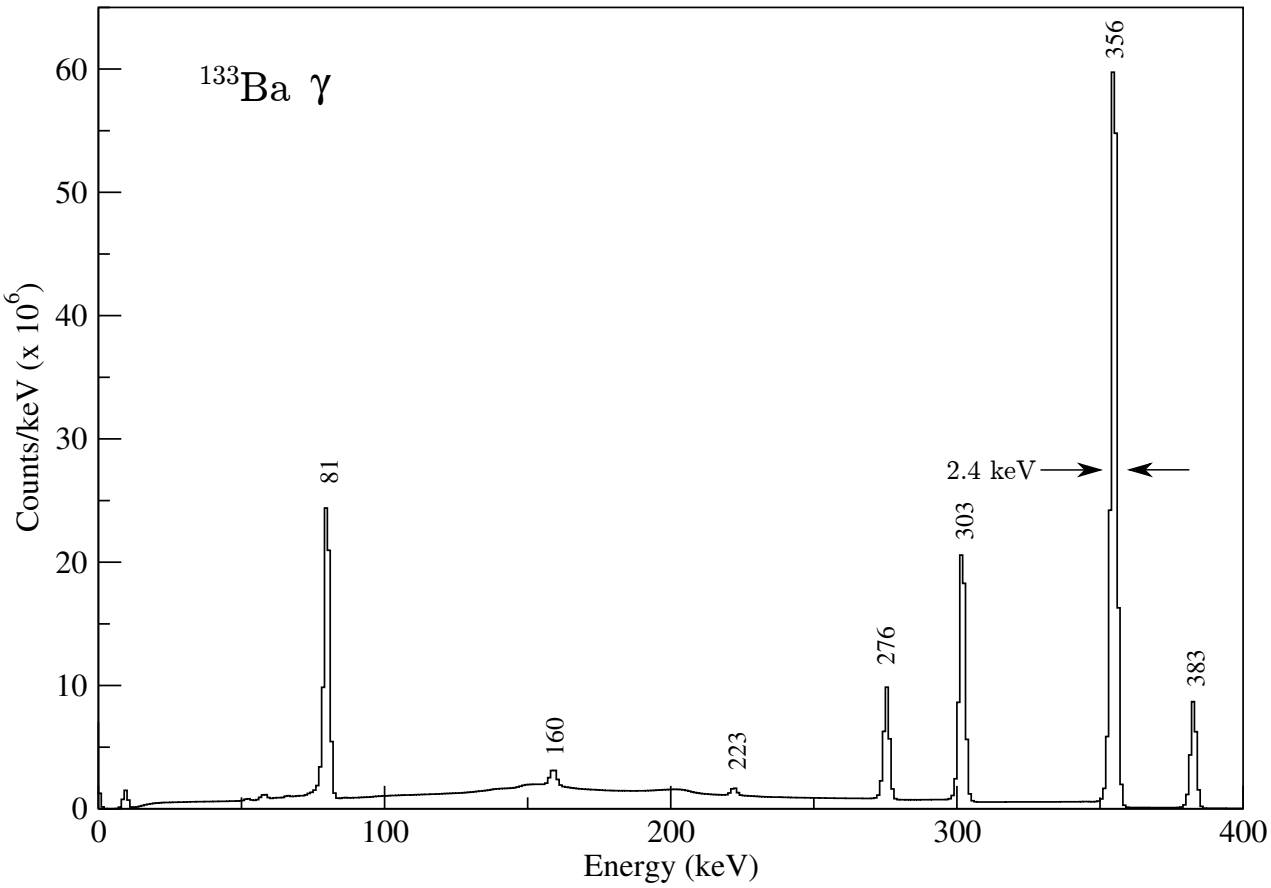

Figure 3.15: *The γ ray spectrum measured in* JUROGAM II *from a ^{133}Ba source.*

Similarly for JUROGAM II the FWHM increases from 2 keV to 3 keV during full experimental running setup.

Measurements from this open ^{133}Ba source yield the efficiency as a function of energy in Figure 3.16 for the silicon detector.

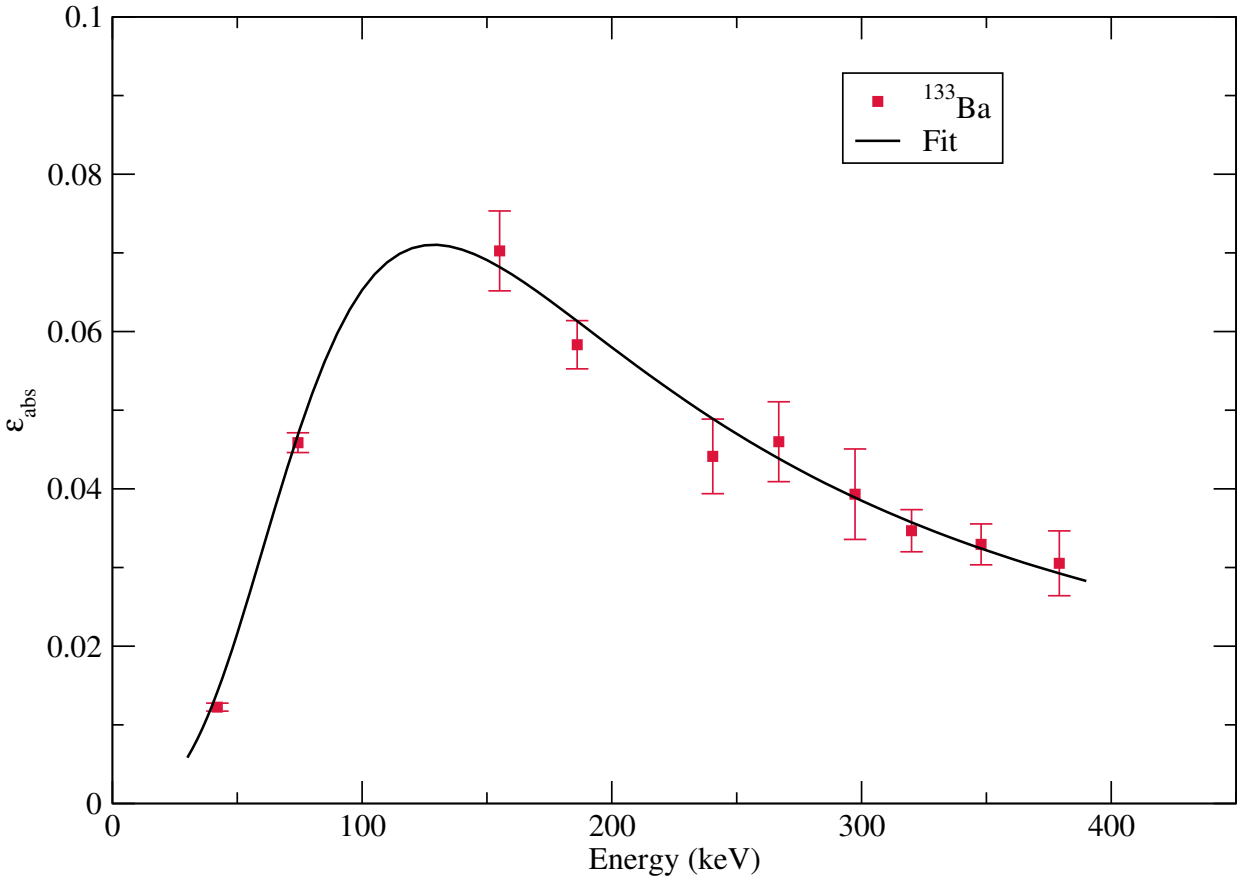

Figure 3.16: *Absolute efficiency for* SAGE *measured using a* ^{133}*Ba open source.*

The efficiency of the detector is heavily dependent on the transmission efficiency of the electrons, hence on the magnetic field coils. A reduction in efficiency is reported at lower energies as a result of the HV barrier, with decreasing impact towards higher energies, becoming negligible around 150 keV [33].

3.2.7 Doppler Shift

The Doppler shift arises from moving recoils emitting γ rays and electrons with velocity v. This results in a 'spread' of the width of γ ray peaks impacting on the resolution of the peaks. The laboratory frame γ ray energy, E'_γ, must be translated into the recoil rest frame γ ray energy, E_γ, using the speed factor $\beta = v/c$ and the angle between the emitted γ ray and the detector, θ

$$E_\gamma = \frac{E'_\gamma}{1 + \beta cos\theta}. \tag{3.8}$$

Considering conservation of energy and momentum leads to the equation

$$\beta \approx \sqrt{\frac{2E_{No}}{M_{No}c^2}} = 0.018, \tag{3.9}$$

where E_{No} and M_{No} are the energy and mass of the ^{253}No recoils respectively. This is then used to determine E'_γ.

For electrons the Doppler shifted energy was calculated through kinematic considerations and expressed as [49],

$$E_e = \frac{E'_e + m_e - \beta cos\theta' \sqrt{E'^2_e + 2m_e E'_e}}{\sqrt{1-\beta^2}} - m_e, \tag{3.10}$$

with E_e as the unshifted energy component in the recoil rest frame, E'_e the measured energy in the laboratory frame, m_e is the electron rest mass and θ' is the emission angle. This is taken as an average angle since the detection of electrons through different angles is not available here. Simulations performed using SOLENOID [35] (discussed previously on page 48) for SAGE are shown in Figure 3.17. This indicates an emission angle of approximately 160° relative to the beam-axis is acceptable. This was also the angle used for a previous electron spectrometer (SACRED) also employed at JYFL.

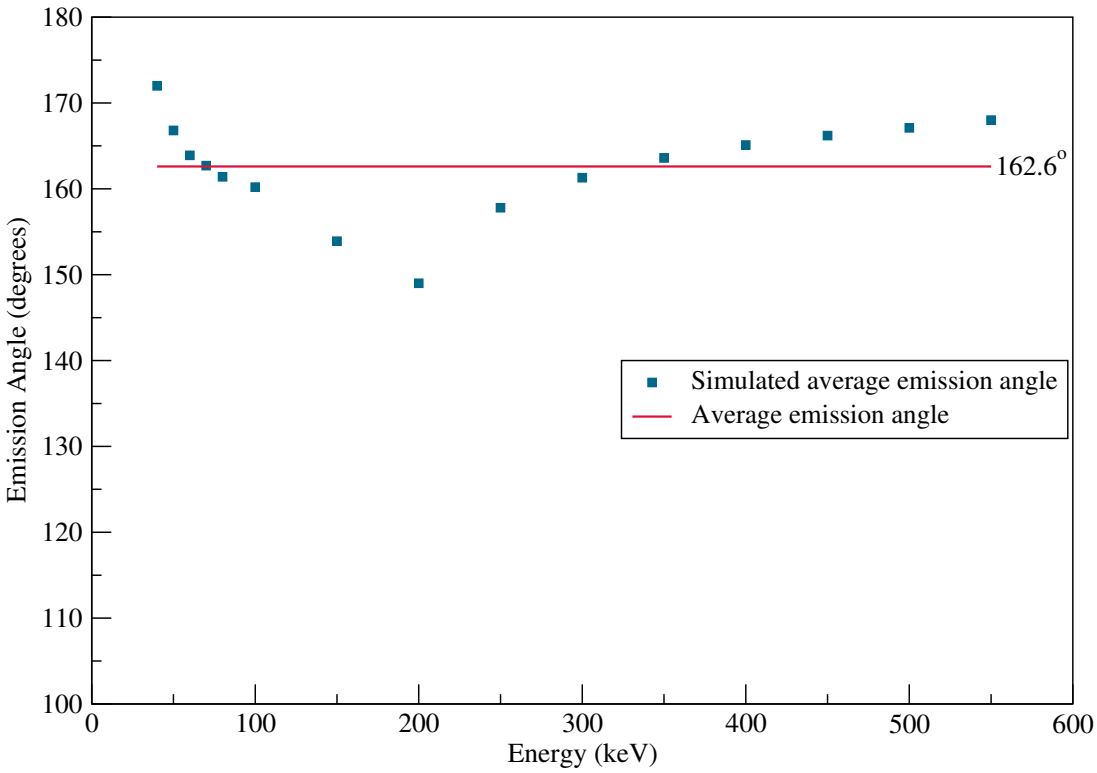

Figure 3.17: *Average emission angle plotted as a function of energy. The average of the simulated points is approximately 160°.*

3.3 Analysis Techniques

When acquiring an experimental data set, much of what is produced is unwanted material. In order to extract the information of interest, various analytical techniques must first be performed.

3.3.1 Recoil and Decay Tagging

In order to establish the measurement of prompt radiation emission from the nucleus of interest, two techniques are used. For the first, 'recoil-tagging', two factors must be examined:

1. The time of flight of the recoil between the gas counter (MWPC) and implantation in the DSSD (establishes the event as a recoil).

2. The time difference between prompt radiation emission in the target position and im-

plantation of the recoil.

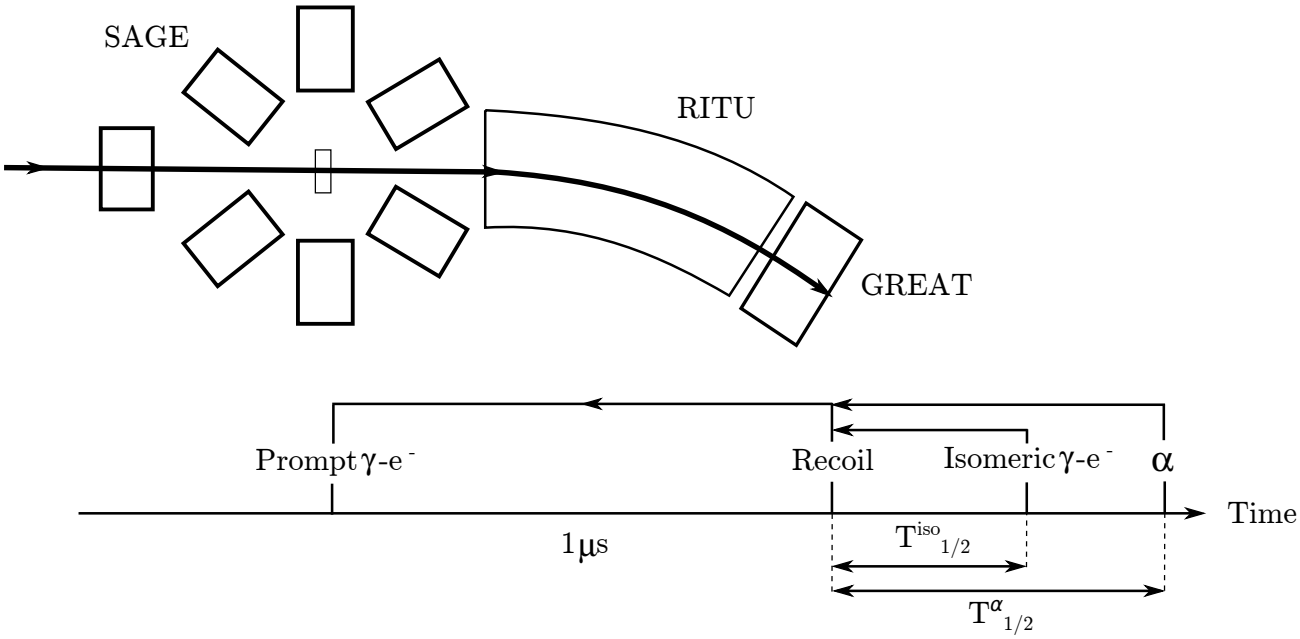

Figure 3.18: *Recoil, Recoil-decay, and isomer tagging techniques. Prompt γ rays and electrons are detected by* SAGE *while the recoil, isomeric decays and α particles are detected by* GREAT. *Prompt spectroscopy can be performed by determining correlation with recoils (and alphas within 3 decay half-lives) and the prompt emissions. Isomeric decays can be searched for through recoil tagging and time correlations.*

Step 1 is achieved by placing a 2-D coincidence gate on the time of flight (between MWPC and DSSD) vs. the energy deposited in the MWPC. This is demonstrated in Figure 3.19. Correlating this matrix with a ^{253}No α particle energy and $3\times T^{\alpha}_{1/2}$ decay (where $T^{\alpha}_{1/2}$ is the alpha decay half-life) within the same pixel as recoil implantation allows for recoil identification (Figure 3.19 (b)).

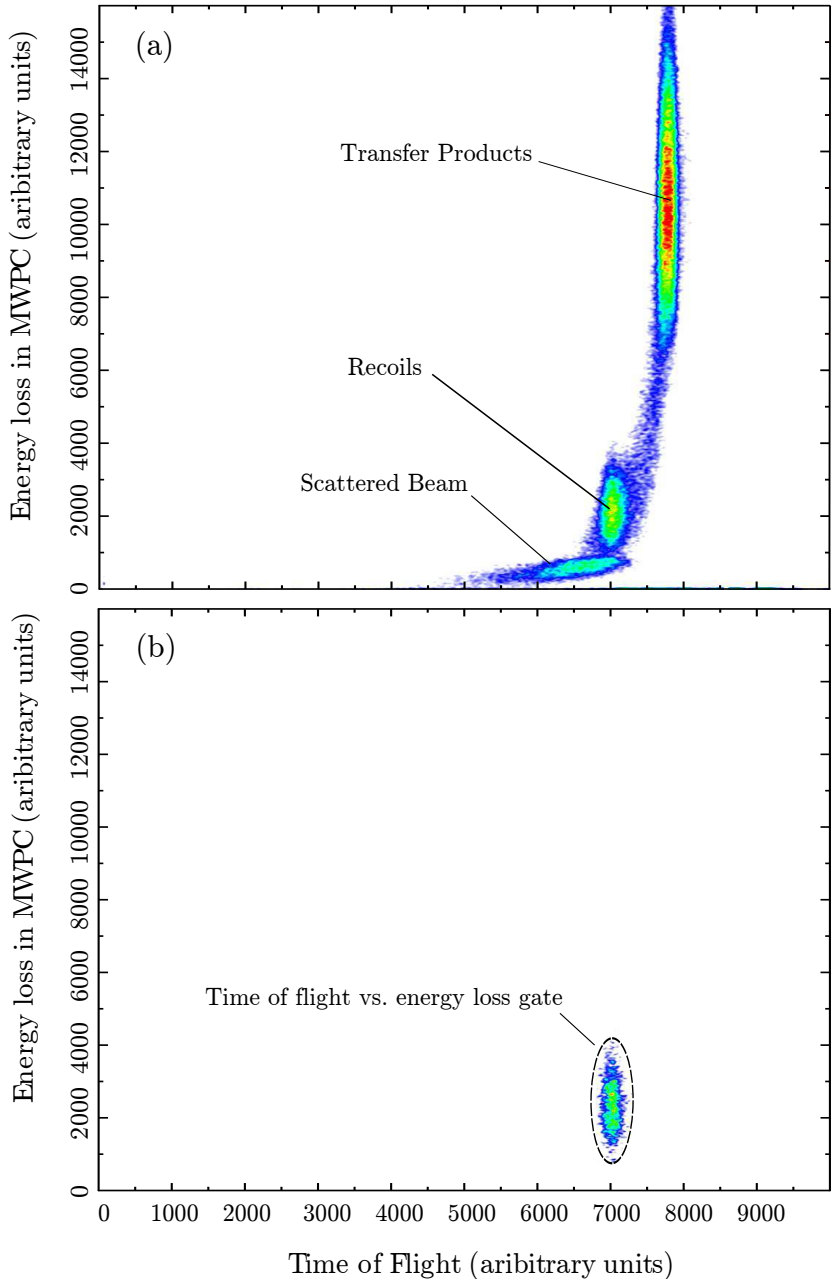

Figure 3.19: *Time of flight vs. Energy deposited in the* MWPC *2-D matrix (a) Raw matrix (b) Correlated with an alpha* ^{253}*No* α *energy and* $3\times T^{\alpha}_{1/2}$ *decay within the same pixel as recoil implantation. The 2-D coincidence gate used as part of the recoil-tagging technique is highlighted.*

The second step involves placing a prompt γ–recoil gate for JUROGAM II and a coincidence gate for SAGE on the e^-– recoil time. For JUROGAM II, each of the detectors has a slightly different γ-recoil correlation time hence individual timing gates were applied for each of the detectors. An example of the γ–recoil time and the coincidence gate applied is shown in Figure 3.20.

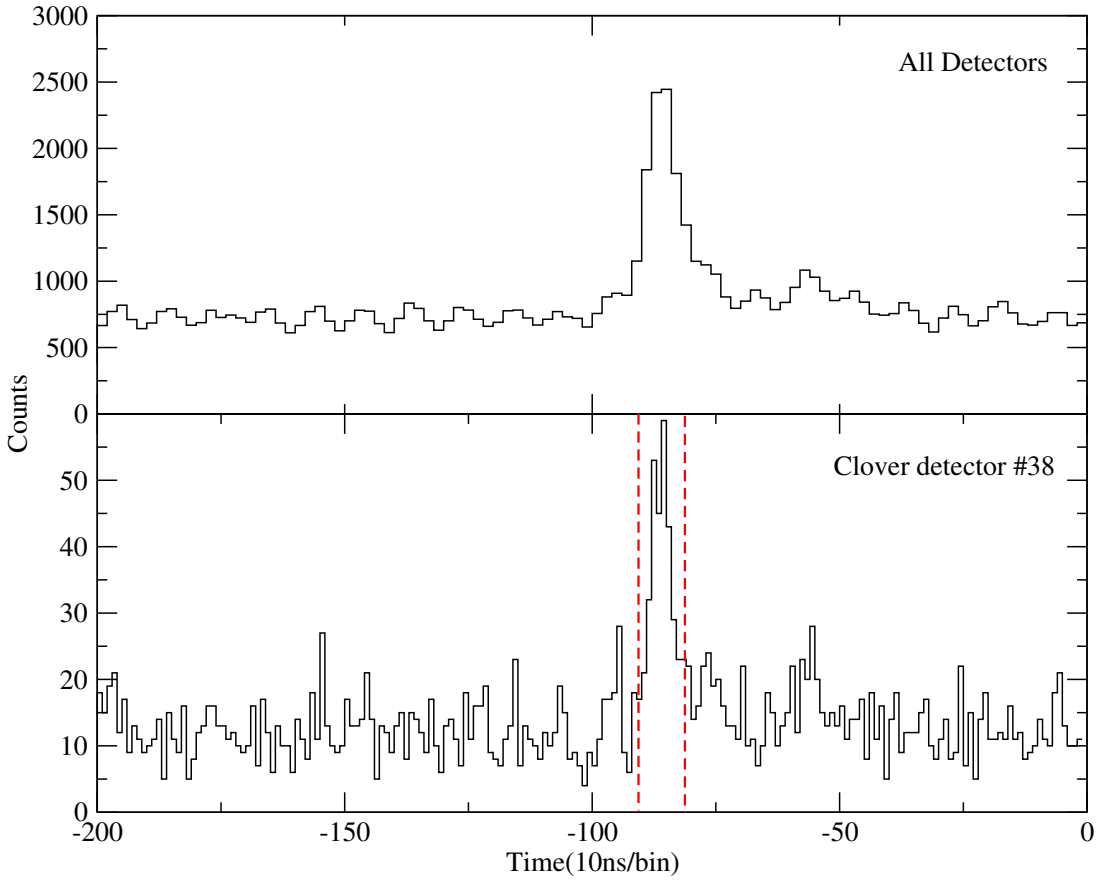

Figure 3.20: *Gamma–recoil correlation time for (a) all* JUROGAM II *detectors and (b) a single clover detector. The gate limits are highlighted by the red dashed line.*

The tail on the right hand side of the Gaussian peak was investigated by progressively increasing the gate size to include it. However, this was found to impair statistics, decreasing the peak-to-background ratio of the recoil tagged γ-ray singles. The periodic structure with a frequency of 10 MHz seen in the background of the spectra is caused by the cyclotron.

For the electron spectrometer a similar gate is placed on the time difference between recoil implantation and prompt electron emission (Figure 3.21). In this case the detector pixels are closely synchronised allowing a single gate to be applied to all pixels. Similarly, including the tail on the right hand side of the Gaussian peak in the gate was found not to aid statistics.

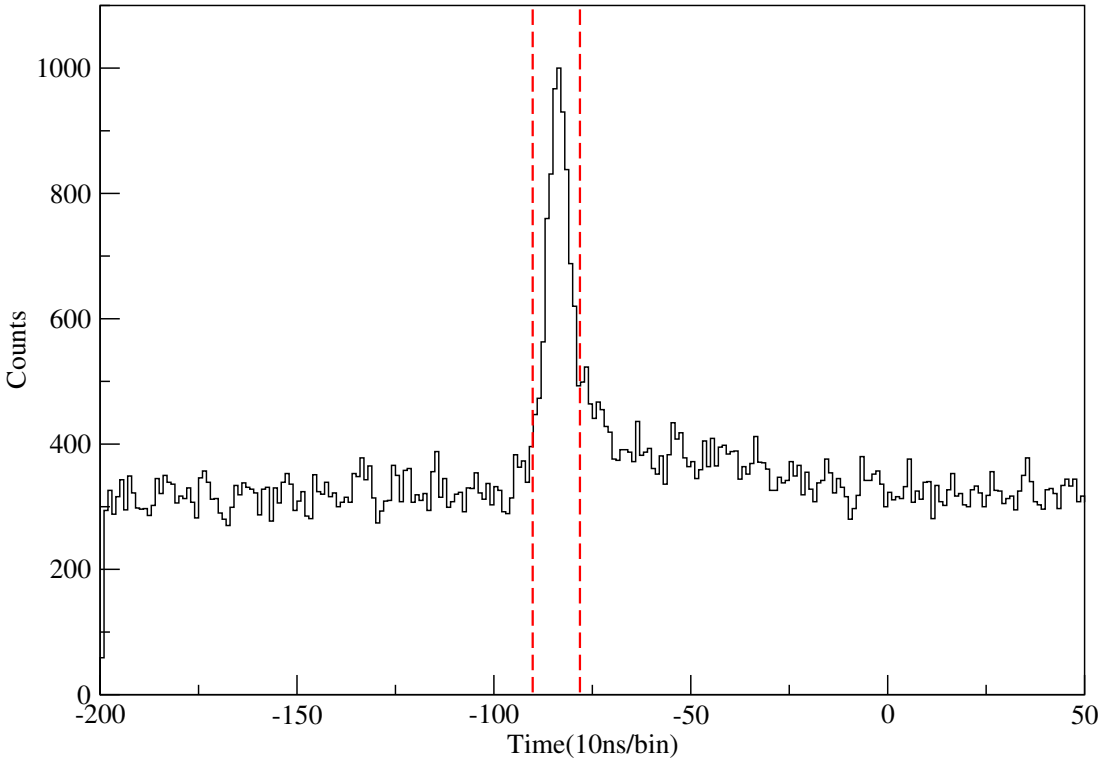

Figure 3.21: *Electron-recoil correlation time for all* SAGE *pixels. The gate limits are highlighted by the red dashed line.*

The second analysis technique is recoil-decay tagging. This involves placing additional conditions on the recoil-tagging correlations in the form of the subsequent α decay of the recoil. The α decay energy (within the same DSSD pixel as the recoil implantation) and α decay half life are simultaneously gated on. This technique is essential for cases when there is more than one reaction channel open for a given nucleus of interest.

Searching for isomeric decays also involves tagging on recoils (and the isomeric decay time if necessary) to extract the delayed γ ray and electron emissions. The criteria for this is for the nuclei to arrive at the focal plane with an isomeric lifetime greater than the time of flight through the separator.

Chapter 4

A Study Using the SAGE Spectrometer: ^{177}Au

In order to assess the capability and performance of the SAGE spectrometer online, a commissioning study was performed. The odd-A neutron-deficient nucleus ^{177}Au was selected as the isotope for study based on its relatively high cross section($\sim$100 µb) providing an acceptable level of statistics with which to test the apparatus. This involved the reaction ^{144}Sm(^{36}Ar,p2n)^{177}Au for approximately 65 hours creating $\sim$42k recoils and $\sim$20k α decays correlated with the α decay time of ^{177}Au (1.3 s) [50]. Using $\gamma - \gamma$ and $\gamma - e^-$ timing coincidences, internal conversion coefficient measurements were made on some of the lower lying transitions.

4.1 Physics Background

A rigorous prompt γ ray analysis from [51] has unveiled a broad level scheme (Figure 4.1) with many new and differing features building on previous knowledge of this isotope [52].

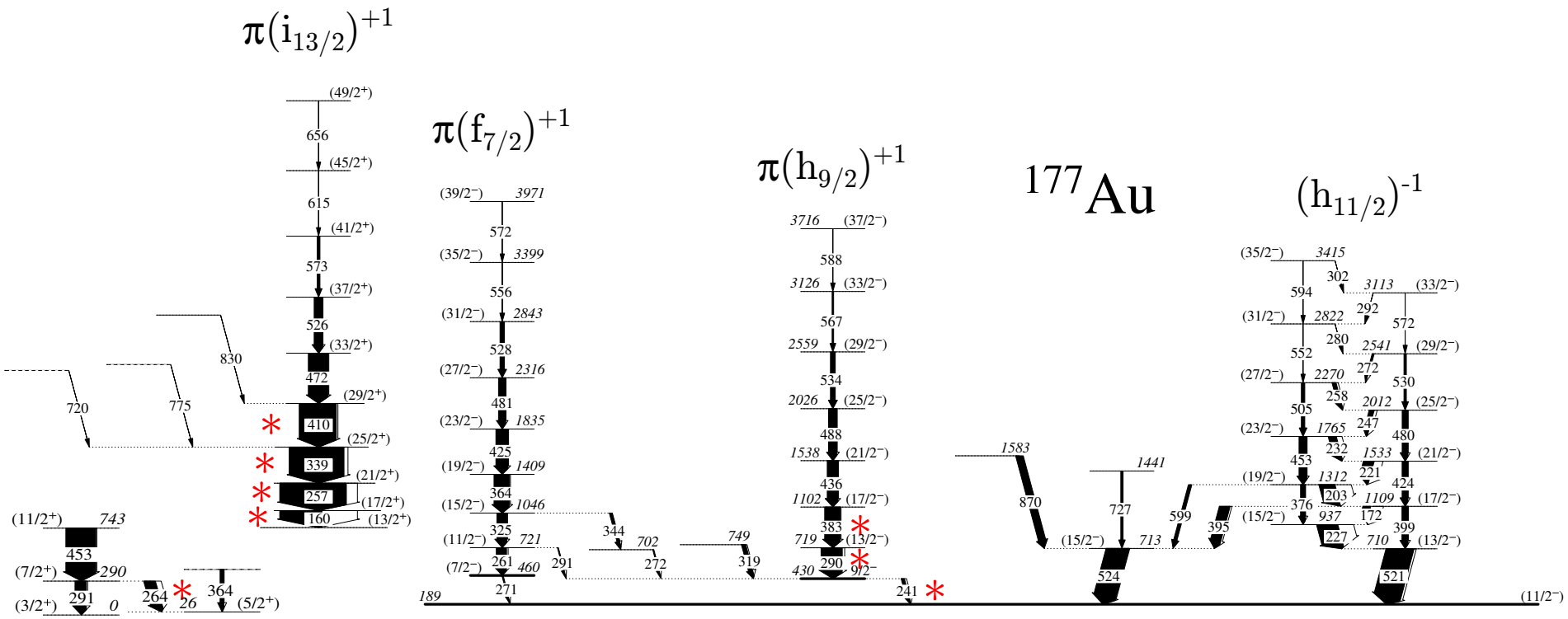

Figure 4.1: *Level scheme of* ^{177}*Au as determined from a* γ *ray analysis by [51]. Transitions for which ICCs have been measured are indicated by red asterisks.*

The level scheme demonstrates a number of features. The $i_{13/2}$ yrast band is a result of a proton-intruder excitation across the Z=82 shell gap from the $11/2^-[505]$ Nilsson configuration to the $1/2^+[660]$ intruder orbital [52]. This can be considered as the unpaired proton coupling to a ^{176}Pt core ($\pi i^{+1}_{13/2} \otimes ^{176}$Pt) resulting in a deformed prolate shape at the bandhead. The excited states above the bandhead are due to rotation of the nucleus and as a result become oblate. Similarly the proton can be excited to the $1/2^-[530]$ ($\pi f^{+1}_{7/2} \otimes ^{176}$Pt) and $1/2^-[541]$ ($\pi h^{+1}_{9/2} \otimes ^{176}$Pt) intruder orbitals forming the other two prolate rotational intruder bands. Observation of the proton orbitals around the Z=82 shell gap in Figure 2.6 demonstrates these intruder orbitals. The decay from the $i_{13/2}$ bandhead follows two decay paths, but currently the linking transitions to the structure above the spherical $11/2^-$ α-decaying state and the $1/2^+$ ground state are too low energy to be measured.

The strongly coupled rotational band can be considered as a hole in the $11/2^-[505]$ $\pi(h_{11/2})$ state coupling to a ^{178}Hg core ($\pi h^{-1}_{11/2} \otimes ^{178}$Hg). Even-even Hg cores have been demonstrated to exhibit low energy E0 transitions [53], thus the band could be considered as a 521 keV $I \rightarrow I$ transition from the $11/2^-[505]$ band head to the 11/2 state with mixed E0+M1+E2 multipolarity.

Shape Coexistence

This phenomena of having different shapes at similar excitation energies is known as shape coexistence, and results from particle-hole excitations from below the shell-gap to intruder states above it. This occurs near to closed shells and has been observed in a number of different nuclei in these regions. A comprehensive discussion on this can be found in reference [54]. An example is a previous SAGE study on ^{184,186}Hg. Prior to upgrades on SAGE leading to this recommissioning experiment, a study was performed which observed a mixed E0 transition between the $2^+_2 \rightarrow 2^+_1$ levels [55]. Measuring E0's gives a good handle on the mixing between shapes of differing deformations and thus on the observance of shape coexistence [56]. Strong mixing between spherical and deformed intruders results in an intense E0 component. The

wave functions of two experimentally observed states can be expressed as

$$|J_1\rangle = \alpha_1 |J_p\rangle + \alpha_2 |J_o\rangle \,, \tag{4.1}$$

$$|J_2\rangle = -\alpha_2 |J_p\rangle + \alpha_1 |J_o\rangle \,,$$

for pure prolate $|J_p\rangle$ and pure oblate $|J_o\rangle$ eigenstates. The E0 monopole strength (transition rate) is related to the mixing amplitudes $\alpha_{1,2}$ and the quadrupole deformation parameter β_2

$$\rho^2(E0) = \left(\frac{3}{4\pi}Z\right)^2 \alpha_{1,2}(1-\alpha_{1,2}^2)[\Delta(\beta_2^2)]^2. \tag{4.2}$$

In odd-A nuclei in the region of interest, shape coexistence results from a lowering of orbitals from the $h_{9/2}$ configuration which lies above the Z=82 shell gap. The change from a Hg core with a hole to a Pt core with a particle results in a shift in deformation hence a large change in the ground state deformation and shape occurs. An example involves E0 transitions measured in ^{185,187}Au which have presented comprehensive evidence on low lying states exhibiting shape coexistence [57].

4.2 Conversion Coefficient Measurements

To obtain the ICCs, transitions of interest must be isolated from potential sources of contamination. This is done first by performing recoil-decay tagging to remove additional channels populated in the reaction. This requires events detected following a recoil implantation then an α decay event within the same DSSD pixel and a correlation time of $3\times T_{1/2}^{177Au}$ (3.9 s). Transition doublets occur (for example the 290 keV $13/2^- \rightarrow 9/2^-$ and $5/2^+ \rightarrow 1/2^+$ transitions). These are removed by cross-correlating the coincidence gates for the γ–γ and γ–e^- matrices. An example of the recoil-decay tagged JUROGAM II spectra produced with this technique is illustrated in Figures 4.2 and 4.3.

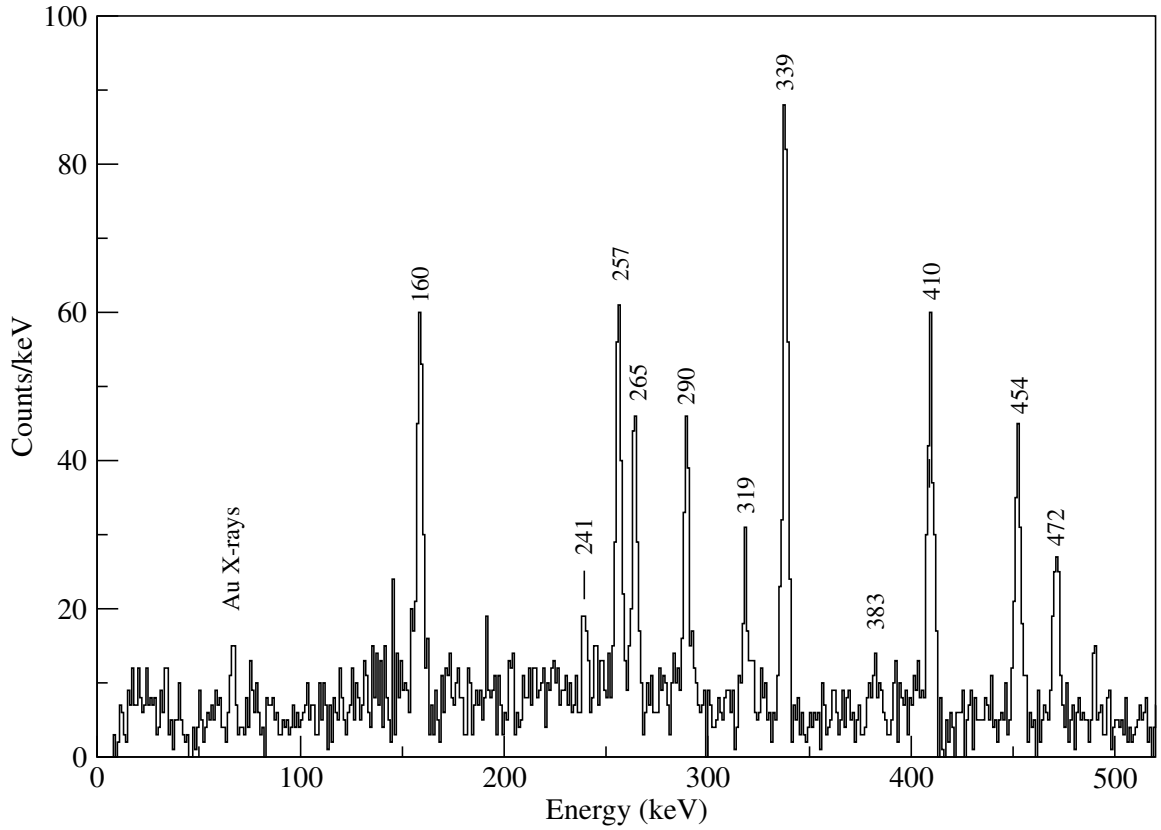

Figure 4.2: *γ rays observed with the 160 keV and 257 keV transitions γ ray sum coincidence from a γ-γ matrix correlated with recoils followed by a ^{177}Au α decay event within the same pixel and a correlation time of $0 < t < 3.9$ s.*

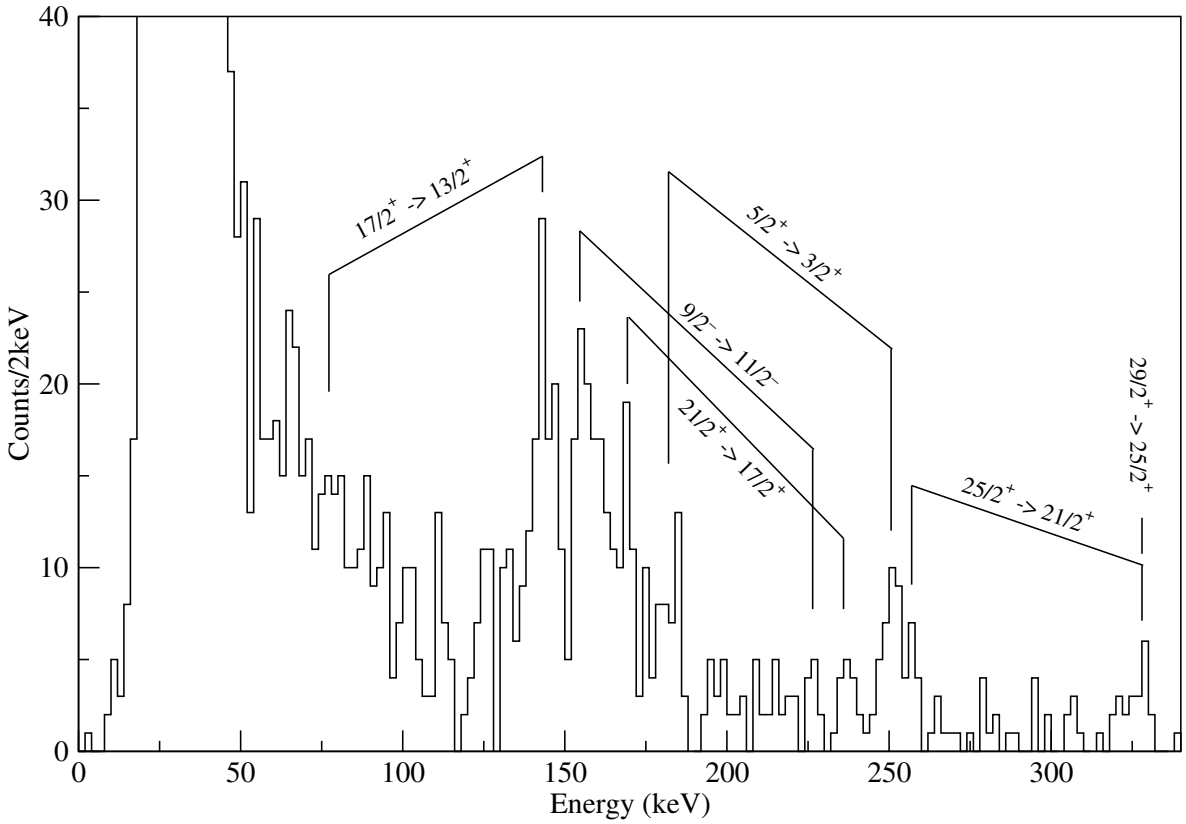

Figure 4.3: *Resulting electrons observed with the 160 keV and 257 keV transitions γ ray sum coincidence from a γ-e^- matrix correlated with recoils followed by a ^{177}Au α decay event within the same pixel and a correlation time of $0 < t < 3.9$ s. K and L shell transitions are highlighted according to their respective spin and parity change.*

While the statistics are limited for the electrons, there are some lower-lying transitions of interest that can be identified. Performing cross coincident $(\gamma\text{–}\gamma) \leftrightarrow (\gamma\text{–}e^-)$ analysis similar to that in the example allowed for the ICCs to be extracted. This involved using the absolute efficiencies ε_{Ge} and ε_{Si} for the germanium and the silicon detector respectively such that

$$\alpha = \frac{N_e \varepsilon_{Ge}}{N_\gamma \varepsilon_{Si}} \tag{4.3}$$

The ICC measurements are shown in Table 4.1 with a plot of the E2 ICC transitions data measured in Figure 4.4.

Energy (keV)	$I_i^\pi \rightarrow I_f^\pi$	E_{e^-} (keV)	Shell	Measured ICC	BRICC ICC [27]	(σL)
160	$17/2^+ \rightarrow 13/2^+$	80.5	K	0.36 (7)	0.290 (4)	E2
		145.5	L	0.42 (8)	0.402 (6)	
241	$9/2^- \rightarrow 11/2^-$	159.5	K	0.61 (7)*	0.18 (1)	M1+E2
		227.0	L	0.19 (9)*	0.05 (1)	
257	$21/2^+ \rightarrow 17/2^+$	175	K	0.07 (2)	0.09 (1)	E2
		244.5	L	0.04 (1)	0.054 (8)	
264	$5/2^+ \rightarrow 3/2^+$	185	K	0.34 (11)	0.234 (4)	M1+E2
		250	L	0.22 (7)	0.056 (8)	
290	$13/2^- \rightarrow 9/2^-$	208	K	0.06 (2)	0.068 (1)	E2
		277	L	0.05 (2)	0.035 (5)	
339	$25/2^- \rightarrow 21/2^-$	257	K	0.09 (2)	0.046 (1)	E2
		325	L	0.03 (1)	0.019 (1)	
383	$17/2^- \rightarrow 13/2^-$	300	K	0.05 (3)	0.035 (1)	E2
410	$29/2^+ \rightarrow 25/2^+$	330	K	0.03 (1)	0.025 (1)	E2

Table 4.1: *Conversion coefficient measurements measured for ^{177}Au using* SAGE *and compared to* BRICC *calculated values [27]. *Isomeric.*

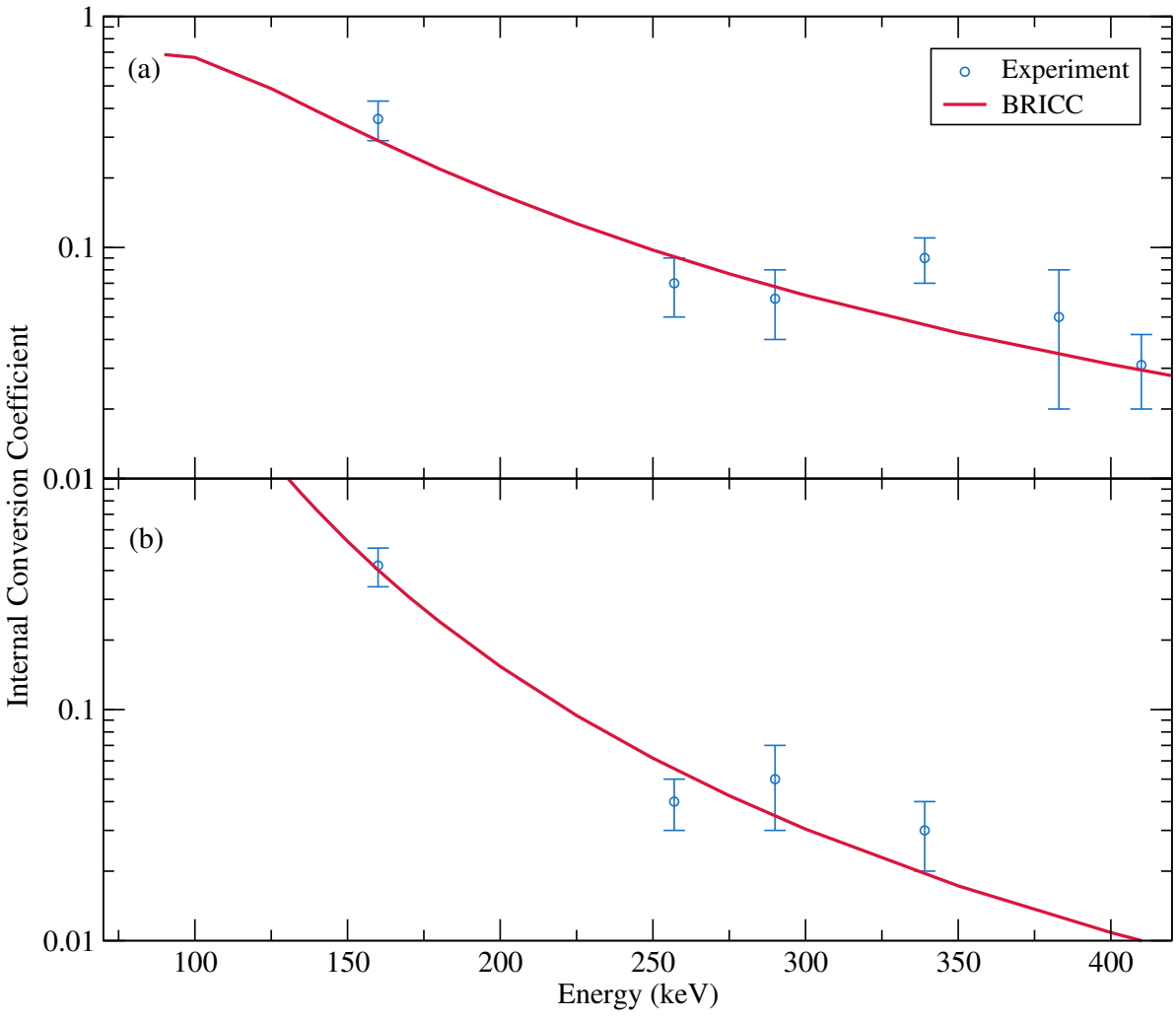

Figure 4.4: *Conversion coefficients of ^{177}Au comparing experimental measurements to* BRICC *theoretical values. (a) K shell E2 transitions, (b) L shell E2 transitions.*

4.3 Discussion

There are several points of interest from these measurements. The 241 keV transition stemming from the $9/2^-$ bandhead is observed, which is expected to have a lifetime in the region of $\tau_{1/2} \leq 17$ ns [52] as observed for a similar M1 $9/2^- \rightarrow 11/2^-$ transition in ^{185}Au [58]. For a half-life of this magnitude the γ rays will be emitted from a point downstream of the target. From this emission point one might expect from kinematic considerations that the γ rays would be shielded from the JUROGAM detectors by the downstream magnet coil. Thus some γ ray transitions will be measured with a lower absolute efficiency. However the electrons will still be transported via the magnetic field to the SAGE silicon detector. Hence the measured conversion coefficients were much higher than the literature values allowing for a lifetime on the order of $\tau_{1/2} \leq 17$ ns. The measured K/L shell ratio is $(\mathrm{K/L})^{exp}_{241} = 3.2 \pm 1.9$ compared to the BRICC value $(\mathrm{K/L})^{BRICC}_{241} = 2.5 \pm 0.1$ (based on a calculated δ=2 from Equation 2.58, page 39) suggests this is a mixed M1+E2' transition.

From the strongly coupled band, the 521 keV transition linking the $11/2^-$ bandhead to the $11/2^-$ alpha-decaying state could have an E0 component alongside M1 and E2 competing multipolarities. Again the recoil-decay tagged γ–γ and γ–e^- are used. The selection of gates requires consideration. The 521 keV transition has several similar energy peaks within this region, one of which is a decay path from higher up the band. Thus only sum coincidences with the 227 keV, 172 keV M1+E2' and 376 keV, 399 keV E2 transitions can be selected.

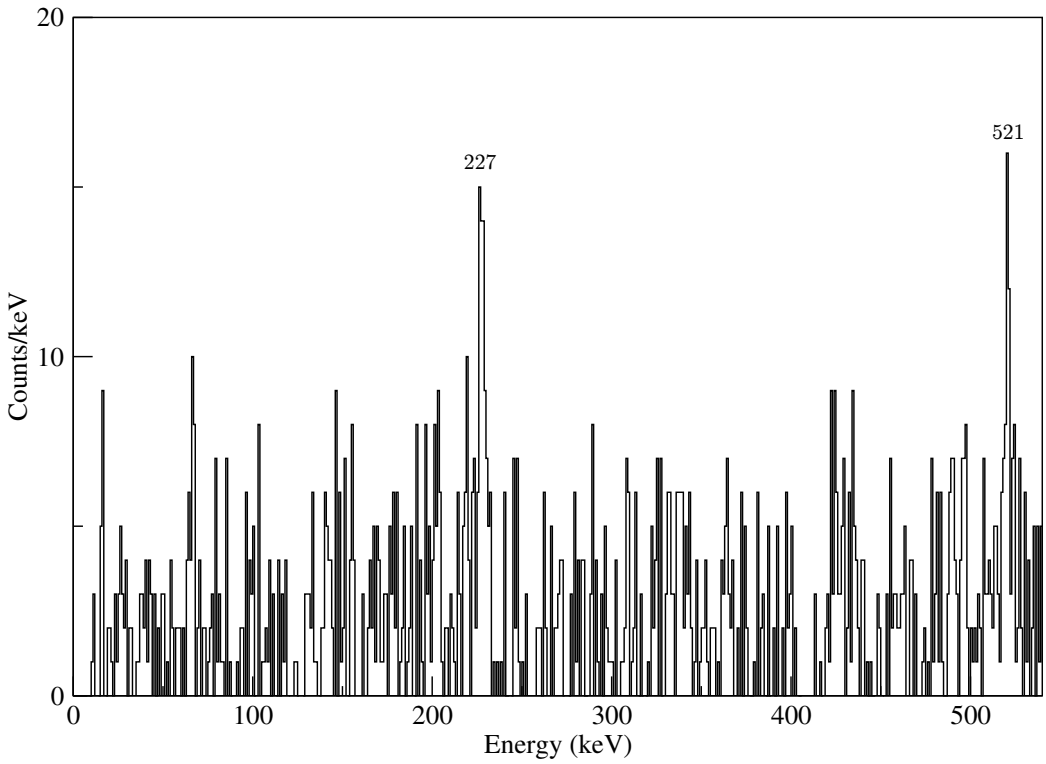

Figure 4.5: *γ rays from the recoil decay tagged γ–γ matrix in sum coincidence with the 227 keV, 376 keV, 172 keV and 399 keV γ ray transitions (background subtracted). The 227 keV and 521 keV transition are the most dominant transitions observable.*

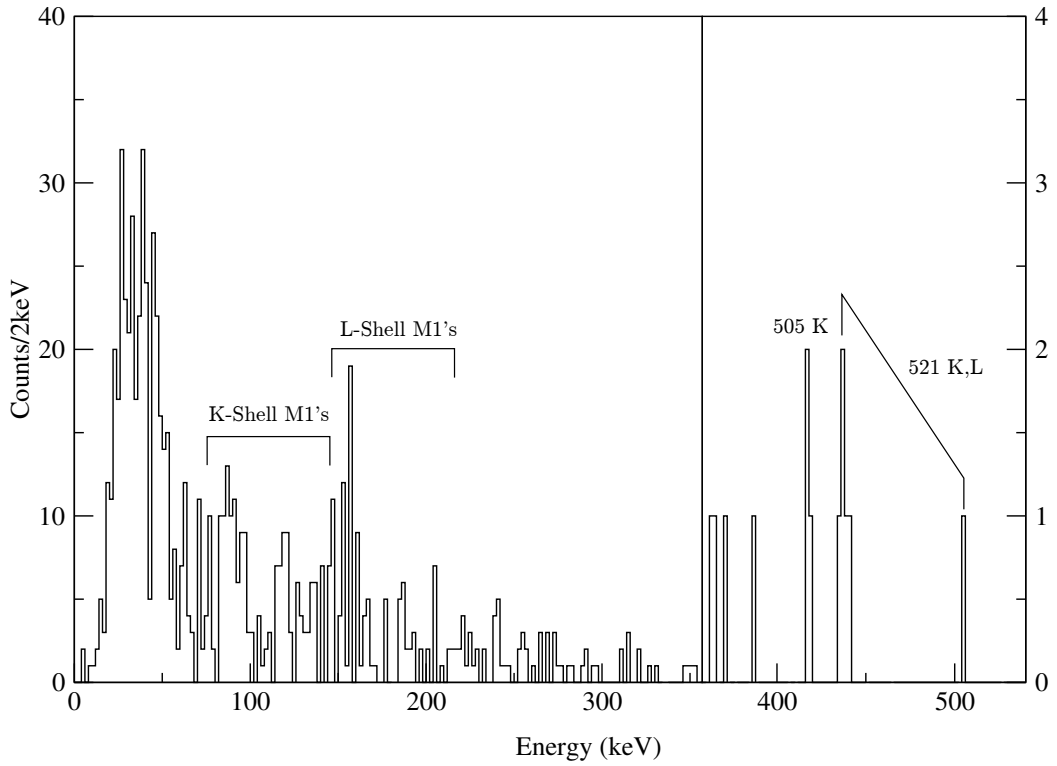

Figure 4.6: *Electrons from the recoil decay tagged γ-e^-− matrix in sum coincidence with the 227 keV, 376 keV, 172 keV and 399 keV (background subtracted).*

The K electron peak is coincident with the selected transitions and is observed with 4 counts, while the L peak is observed with only one count and so could be considered as background. The conversion coefficient from this was measured to be α_K=0.08±0.03. While statistics remain limited, based on the calculated BRICC values of α_K^{E2}=0.02 and α_K^{M1}=0.06, then it is difficult to judge any form of E0 component. Indeed based on data from the Hg cores one would expect much more intensity in the electron emission than is observed. From the independent ^{177}Au experiment currently under analysis conclusions are yet to be drawn regarding intensity balance arguments [59]. The bandhead configuration thus remains open to debate.

Further transitions were too weak for measurement due to low population or a low conversion coefficient. This commissioning experiment has allowed a comparison of the results to the literature values and indicates that when SAGE is fully operational, it will allow for cross coincidence analysis to be performed successfully.

Chapter 5

Previous studies on ^{253}No

There have been a number of recent efforts made to study ^{253}No through in-beam and decay spectroscopy studies. Low cross-sections make experimental work challenging. This is compounded by the fact that odd-A nuclei typically exhibit coupled band structures compared to even-even nuclei, having strong M1 interband transitions, and this, combined with the large mass of the nucleus leads to internal conversion competing strongly with γ ray emission. This has meant sophisticated and novel experimental devices and techniques are required to fully understand the single-particle structure of this nucleus, and others in the heavy mass region.

5.1 In-beam Studies

Two in-beam γ ray spectroscopy studies performed have produced opposing experimental results. The first prompt γ ray study performed by Reiter at GAMMASPHERE, USA in 2005 identified two rotational bands built on the $7/2^+[624]_\nu$ bandhead which decays to the $9/2^-[734]_\nu$ ground state via a ∼355 keV multiplet [60].

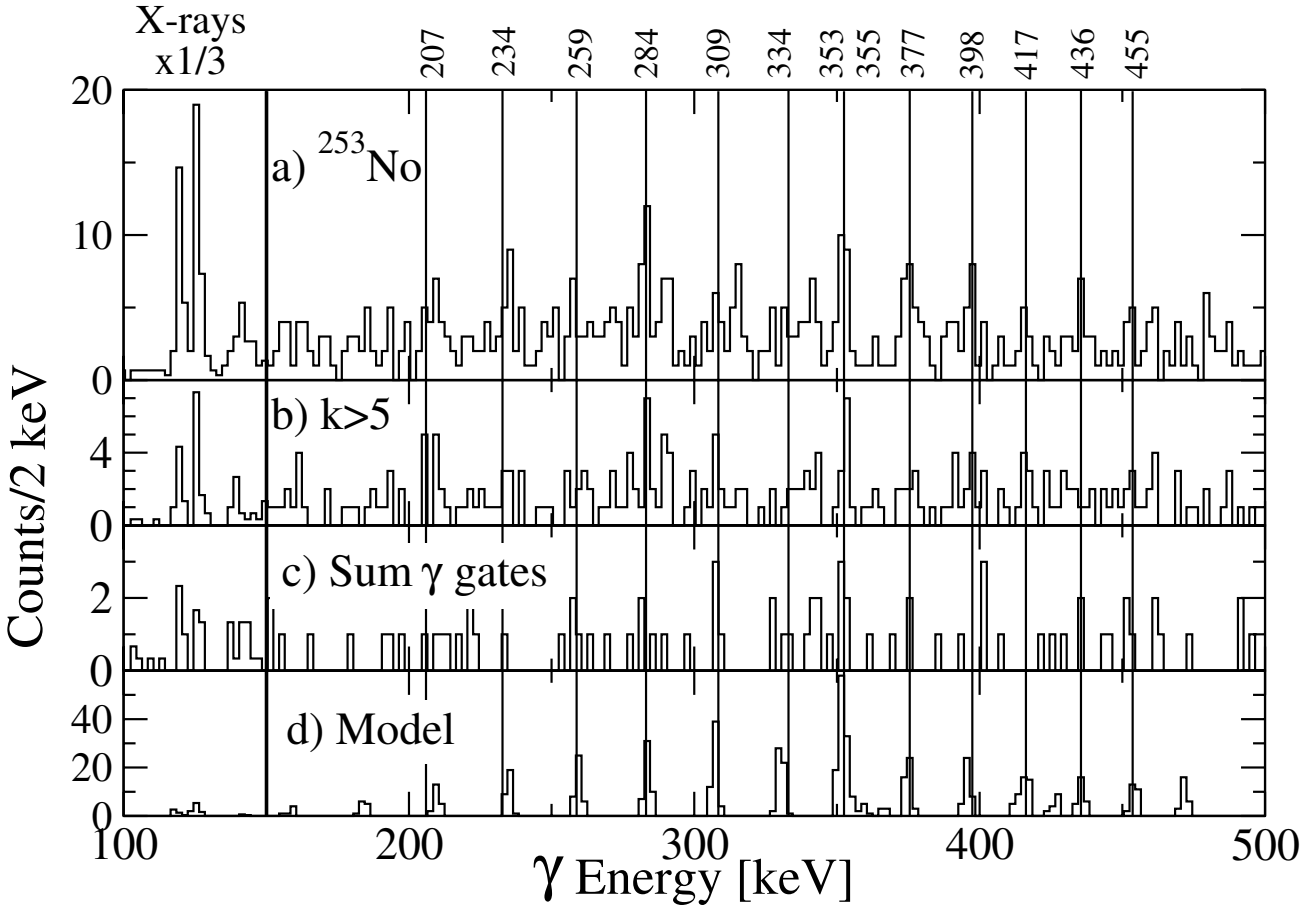

Figure 5.1: *Prompt γ rays measured at* GAMMASPHERE *[60]. (a) Coincident with ^{253}No residues, (b) $\geq$ 6 fold γ ray multiplicity (i.e. more than 5 germanium detectors measuring a signal within a very short time period), (c) sum of γ–γ coincidence gates, (d) Simulated spectrum based on a 7/2$^+$[624] bandhead.*

The data shows a strong 355 keV transition and a lack of interlinking M1+E2' transitions. Based on this γ–γ analysis and moment of inertia calculations the level scheme was deduced.

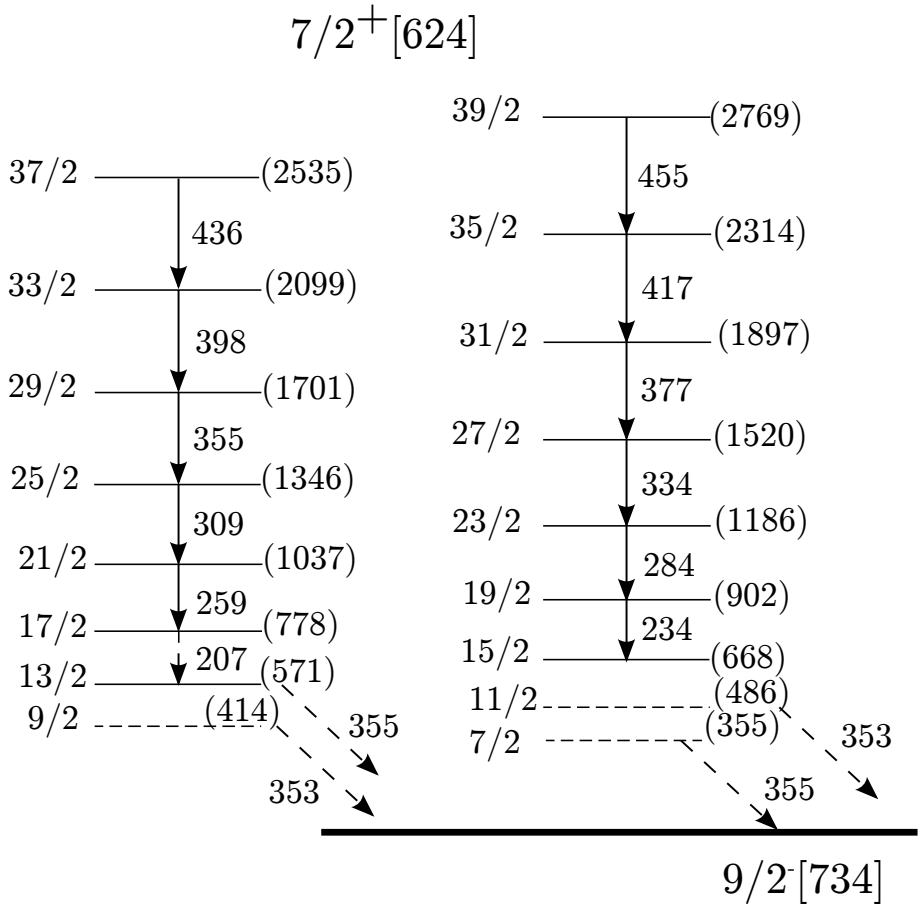

Figure 5.2: *Prompt level scheme for* ^{253}*No deduced by an in-beam* γ *ray study at* GAMMASPHERE *[60].*

The intensity flow is predominately of E2 multipolarity through two rotational bands. A combination of γ–γ coincidences, moment of inertia measurements and model calculations are the basis behind energy and single-particle level assignments; however it is clear from the data available that statistics are severely limited.

In contrast, Herzberg and Moon *et al.* performed an in-beam γ ray study at JYFL, Finland using the JUROGAM germanium detection array, which established two strongly coupled rotational bands built on a $9/2^-[734]_\nu$ bandhead [61].

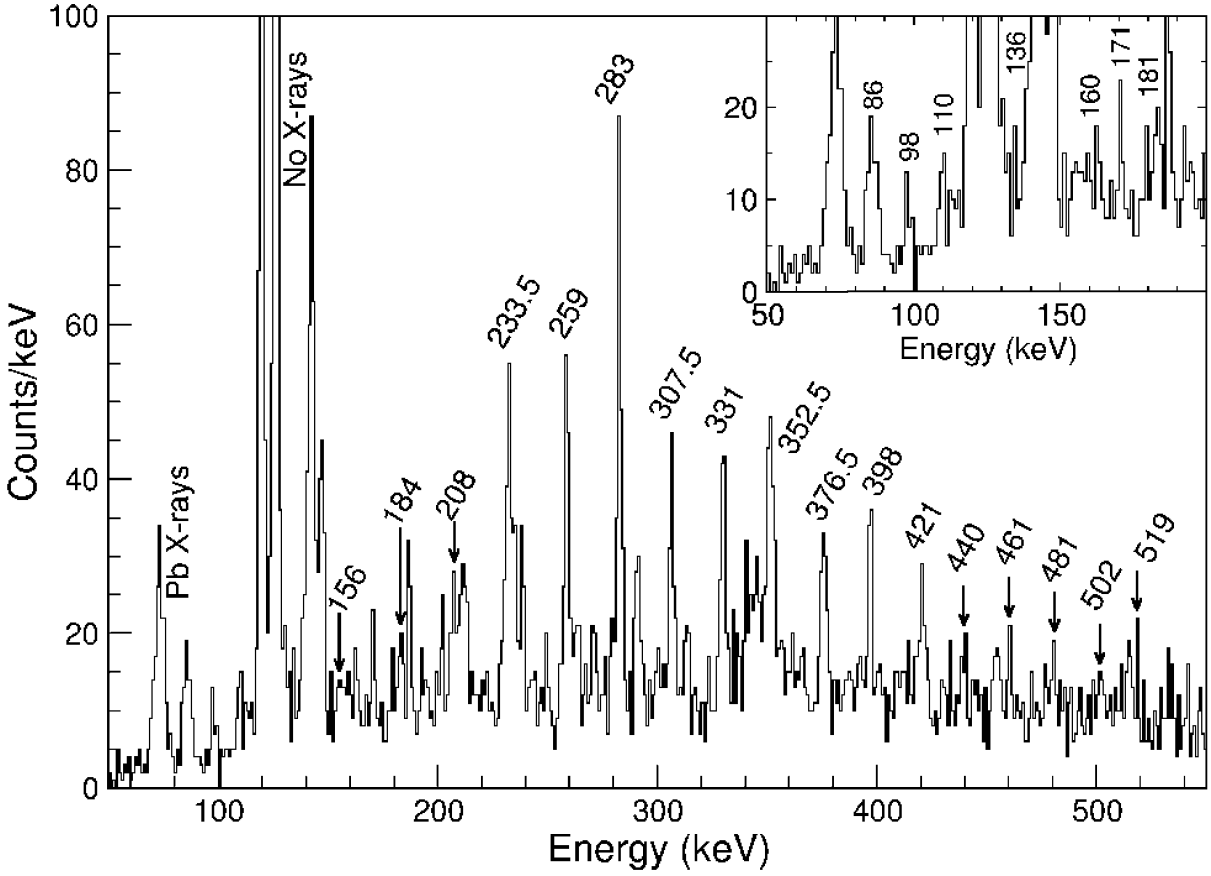

Figure 5.3: *Recoil-tagged γ ray-singles spectrum using* JUROGAM. *The inset shows lower energy interlinking M1+E2' transitions [61].*

Statistics are improved in this study, with interlinking transitions between the two rotational bands evident, alongside the intense yrast band stretched E2 transitions. The level scheme deduced in this study is shown in Figure 5.4.

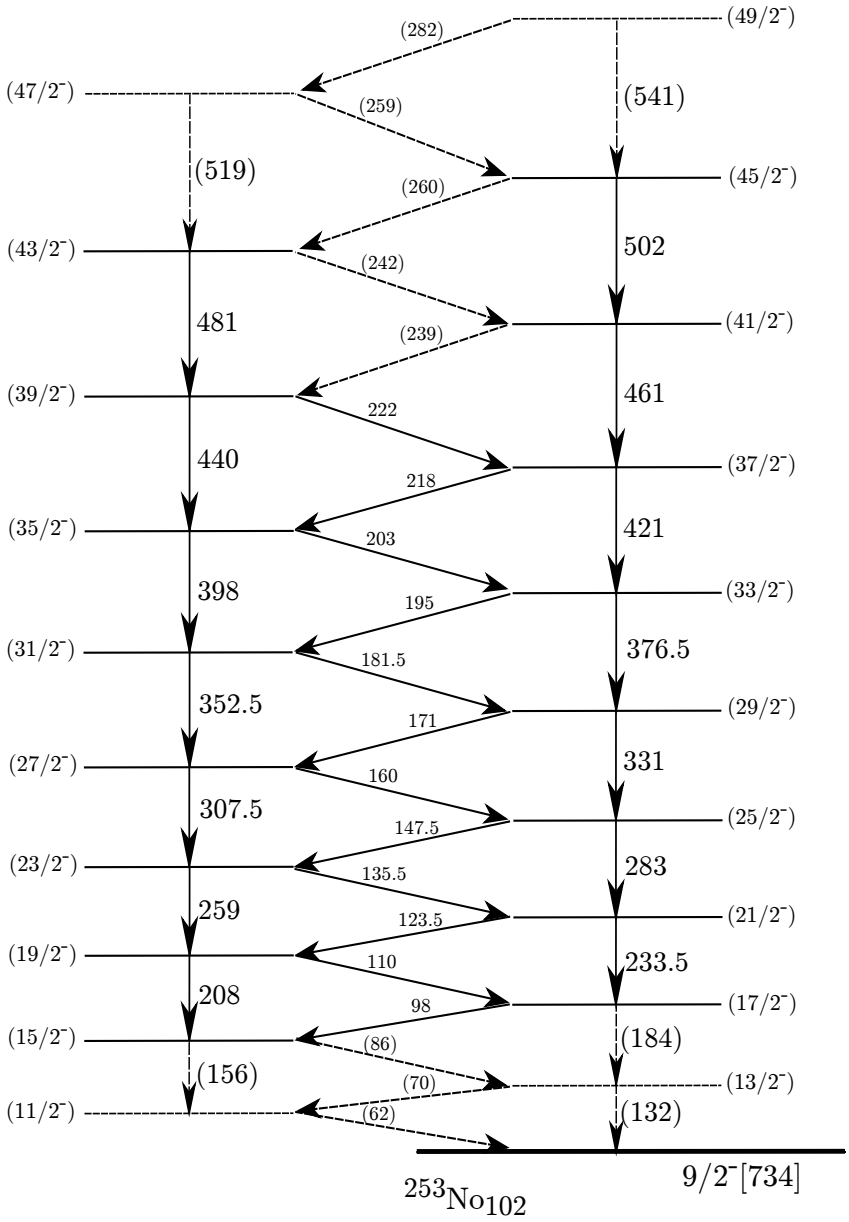

Figure 5.4: *Coupled rotational bands for ^{253}No deduced by an in-beam γ ray study at* JYFL *[61].*

The lower energy transitions are tentatively placed with ambiguity over energy assignments. The stretched E2 energy transitions are in agreement with Reiters' work, however the 355 keV transition found to be a multiplet in the previous study is only measured to be a higher spin E2 singlet in this study.

The final piece of in-beam data to be considered is a conversion electron spectroscopy experiment performed in 2002 using the SACRED spectrometer [62].

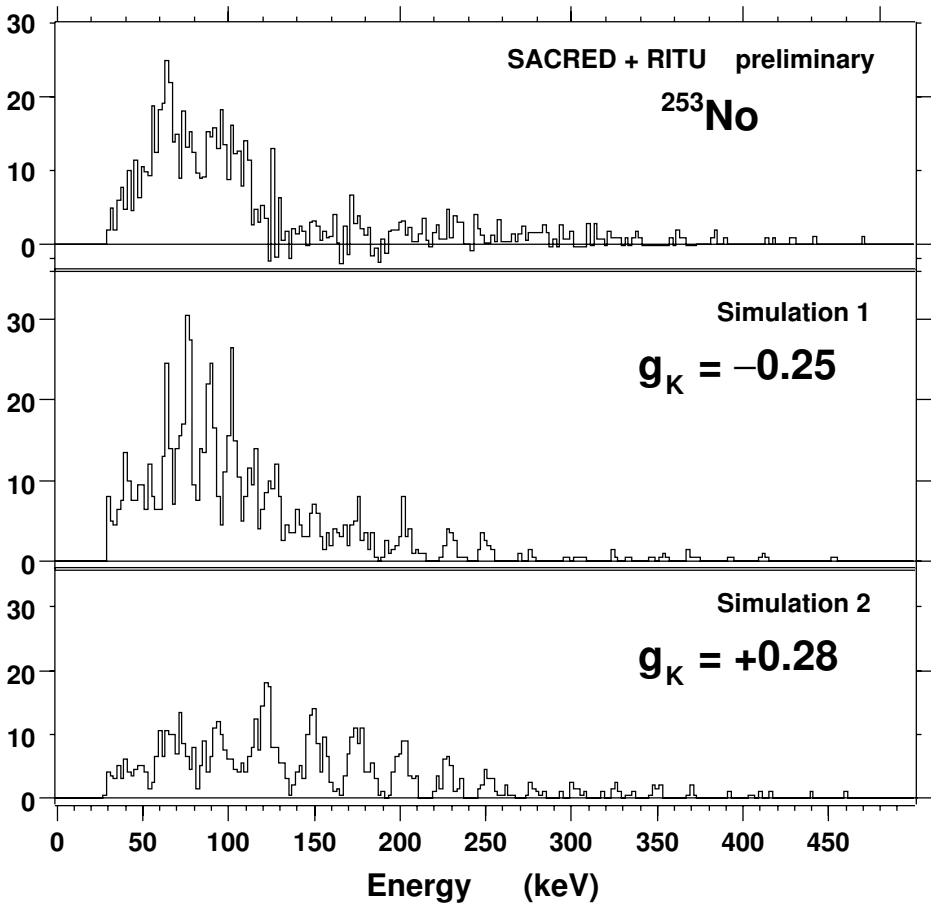

Figure 5.5: *Electron spectrum detected using the* SACRED *electron spectrometer [62]. This is compared to Monte Carlo simulations based on the 9/2⁻[734] (g_K=-0.25) and 7/2⁺[624] (g_K=+0.28) single particle bandhead structures.*

Experimental data is sparse hence further study with conversion electrons is essential. While the comparison of single energy peaks with the simulations remains ambiguous, comparing the structure of the data sets show intensity flows predominately through the lower energy L shell M1+E2' transitions compared to the E2 K-shell electrons. This points towards the $9/2^-[734]$ as the bandhead configuration.

Measurement of the intensity ratio between interband and intraband transitions (T(M1+E2')/T(E2)) (as well as moment of inertia calculations) leads to the assignment of the $9/2^-[734]$ bandhead single-particle configuration in both the JUROGAM γ ray study and the SACRED conversion electron study.

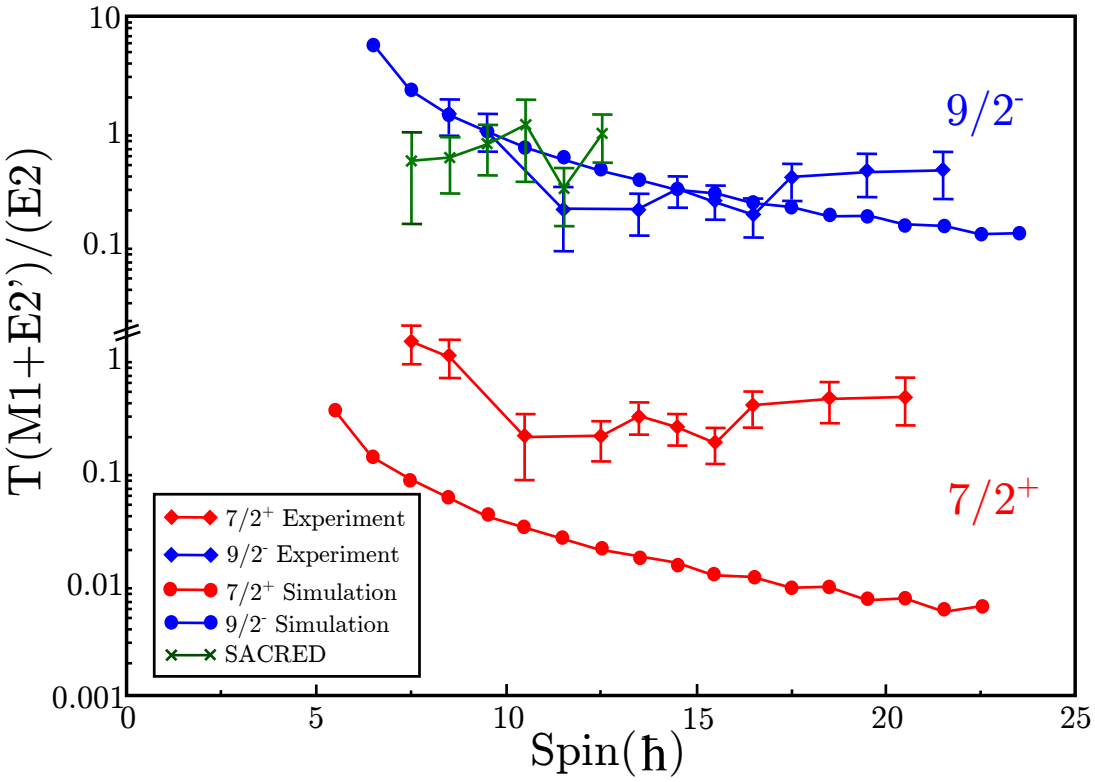

Figure 5.6: *Ratio between the interband and intraband transitions measured with γ ray-singles in [61]. The $9/2^-[734]$ bandhead configuration is favoured. Data from the* SACRED *spectrometer is included.*

It is now worth considering the importance of the configurations, the role they play in determining the structure of odd-A nuclei and the reflection of this in experimental data.

5.2 Systematics for N=151 Nuclei

The flow of transition intensity through the yrast bands of ^{253}No is dependent on the contribution of the single unpaired neutron (g_K) to the magnetic dipole moment given in Equation 2.40, page 30. If the bandhead is $7/2^+[624]$, then due to the anti-alignment of the spin and orbital angular momentum of the single unpaired neutron, then the g_K-factor is positive; for the $9/2^-[734]$ configuration, the g_K-factor is negative as a consequence of alignment. The g_R-factor for ^{253}No is ≈ 0.4, thus for the $9/2^-[734]$ (g_K=−0.25) single neutron configuration one would expect to see strong interband mixed M1+E2' transitions (see Section 2.8.1, page 34), whereas for $7/2^+[624]$ (g_K=+0.28) then most of the intensity flow would be through the stretched E2's.

The argument over the bandhead configuration lies in systematics around the N=151 isotones. Theoretical model calculations by Ćwiok *et al.* [63] are shown in Figure 5.7.

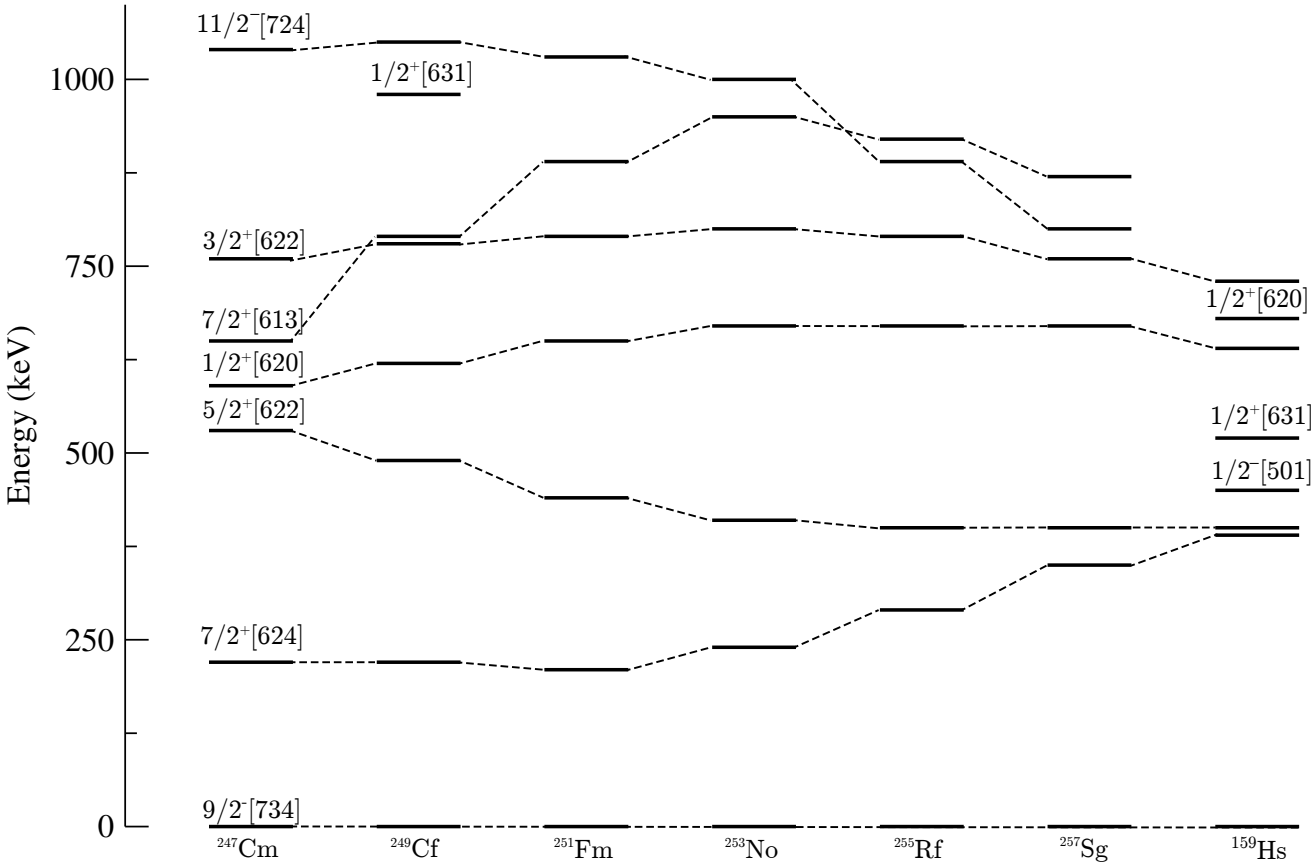

Figure 5.7: *Systematics of theoretically calculated single particle neutron states for the N=151 odd-A isotones from Z=96-108. Data obtained from Ćwiok [63].*

The model uses the Nilsson-Strutinsky approach with an average Wood-Saxon potential and monopole pairing residual interaction. The lower energy states follow similar ordering with a tendency to converge to an increased level density at higher Z. The model assumes a $9/2^-[734]$ ground state configuration. The next levels increase as $7/2^+[624]$, $5/2^+[622]$ and $1/2^+[620]$ respectively for all isotones. A more recent study by Parkhomenko and Sobiczewski applied the same Wood-Saxon potential but differed in parametrization [64]. The single particle levels from this study are shown in Figure 5.8.

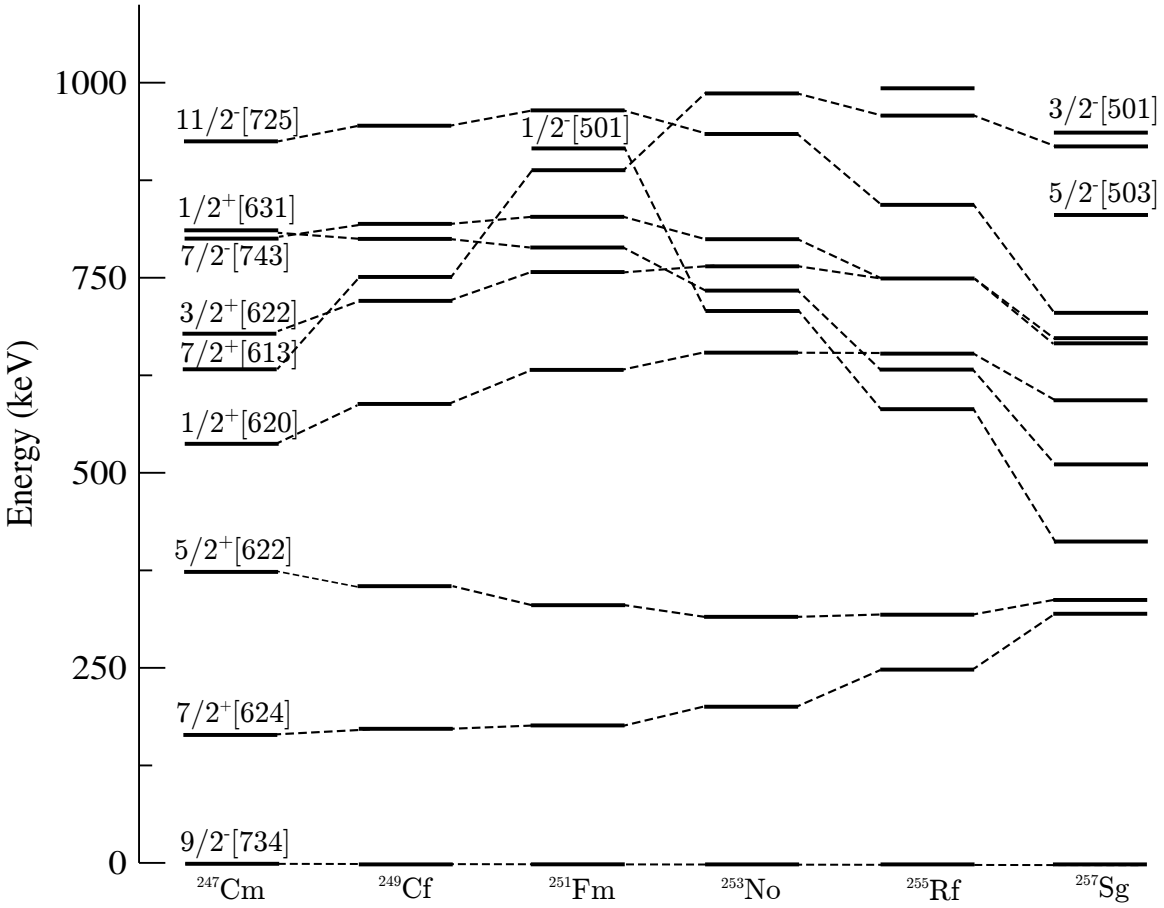

Figure 5.8: *Systematics of theoretically calculated single particle neutron states for the N=151 odd-A isotones from Z=96-106 using different model parameters to Figure 5.7. Data obtained from Parkhomenko and Sobiczewski [64].*

The general trend of convergence towards increased level density for heavier isotopes is evident again. The ordering of states is in agreement for lower lying states, but with the increased number of states predicted by Parkhomenko and Sobiczewski, this differs at higher energies. Both models can be compared to experimentally deduced results from both in-beam and decay spectroscopy studies.

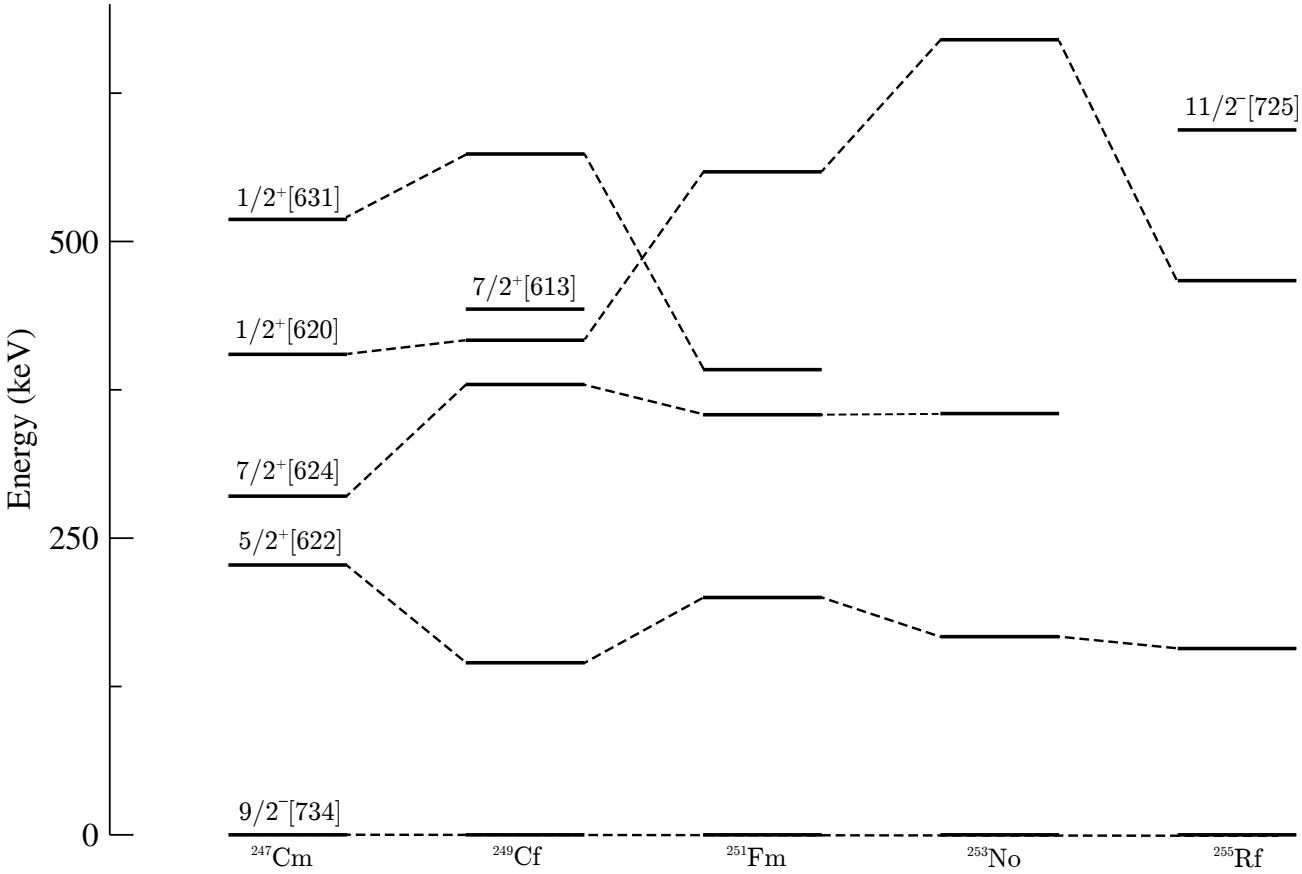

Figure 5.9: *Experimentally measured single particle states for N=151 isotones.* ^{247}*Cm measured by [65] [20],* ^{249}*Cf [66] [67],* ^{251}*Fm [68],* ^{253}*No [69] [70],* ^{255}*Rf [71].*

Clearly there are discrepancies between model and experiment. The $5/2^+[622]$ and $7/2^+[624]$ levels are inverted. Experimental data is limited in this region so any trend towards a general convergence of levels as Z increases is difficult to deduce. However there is a strong agreement on the ground state configuration of $9/2^-[734]$ for all of the N=151 isotones. This is simply from the single unpaired valance neutron occupying this orbital.

5.3 Focal Plane Studies

Focal plane based decay spectroscopy experiments have proved a useful tool in determining the ordering and energy levels of the single-particle states in ^{253}No. Measurements on isomer decays have advanced understanding of how the structure evolves as a result of quasi-particle states while α–γ studies have contributed to helping to unveil the excited level structure in ^{249}Fm.

5.3.1 Isomer Decay Studies

An isomeric state in ^{253}No was first established by Bemis *et al.* with a half-life of 31.3±4.1 µs [72] and has been confirmed in a number of further studies [69] [73] [74]. These more recent studies have determined this to be a single-neutron hole in the $5/2^+[622]$ state with energy of 167 keV, which decays via an M2 transition. A second, slower decaying multi-quasiparticle isomeric state has been observed, with a half-life measured by Lopez-Martens *et al.* to be of 706±24 µs using the VASSILISSA separator setup in FLNR, Russia [73]. Antalic *et al.* measured 627±5 µs with decay energy of at least 1440 keV using the SHIP separator setup in GSI, Germany [74]. This is predicted to be a decay from a high-K state and potentially has 3-quasiparticle configurations of 1 neutron and 2 protons with either the $\{9/2^-[734]_\nu \otimes 7/2^-[514]_\pi \otimes 9/2^+[624]_\pi\}$ or $\{9/2^-[734]_\nu \otimes 1/2^-[521]_\pi \otimes 9/2^+[624]_\pi\}$ configuration postulated such that $K^\pi = 25/2^+$ and $19/2^+$. The deduction of such states is based on the $K^\pi = 8^-$ isomeric state in ^{254}No [73]. This comparably short-lived isomer in ^{253}No potentially populates a non-yrast structure which decays to the yrast band via an intense 802 keV and a weaker 714 keV M1 transition [69], [74]. This 802 keV transition has also been observed in prompt spectroscopy studies [75]. Again, consideration of the states in ^{254}No, leads to the configuration of this structure likely to be $\{9/2^-[734]_\nu \otimes 1/2^-[521]_\pi \otimes 7/2^-[514]_\pi\}$ with $K^\pi=15/2^-$ [73]. An example of the γ rays resulting from such states is shown in Figure 5.10. Figure 5.11 gives an overview of the predicted structures.

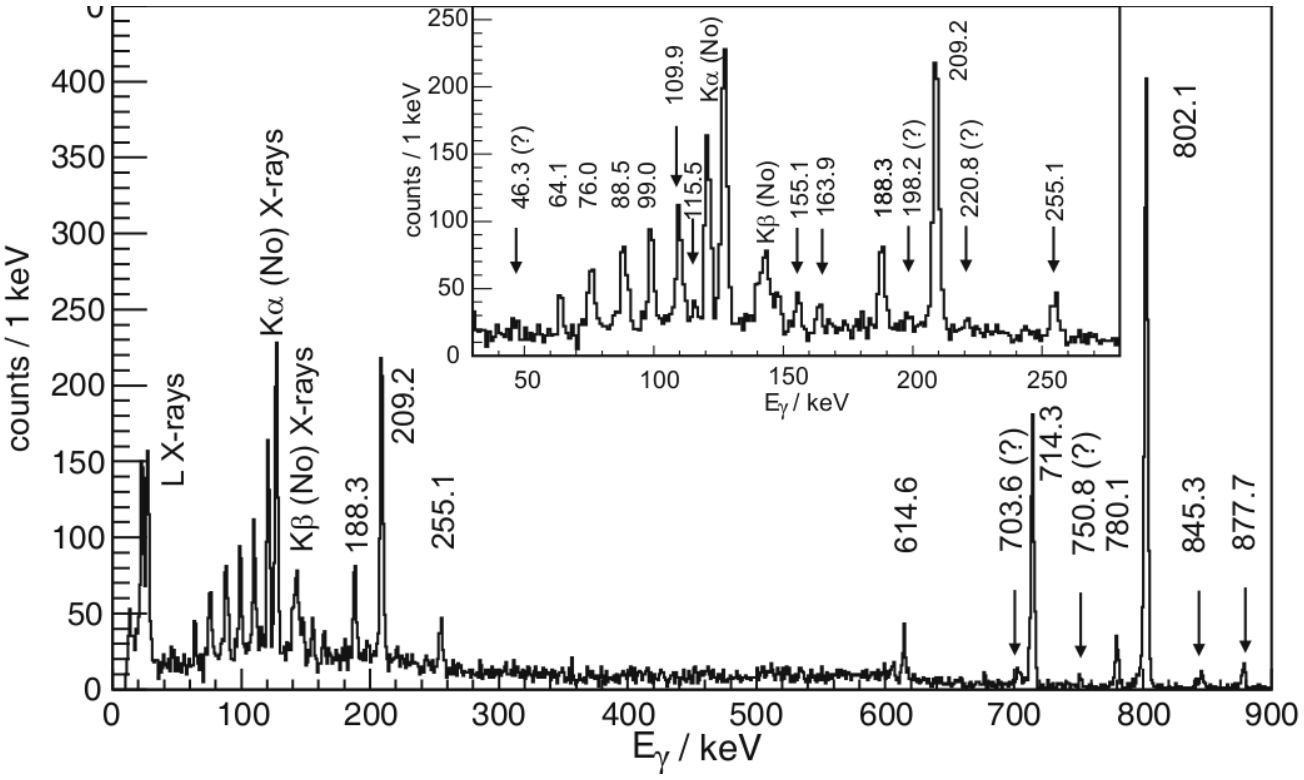

Figure 5.10: *Focal plane γ ray spectrum within 5 ms following recoil implantation. The intense 802 keV transition is evident alongside lower lying ground state band decays. The study was performed using the* SHIP *velocity separator in GSI. Adopted from [74].*

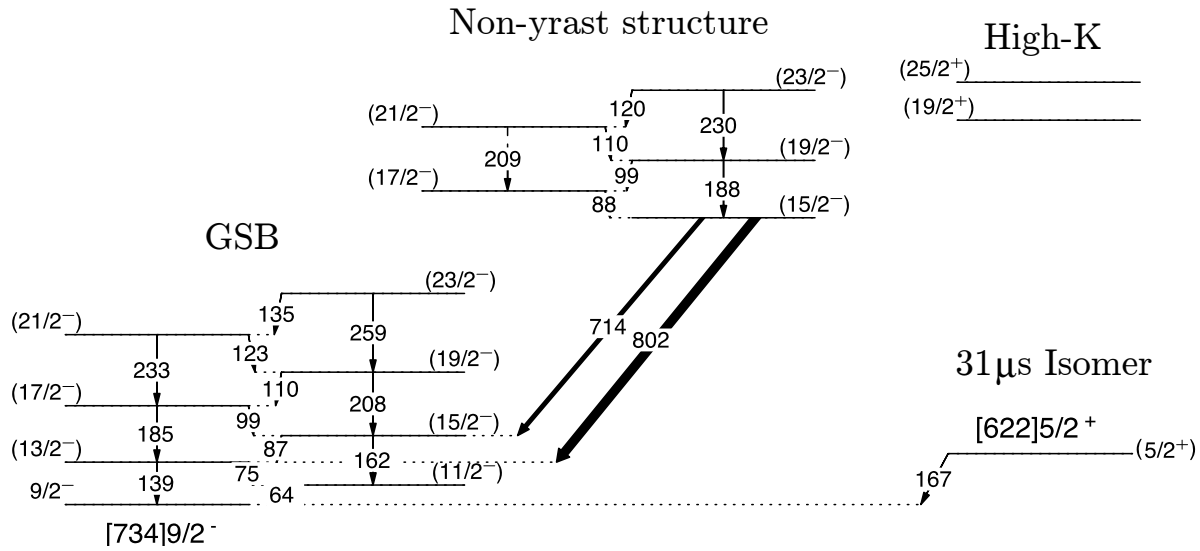

Figure 5.11: *Tentative level scheme measured by Lopez-Martens. The ground state band, $5/2^+$ 31 μs isomeric state, intermediate structure and potential high-K bands (included for completeness) are labelled. Adopted from [69].*

5.3.2 Excited States in ^{249}Fm

^{253}No has been observed to have three decay channels through α transitions into populated excited states in ^{249}Fm in a number of studies [13] [73] [76]. The most prominent decay path is through the 8.004 MeV α emission which results in population of the $9/2^-[734]$ level. The half-life measured in these studies are in agreement with 1.7(3) minutes. Subsequent E1 and M1 transition decays to the $7/2^+[624]$ ^{249}Fm ground state. Multipolarity assignments were based on intensity balance arguments and conversion coefficient measurements. They are also supported by the E1 character of the dominant transitions having a low conversion electron component. This results in the summing effect between conversion electrons and the α particles being small, with only the 58.3 keV M1 transition impacting on the energy distribution of the α peak. The summing effects of conversion electrons and α particles cause a higher energy tail for the α peak hence for the α peak in coincidence with the 279.5 keV E1 transition, summing would be weak, whereas coincidence with the 221.5 keV and the 58.3 keV transitions with higher conversion coefficient, a peak shift would be evident. These considerations allow for the assignment of energy levels in the structure observed by Hessberger is shown in Figure 5.12 [77].

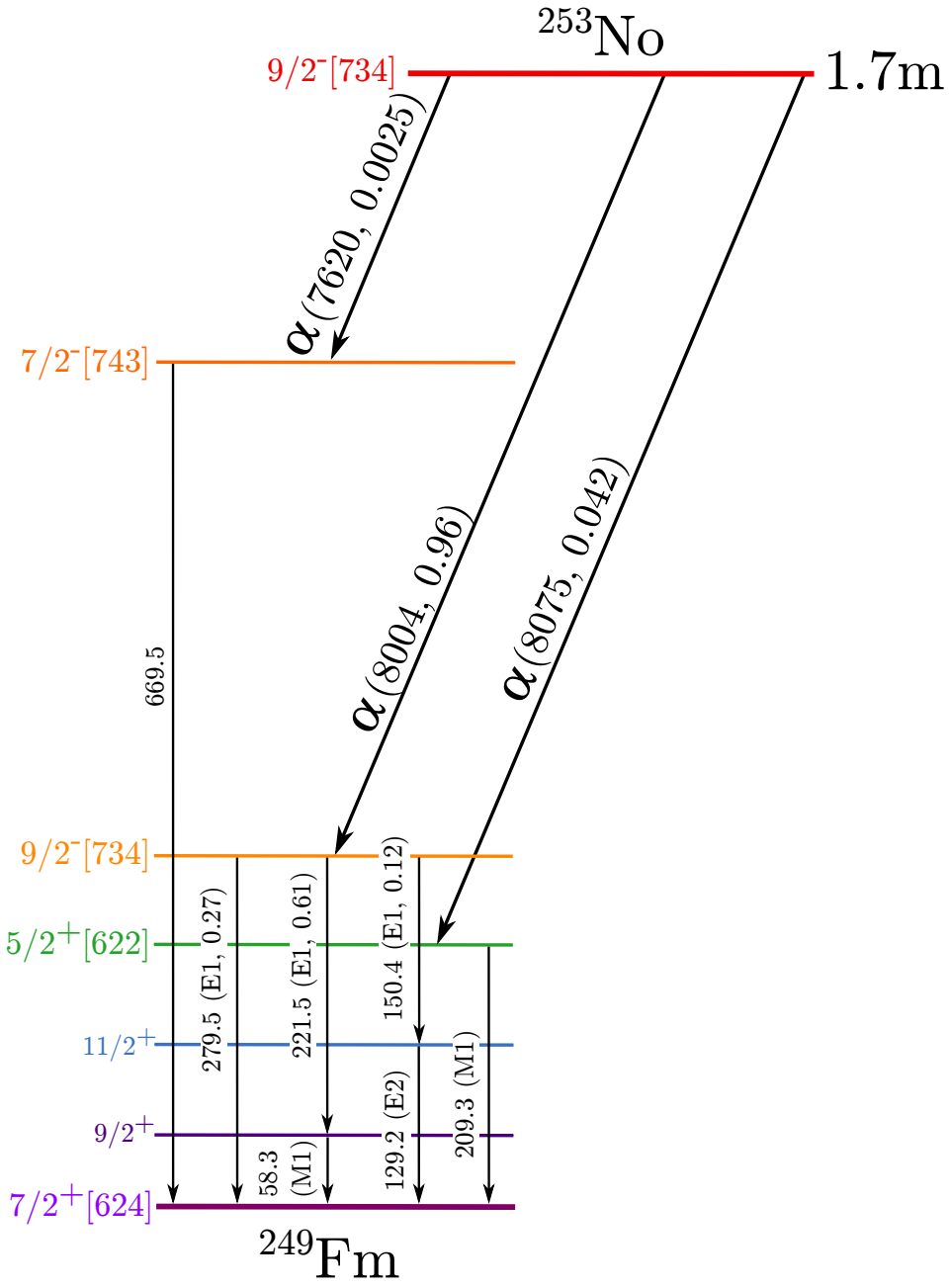

Figure 5.12: *Excited states in ^{249}Fm populated through the α-decay of ^{253}No. Energy assignments and intensities are labelled. Adapted from [77].*

^{249}Fm subsequently α-decays to the granddaughter ^{245}Cf with a measured half life of 2.6 minutes [20]. The half life of ^{245}Cf is 100 years [20] and hence no further α-decays would be observed.

Chapter 6

Analysis and Discussion

6.1 ^{253}No In-Beam Spectroscopy

During the experiment, a total of ∼5900 ^{253}No recoils were detected (those which had been correlated with the time of flight between the gas counter and the DSSD) with ∼3200 ^{253}No alpha decay events. Using the analysis techniques outlined in Chapter 3, ^{253}No is studied through the recoil-tagging technique, with γ–electron coincidences forming the basis for construction of the level scheme. The assignment of the bandhead is determined through intensity considerations and comparisons to theoretical models.

6.1.1 Recoil-Tagged Prompt Decays

The prompt recoil tagged γ ray spectra are shown in Figures 6.1 and 6.2. The γ rays shown include those that have deposited their full energy into one Ge crystal, or have scattered into a neighbouring crystal in a clover detector. Including events that had scattered into three or four crystals did not improve on statistics of interest and indeed contributed to background events from random scatters.

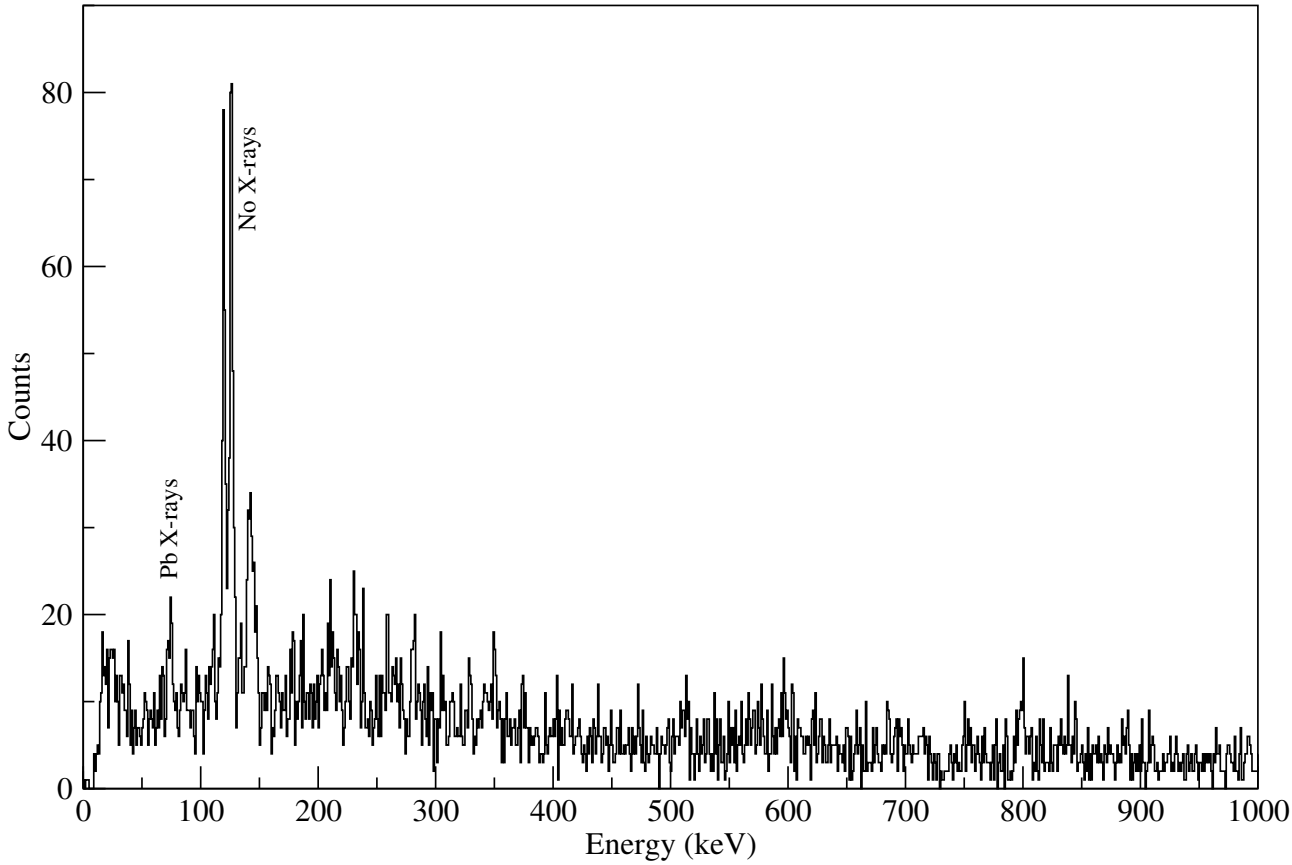

Figure 6.1: *Recoil-tagged γ-ray singles from* JUROGAM II.

Strong K_α and K_β X-ray peaks dominate the spectrum at around 120 keV and ∼140 keV indicating a high degree of internal conversion. Contributions to this may come not only the yrast band, but from highly converted sidebands. The level of statistics is limited, typical of low cross-section odd-A heavy transfermium nuclei. Evidence of peaks are observed across the lower energy portion of the spectrum. This is expanded upon to observe the potential transitions of interest.

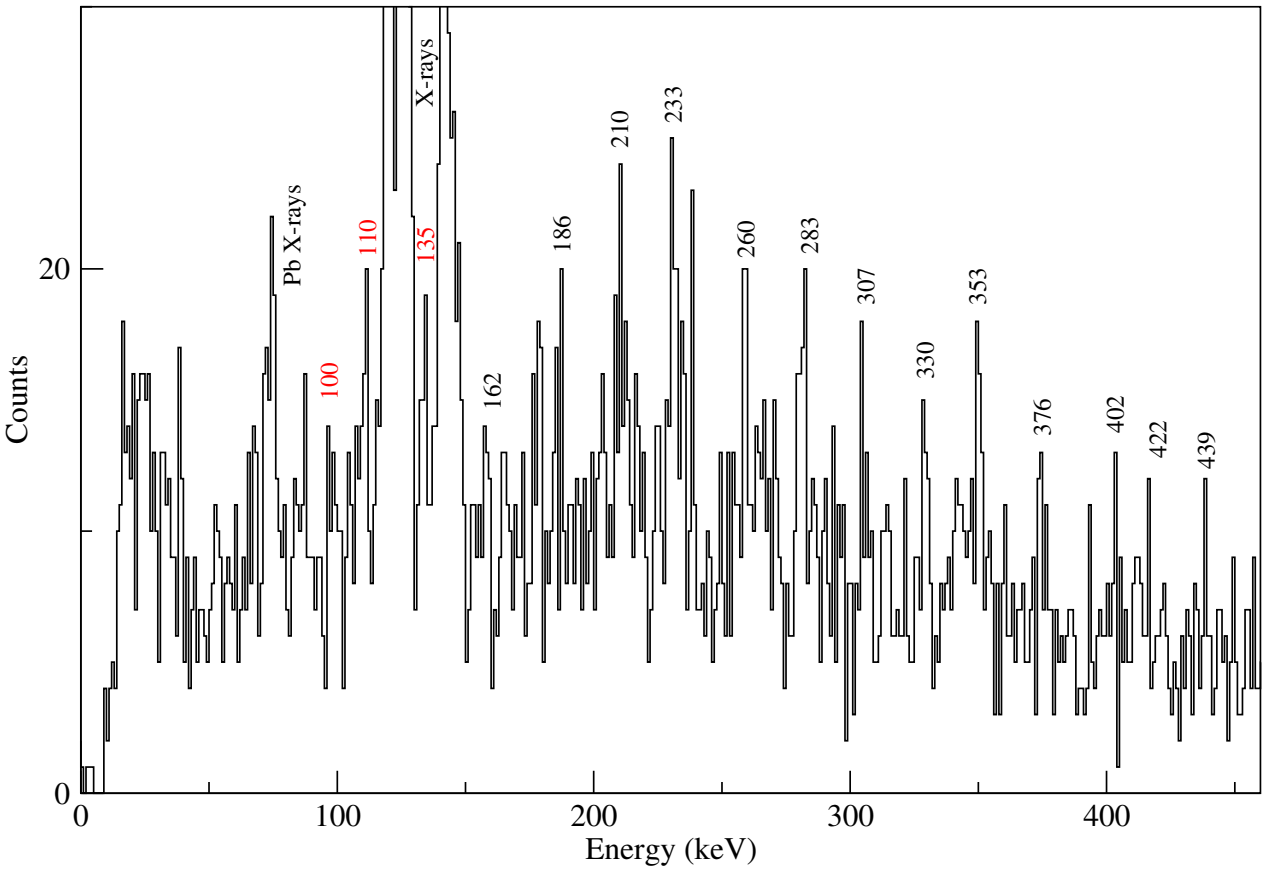

Figure 6.2: *Recoil-tagged γ ray singles from* JUROGAM II *(expanded at lower energies) The black labels correspond to potential intraband E2 transitions and the red labels correspond to mixed M1+E2' interband transitions*

A 'picket fence' like structure can be observed which is a well known feature of a rotational band structure. Potential interlinking transitions appear in the lower energy region below the X-ray energy threshold. Rotational bands have increasing energy with increasing spin which conforms to this spectrum. Beyond energy 439 keV statistics are too low to determine any further peaks. There are also additional peaks (such as the peak around 800 keV) which will be discussed later on.

The recoil-tagged prompt electrons are shown in Figure 6.3. In this case the electron recoil coincidence gate from Chapter 3 Figure 3.21 is used as the recoil-electron timing filter.

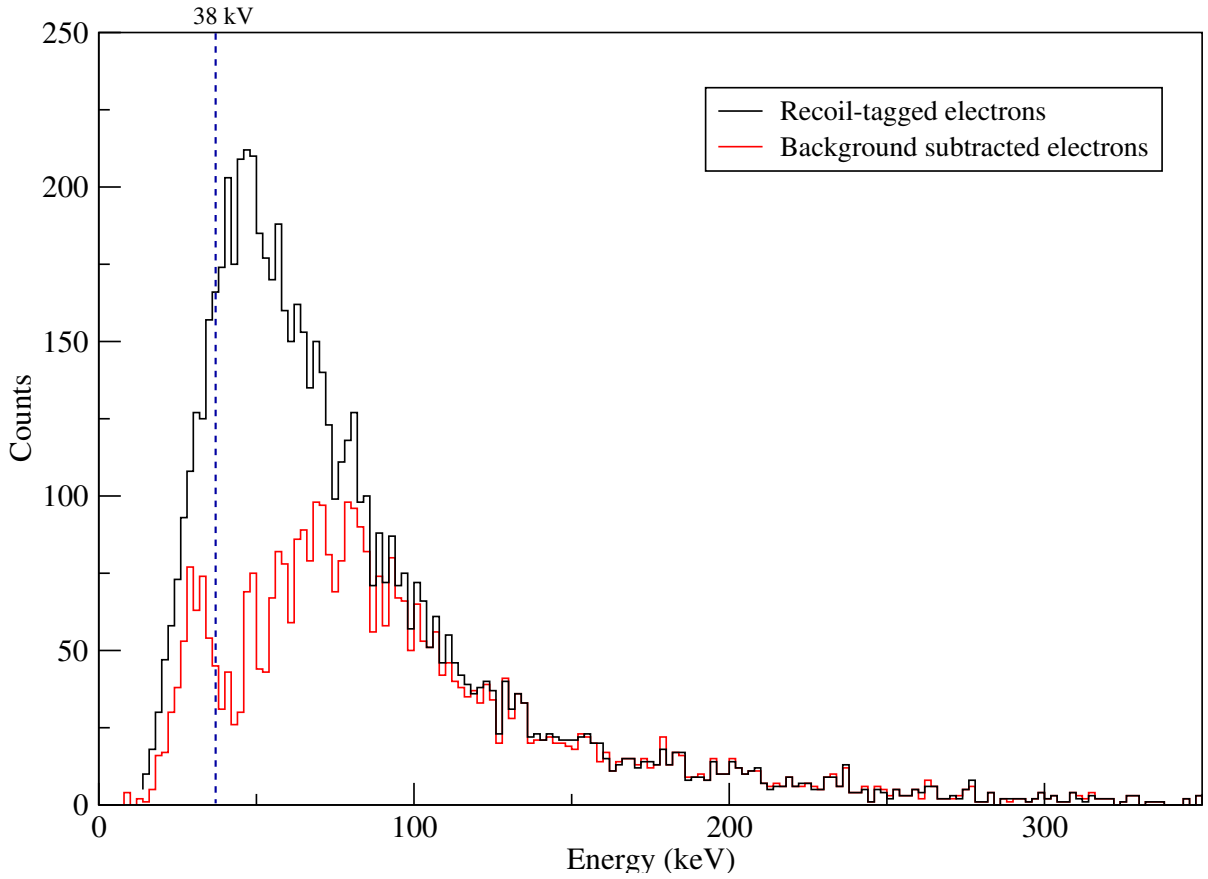

Figure 6.3: *Recoil-gated electrons (black) and after a background subtraction (red) (anticoincidence with recoil and prompt time coincidence gates) applied. The high voltage barrier is indicated by the blue dashed line.*

The dominance of low energy electrons stems from large conversion at lower transition energies and δ-electrons. Below 38 keV the high-voltage barrier prevents any further measurements caused by electrical discharges in the barrier which can impinge on the silicon detector, potentially contaminating this region. A background subtraction method was applied whereby an appropriate fraction of electrons in anticoincidence with the recoil and electron timing gates were treated as background and subtracted from the spectrum. At lower energies this proves useful in uncovering transitions hidden in the background, with decreasing scope at higher energies.

Potential peaks in the background subtracted spectrum are indexed and labelled.

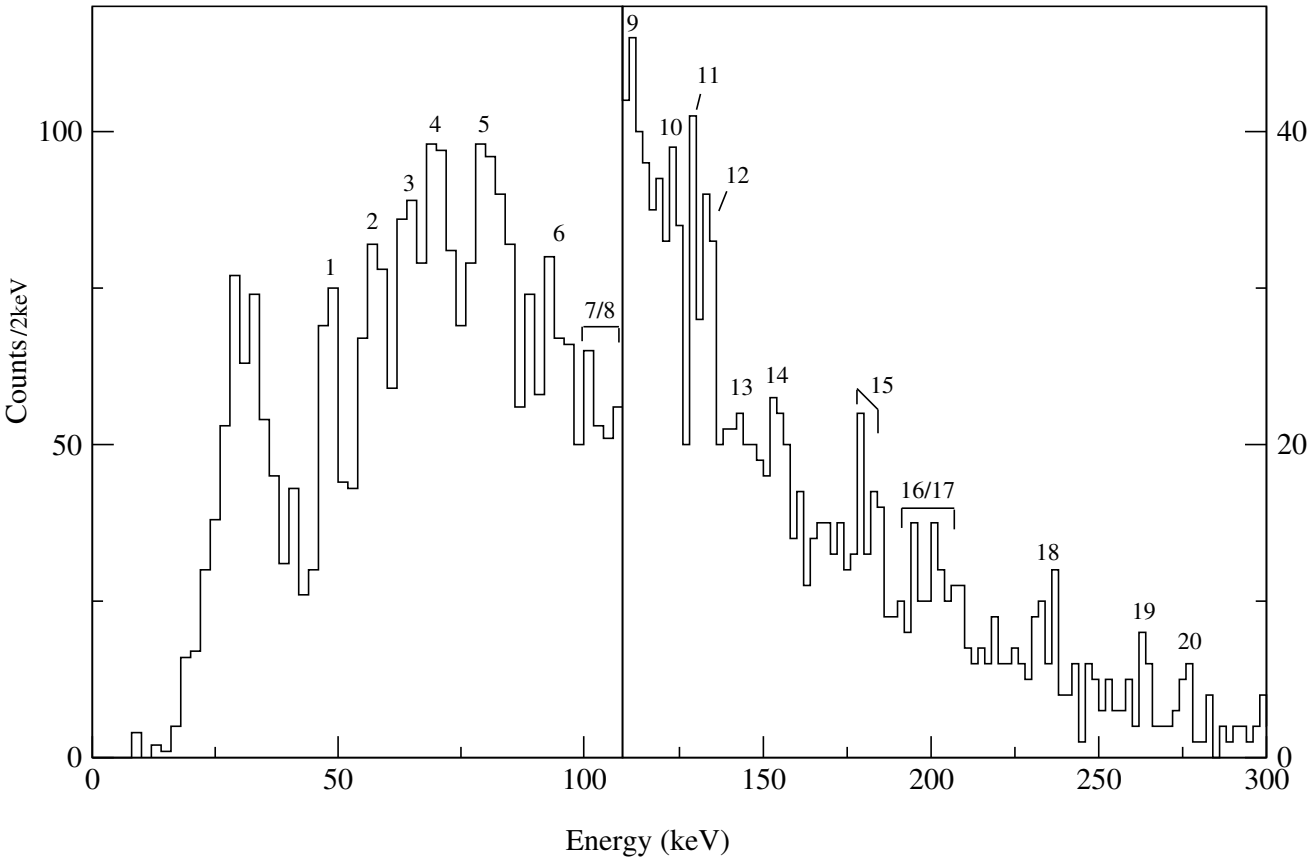

Figure 6.4: *Background subtracted recoil-tagged electrons. The peaks are indexed and labelled as given in Table 6.2.*

Figure 6.4 has peaks indexed according to Table 6.2. On the consideration of whether a given number of counts constitutes a peak (and hence a transition) two approaches were utilised. If the net peak area (counts above the average background) is at or above 10 counts then a Gaussian distribution can be used and a critical limit determining whether the net count is significant can be defined.

$$L_c = 2.33\sqrt{B} \tag{6.1}$$

with a 95 % confidence limit, where B is the background count underneath the peak area. For the case where there is less than 10 counts then a Poisson fitting distribution must be applied and careful consideration of the background region must be taken into account when assessing the viability of a peak. Assume that the number of counts in the region of interest in a randomly generated sample is given as x, and the mean background rate is λ. The number of counts above the background must be significant enough to give a confidence limit of 95 % to assign

a peak. If one knows the number of counts in the background, a minimum number of counts above the background can be established for a given confidence limit from tabulated values on Poisson statistics. As an example if the given background count is λ=2, then the minimum number of counts above the background, for a 95 % confidence limit gives x=4 counts. In this study all peaks labelled were found to be at or above the 95 % confidence limit assigned for when either Gaussian or Poisson statistics were applied. The electron shell binding energies for nobelium are listed

Shell	Binding Energy (keV)
K	149.2
L_1	29.2
L_2	28.3
L_3	21.9
M	7.7

Table 6.1: ^{253}*No electron binding energies.*

N,O,P shell electrons are within 1 keV of the transition energy.

Index	e^-energy (keV)	K (keV)	L_1+L_2 (keV)	L_3 (keV)	M (keV)
1	48	197	77[a]	70	56
2	58	207	87[a]	80	66
3	64[a]	213[b]	93	86[a]	72
4	70	219	99[a]	92	78[a]
5	81	230	110[a]	103[a]	89[a]
6	85[a]	234[b]	114	107[a]	93
7	95	244	124[a]	117	103[a]
8	104	253	133[a,b]	126[a]	112[a]
9	112[a]	261[b]	141	134[a,b]	120
10	121	270	150[a]	143	129
11	130	280	160[a,b]	152	138[a,b]
12	134[a,b]	283[b]	163	156	142
13	143	292	172[a]	165[b]	151
14	156	305[b]	184[a]	177	164[b]
15	183[a]	332[b]	212[b]	205	191[a]
16	194[a]	343	223	216	202
17	202	351[b]	231[a]	224	210[a]
18	234[b]	383	262[b]	255	242
19	264	413	293	286[b]	272
20	276	425	305[b]	298	284[b]

Table 6.2: *Electron energies of peaks in the recoil-tagged prompt electron spectrum, and the K, L, and M shell transitions they could correspond to. Label 'a' refers to the interband M1+E2', and label 'b' to the intraband E2 transitions. All labelled transitions are within ±3 keV of the transition energy assigned. 'a' and 'b' labelled on energies in the electron energy column refer to possible higher orbital N,O or P electron shell emissions.*

There are clearly a number of potential transitions that can be observed within the data set, however it is essential to perform a rigorous coincidence analysis in order to provide a more solid basis for any level scheme construction prior to measurements. This is discussed in Section 6.2. The online energy resolution of SAGE is 10 keV at 300 keV, and so definitive energy assignments prove challenging as the peaks are spread across a number of channels.

While one primary reaction channel is open in this study (2-neutron evaporation), it is also worth observing the recoil-decay tagged spectra to confirm the absence of any other contaminants. The spectra are recoil-tagged plus energy gated on the ^{253}No α particle energy peak in the range 7700 – 8300 keV and within 3 half-lives (306 s). The labelled transitions are based on previous studies to highlight where peaks would be expected. The resourcefulness of recoil-decay tagging here is limited due to low statistics.

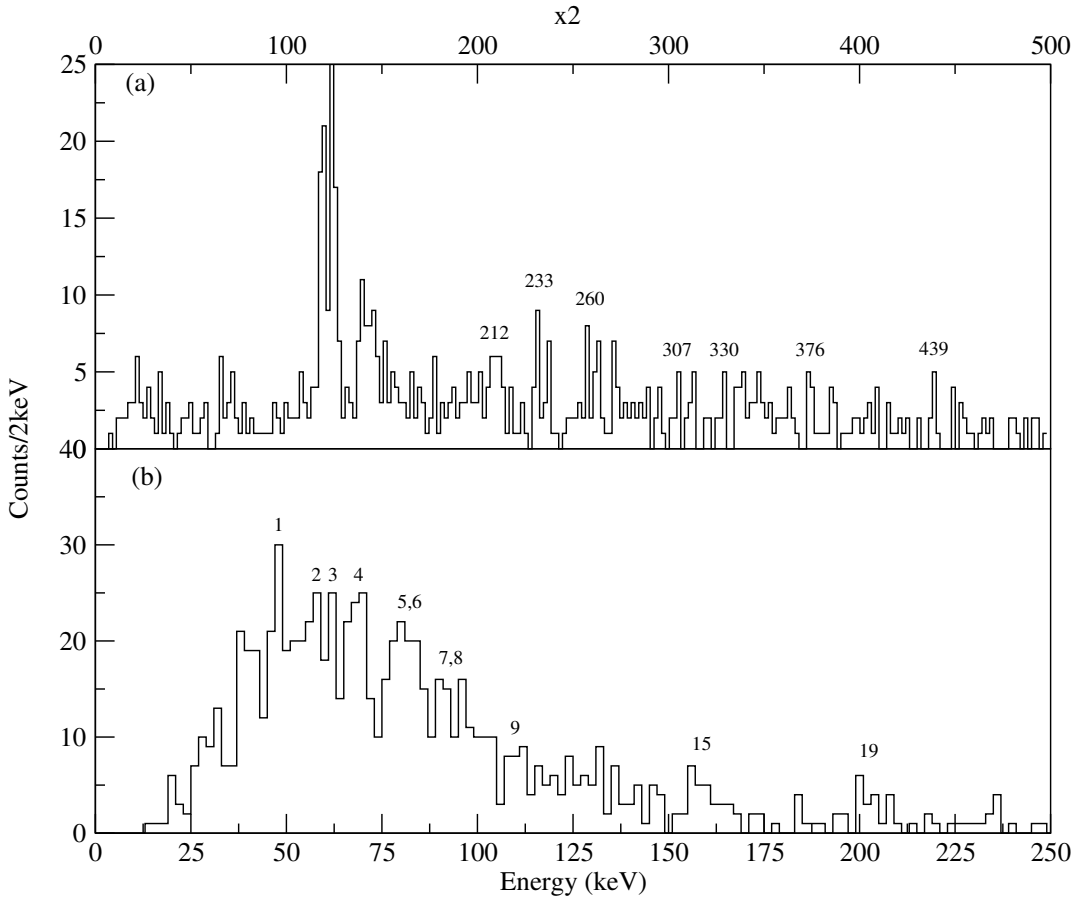

Figure 6.5: *Recoil-decay tagged prompt spectra. (a) γ rays detected with* JUROGAM II *with transition energies identified. (b) Electrons from* SAGE. *The peak numbers correspond to the index in Table 6.2 The energy labels on potential peaks are based around previous studies for clarity.*

6.2 Level Scheme Construction

Use of the SAGE spectrometer gives greater scope in constructing a level scheme in this heavy mass region where conversion is a dominant mechanism of decay. Full γ–γ and γ–e^- timing coincidences can be performed giving a better handle on the structure of the nucleus as it undergoes electromagnetic decays.

6.2.1 γ–γ coincidences

Construction of the level scheme involves initially observing the picket fence like structure of the recoil-tagged γ rays. Based on previous work across the nuclear chart of odd-A nuclei with a single unpaired valance nucleon, then it can be concluded that these must be stretched E2 transitions in two rotational bands. Creating a γ–γ coincidence matrix and placing coincidence gates on the more intense transitions allows for correlations to be deduced. This leaves the structure in Figure 6.6:

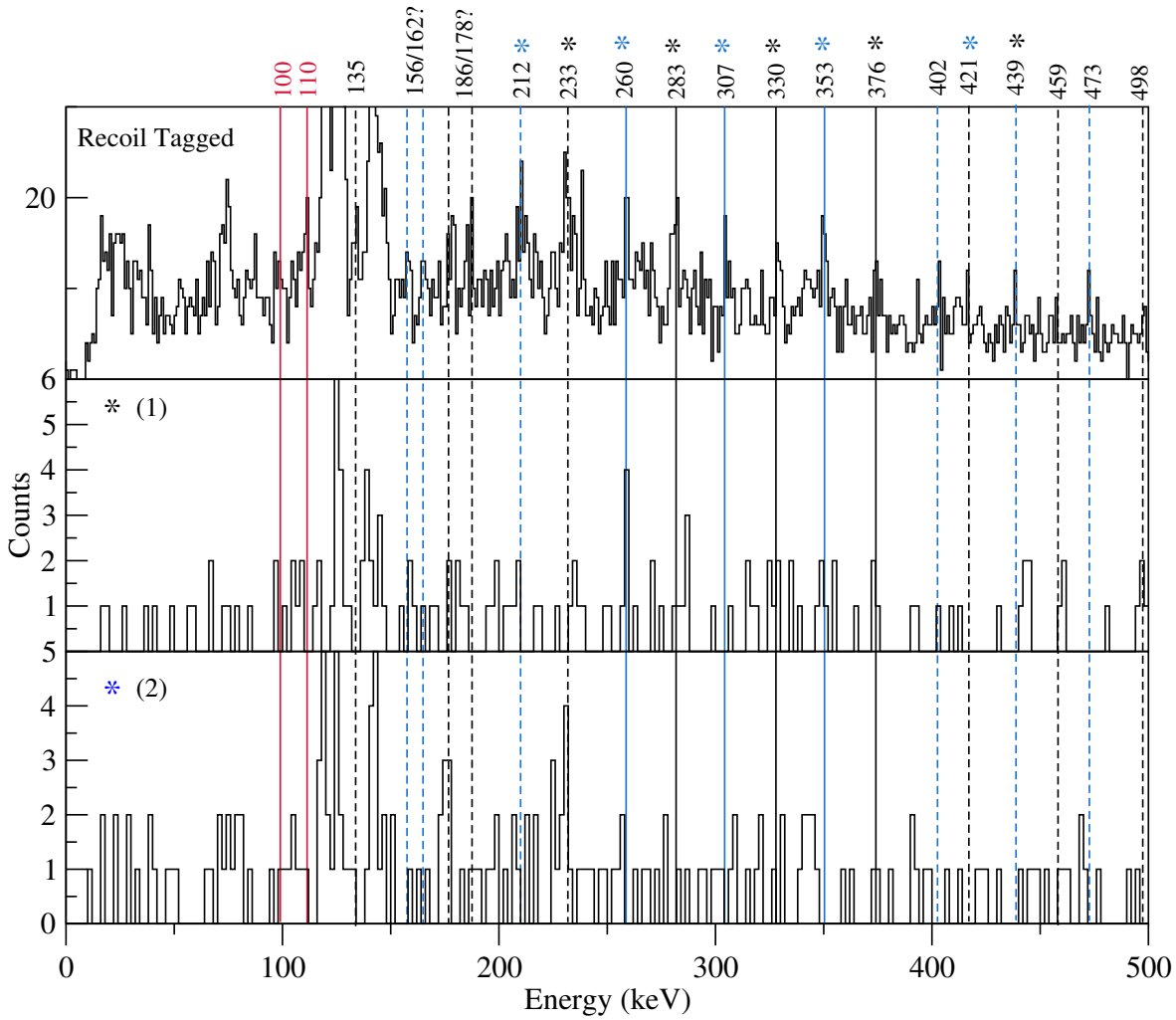

Figure 6.6: *Recoil-tagged γ ray singles(top), γ rays coincident from sum gating on γ ray transitions marked by the black asterisks (1), sum gating on γ ray transitions marked by the blue asterisks (2). Interband transitions are marked in red. It is clear that statistics are too low to draw any unambiguous conclusions.*

The two signature bands are labelled (1) and (2), with the coincidence gates applied listed in Table 6.3. It remains of limited use here to attempt to deduce whether a given transition fits into a given band. Low statistics hinder attempts to draw such conclusions from the data. Transitions that have a suspected doublet are not coincidence gated on such as the 156/162 keV and 186/178 keV. Furthermore the higher energy transitions become too low in intensity to make any assumptions. Hence one must turn towards the γ–e^- coincidence matrix and apply the same γ ray coincidence gates to observe the electron peaks.

Band	Gate (keV)
(1)	233, 283, 330, 376, 439
(2)	212, 260, 307, 353, 421

Table 6.3: *List of the γ ray energy sum coincidence gates applied to produce Figure 6.6.*

6.2.2 γ–e^- coincidences

The interlinking M1+E2' transitions dominate over the intraband (stretched E2) transitions for conversion electrons due to the low energy nature and magnetic component introducing a higher degree of conversion. Coincidence gating on individual γ ray transitions in the γ–e^- matrix produces clean, low background spectra; useful in assigning energies.

E2 Transition Gating

The assignment of energies using the regular spacing of the γ rays is done through both observation and simulation (demonstrated in Section 6.3.2 page 132.) Searching for coincidences also proves strong backing for assignments as will be demonstrated here.

Initially the X-rays in the γ projection of the recoil-tagged γ–electron matrix are coincidence gated on.

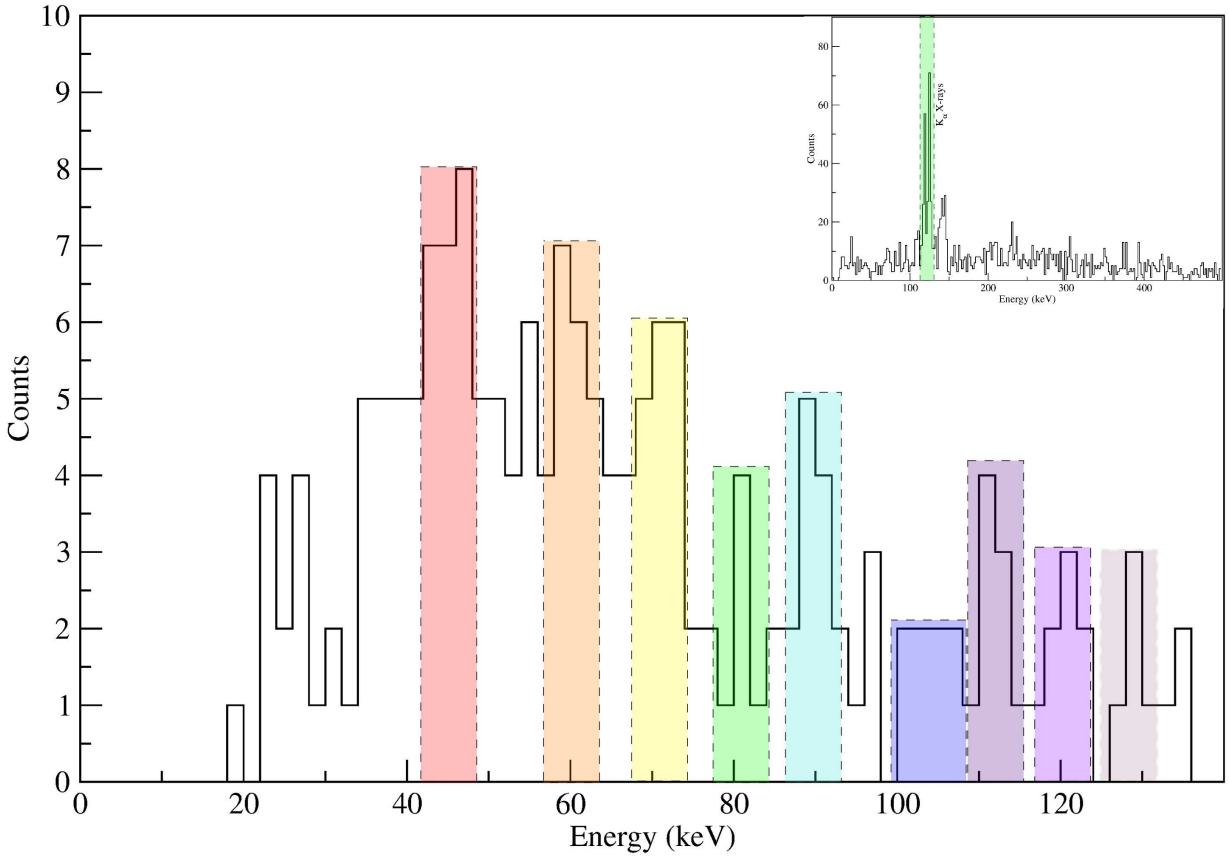

Figure 6.7: *Coincidence gating on the $K\alpha_1$ X-rays in the γ projection of the recoil-tagged gamma–electron matrix to observe the coincident electrons. There are a number of potential transitions which are then coincidence gated on to observe the coincident γ rays in Figure 6.8. The coincidence gates corresponding energies based on colour are referenced in Table 6.4.*

Colour	E_e keV	Transition Energy keV
Red	48	76L
Orange	58	86L
Yellow	71	100L
Green	81	233K, 110L
Turquoise	93	124L, 100M
Blue	105	135L
Indigo	111	260K
Violet	121	150L
Grey	132	283K, 160L

Table 6.4: *Table indicating the electron coincidence gates used in Figure 6.8. The coincidence gates are used in summation.*

Based on the electron coincidence gates in Figure 6.7 (labelled in Table 6.4) the following γ ray peaks are extracted.

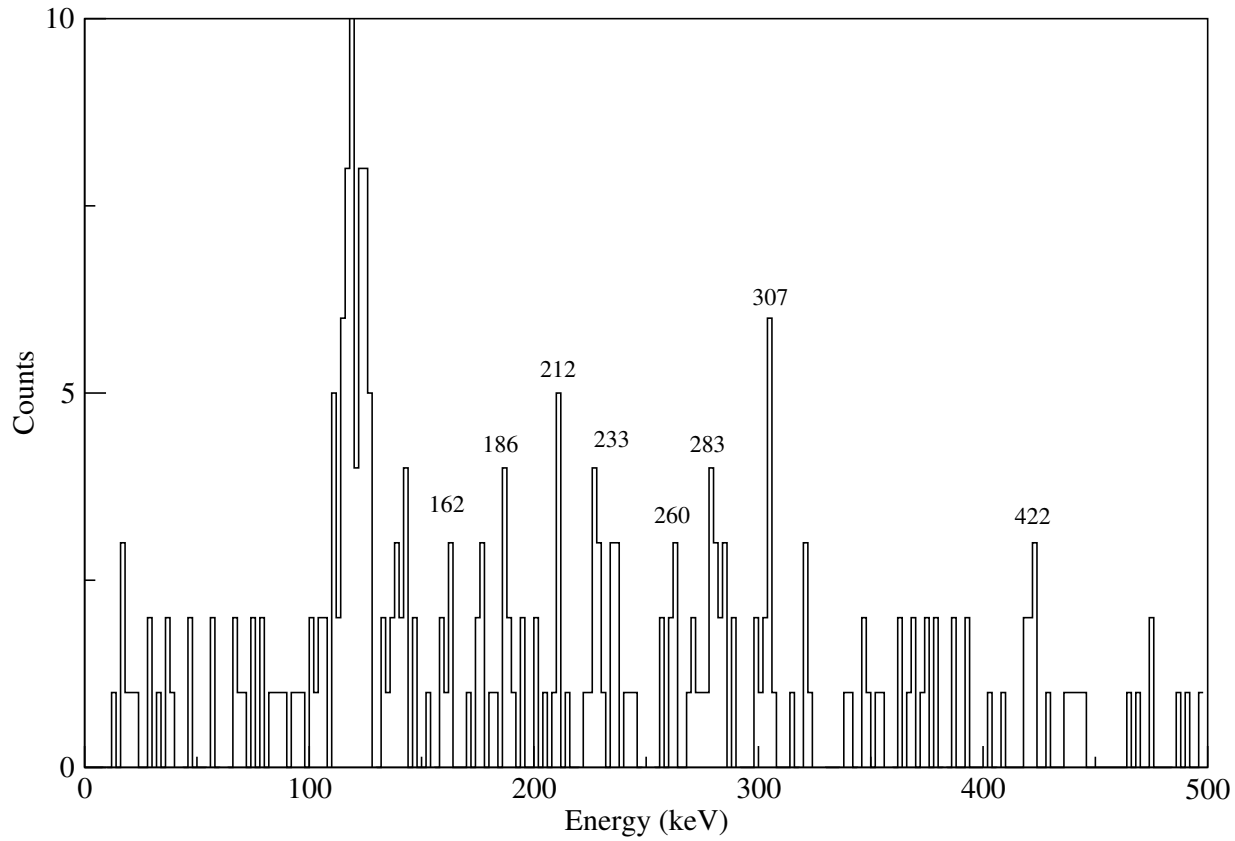

Figure 6.8: *γ rays in coincidence with the electron peaks sum coincidence gated on in Figure 6.7. Some of the E2 transitions are evident.*

This combined with simple observation of the energy separation of the recoil-tagged γ ray spectrum allows for the transitions shown in Figure 6.9 to be placed.

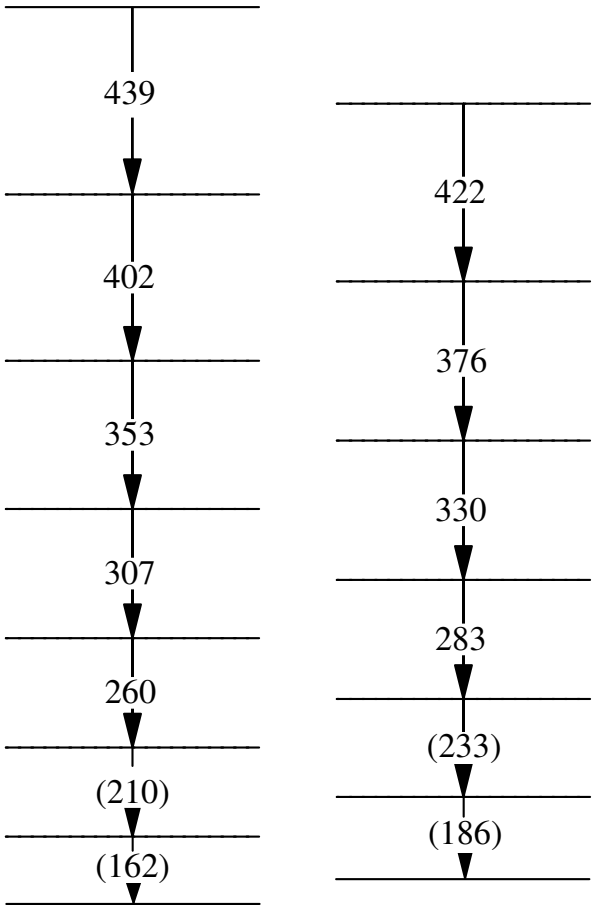

Figure 6.9: *The two signature rotational bands as seen from the recoil-tagged* JUROGAM II *spectrum. γ–e^- coincidences will be required to determine lower energy transitions.*

As discussed in Section 5 (see page 82), previous work has shown that there are indeed further transitions below this structure, and the following analysis discussion will identify and place these levels, as well as any interlinking mixed M1+E2' transitions. Furthermore it will confirm the energy for transitions with suspected doublet/triplet peaks in the region of interest. The level scheme shown in the subsequent energy plots is the completed level scheme, and is included in order to assess and justify the placement of levels. This is shown here.

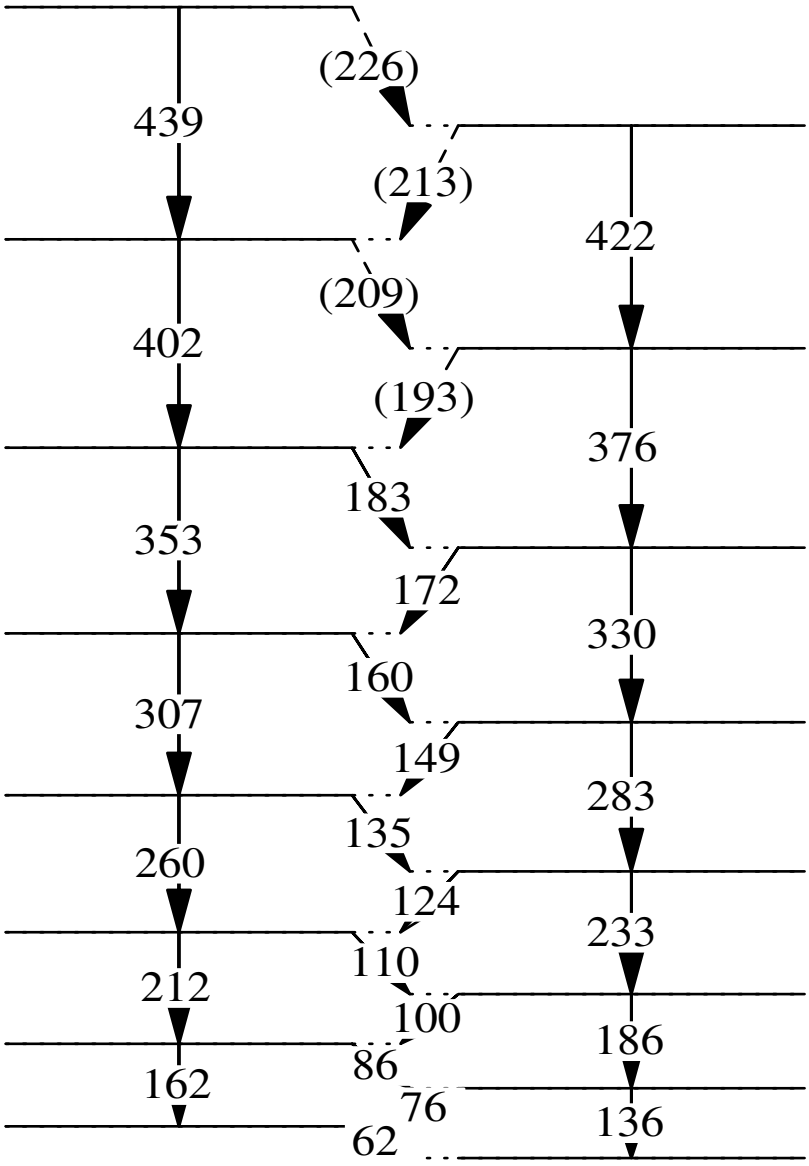

Figure 6.10: *The level scheme deduced from this study. The following section will demonstrate the energy assignments placed.*

In the construction of the level scheme, the γ rays are coincidence gated on to show the subsequent electrons. Coincidence gating on the electron peaks is challenging. Low resolution and multiple electron shells grouping together in the same peak (e.g. the 135 $L_{1,2}$, 125 L_3, and the 110 M shell electrons all have an energy around 103 keV), means that contamination can be an issue. Hence one must be selective about using given coincidence gates.

136 keV Transition

The final E2 multipolarity linking transition to the bandhead has been tentatively assigned through previous work [78] to be 132 keV. The 132 keV transition lies in the region between the K_α and K_β X-rays (evident in Figure 6.2), so electron data should provide a more solid basis for assignment. Gamma coincidence gates are placed on transitions at 186 keV (see 186 keV analysis below) and 86 keV corresponding to E2 and M1+E2' γ rays.

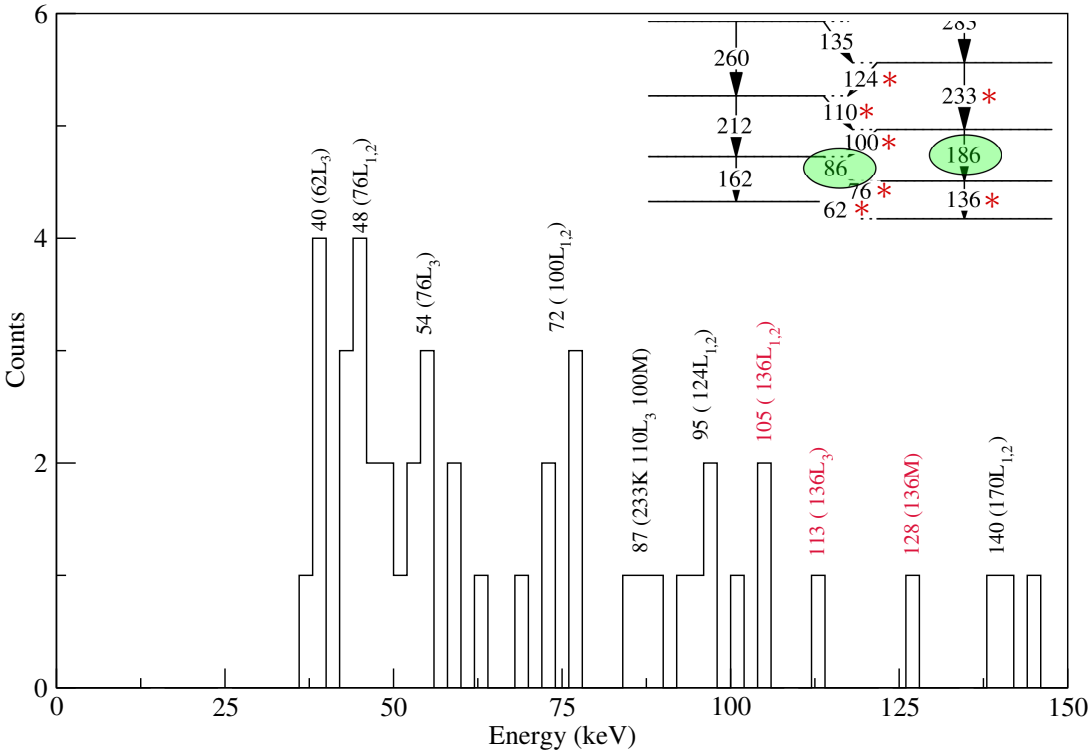

Figure 6.11: *γ ray coincidence gates on the 86 keV M1+E2' and 186 keV E2 transitions in the recoil-tagged γ–e^- matrix to observe the coincident 136 keV L and M shell electrons (red).*

Some of the transitions that are coincident have a higher energy compared to what has been observed in previous studies, for example the 76 keV interband transition which was previously measured to be 70 keV [10]. Four counts are in coincidence with the selected transitions which could correspond to the L and M shell electrons from a 136 keV transition. There is also an absence of counts in the region of a potential 132 keV peak which was tentatively placed in the aforementioned study by T. Page [78]. However there is also the 135 keV interband transition higher up the band which may prove as a contaminant. Coincidence gating on the electron

peaks corresponding to the 136 keV transition show the 184 keV and the 212 keV stretched E2 transitions in coincidence.

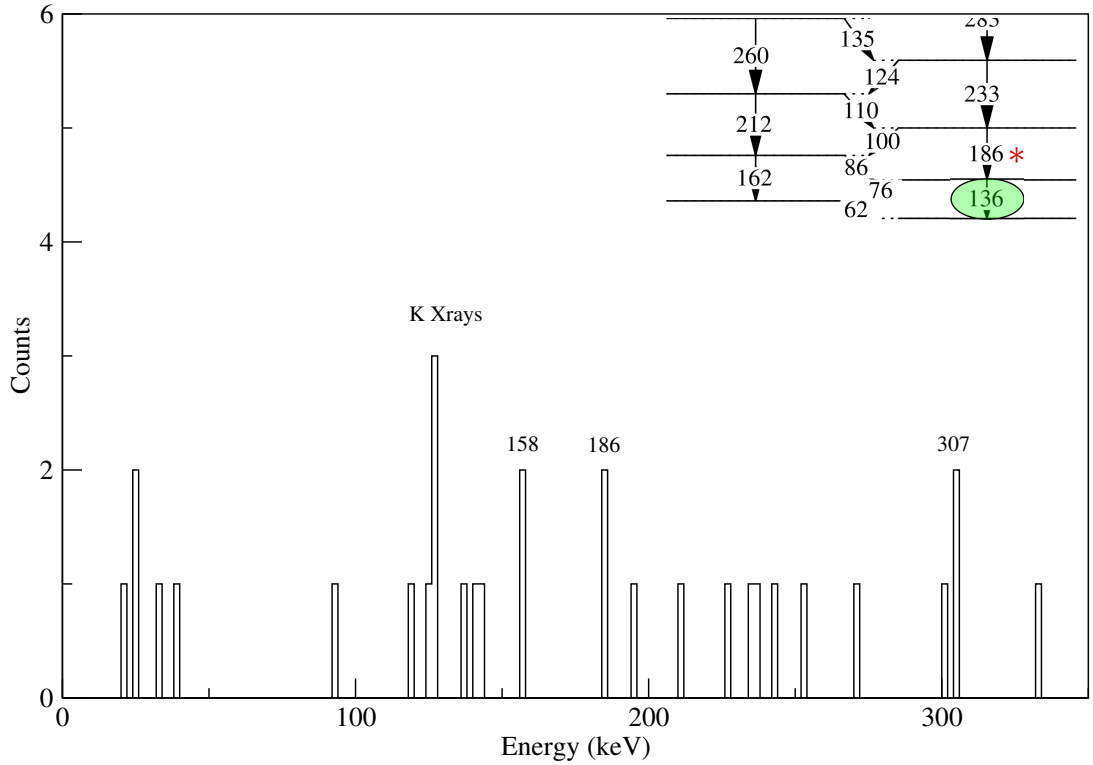

Figure 6.12: *Electron coincidence gates on the 105 keV and 113 keV (136 keV transition energy) electron peaks in the recoil-tagged γ–e^- matrix to observe γ rays in coincidence.*

Based on the relative intensity of the 186 (and 233 keV) peaks the final E2 transition is assigned as 136 keV. Note that the 307 keV peak that appears is from the transition feeding the 135 keV M1+E2' interband transition further up the band.

178/186 keV Transitions

A doublet appears in this region of interest, and so to assess which peak results from decays in the yrast bands, both are γ ray coincidence gated to observe electrons in time coincidence. Where no green ellipsoid gate is labelled on the level scheme inset indicates that the transition does not belong to the yrast band based on the evidence surmised. Potential transitions in coincidence however are still labelled.

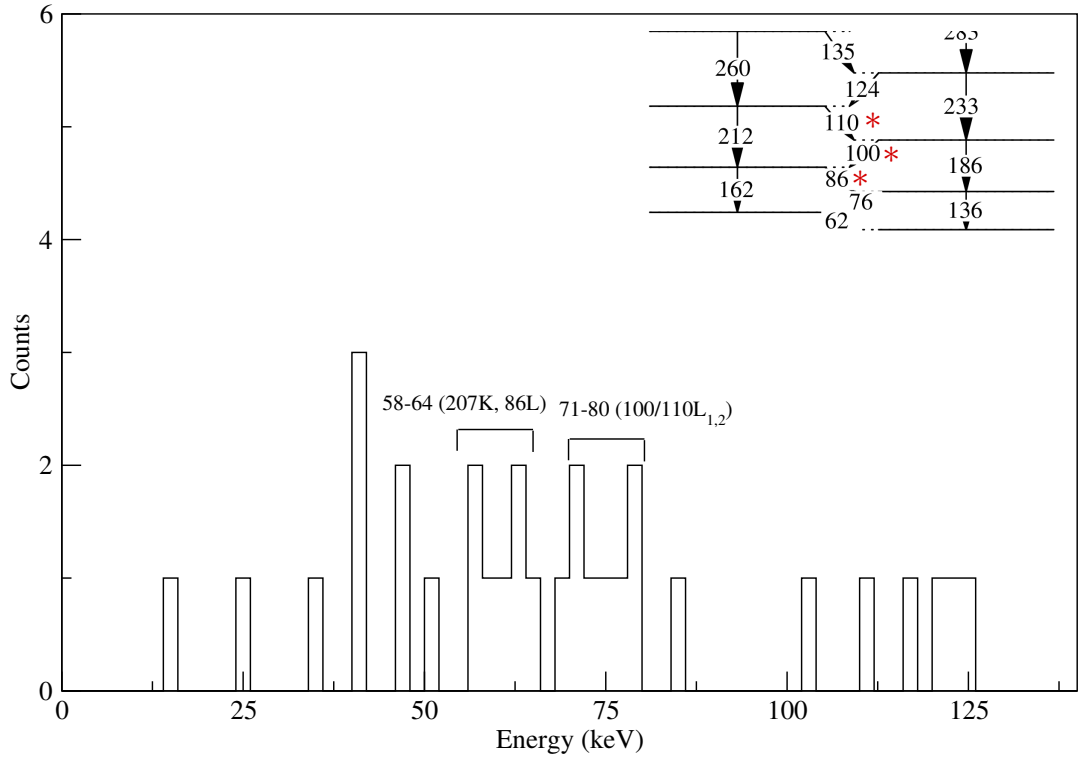

Figure 6.13: *γ coincidence gate on the 178 keV transition in the recoil-tagged γ–e^- matrix to observe electrons in coincidence.*

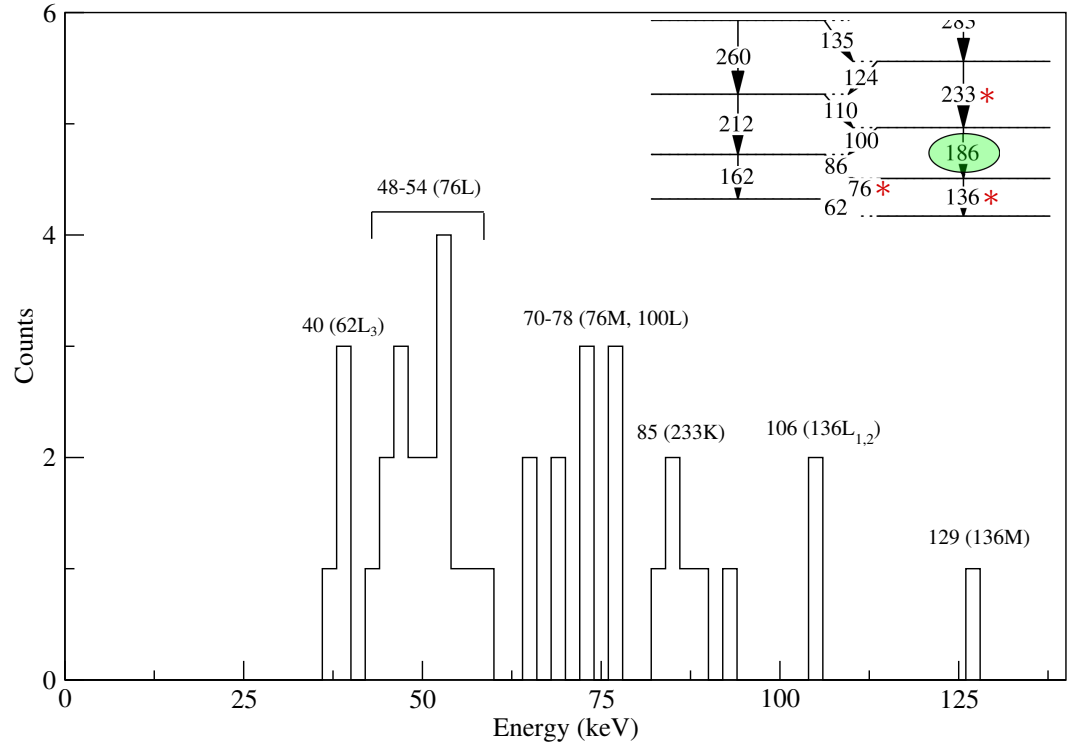

Figure 6.14: *γ coincidence gate on the 186 keV transition to observe electrons in coincidence.*

The 178 keV γ coincidence gate shows transitions that are not consistent in energy with neighbouring level coincidences, for example the 86 keV transition should not be seen here, as it is the M1+E2' interband stemming from a non-coincident energy level. The 186 keV transition shows coincidences with several transitions, most notably the relatively intense 85 keV electron peak corresponding to the 233 keV K shell electron from the E2 transition feeding from above. The two separate 70-78 keV peaks containing three counts that appear should not be the 100 keV L-shell transition but may be some component of the 76 keV M-shell electrons. With all these coincidence gates however, given the resolution of the device, there is a risk of close transitions 'bleeding' into one another causing potential sources of contamination. To confirm the 186 keV transition, a coincidence gate on the 105 (136 keV $L_{1,2}$ shells) and 85 keV (233 KeV K shell) electrons gives the γ rays in coincidence. The 186 keV peak is clearly evident here alongside the 212 and 233 keV E2 transitions.

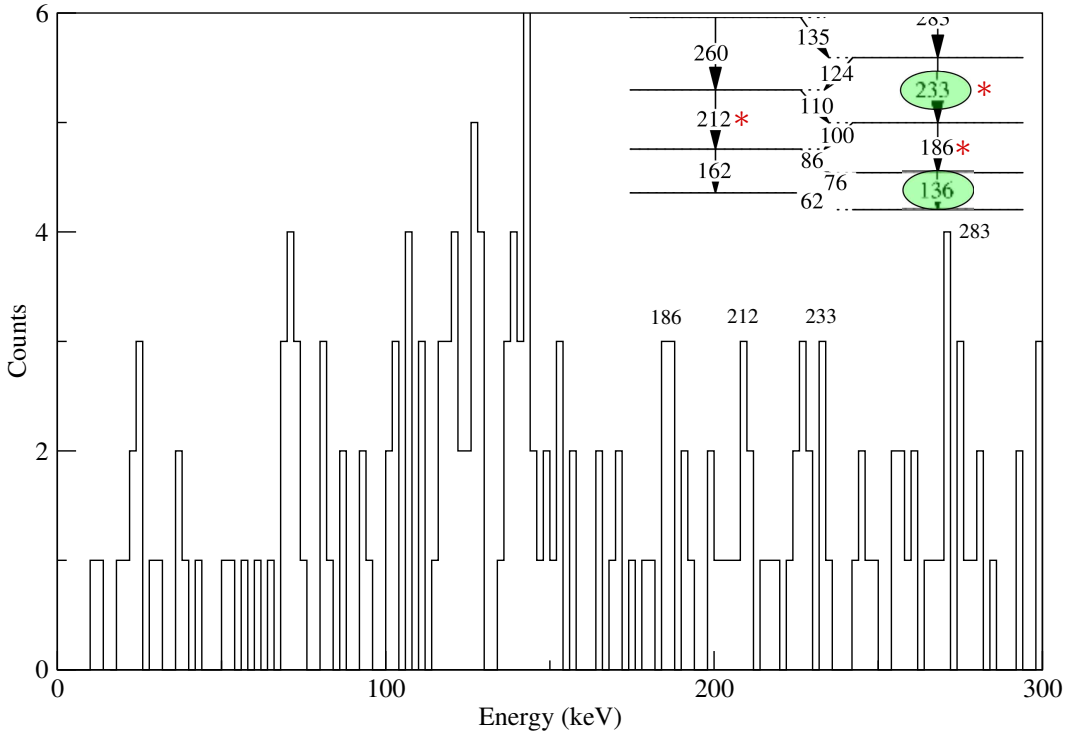

Figure 6.15: *Electron coincidence gates on the 105 and 85 keV electron peaks (corresponding to the 135 keV $L_{1,2}$ shells and the 233 keV K shell electrons) in the recoil-tagged γ–e^- matrix to determine γ rays in coincidence.*

158/162 keV Transitions

Similarly the 158/162 keV γ rays are coincidence gated on. Again a doublet appears in this region and thus each one is gated on separately to determine the correct energy and peak assignment.

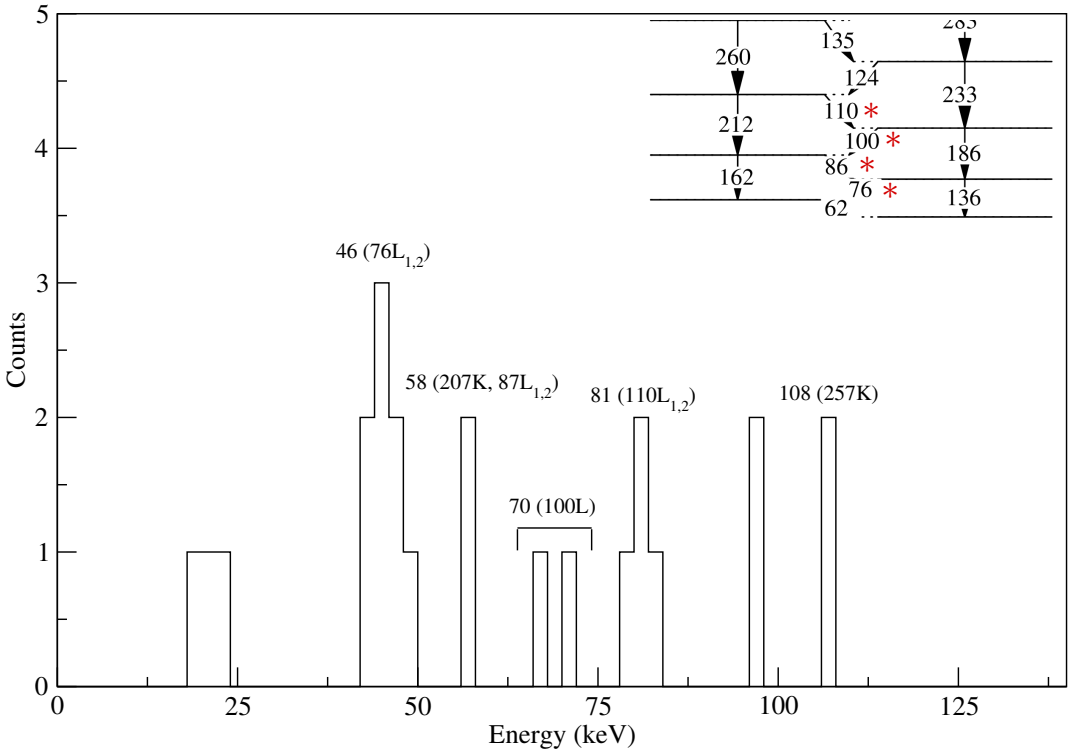

Figure 6.16: *γ ray coincidence gate on the 158 keV transition in the recoil-tagged γ–e^- matrix to observe electrons in coincidence.*

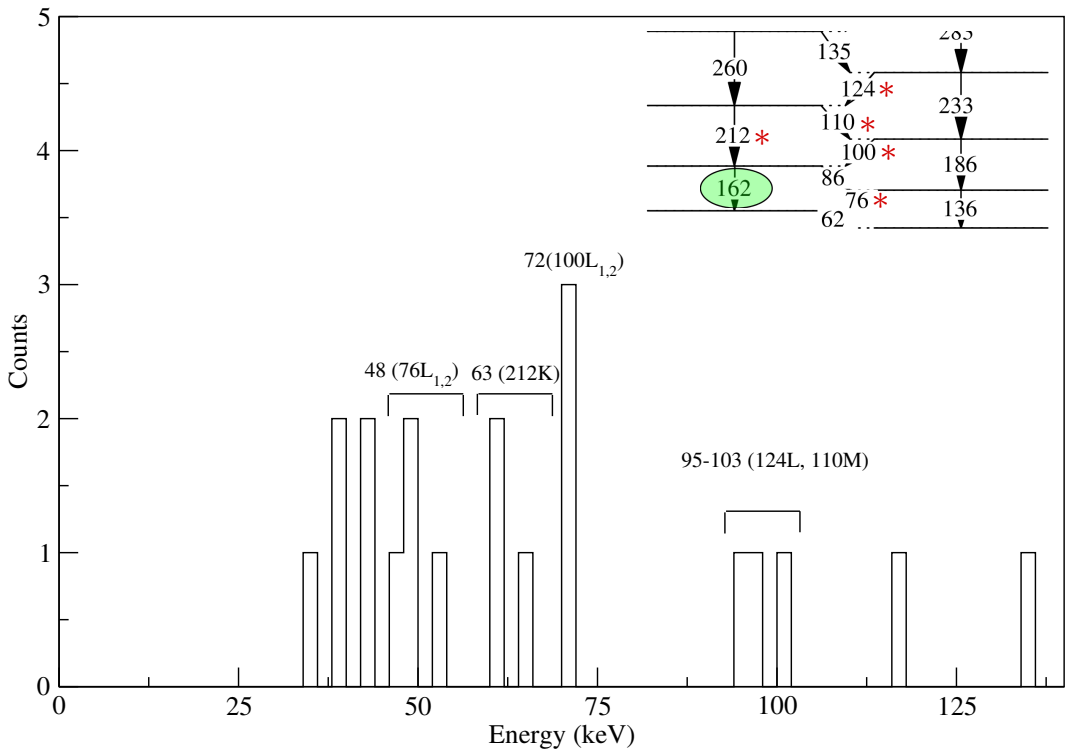

Figure 6.17: *γ ray coincidence gate on the 162 keV transition in the recoil-tagged γ–e^- matrix to observe electrons in coincidence.*

For this case the 158 keV γ ray coincidence gate demonstrates coincidences with transitions such as the relatively intense 48 keV electron peak which, if corresponding to the 76 keV transition, should not be coincident. While counts are very low, the 162 keV appears to show more coincidences with known transitions such as the 212 keV K electron shell stretched E2 and the 100 keV $L_{1,2}$ electron shell interband M1+E2'. However the 46-48 keV transition appears again, albeit weaker than in the 158 keV coincidence gate indicating some of the 158 keV transition may be plaguing the 162 keV coincidence gate (given the close proximity of the γ ray peaks this is a reasonable assumption). The lower energy peaks (below 43 keV) seen here do not sum to anything in the known level scheme, but as discussed previously in the lower energy region the high voltage barrier discharges can create low energy background and random miss-coincidences may occur. To confirm the assignment, the 64 keV (212K and $86L_3$ shell) and 70 keV ($100L_{1,2}$ shell) electron peaks are coincidence gated in the recoil-tagged γ–e^- matrix to observe the γ rays.

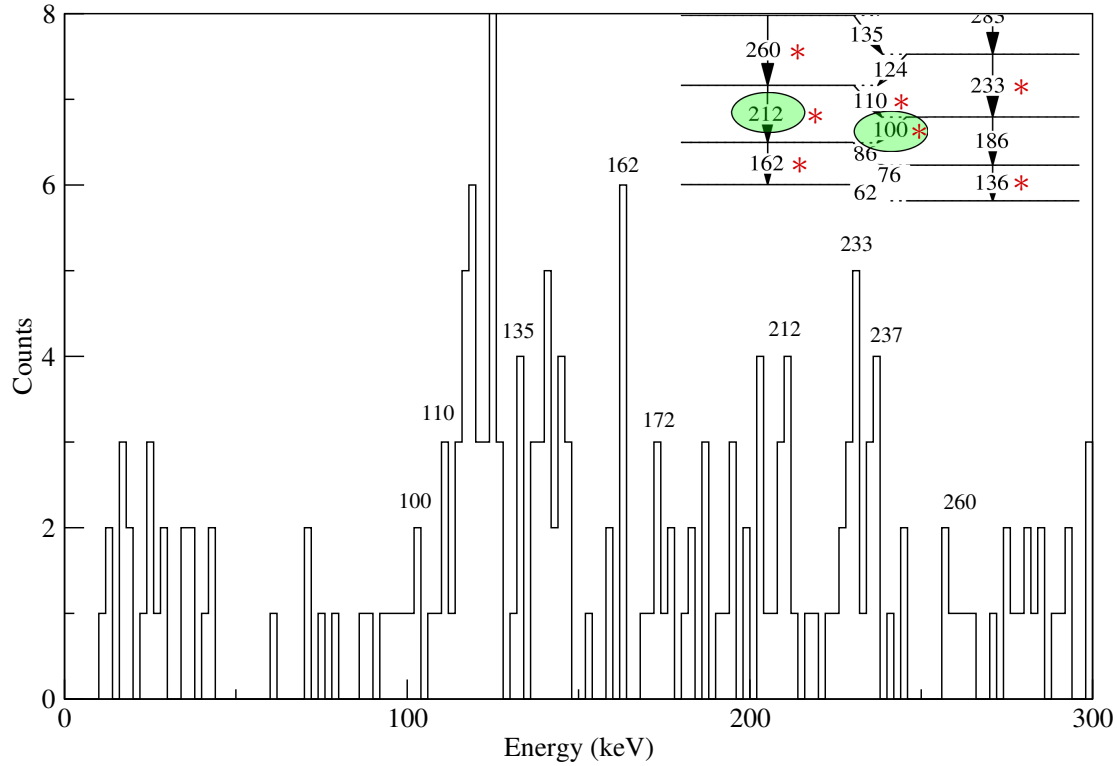

Figure 6.18: *Electron coincidence gate on the 64 and 70 keV electron peaks in the recoil-tagged γ–e^- matrix to observe γ rays in coincidence.*

Again the intensity of the peak clearly points to an energy of 162 keV. There are also additional transitions evident here stemming from a potential sideband, for example the relatively intense 237 keV transition. It is likely that some form of sideband feeds into the yrast band close to this region but current statistics remain limited in defining where that may lie.

208/212 keV Transitions

The doublet that occurs around this energy region is of interest due to previous assignments of 207 keV[60], 208 keV[61] and 211 keV[45]. Initially the 208 keV γ ray peak is coincidence gated on followed by a peak at 212 keV.

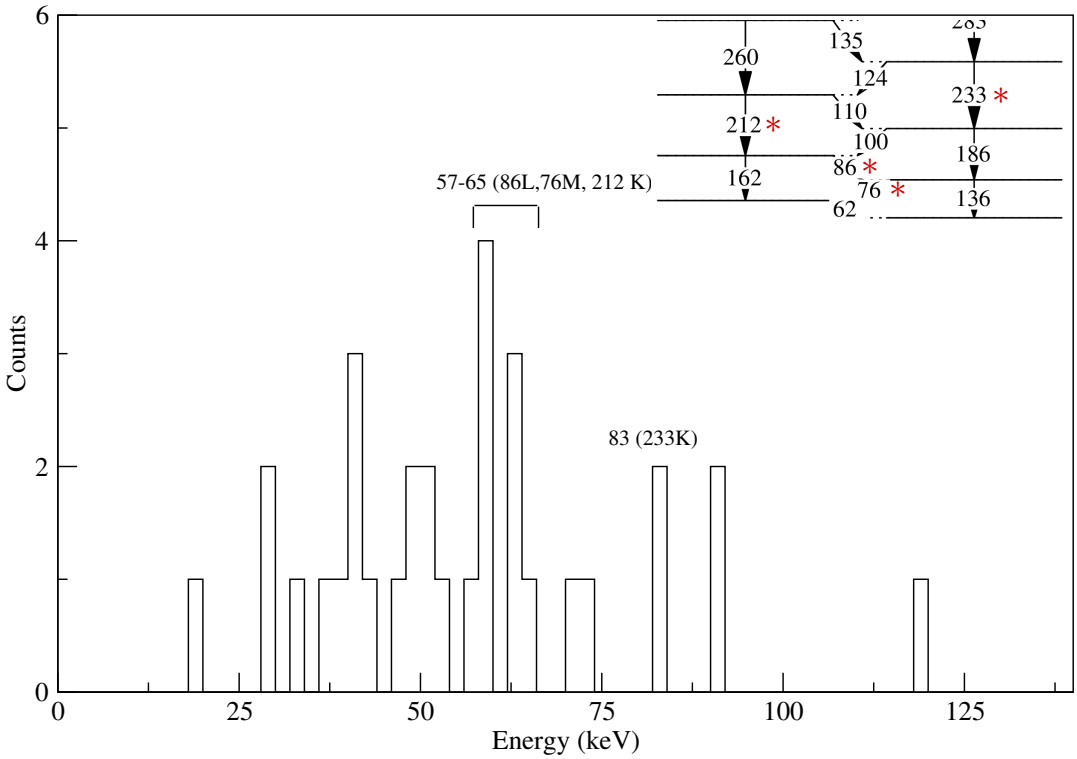

Figure 6.19: *γ ray coincidence gate on the 208 keV transition in the recoil-tagged γ–e^- matrix to observe electrons in coincidence.*

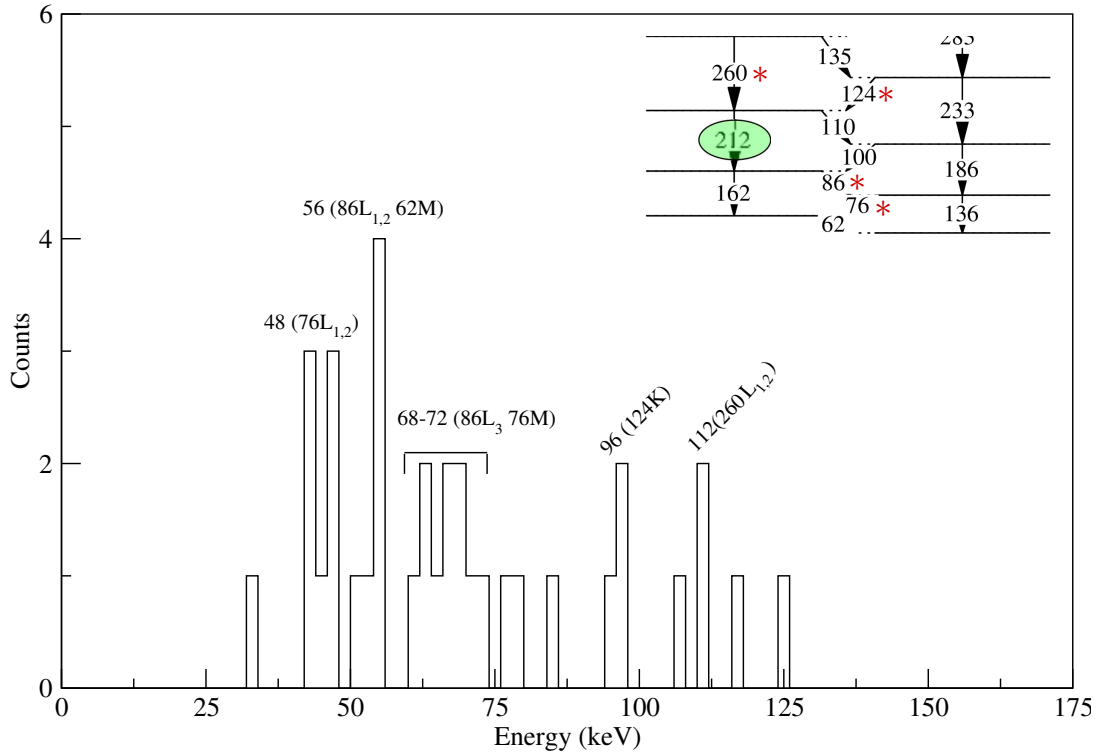

Figure 6.20: *γ ray coincidence gate on the 212 keV transition in the recoil-tagged γ–e^- matrix to observe electrons in coincidence.*

The 208 keV transition demonstrates coincidences with some transitions corresponding to the lower interband transitions. However the 212 keV also demonstrates these transitions and more importantly the 260 keV transition feeding it. The assignment is thus given as 212 keV. The 208 keV transition, again possibly belongs to a sideband. It is coincident with the 212 keV E2 transition and also with the 800 keV (Section 6.8.4).

The doublet that appears around the 233 keV region lacks the level of statistics to complete a full γ-e^- analysis. The 233 keV K shell electron falls within a similar energy regime as the 110$L_{1,2}$ shell, while the 237 keV has similar energies to 110L_3 so discerning between the two is not simple. Thus the assignment is made based on observation of the linking M1+E2' transitions summing to the energy of the stretched E2 transition. Furthermore the relative intensity of the 233 keV is higher in the recoil tagged γ ray singles (N_{233}/N_{237}=2.3±1.1). This is based on the assumption that the yrast band is more populated than the non-yrast structure and thus the 233 keV is the decay occurring within the yrast band.

Dipole interband (M1+E2') Transition Gating

An expanded view of the lower energy recoil-tagged γ ray transitions demonstrates peaks energetically consistent with potential linking transitions.

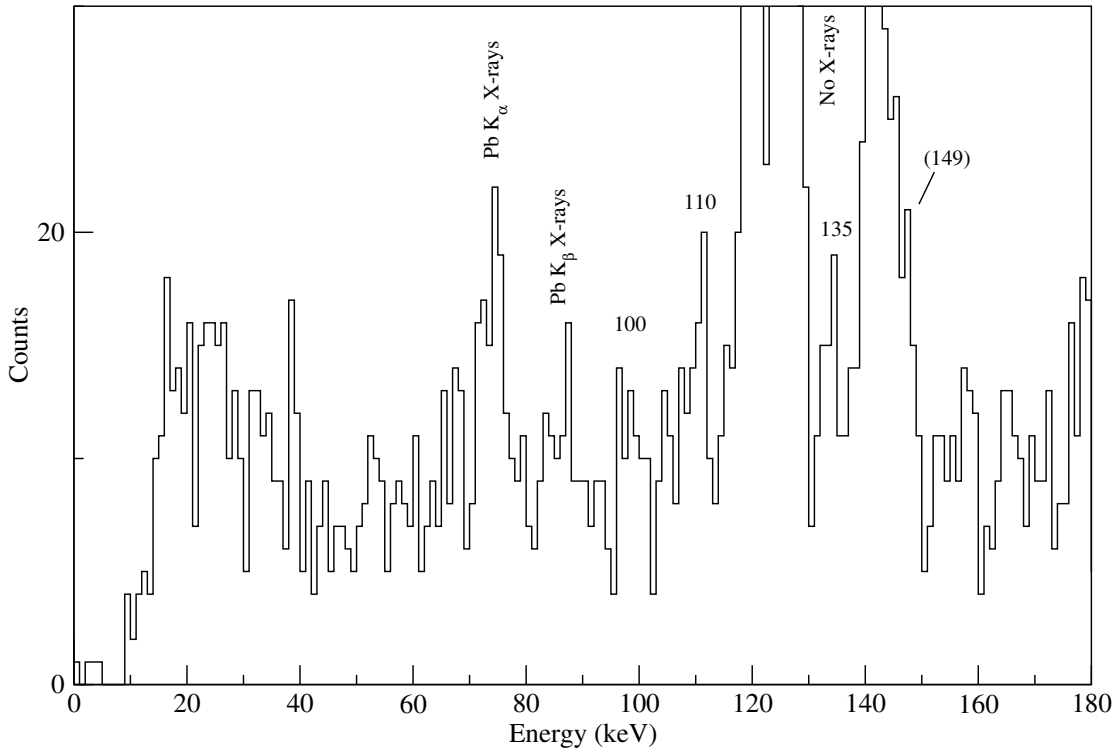

Figure 6.21: *Recoil-tagged γ ray singles. Expanded in the lower energy region to highlight potential M1+E2' peaks.*

62 keV Transition

Initially, transitions at the bottom of the band are considered. The first $\Delta I = 1$ transition is low in energy and so the $L_{1,2}$ shell electrons are below the detection threshold of SAGE, being within the δ-electron and HV contamination region. An additional problem arises due to the 76 keV γ ray being energetically similar to the lead K_α X-ray peak produced by the target. Thus the 162 keV coincidence gate and the 186 keV are selected as coincidence gates.

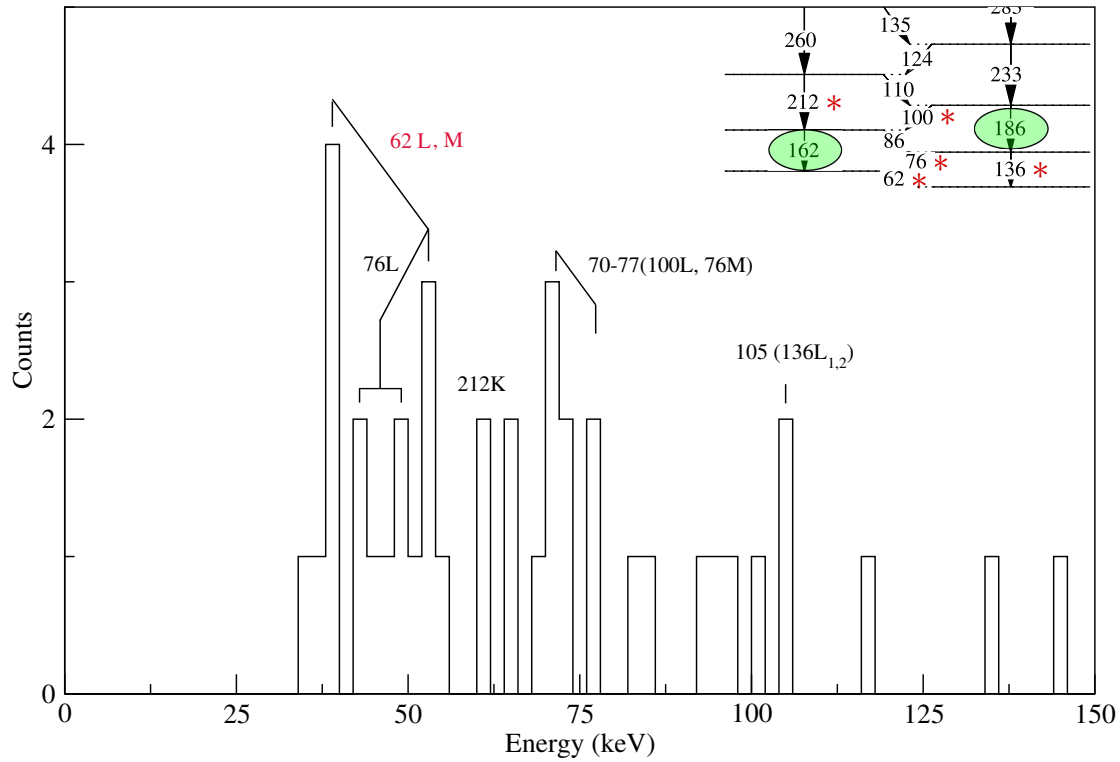

Figure 6.22: *γ ray coincidence gate on the 162 keV and 186 keV transitions in the recoil-tagged γ–e^- matrix to observe electrons in coincidence.*

At around 50 keV there is potentially a peak at low energy which would correspond to the 62 keV L shell electrons and at 54 keV which would be the 62 keV M shell electrons. This would approximately be energetically favourable, in terms of summing between the 76 keV M1+E2' and the 136 keV E2 rather than a lower energy assignment. Given the resolution of the spectrometer with 10 keV FWHM during online experiments then the 2 keV discrepancy is within statistical uncertainties.

76 keV Transition

In the γ ray spectrum, strong Pb K X-rays from the target occur at 75 keV thus only the electrons can point towards this energy assignment. Justification for a 76 keV M1 is found through γ ray coincidence gates on the 86 and 186 keV transitions.

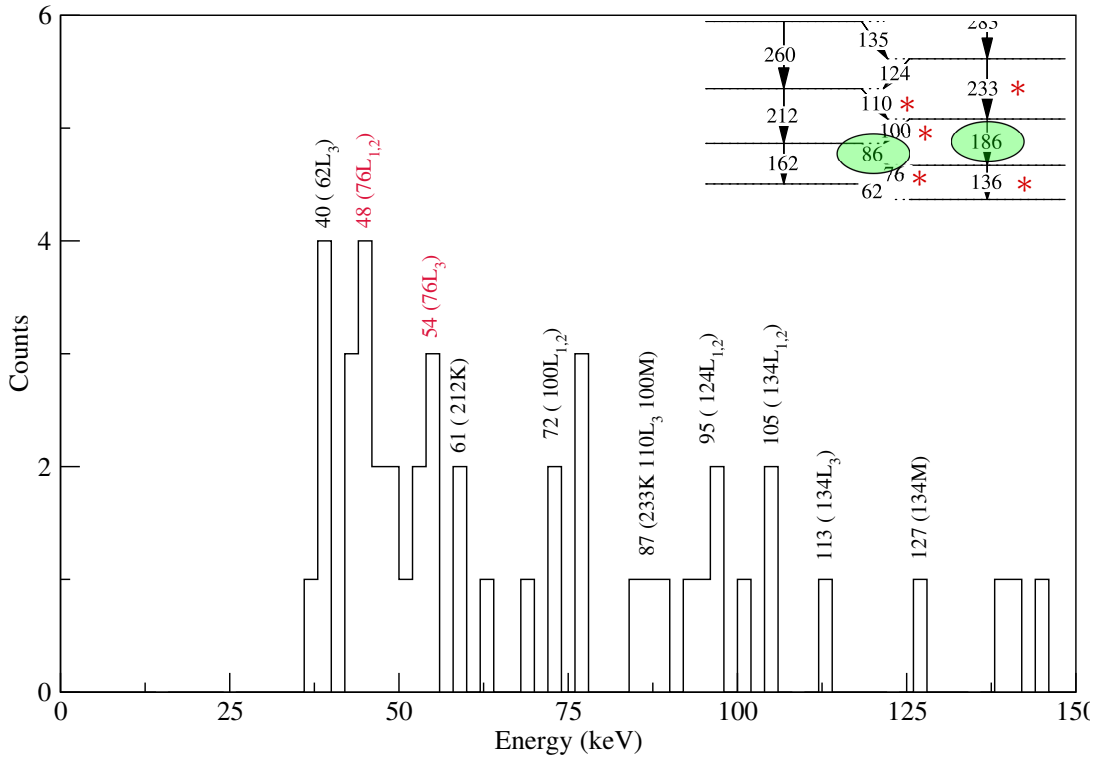

Figure 6.23: *γ ray coincidence gates on the 86 keV and 186 keV transition in the recoil-tagged γ–e^- matrix to observe electrons in coincidence.*

Previous work has placed the energy of this transition at 70 keV [61]. However Antalic's study of the isomeric decay of ^{253}No have placed it around the 76 keV range [74] in agreement with this study. The 76 L shell electrons appear in coincidence with the selected gates. A number of further intraband and interband peaks are coincident, consistent with the energy assignments determined. Thus energy assignment of 76 keV here is based on the L shell electron peaks in coincidence with the two transitions feeding it.

86 keV Transition

Similar to the 76 keV transition, the 86 keV γ ray peak is held within Pb X-rays (K_β). Thus electrons are the only in-beam way to determine the energy of this decay in this study. The two yrast states through with the transition links are coincidence gated on.

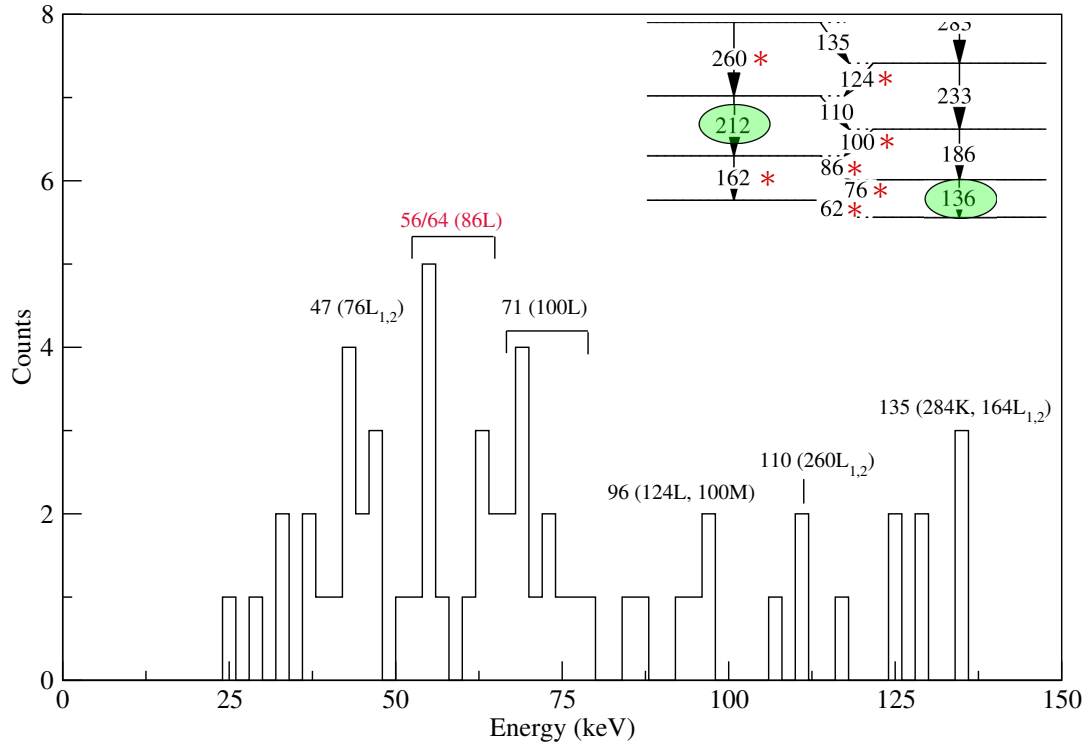

Figure 6.24: *γ ray coincidence gate on the 136 keV and 212 keV transitions in the recoil-tagged γ–e^- matrix to observe electrons in coincidence.*

The 86 keV L electron transitions appear following 136 keV and the 212 keV coincidences, alongside other expected transitions in the vicinity. This transition can also be seen in the recoil-tagged γ ray singles spectrum Figure 6.21 page 118. This energy is consistent with previous focal plane studies [74] [69], where Pb X-ray contamination is not a factor.

100 keV Transition

Coincidence gates are placed on the 162 keV and 233 keV γ rays above and below the transition of interest.

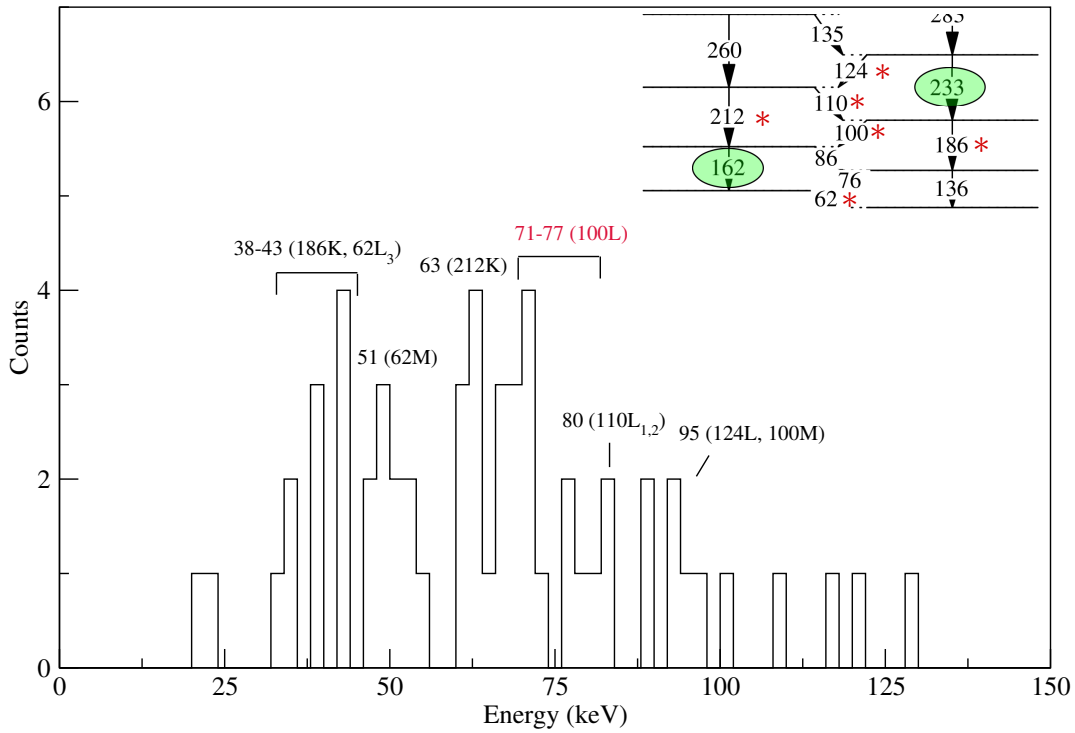

Figure 6.25: *γ ray coincidence gate on the 162 keV and 233 keV transitions in the recoil-tagged γ–e^- matrix to observe electrons in coincidence.*

The 100 keV L shell electrons appear along with others from nearby levels, consistent with previous studies ([10][74]), and again the recoil-tagged γ singles spectrum Figure 6.21 provides support for this assignment. Note that compared to Figure 6.22 the relative intensity of the 62 keV M shell electron and the 212 keV K shell electron peak have increased in intensity. From this one can again infer the interpretation of the sideband with similar energies to the yrast band feeding in somewhere in the vicinity of the 233 keV E2 transition. The broader nature of the 50 keV electron peak supports this.

110 keV Transition

The 110 keV L shell electron transition shares a similar energy to the 233 keV K shell electron leading to problems over the choice of coincidence gates in this region. This is compounded by the fact that the 124 keV γ ray transition is held within the K_α nobelium X-rays. Thus only the 260 keV γ ray can be coincidence gated on producing the following spectrum.

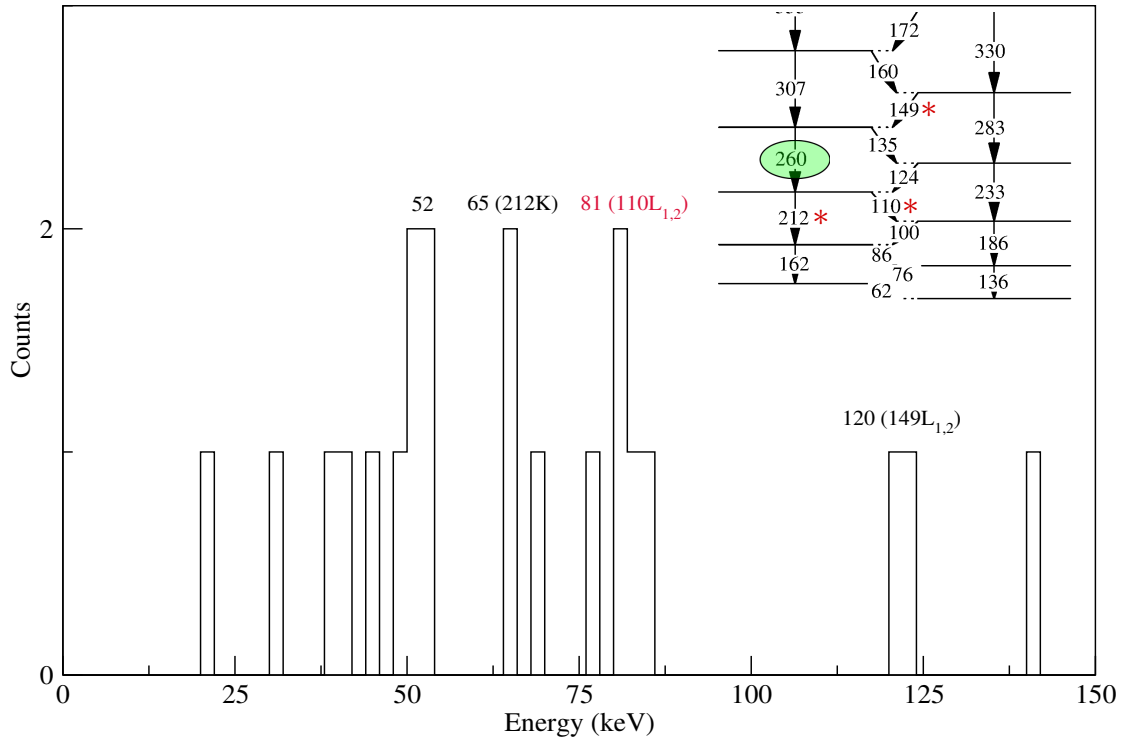

Figure 6.26: *γ ray coincidence gate on the 260 keV transition in the recoil-tagged γ–e^- matrix to observe electrons in coincidence.*

The 110 and 150 keV M1+E2's are coincident with the selected coincidence gates, as well as the 212 keV E2 transition as expected. We can further support the 110 keV transition by observing it in the recoil gated γ ray singles spectrum in Figure 6.21 (page 118). Placing a γ ray coincidence gate on the 110 keV transition in the recoil-tagged γ–e^- matrix this gives the following electron transitions.

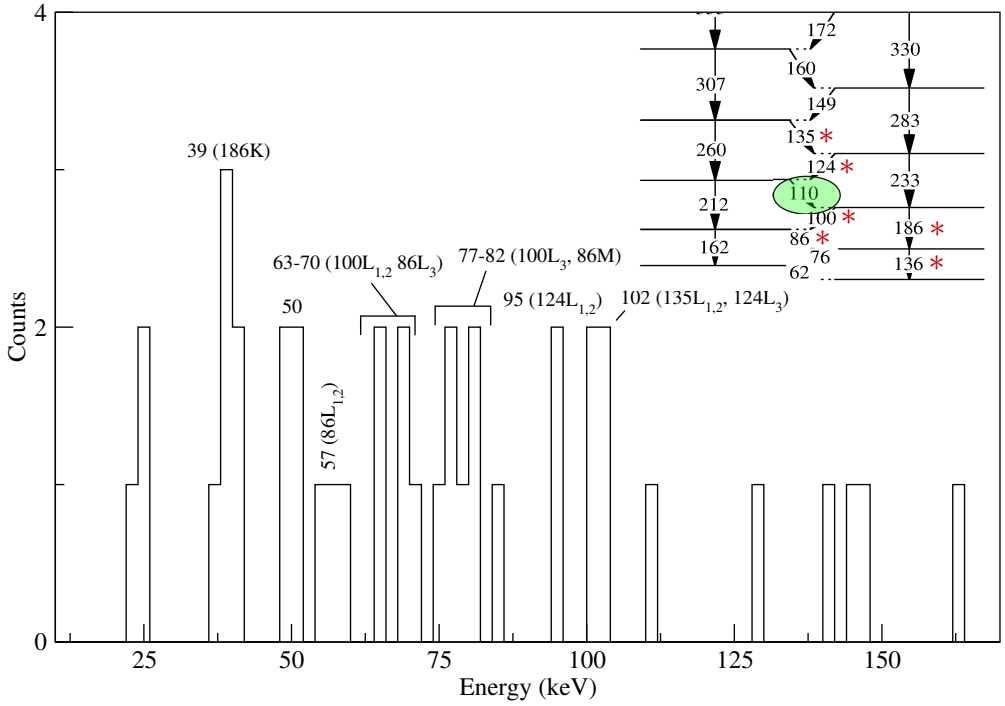

Figure 6.27: *γ ray coincidence gate on the 110 keV transition to observe electrons in coincidence.*

The 62 keV transition which has the M shell electron at an energy of 50 keV at a lower spin from the selected coincidence gates so one would not expect such intensity at this energy. As discussed with the 100 keV transition, the sideband around this region could be coincident with the gates selected feeding into the band in this region. The 186 keV K shell transition appears relatively intense, however absence of L (and higher order) shell electrons, with only one count in the 156 keV vicinity implies that the HV barrier may be creating false coincidences in this lower energy (39 keV) region.

124 keV Transition

The 124 keV γ ray is held within the K_α nobelium X-rays and hence cannot be observed in the recoil tagged γ rays. Thus conversion electrons must be used to confirm this transition. Coincidence gates in the recoil-tagged γ–e^- matrix are placed on the 212 keV and the 283 keV γ rays to observe coincident electrons.

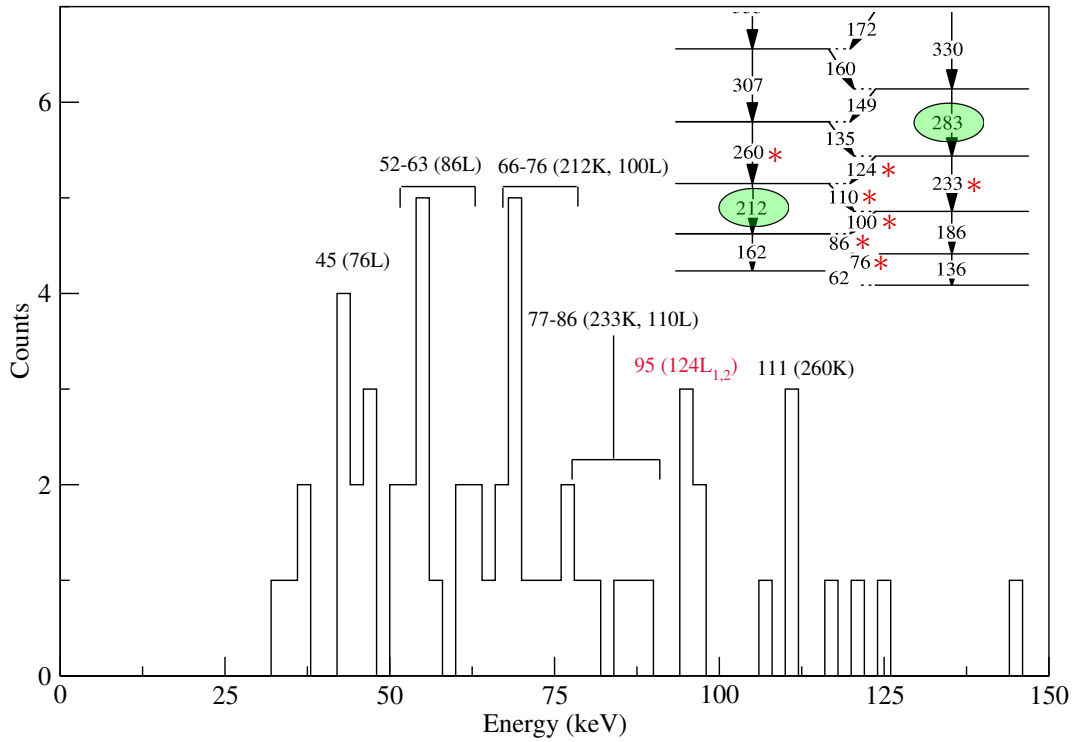

Figure 6.28: *γ ray coincidence gates in the recoil-tagged γ–e^- matrix on the 212 keV and 260 keV transitions to observe electrons in coincidence.*

The 95 keV electron peak appears relatively strongly (5 counts) in coincidence with the selected gates, corresponding to the 124 keV M1+E2' $L_{1,2}$ shell electron peak. Stretched E2 intraband and M1+E2' transitions further down the scheme also appear in coincidence.

135 keV Transition

The 135 keV transition M1+E2' is a doublet with the final stretched E2 transition at the bottom of the band. However this essentially should be relatively weak if the 307 keV and 233 keV E2 γ rays are coincidence gated on.

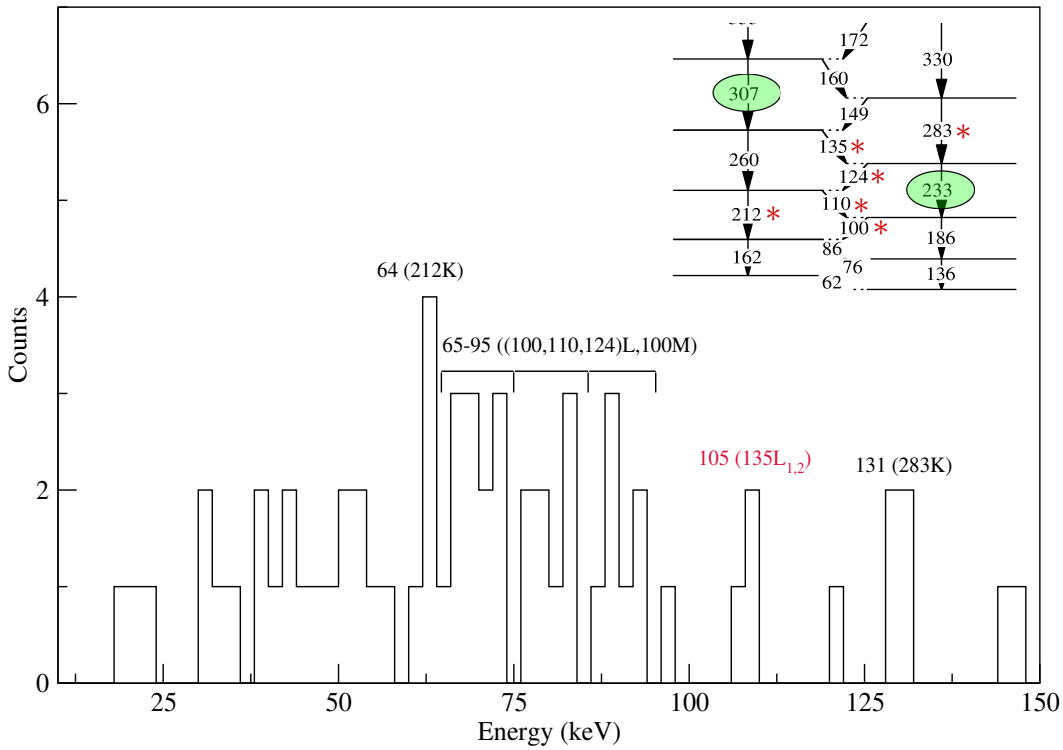

Figure 6.29: *γ ray coincidence gates on the 260 keV and 307 keV transitions in the recoil-tagged γ–e^- matrix to observe electrons in coincidence.*

The 135 keV transition appears in coincidence with the 233 keV and 307 keV γ rays. The 3 $L_{1,2}$ counts that appear are unlikely to be considered as the $\Delta I = 2$ transition at the bottom of the band and thus is attributed to be the $\Delta I = 1$ transition.

149 keV Transition

Coincidence gates selected here include the 260 keV and 330 keV γ ray transitions. As the $\Delta I = 1$ transitions increase in spin and energy, their intensity will decrease with the $\Delta I = 2$ transitions becoming increasingly dominant. The decreasing ICC will also play a role in scope of observing higher energy $\Delta I = 1$ transitions.

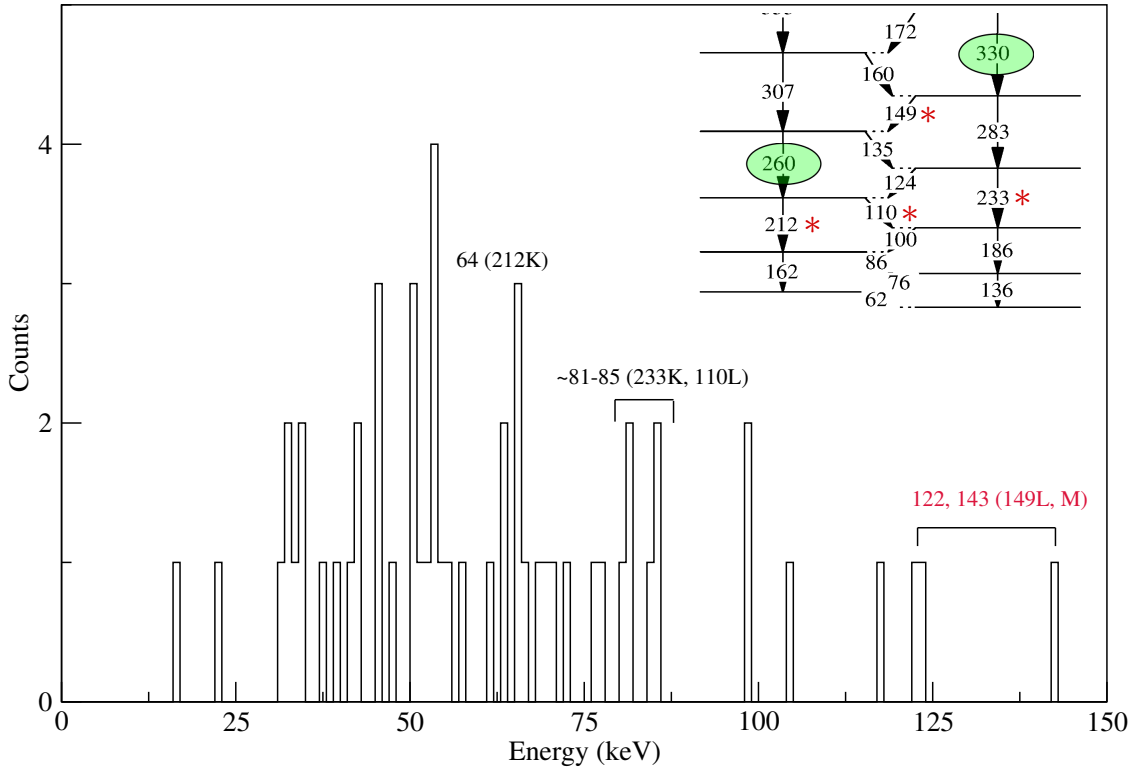

Figure 6.30: *γ ray coincidence gates on the 260 keV and 330 keV transitions in the recoil-tagged γ–e^- matrix to observe electrons in coincidence.*

Here, statistics are severely limited with the L and M shell electrons appearing with few counts. However, the level of background around the peaks is low and the assignment is made as 149 keV. This is also confirmed by observation of the 121 keV electron peak in the recoil-tagged electron spectra, and the additional peak on the tail of the K_β X-ray in the recoil tagged γ ray singles spectrum.

Meagre statistics limits further searches for M1+E2' transitions of higher energy than the 149 keV transition through gating. They can however be observed through the recoil-tagged electron spectrum in Figure 6.4, page 97 and are deduced based on a combination of the sum of the E2 transitions and evident electron peaks.

Based on the interpretation of data observed and the coincidence analysis discussed, the level scheme in Figure 6.10 is constructed.

In general, agreement is found with the study by Herzberg *et. al.* [10], and the focal plane studies [69][74] favouring a coupled rotational band structure albeit with some energy differences. However major differences are found compared to Reiter's study [60]. In particular the absence of the 355 keV multiplet from the bandhead to the ground state, is not evident here (or in the other in-beam study) and must be considered as a statistical fluctuation given the level of statistics that was used in the analysis of that data. The observation of interband transitions is also clear in this study unlike the Reiter's and again a lack of statistics is clearly the primary reason for any conclusions regarding intensity flow. Attention will now turn to obtaining information on the single-particle structure of ^{253}No through further analysis on the data.

6.3 In-beam Discussion

The SAGE data provides a wealth of information on the structure of the nucleus of interest. This will be discussed with comparisons with simulations, internal conversion coefficient measurements, intensity ratio measurements to determine the bandhead configuration, and moment of inertia calculations. Such evidence will support or differ from previous studies.

6.3.1 Simulations Overview

In order to assess the rotational structure of ^{253}No based on the spectra shown, Monte Carlo simulations are performed that allow comparisons with experimental data. Ideally a simulation using the GEANT4 package would be suited to compare with the experimental data. This is still under development and will be available in the near future [79].

Codes

The main Monte Carlo code is a C code CALOBRANCH [76]. This requires a number of nuclear properties to be input:

- The transition energy
- The branching ratio between interband and intraband transitions
- The internal conversion coefficients (ICCs)
- The spin population of each level
- Resolution and efficiency of SAGE.

The ICCs are taken from BRICC (see page 37). The simulation includes K, and $L_{1,2,3}$ shell electrons and requires a model for the spin entry distribution. The B(M1+E2')/B(E2) ratios, and transition energies are obtained from a separate C code BM1E2 [80] which calculates the reduced transition probabilities through the Dönau and Frauendorf approach (see [81] for more details). Further parameters are required to be input into this code:

- The intrinsic quadrupole moment Q_0. This has been measured in the neighbouring nucleus ^{254}No as 13.1 eb [60], and thus is used for ^{253}No as a good approximation
- The collective rotational g-factor g_R of which two different scenarios are considered. Unquenched g_R = Z/A = 0.40 and quenched g_R = 0.7 Z/A = 0.28
- The single particle rotational g-factor g_k which is dependent upon the bandhead configuration. For $7/2^+[624]$ Nilsson configuration g_K=+0.28. For the $9/2^-[734]$ configuration then g_K=−0.25 is used [62].
- The initial (I_i) and final spins (I_f) of the transitions in question
- The K quantum number of the configuration
- The rigid body moment of inertia, $\mathcal{J}_{rigid}$.

One of the issues is a difference in the experimental spin population of levels compared to previous studies. Figure 6.31 shows a fit the intensity of ^{253}No in this study compared to the similar reaction ^{208}Pb(^{48}Ca,2n)^{254}No at a beam energy of 219 MeV measured by Reiter *et al.* [82]. The experimental data assumes the maximum spin for the bandhead (9/2). It can be seen the lower spin transitions are more heavily populated in comparison to the ^{254}No distribution. This is contrary to a previous study which demonstrated good agreement between the ^{254}No distribution and the ^{253}No peak area [75]. Thus for this study the beam energy is slightly lower than previously thought and has the effect of populating more lower energy states than previously. However this is favourable since the one of the key aims of this study is to probe the lower energy transitions.

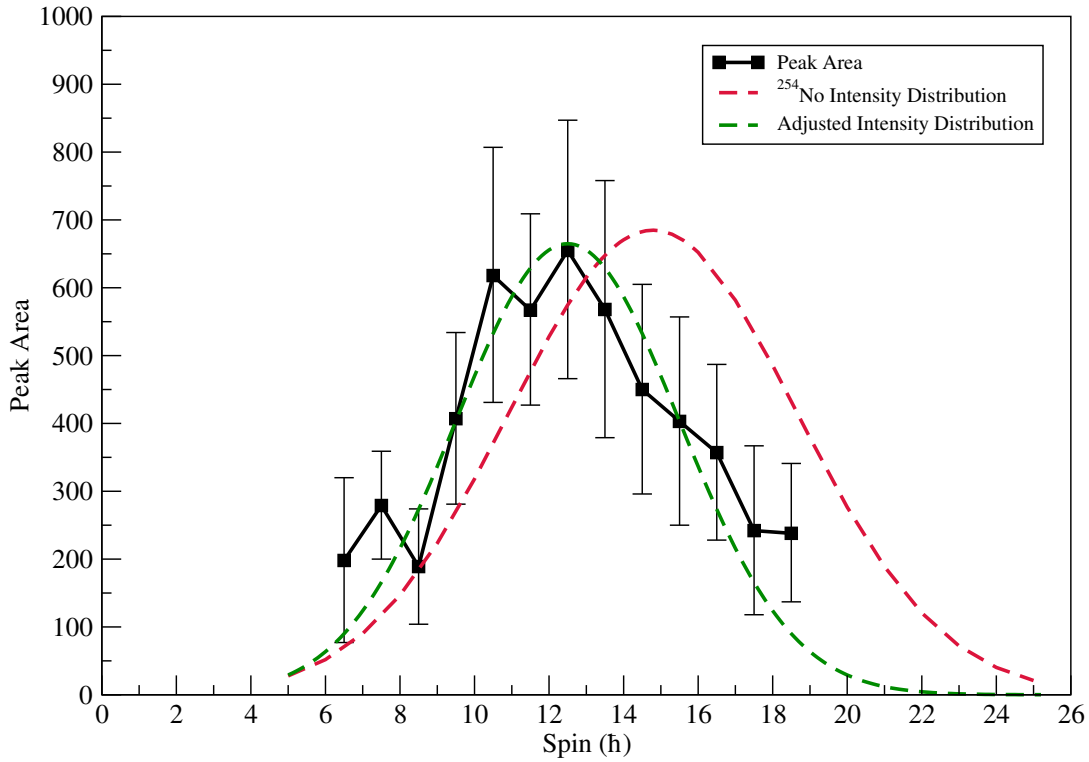

Figure 6.31: *A comparison of the γ ray peak area (corrected for efficiency) to the intensity distribution of ^{254}No. The spin distributions have been normalised to the measured peak area.*

The reasoning behind this shift in distribution can be considered in terms of the beam energy at the centre of mass of the target. The uncertainty on the experimental beam energy compared to the preselected energy is approximately 1% thus giving scope to a slightly lower beam energy than anticipated within around 2 MeV. Furthermore the targets were backed with 5 µgcm^{-2} of carbon. Whilst this thickness was taken into consideration when calculating the required beam energy, uncertainties on the uniformity of thickness measured during the production of the target remain. This increase in the population of lower spin states is favourable, since one of the primary goals of this study is to explore these lower energy states. This adjusted intensity distribution is incorporated into the simulations.

The output from CALOBRANCH is a data file with energy and counts included. This can then be compared with experimental data.

6.3.2 Experiment and Simulation Comparisons

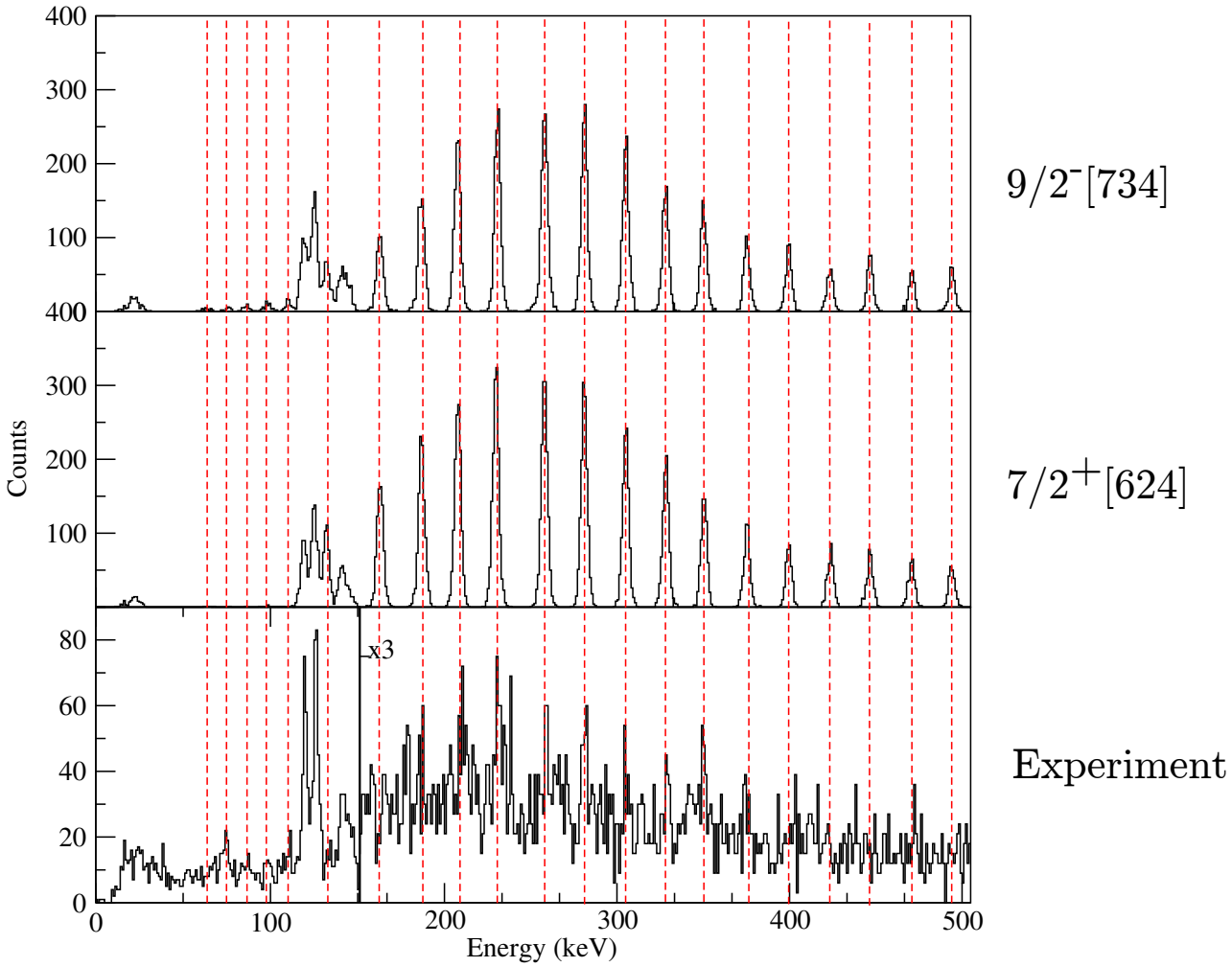

Figure 6.32: *γ-ray singles simulation for the two different possible configurations vs. Recoil-tagged γ ray experimentally measured.*

Simple observation demonstrates good agreement between the calculated values for the transition energies of the E2 γ rays and the experimental data at lower energies. While the intensities for the E2 transitions do not match for simulation and experiment, the two simulated cases look very similar, requiring a more detailed view of the region of interest.

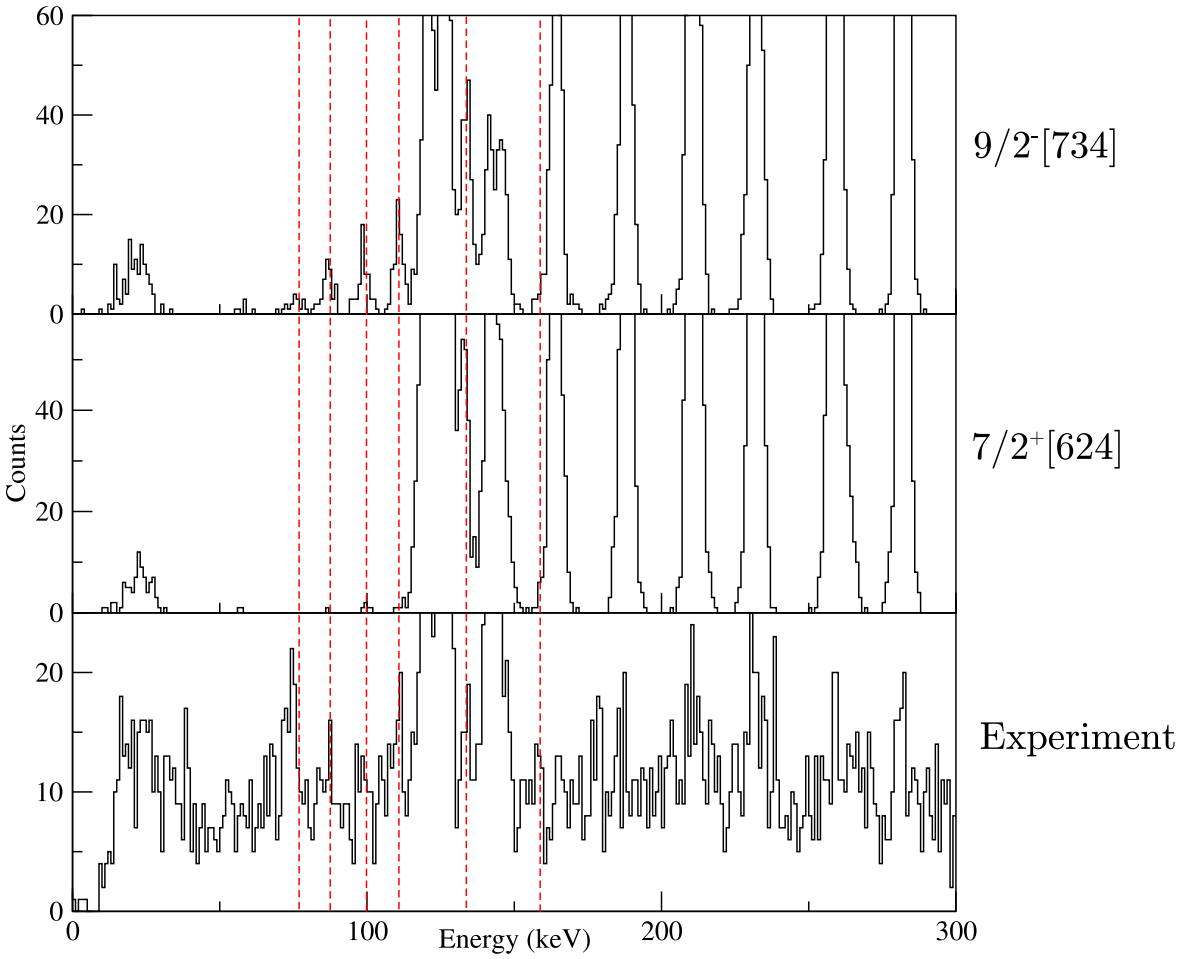

Figure 6.33: *Expanded view of the lower energy γ ray transitions. The low energy $\Delta I = 1$ transitions for the $9/2^-$ simulated spectra are more intense in agreement with the experiment.*

As discussed in Section 5.2, for the $9/2^-$ bandhead, the interband transitions are stronger than for the $7/2^+$. This is also reflected in the experimental γ-ray singles where there are clearly strong mixed M1+E2' transitions in the lower energy region. This hints at the intensity flowing through these inter-band transitions, as well as the E2 intra-band transitions. Comparisons are made with the electron spectra too.

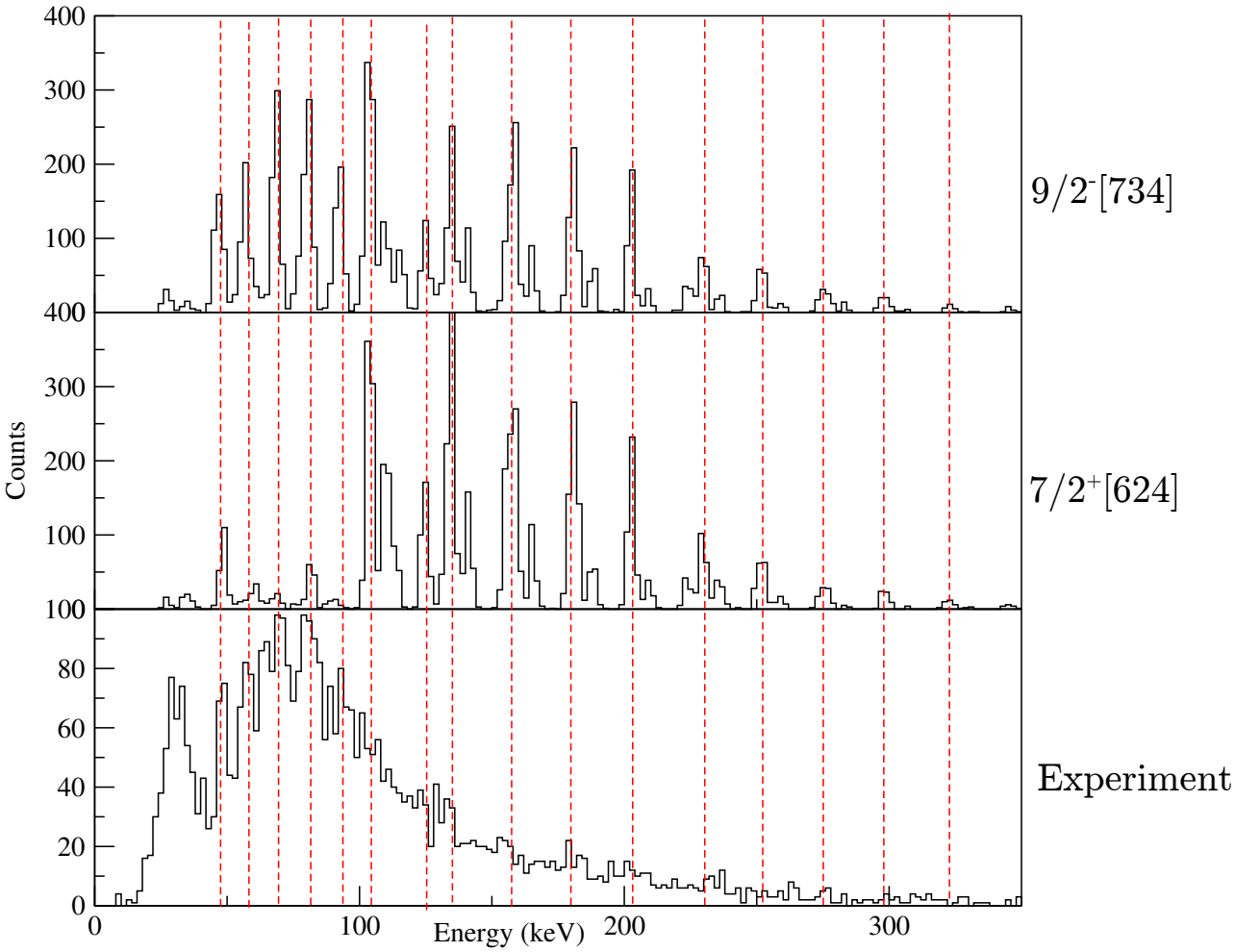

Figure 6.34: *Comparison of the electron experimental data and simulations.*

Observation of the experimental data shows that there is a similar electron peak structure at lower energy to the $9/2^-$ case with strong M1+E2' L electron peaks. The E2 K shell electron peaks appear intense in the simulations as with the γ rays. However if we remove the ideal resolution of 2 keV from our electron simulation then we begin to see a broadening effect of the peaks as the resolution (due to the Doppler effect) is adjusted to approximately 10 keV at 300 keV.

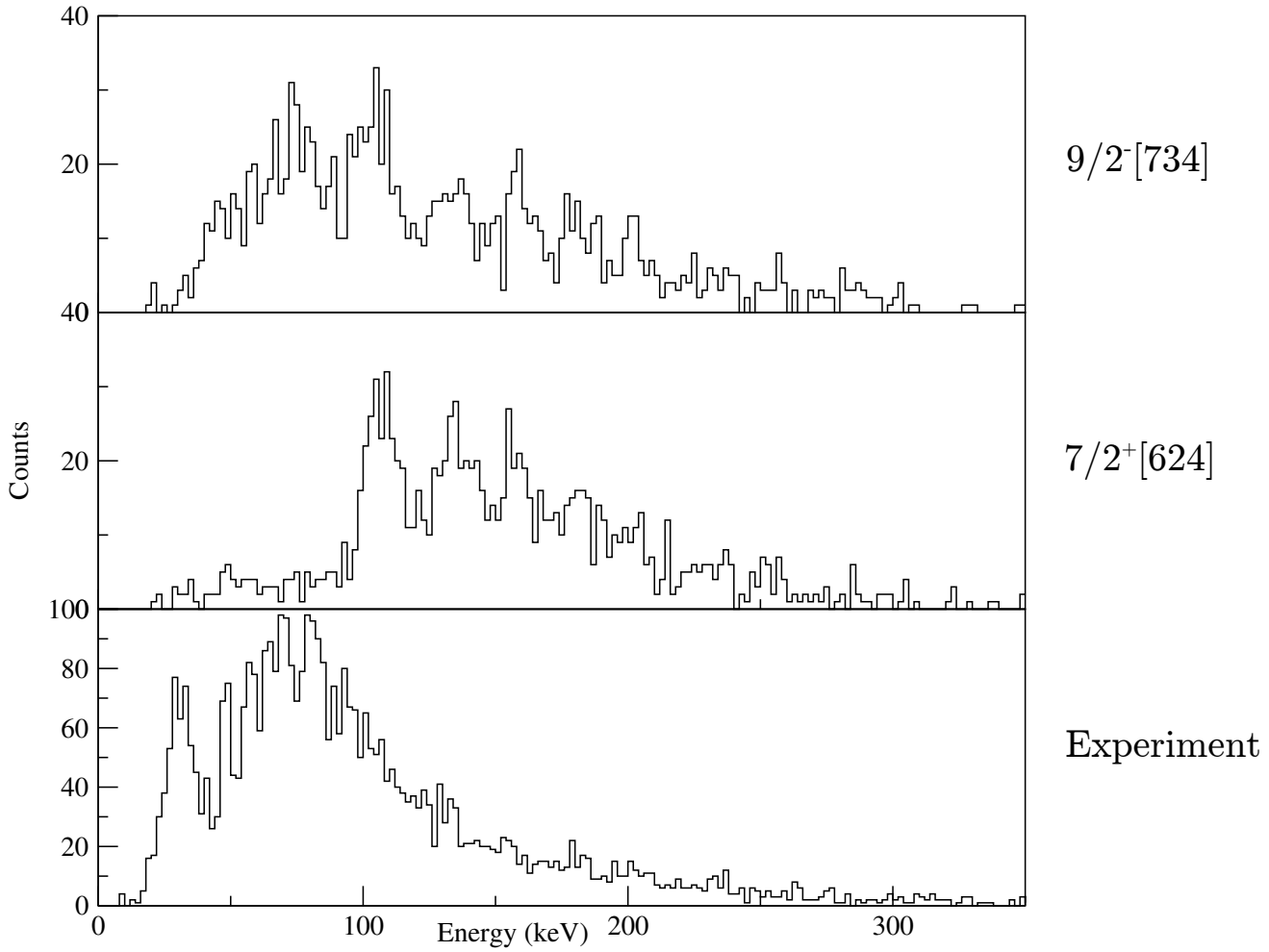

Figure 6.35: *Realistic* SAGE *resolution applied to the 9/2⁻ case simulation compared with the experimental background subtracted electron spectrum.*

The important point to consider here is whether the intensity flows predominately through the stretched E2 transitions, or through the interlinking M1+E2' transitions. The simulation comparisons with the experimental work have demonstrated an preference with the latter case and as such pointing toward the $9/2^-[734]$ configuration. However further measurements will subsequently be discussed to justify and support this claim.

6.4 Internal Conversion Coefficient Measurements

The ICCs were measured using the recoil-tagged experimental data and calculated using Equation 4.3 (page 74). As discussed in Chapter 4 conversion coefficient measurements provide a useful technique in determining the multipolarity of transitions and hence justifying spin and parity assignments.

For the γ rays the recoil-tagged JUROGAM II singles spectrum is used (Figure 6.2, page 95) to measure counts and for electron the background-subtracted recoil gated SAGE spectrum (Figure 6.4). As with the ^{177}Au data, the peaks are fitted using *tv* [48]. Given the level of statistics, a Poisson fitting distribution was favoured. The method involved accounting for the multiple transitions in one electron peak (e.g. the 64 keV electron peak with 213 keV K shell and 86 keV $L_{1,2}$ shell included) and taking the fractional ICC (from BRICC) of each transition into account. This results in the ICCs demonstrated in the following plots with a table summarising the values attained.

Trans Energy (keV)	Multipolarity	E_{e^-} (keV)	e^- Shell	Measured ICC	BRICC ICC $^*\delta = 0.22$ $^\dagger\delta = 1.18$
100	M1+E2'	70	$L_{1,2}$	2.8 $(^{+2.5}_{-1.0})$	9.7 (1)* 12.6 (1)†
110	M1+E2'	81	$L_{1,2}$	4.0 $(^{+3.2}_{-1.4})$	7.3 (1)* 8.7 (1)†
135	M1+E2'	104	$L_{1,2}$	3.7 $(^{+7.3}_{-1.7})$	3.96 (5)* 4.0 (4)†
136	E2	105	$L_{1,2}$	3.5 $(^{+6.9}_{-1.6})$	3.9 (1)
162	E2	131	$L_{1,2}$	0.40 $(^{+0.33}_{-0.18})$	1.82 (7)
186	E2	156	$L_{1,2}$	0.35 $(^{+0.53}_{-0.20})$	1.03 (4)
212	E2	64	K	0.12 $(^{+0.09}_{-0.05})$	0.13 (1)
		183	$L_{1,2}$	0.23 $(^{+0.29}_{-0.15})$	0.61 (2)
233	E2	85	K	0.07 $(^{+0.11}_{-0.06})$	0.12 (1)
		202	$L_{1,2}$	0.31 $(^{+0.39}_{-0.20})$	0.42 (1)
260	E2	112	K	0.04 $(^{+0.05}_{-0.03})$	0.10 (1)
		202	$L_{1,2}$	0.35 $(^{+0.45}_{-0.27})$	0.11 (1)
283	E2	134	K	0.07 $(^{+0.05}_{-0.03})$	0.09 (1)
307	E2	160	K	0.04 $(^{+0.06}_{-0.03})$	0.08 (1)
330	E2	183	K	0.03 $(^{+0.04}_{-0.02})$	0.08 (1)
353	E2	202	K	0.08 $(^{+0.12}_{-0.05})$	0.07 (1)

Table 6.5: *Conversion coefficient measurements measured using* SAGE*, and compared to* BRICC *[27] calculated values.*

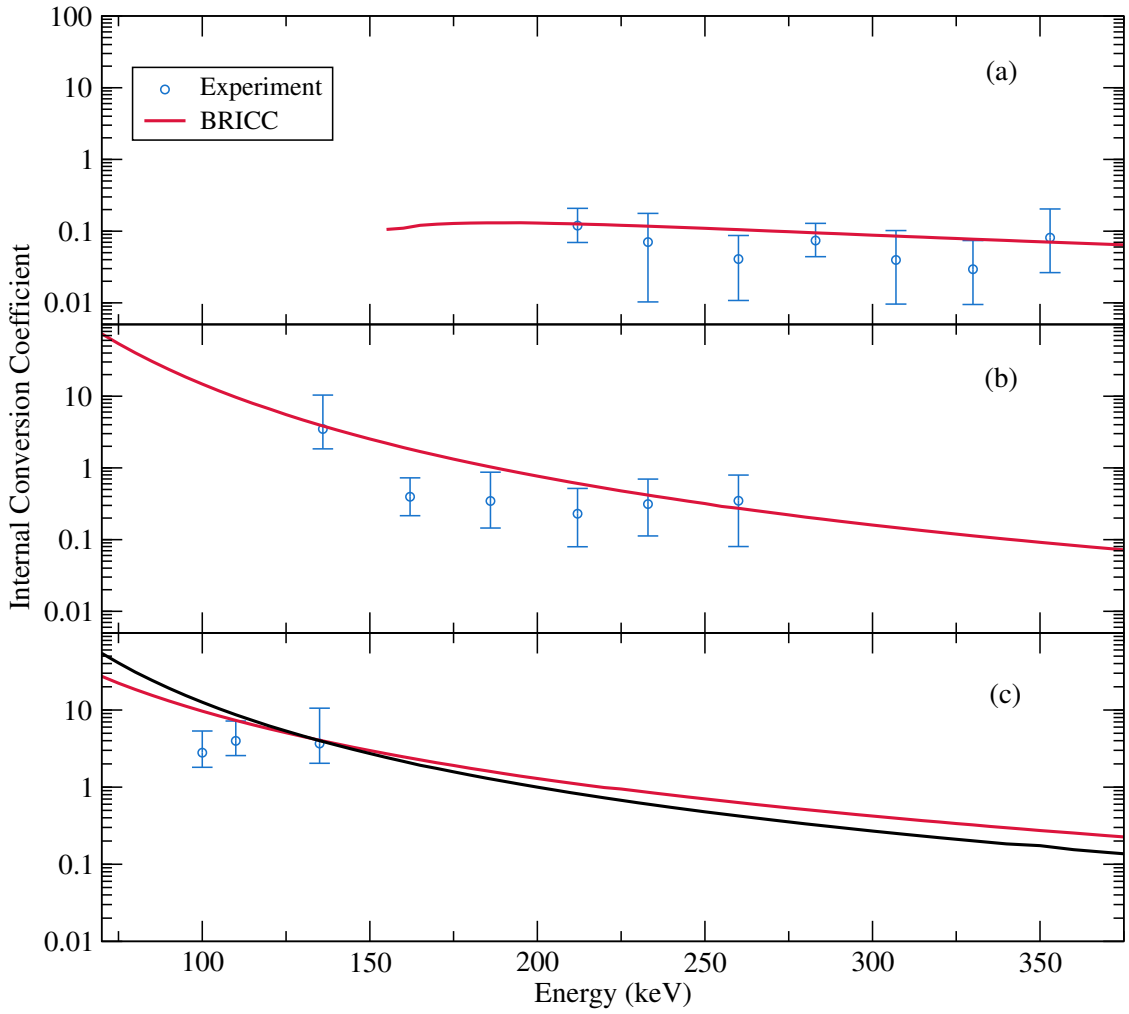

Figure 6.36: *ICCs plotted as a function of energy. (a) K-shell E2 transitions. (b) $L_{1,2}$-shell E2 transitions. (c) $L_{1,2}$-shell M1+E2' transitions compared to BRICC values given mixing ratios for the 7/2[624] bandhead (black line) and 9/2[734] bandhead (red line).*

Consistency is found for values when compared to the theoretically calculated BRICC values. The measured coefficient confirms the intraband transitions as E2 multipolarity. For the mixed $L_{1,2}$ transitions differentiating between the two potential bandhead configurations based on their mixing ratios ($\delta_{9/2^-}$=0.22 and $\delta_{7/2^+}$=1.18) proves more challenging given the small deviations between both. The mixing ratios utilised are calculated from the BM1E2 [80] simulation program using the Dönau and Frauendorf method (discussed on page 129). Figure 6.37 shows an expanded view of this region (on a linear scale for further clarity).

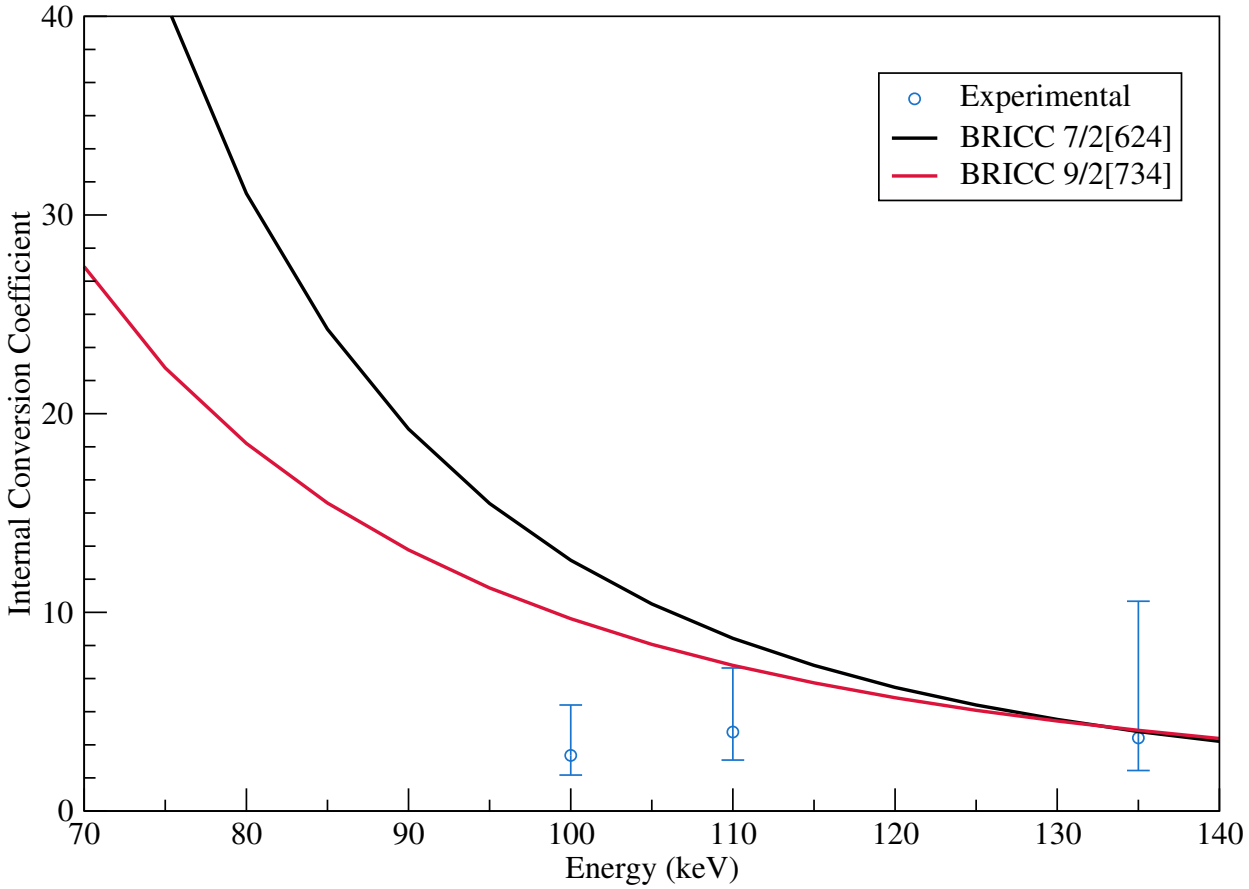

Figure 6.37: *Linear scaling of the ICC from the bottom panel of Figure 6.36. The two potential bandhead configurations differ based on the mixing ratios for a given bandhead, and hence the ICC. (Multipole mixing ratios $\delta_{9/2^-}$=0.22 and $\delta_{7/2^+}$=1.18) have been theoretically calculated.*

The 76 keV, 86 keV and 124 keV transitions are absent given that the γ rays are at the same energies as lead and nobelium X-ray peaks. The remaining transitions show a preference for the lower ICC $9/2^-[734]$ configuration. Improving the level of statistics would prove useful in gaining a better handle on the bandhead using ICC measurements. Note that at lower energies the $7/2^+$ has a larger ICC than $9/2^-$, however in the data more electrons will be seen for the $9/2^-$ as the transition probability is independent of the conversion coefficient.

6.5 B(M1+E2')/B(E2) ratio

Utilising the B(M1+E2')/B(E2) provides a useful tool in determining the bandhead configuration as shown before with the previous study outlined on page 83. The transition intensity is determined using

$$I_\gamma = \frac{N_\gamma}{\varepsilon_{Ge}}(1+\alpha), \tag{6.2}$$

or for electrons,

$$I_e = \frac{N_e}{\varepsilon_{Si}}(1+\frac{1}{\alpha}). \tag{6.3}$$

Based on the intensities, the experimental data can be used to calculate the B(M1+E2')/B(E2) values as a function of spin using the equation

$$\frac{B(M1)}{B(E2)} = \frac{\lambda}{1.43\times10^4}\frac{1}{(1+\delta^2)}\frac{[E_\gamma(\Delta I=2)]^5}{[E_\gamma(\Delta I=1)]^3} \qquad (\mu_N^2 e^2 fm^{-4}), \tag{6.4}$$

where λ is the branching ratio λ =T(M1+E2'; I $\rightarrow$ I-1)/T(E2; I $\rightarrow$ I-2) (i.e. the intensity ratio) and δ is the multipole mixing ratio between the competing M1 and E2' components. This can be determined through the measurement of the internal conversion coefficients

$$\alpha_m = \frac{\alpha_{M1}+\delta^2\alpha_{E2}}{1+\delta^2} \tag{6.5}$$

where α_m is the measured ICC, and $\alpha_{M1(E2)}$ are the calculated pure multipolarities for M1 and E2 transitions. The value of δ obtained from the ICCs measured was δ=0.4$\pm^{0.3}_{0.1}$. The B(M1+E2')/B(E2) values are then plotted as a function of spin and compared to calculated values obtained using the code BM1E2 (used for the Monte Carlo simulations).

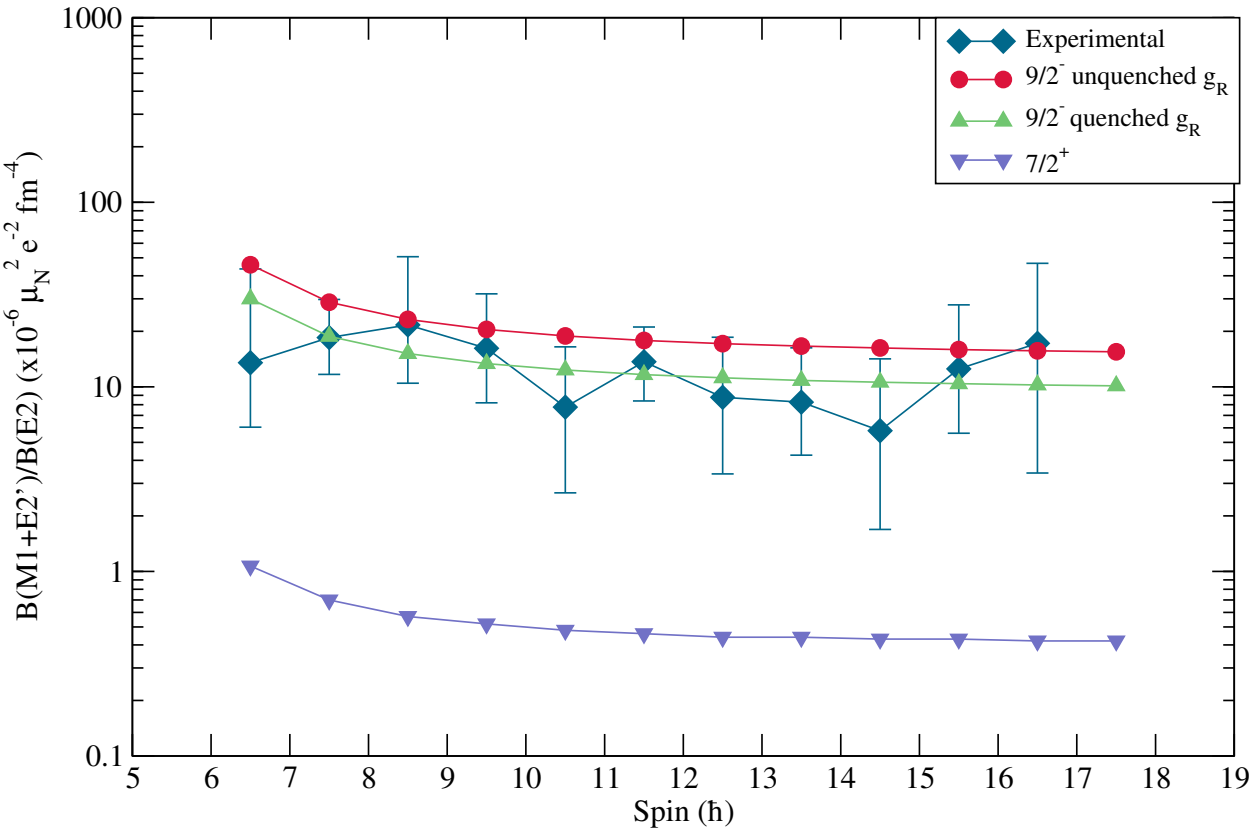

Figure 6.38: *The B(M1+E2')/B(E2) ratio plotted as a function of spin. The calculated values are plotted for the 9/2⁻[734] (g_K=−0.25) quenched and unquenched g_R factor, and for the 7/2⁺[624](g_K=+0.28). The spin is given as from the initial level the transition depopulates.*

The experimental data shows a clear preference towards the 9/2⁻[734] configuration compared the 7/2⁺[624] with strong M1+E2' transitions dominating intensity flow. Again this is in agreement with [10] and also [45], but disagreement with [60]. Also shown is the quenched vs. unquenched collective rotational g-factor with quenched having g_R=0.28 and unquenched g_R=0.40. Determination of this value is inconclusive due to the small deviation in intensity between the two, coupled with the uncertainties on the experimental data. For completeness a table of the values is included.

Initial Spin (ħ)	E(I→I-2) (MeV)	E(I→I-1) (MeV)	λ	B(M1+E2')/B(E2) $10^{-6}\mu_B^2 e^{-2} fm^{-4}$
6.5	0.136	0.076	2.5 $(^{+5.5}_{-1.3})$	13.5 $(^{+30.0}_{-7.5})$
7.5	0.162	0.086	1.9 $(^{+1.2}_{-0.7})$	18.5 $(^{+11.3}_{-6.8})$
8.5	0.186	0.100	1.8 $(^{+2.4}_{-0.9})$	21.7 $(^{+29.0}_{-11.2})$
9.5	0.212	0.110	0.9 $(^{+0.9}_{-0.5})$	16.2 $(^{+15.7}_{-8.0})$
10.5	0.233	0.124	0.4 $(^{+0.4}_{-0.3})$	7.8 $(^{+8.7}_{-5.1})$
11.5	0.260	0.135	0.5 $(^{+0.3}_{-0.2})$	13.7 $(^{+7.4}_{-5.3})$
12.5	0.283	0.149	0.3 $(^{+0.3}_{-0.2})$	8.8 $(^{+9.8}_{-5.4})$
13.5	0.307	0.160	0.2 $(^{+0.2}_{-0.1})$	8.3 $(^{+8.0}_{-4.0})$
14.5	0.330	0.172	0.1 $(^{+0.2}_{-0.1})$	5.8 $(^{+8.4}_{-4.1})$
15.5	0.351	0.183	0.3 $(^{+0.3}_{-0.1})$	12.5 $(^{+15.6}_{-6.9})$

Table 6.6: *Measured B(M1+E2')/B(E2) values. λ is the T(M1+E2')/(E2) branching ratio.*

6.6 Moments of Inertia

The kinematic and dynamic moments of inertia (see Chapter 2 Section 2.5.1) can be calculated from the experimental spin and energy data and tested against a theoretical model.

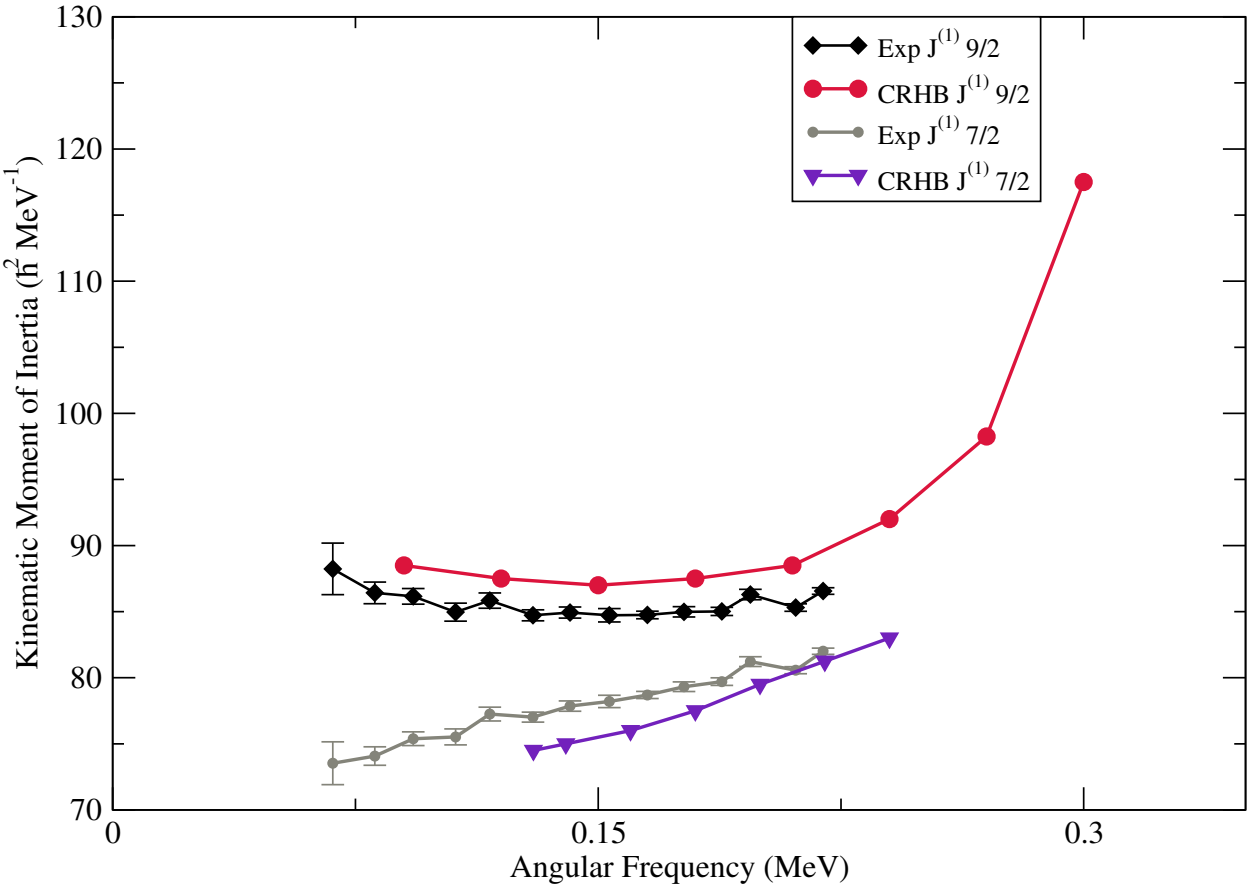

Figure 6.39: *Kinematic moment of inertia plotted as a function of angular frequency. Experimental values are compared to theoretical values calculated by Afanasjev [76].*

The experimental data for the kinematic moment of inertia $\Im^{(1)}$ is taken for the bandhead spin being 7/2 or 9/2 and compared to the Cranked Relativistic Hartree-Bogoliubov (CRHB) model from Afanasjev [23] The values were obtained from [76]. Comparing the two potential spins to theory shows that either one could well be considered as valid. Higher spins would be need to be reached in order to make any conclusions with the upbend evident in the 9/2 CRHB model, giving a basis to compare model and experiment. The dynamic moment of inertia $\Im^{(2)}$ is independent of spin being only dependent upon the energy, and thus has the same values for

both 7/2 and 9/2 experimentally.

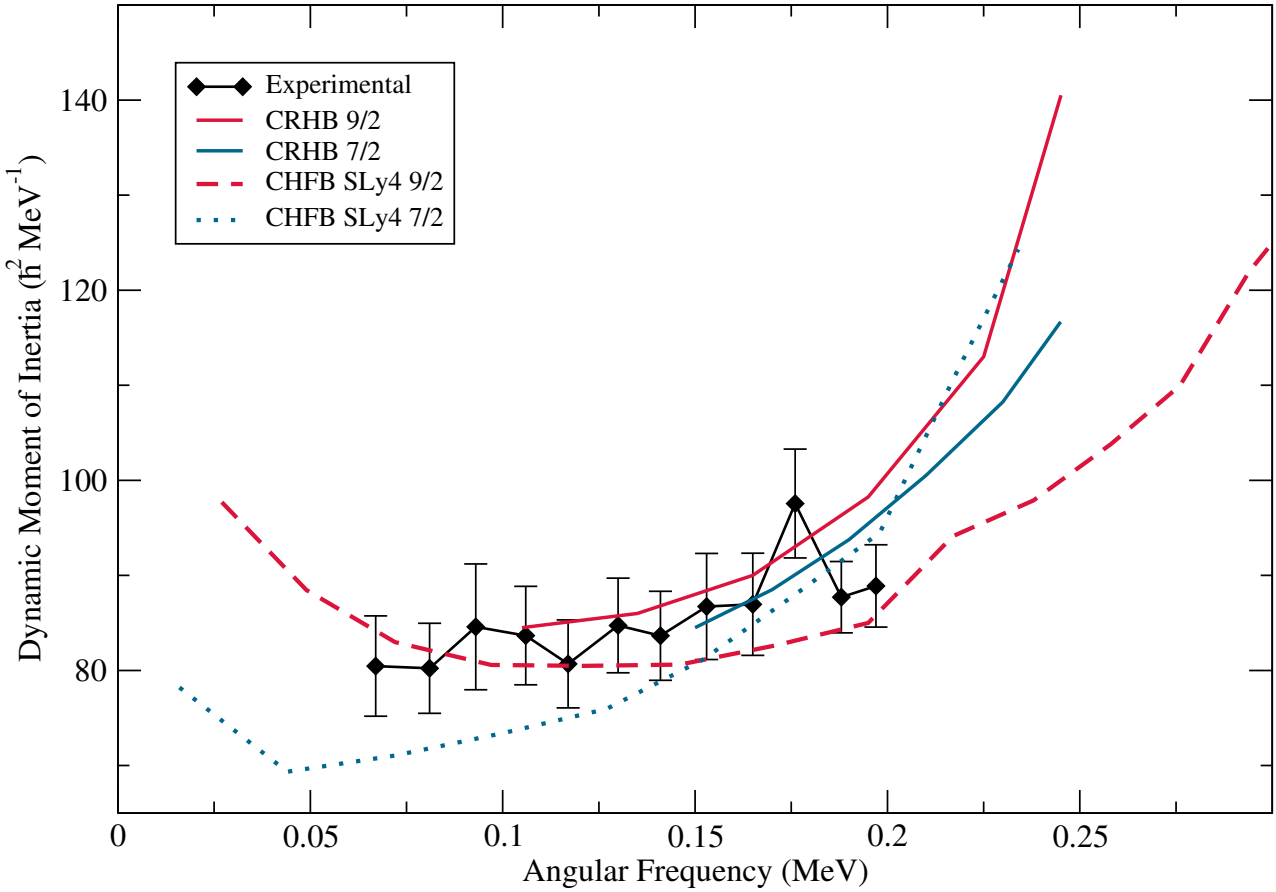

Figure 6.40: *Dynamic moment of inertia plotted as a function of angular frequency. Again the theoretical values compared with are from models by [22] and [23] (values obtained from [76]).*

The experimental data in this case is compared to two models. The CRHB model is used again but also included are calculations taken from [22] using the self consistent Cranked Hartree-Fock-Bogoliubov (CRFB) model with the Skyrme SLy4 parametrisation. At lower energies, the data tends to the 9/2 bandhead spin for CHFB SLy4, yet at higher energies the magnitude of the uncertainties make the determination of any assignment difficult.

6.7 Summary of the In-Beam Interpretation

The arguments presented using the in-beam γ ray and conversion electron data analysis strongly point towards intense linking M1+E2' transitions between two rotational bands. This is supported through a number of considerations. Comparisons have been made with simple Monte Carlo simulations with strong interlinking transitions in both simulation and experiment. Internal conversion coefficient measurements have confirmed inferred E2 multipolarities, with mixed M1+E2' transitions favouring a mixing ratio calculated for the 9/2[734] configuration. Branching ratio measurements between the interlinking and stretched E2 transitions have further supported such arguments. Finally moment of inertia calculations are compared with advanced models with further data being required to make any firm assignments, however the data had a lower energy trend for final spin 9/2 CHFB data with the Skyrme parametrisation compared to a 7/2 final spin. Based on the evidence each of these measurements and comparisons has determined, the $9/2^-[734]$ configuration is assigned to be the bandhead. This is in agreement with [61] and [45] but in disagreement with [60] which assigns the $7/2^+$ bandhead decaying to the $9/2^-[734]$ ground state (see page 79). Attention will now turn to the measurement of longer lived decays.

6.8 Focal Plane

The GREAT spectrometer has allowed for studies to be performed on the subsequent longer lived decays of ^{253}No and excited states in ^{249}Fm. While the main focus of the study remains on in-beam spectroscopy, α-decay and α-γ studies were accessible, alongside measurements on an isomeric decay.

6.8.1 Alpha Decay

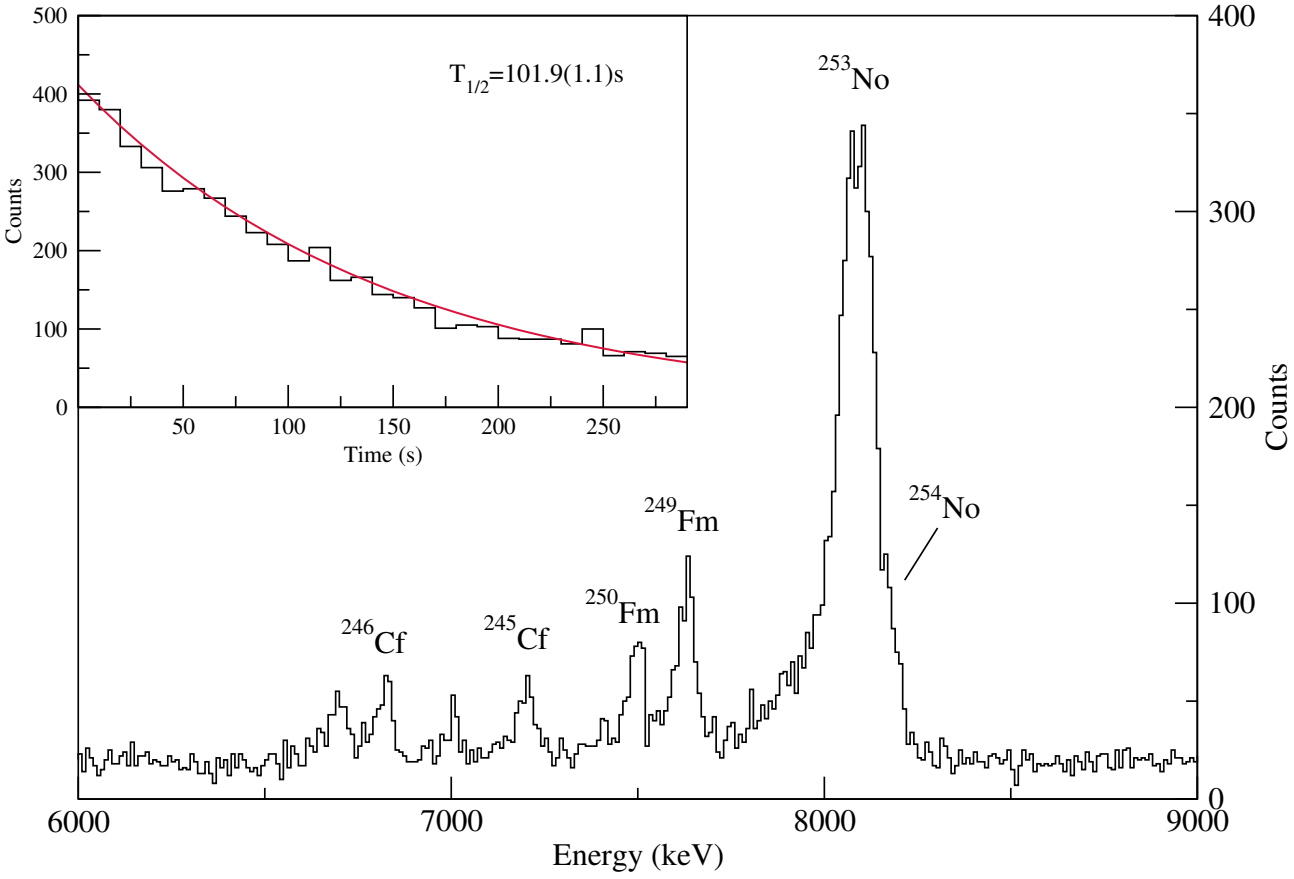

Figure 6.41: *Alpha decay energy and time. The half-life is consistent with the literature value of* $T^{Lit}_{1/2}$ *= 102 s [20]. The subsequent decay chain is evident with the number of additional peaks.*

The α decay energy is found to be E^{Exp}_{α} = 8090±36 keV, which is consistent with the literature value E^{Lit}_{α}= 8010±20 keV [20]. The reasoning behind the experimental lower energy shift systematic error can be explained by consideration of the calibration method of the DSSD-y

strips. The energies of the triple α calibration sources are 5-6 MeV. However the decay energies measured in this study are around 8 MeV. Thus this may contribute to a shift based on the energy discrepancy between calibrated source and measured data. Another reason is that the calibration source is external to the detector face and thus the α particles have to pass through a dead layer on the detector face with different thickness's depending upon emission angle. Thus the calibrated energies will be lower than expected compared to the α decays resulting from the recoils implanted into the DSSDs. Since the primary aim of this study is not to measure the α decay energy, then this is not a major issue. If one wanted to avoid this then an internal calibration could be performed whereby recoils are created with known α decay energies similar to the nucleus of interest. Thus the α decay energies are calibrated close to the α decay energy of interest and the dead layer issue is circumvented. The half life measurement was obtained through the application of an exponential fit to the time difference between recoil implantation and α decay with a value of $T_{1/2}^{Exp}$=101.9±1.1 s, again, consistent with literature; $T_{1/2}^{Lit}$= 102 s [20].

The decay chain ^{253}No $\rightarrow$ ^{249}Fm $\rightarrow$ ^{245}Cf is evident. There are also some additional peaks established as the decay chain ^{254}No $\rightarrow$ ^{250}Fm $\rightarrow$ ^{246}Cf through mother–daughter correlations. The mother–daughter correlations are obtained from a coincidence matrix with the criteria of a recoil implantation followed by a mother decay and subsequent daughter decay in time order. ^{254}No is produced in the 2 neutron channel as a result of the target having some additional ^{208}Pb contamination. Figure 6.42 shows projections from two separate mother–daughter matrices. The first matrix projections labelled (a) and (b) relies on the condition of a time 302 s after recoil implantation and then 470 s after 302 s. The second projections ((c) and (d)) follows similar conditions, but with times of 165 s after recoil implantation and then a subsequent 90 minutes following this.

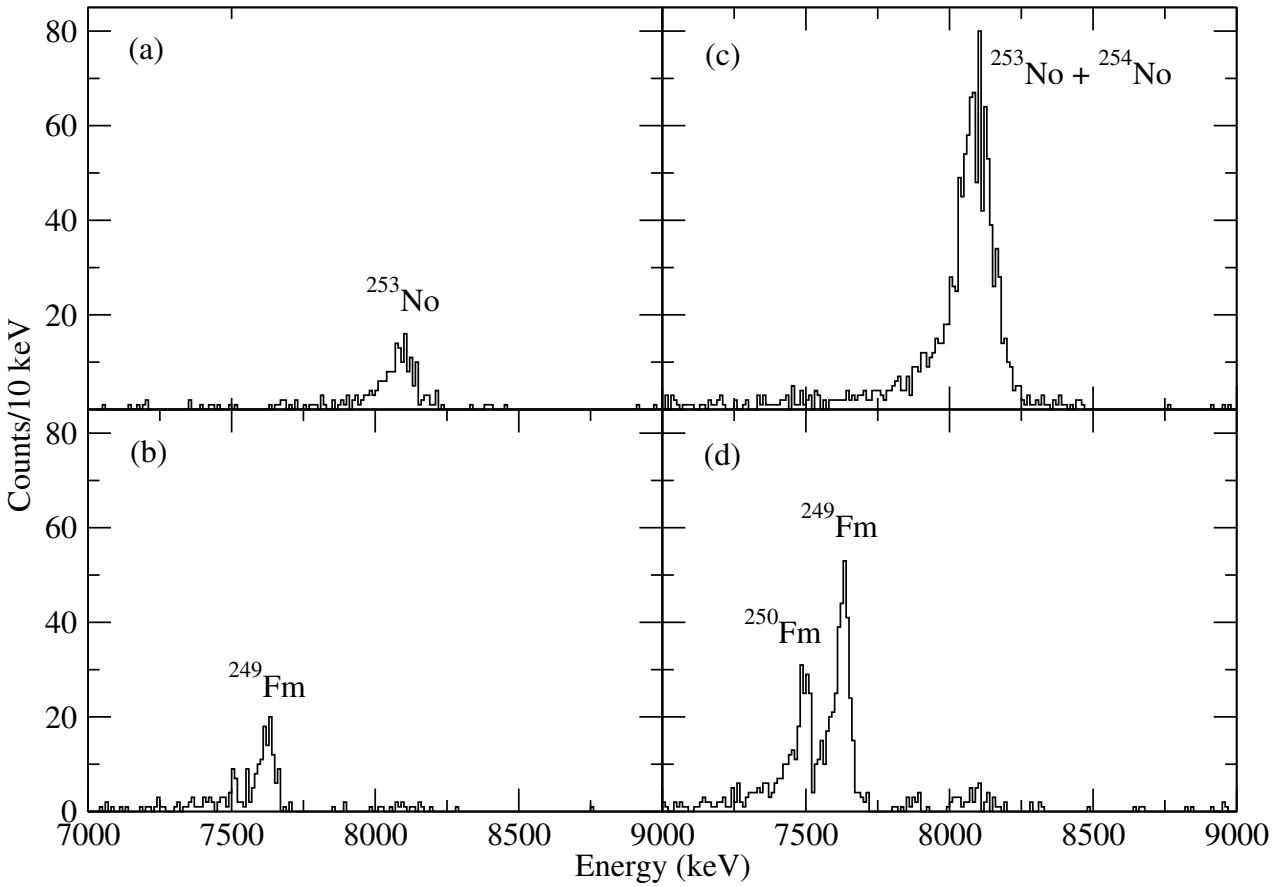

Figure 6.42: *Mother-Daughter projections from time correlations observed in the* DSSD-*y detector. (a)* ^{253}*No decay projection with a search time criteria of 302 s followed by a subsequent* ^{249}*Fm decay within 470 s, (b)* ^{249}*Fm decay within a subsequent 470 s after the 302 s* ^{253}*No decay, (c)* ^{254}*No projection after 165 s and subsequent* ^{250}*Fm in 90 mins, and (d)* ^{250}*Fm within 90 mins of the 165 s* ^{254}*No decay.*

The search times for the plots were based on 3 half-lives for each of the respective nuclei in question. This established both ^{253}No and ^{254}No decays for projections (c) and (d) whereas for the shorter times ((a) and (b)) the contaminants are suppressed and only the decay chain of interest appears. The larger number of counts in projections (c) and (d) stem from the longer correlation time selected on the ^{250}Fm decay search time.

The ^{254}No peak is confirmed through gating on the ^{250}Fm peak.

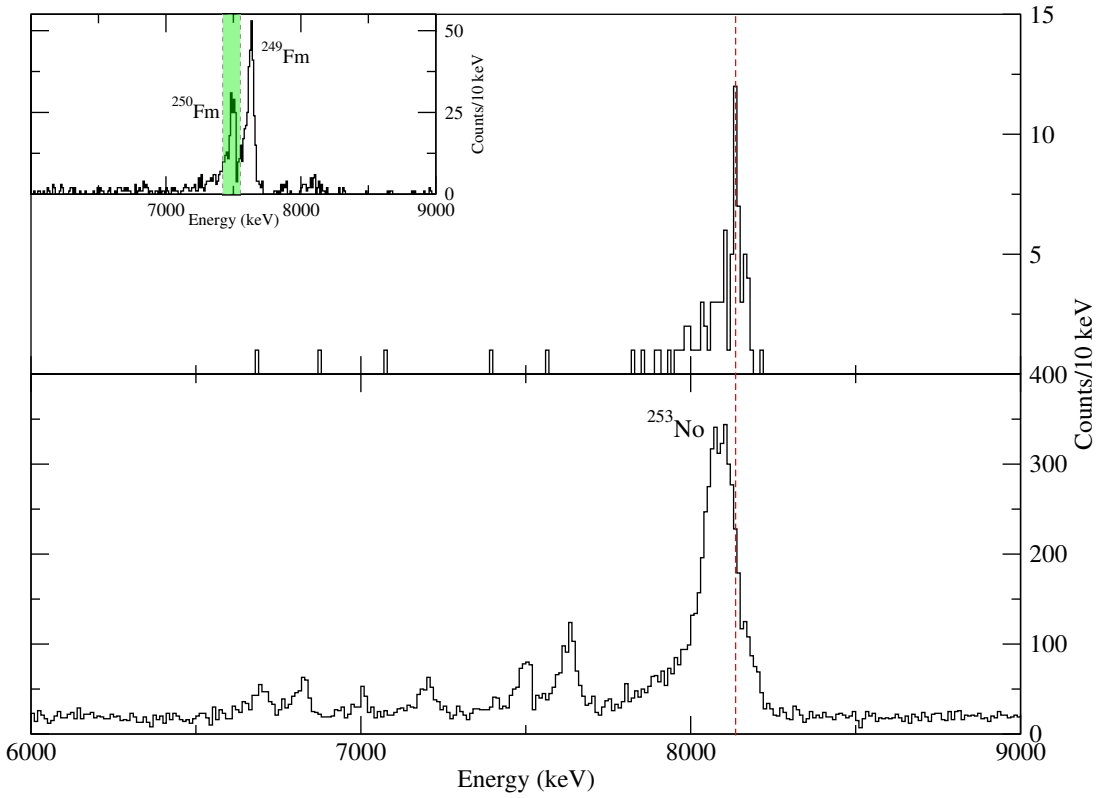

Figure 6.43: *Top panel: gating on the ^{250}Fm peak (inset) from the longer mother-daughter correlation (Figure 6.42 panel (d)) produces the full energy peak shown. The bottom panel shows the raw alphas for a comparison of the energy difference.*

The ^{254}No is produced in beam and so could produce potential electron and γ ray contamination. The most intense γ rays have energies of 214.5 keV, 267.6 keV, and 318.4 keV [83] yet no strong peaks appear at these energies in this study (see Figure 6.1 page page 94). Thus any contamination may be considered as minimal.

6.8.2 Excited States in ^{249}Fm

To observe the excited structure in ^{249}Fm, the planar, clover and PIN diode detectors were placed under the same recoil-decay tagged coincidence gates for the RDT spectra (7700–8300 keV and within 3 half-lives (306 s) of the recoil implantation). In the subsequent plots, experimental α-tagged γ ray and electron data is compared to a Monte-Carlo simulation using the CALOBRANCH code used in Section 6.3.1 and based the level scheme shown in

Section 5.3.2, page 92.

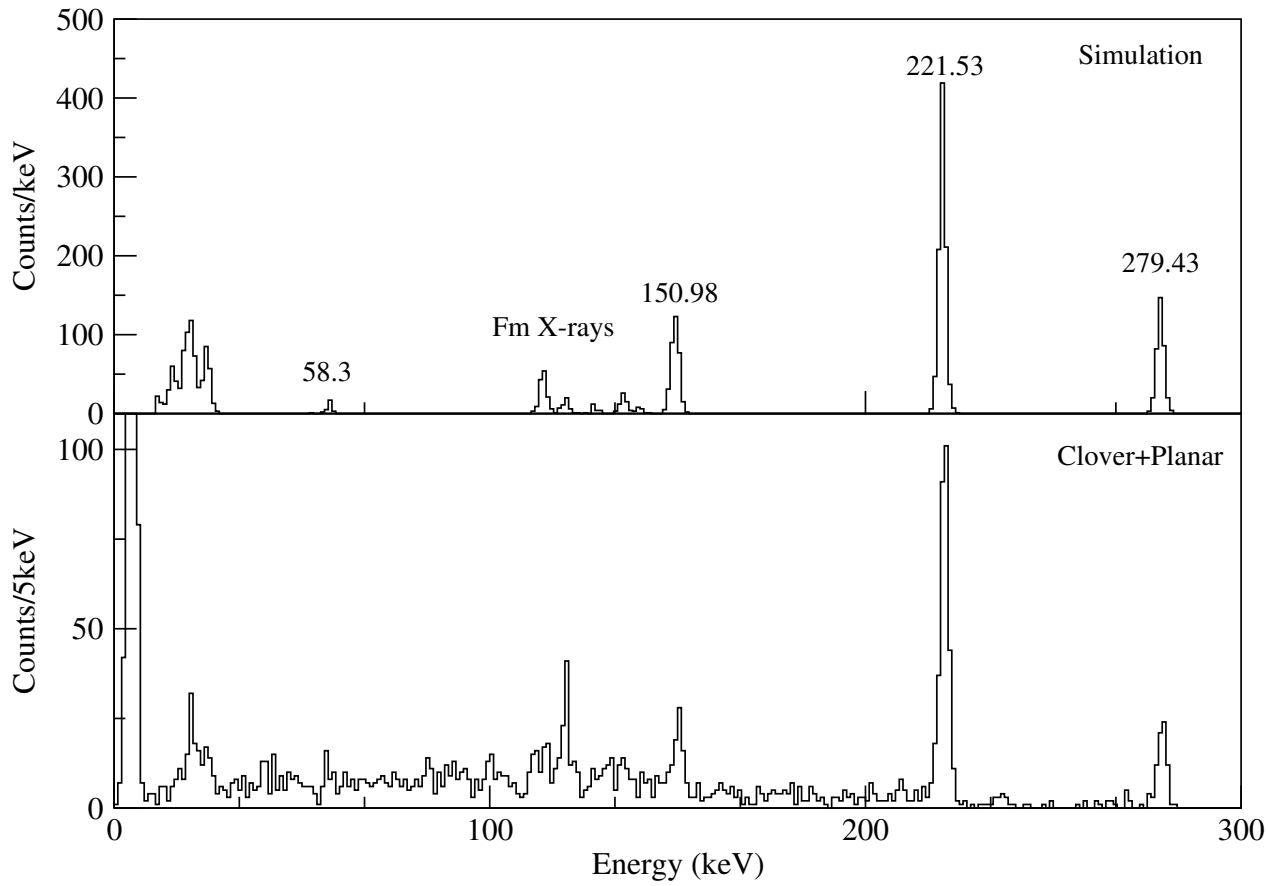

Figure 6.44: *Sum of focal plane clover and planar-X detector γ rays observed in coincidence with a recoil implantation and subsequent ^{253}No α-decay (bottom panel). Compared to a simulation using* CALOBRANCH *[76] (top panel). The level scheme and transition intensities used in the simulation were taken from experimental data measured by Hessberger et al. [71].*

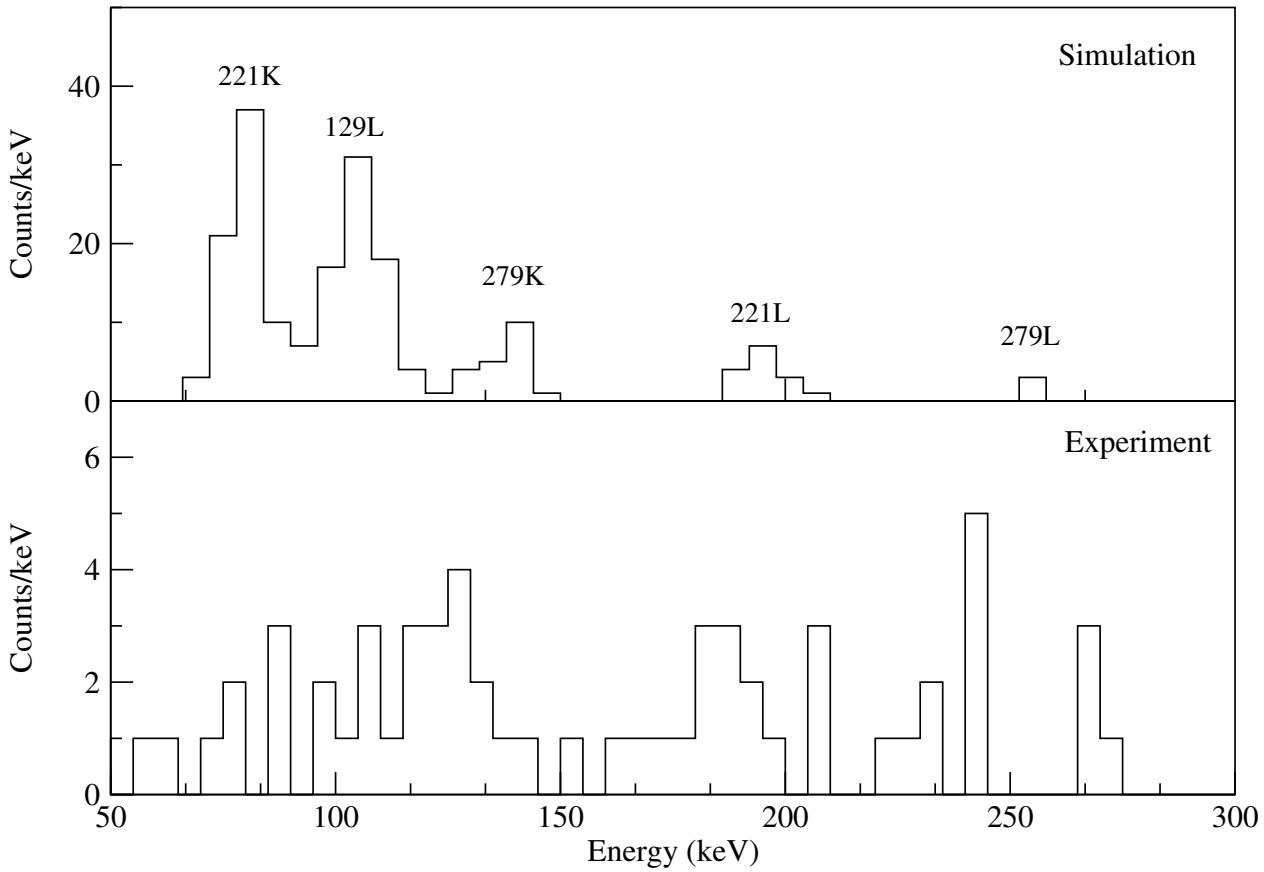

Figure 6.45: PIN *diode conversion electrons observed in coincidence with a recoil implantation and subsequent* ^{253}*No* α *decay energy and 3×half-life (bottom panel). This compared to the electron simulation from the* CALOBRANCH *simulation with intensities and energies deduced from the previous study [71]. Please note the different scaling of the y-axis.*

The clover and planar-X efficiency for each of the peak energies in the CALOBRANCH simulation was applied from a GEANT Monte Carlo simulation of the GREAT spectrometer by Andreyev [84] and the ICCs calculated in BRICC [27]. For the γ rays, there is good agreement between both energies and intensities of the transitions representing the decay from the α populated $9/2^-[734]$ level in ^{249}Fm. However for the electrons there are clearly some discrepancies between data and simulation. The energies differ by approximately 10 keV. During calibration the ^{133}Ba electron source is placed exterior of the PIN diodes and thus emitted electrons will have differing levels of dead layer on the face of the detector to pass through dependent upon the angle between emission and detector interaction. This geometry is different online, with electron emission occurring from the implanted recoils in the DSSDs. Thus the energy appears

reduced from mis-calibration. Ideally, one would perform an internally based calibration from a known decay, however this would prove challenging given the low cross section of an isotope with energies similar to the regime probed. The lack of robustness of the PIN diodes and the absence of any meaningful statistics also hinders analysis. The measured intensities are compared in Table 6.7.

E_γ (keV)	Peak Area (Counts)	πL	ICC (BRICC)	I_{rel} Exp	I_{rel} Ref [71]	I_{rel} Ref [69]
58.1	14 (6)	M1	51.1 (8)	1.21 (6)	0.73 (3)	N/A
150.9	43 (14)	E1	0.214 (3)	0.17 (4)	0.12 (5)	0.22 (1)
221.5	174 (14)	E1	0.092 (10)	1.00	1.00	1.00
279.4	43 (8)	E1	0.056 (1)	0.35 (0.12)	0.44 (1)	0.48 (1)

Table 6.7: *Relative intensities of the recoil-decay tagged focal plane γ rays. Experimental results from this study are compared with previous studies.*

Comparing the relative intensities of the γ rays to previous studies demonstrate a statistical consistency for the 150.9 keV and 279.4 keV E1's but the 58.1 keV M1 is not consistent. The basis of this being an M1 and thus highly converted is a likely factor in this, there are a lower number of γ rays and so statistics are reduced. Furthermore the electron energy would be such that it would fall below the limit of detection from the PIN diodes. The simulated data based on the previous study confirms the γ ray multipolarity assignments. From the small number of X-rays in the γ ray data one can infer that a low level of conversion is occurring and thus likely that the majority of transitions are electric based in terms of multipolarity compared to magnetic based.

6.8.3 Fast Isomer Decay

There is a known ∼31 µs isomer in ^{253}No [69][71][74] as discussed in section 5.3.1 (page 89). The x-strips in the DSSD were set to sensitive to low energy transitions whereas the y-strips were set to be sensitive to higher energy α decays. Thus measuring decay cascade of electrons in the x-strips of the DSSD detector as a function of time within a time window of 100 us after recoil implantation demonstrates the decay of this isomer.

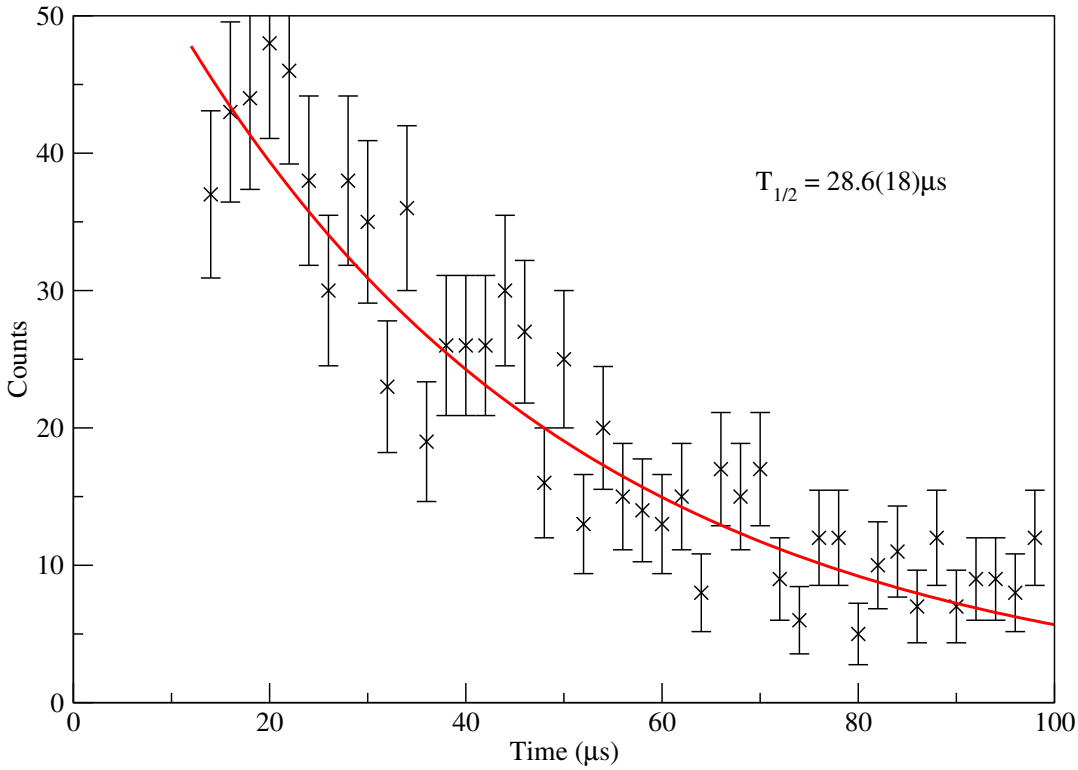

Figure 6.46: *Count rate in the x-strips of the* GREAT DSSD *detector as a function of time within 100 µs following recoil implantation. The absence/drop of counts below around 15 µs stems from the dead time between charge pulses in the detector.*

The half-life is measured as $T_{1/2}^{Exp}$=28.6±2.3 µs, which is consistent with the literature value $T_{1/2}^{Lit}$ =31±4 µs [20]. The planar detector is also sensitive to the low energy M2 transition from the decay of the isomer. Note that the addition of a baseline correction to account for the background was investigated. The value obtained from this for the half-life was $T_{1/2}^{Sub}$ = 22.7±4.7 µs which remains consistent with the literature value. The deviation in both values is primarily caused by the level of statistics available. Indeed the systematic error of the fitting method

also plays a role here.

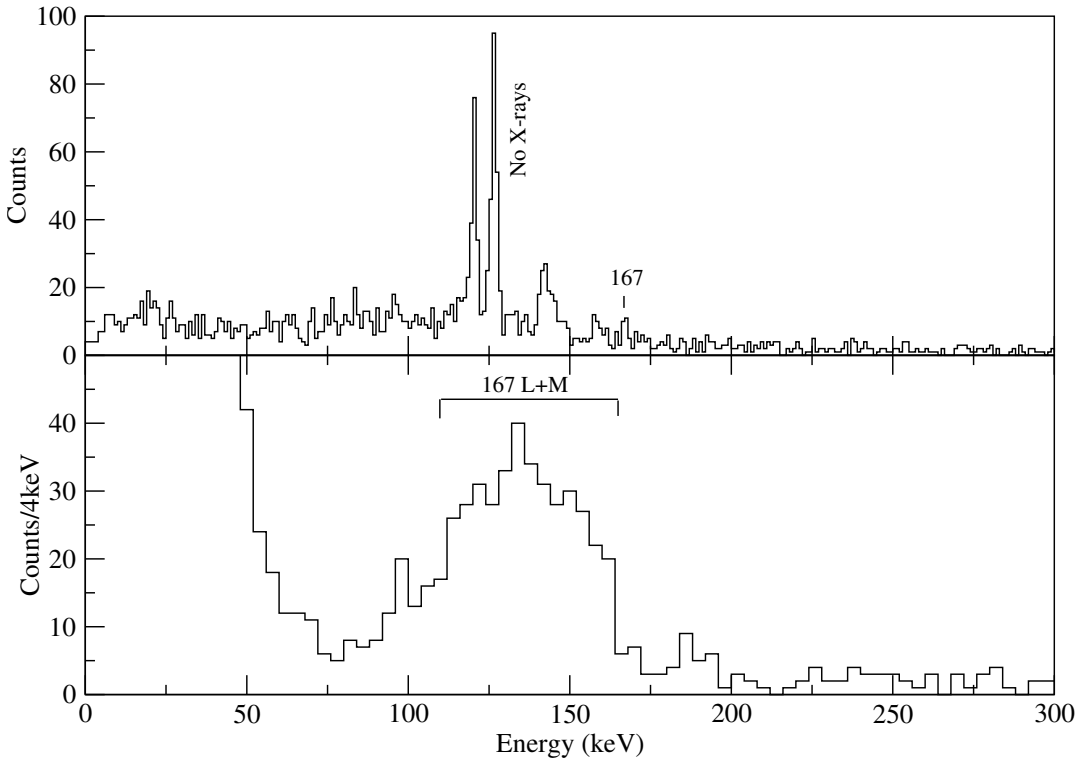

Figure 6.47: *Top panel: Gamma's detected in the planar germanium detectors 90 μs following recoil implantation. The K X-rays appear intense and the low lying 167 keV peak is evident. Bottom panel:* PIN *diodes 90 μs following recoil implantation. A multiplet peak appears in the region corresponding to the 167 keV L and M shell electrons.*

The 167±2 keV transition, whilst weak, appears above the background above the statistical critical limit (Equation 6.1). Intense K X-ray peaks point to the high degree of conversion occurring; the 167 keV transition is known to be an M2 thus this is expected. The total theoretical conversion coefficient of this transition α_T= 51.6 based on BRICC calculations [27]. A broad peak appears in the PINs spectrum in the energy range associated with the L and M shell electrons corresponding to a peak with energy around that of the 167 keV transition. The lower resolution in the PIN diodes makes for large uncertainty when extracting any data from such a broad structured multiplet. However measuring the ratio between the K X-ray peaks and the 167 keV peak yields a value of $N_{X-ray}/N_{167\ kev} = 18.4 \pm 8.7$ which, although lower than the K ICC for an M2, ($\alpha^K_{M2} = 28.8 \pm 0.4$) is statistically consistent with being an M2 transition. As discussed previously, the isomeric decay results from a neutron hole in

$5/2^+[622]$ configuration following excitation to the $9/2^-[734]$ state. This is in agreement with experimental systematics in the N=151 isotones.

The final level scheme including tentative spin assignments is shown in Figure 6.48. The $5/2^+[622]$ isomer is included.

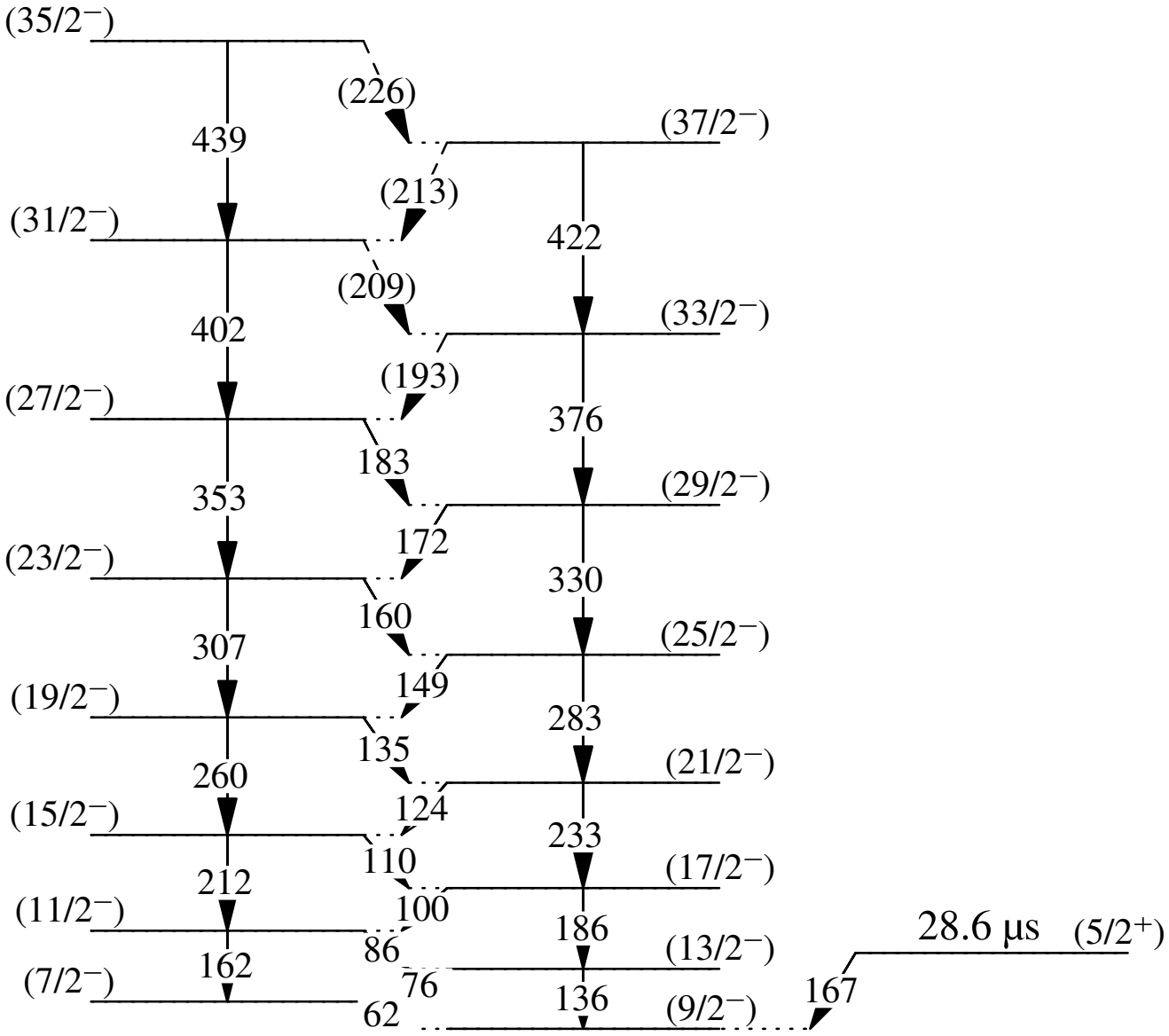

Figure 6.48: *The level scheme deduced from this study. Spin assignments are tentative and hence enclosed in brackets.*

6.8.4 Slow Isomer Decay

In addition to the faster isomer there has also been a slower isomer decay reported by Lopez-Martens ($T_{1/2} = 706 \pm 24$ µs) [69] and Antalic ($T_{1/2} = 627 \pm 5$ µs) [74]. This has is expected to populate a non-yrast structure as the transition is in coincidence with additional prompt transitions observed in both in-beam [75] and decay spectroscopy data in these studies.

The ratio between half-lives of the slower and faster isomer is large. Thus to retain sufficient accuracy in this study, the count rate as a function of logarithmic time scale was adopted. The result of this is the typical exponential decay curve becomes a peak for each separate decay lifetime. The frequency distribution of the decay per unit time

$$\frac{dN(t)}{dt} = N\lambda e^{-\lambda t}, \tag{6.6}$$

is changed to

$$\frac{dN(t)}{d\theta} = N\lambda e^{\theta} e^{-\lambda e^{\theta}}, \tag{6.7}$$

with θ=ln(t) and N the total number of counts. The advantage of this is that the relation between the lifetime and the peak maximum given by

$$\theta_{max} = \tau = \frac{1}{\lambda} \tag{6.8}$$

such that distinguishing between events with a sufficiently large time interval between them becomes simpler. Furthermore, the method also relates to low statistical cases well. For the data in this study there will be four free parameters based on this: N_1 and λ_1 for the faster decay, and N_2 and λ_2 for the slower decay.

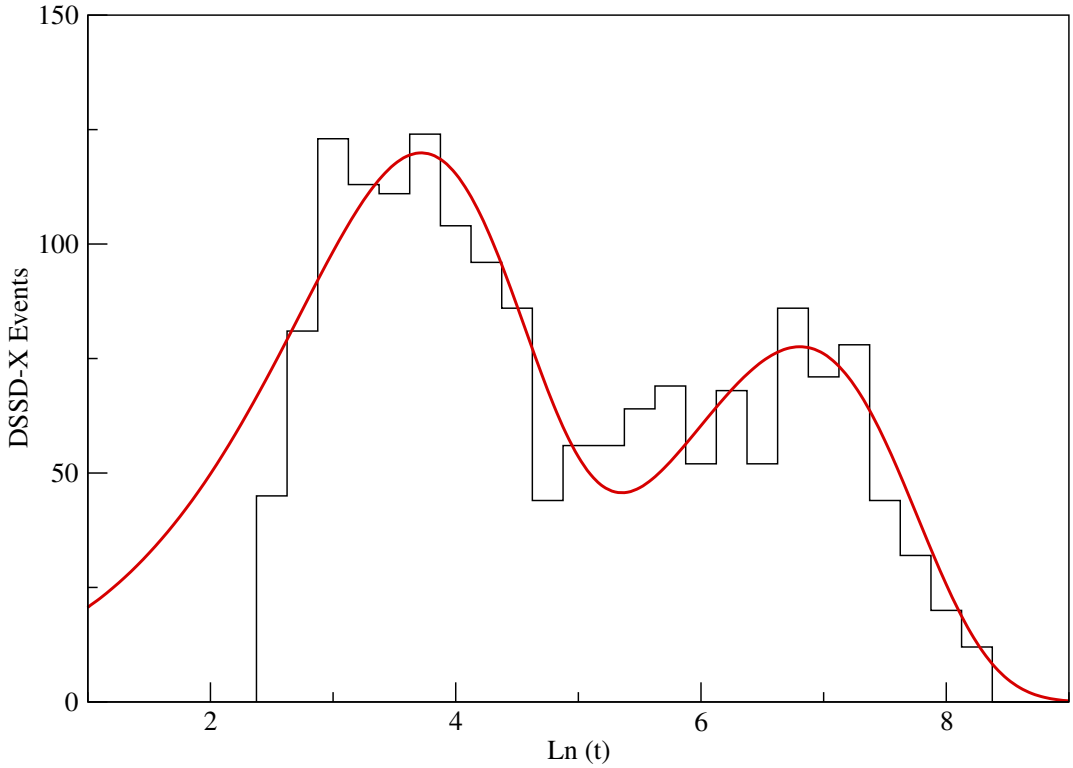

Figure 6.49: *Electron events in the* DSSD-x *detector following recoil implantation up to a maximum of 6 ms as a function of natural logarithmic time. Two distinct peak areas appear corresponding to the faster and slower isomer decays through electron cascades. The red line represents a fit of the form* $dN_1/d\theta + dN_2/d\theta$ *(Equation 6.7) for the two respective peaks with free parameters* N *and* λ *acquired through* χ^2 *minimisation. Note that the first bin is disregarded in the fit as it only partially fills due to the dead time between charge pulses in the detector.*

From this fit values are acquired for the half-life of the faster isomer $T_{1/2}^{fast}$=ln(2)/λ_1=26.5±1.6 µs, while for the slower isomer $T_{1/2}^{slow}$=ln(2)/λ_2=608.4±20.0 µs. Both values are consistent with previously measured half-lives (see Table 6.8).

Study	Year	'Fast' Isomer $T_{1/2}$ (µs)	'Slow' Isomer $T_{1/2}$ (µs)	Ref
This Study	2014	26.5±1.6	608±20	-
Antalic *et al.*	2011	22.7±0.5	627±5	[74]
Lopez-Martens *et al.*	2011	-	706±24	[69]
Moon	2007	22±2	-	[75]
Lopez-Martens *et al.*	2007	31.1±2.1	-	[73]
Bemis *et al.*	1973	31.3±4.1	-	[72]

Table 6.8: *A comparison of the half-life measurements made on the fast and slow isomer decays in* ^{253}*No.*

Based on the value of the measured half life, the focal plane germanium clovers and PIN diodes are time correlated within the range 0.1 ms $< t <$ 2 ms.

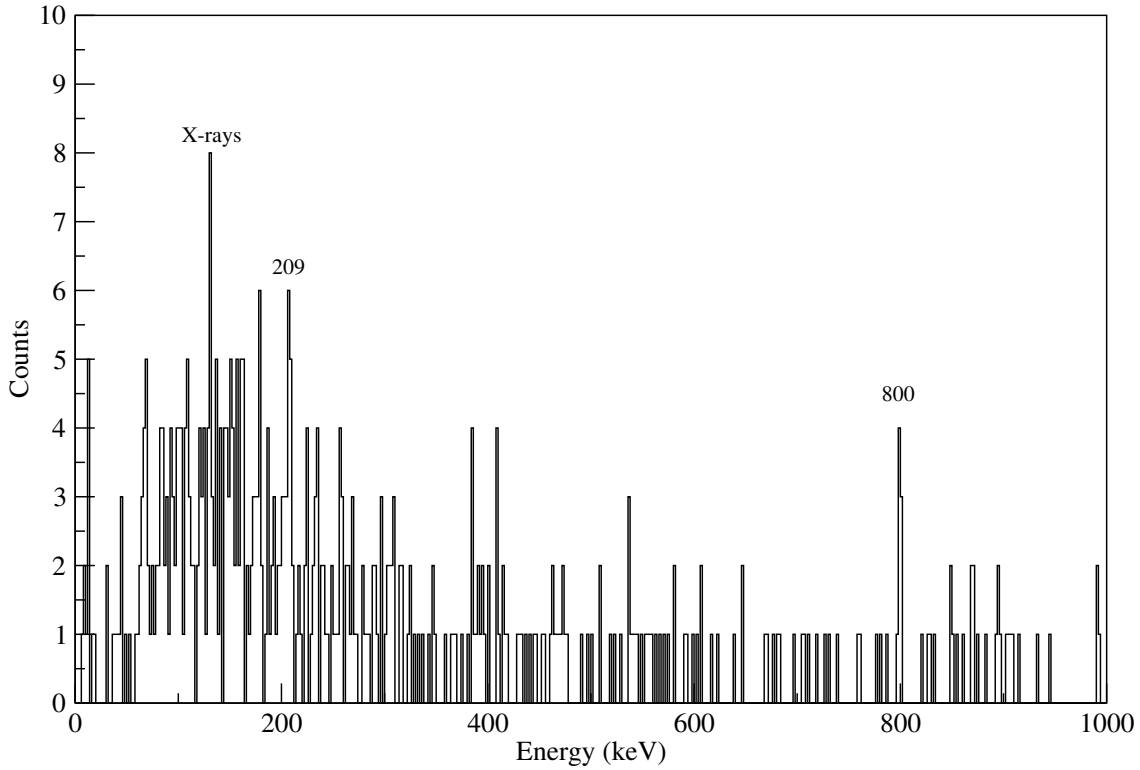

Figure 6.50: *Focal plane clovers to detect γ rays 0.1 ms $< t <$ 2 ms after recoil implantation in the* DSSD*s. A higher energy 800 keV transition is evident, along with a number of lower energy transitions.*

As can be seen, in the focal plane clover detector, the 800 keV transition (discussed on page 89) is evident as potentially stemming from a multi-quasiparticle state with $K^{\pi}=15/2^{-}$ [73]. Focussing on the lower energy region of the clovers for γ rays and the PIN diodes for conversion electrons:

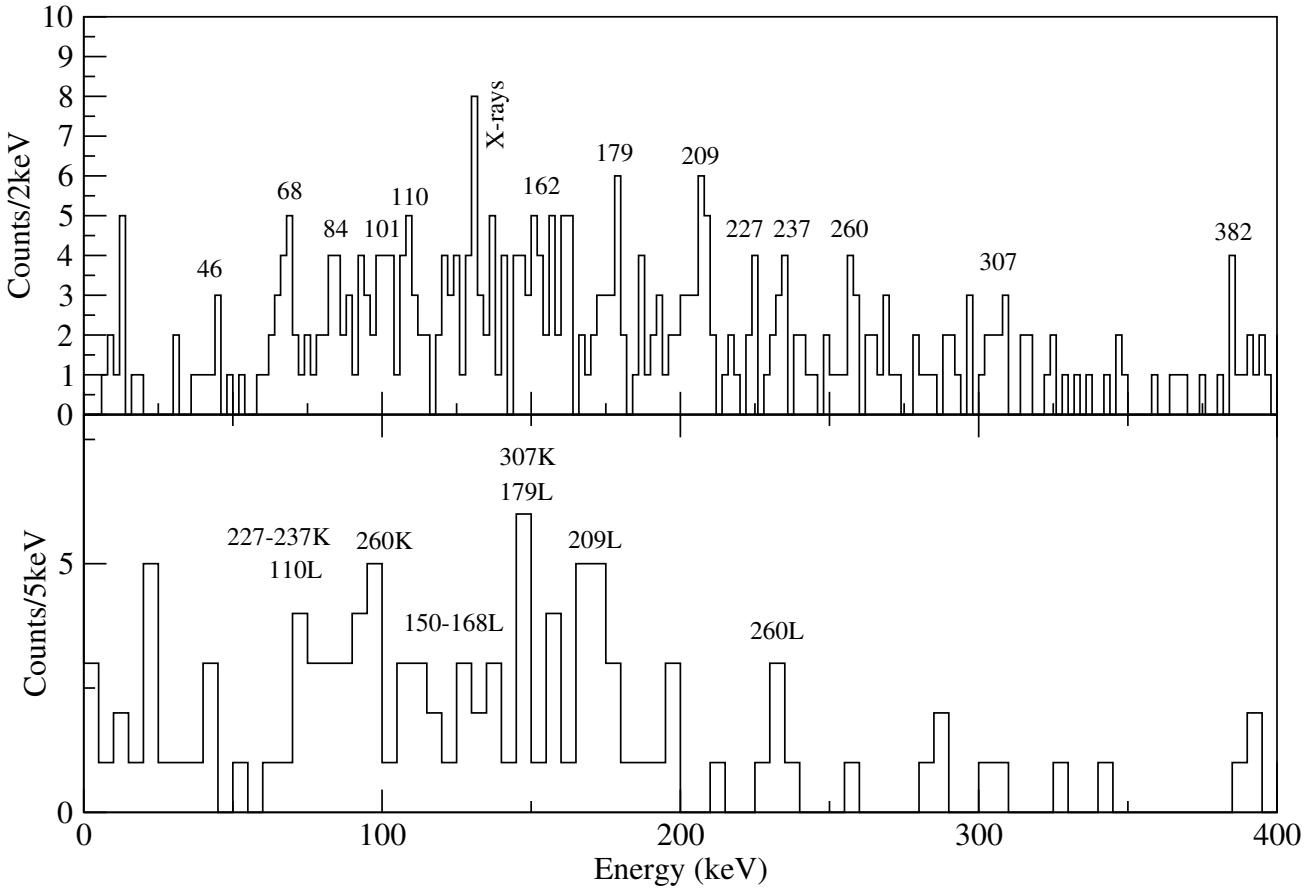

Figure 6.51: *Top panel: Focal plane clovers to detect γ rays and bottom panel:* PIN *diode detectors to detect internal conversion electrons 0.1 ms $< t <$ 2 ms after recoil implantation.*

Given that this can be observed after recoil implantation indicates the structure is populated by an isomer, potentially the slower isomer. Ideally one would like to measure internal conversion coefficients here in order make transition multipolarity assignments, however, while simulations of the PIN diode efficiency do exist [84], 11 of the strips were unavailable during the experiment. Further attempts to measure the efficiency using a known calibration source is not possible given the position differences between source and electrons emitted by the recoils. Energy assignments can be made confirming a number of transitions decaying from populated levels in both the yrast and non-yrast structure.

This structure is also detected in-beam with SAGE. Figure 6.52 shows the projection from the recoil-tagged in-beam γ-e$^-$ matrix with the intense 800 keV transtion highlighted. Figure 6.53 demonstrates electron coincidences with the 800 keV transition.

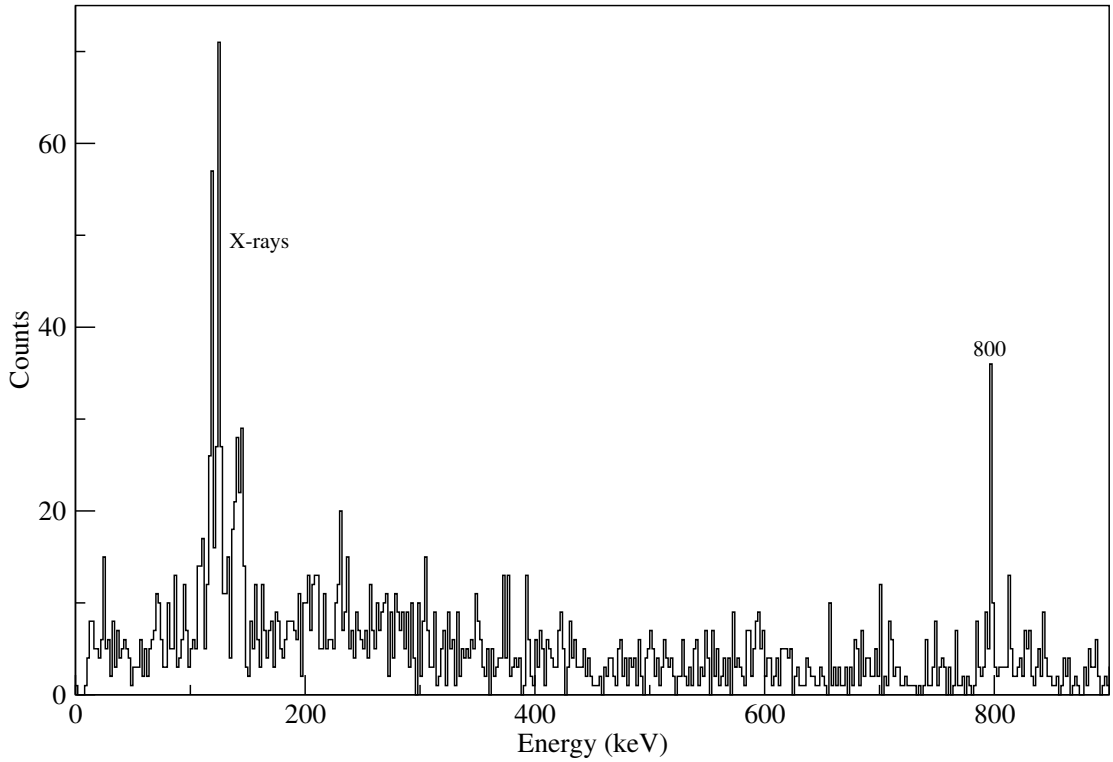

Figure 6.52: *The γ ray projection from a prompt recoil-gated γ–e^- matrix detected by* SAGE. *The relative intensity of the 800 keV transition is clear.*

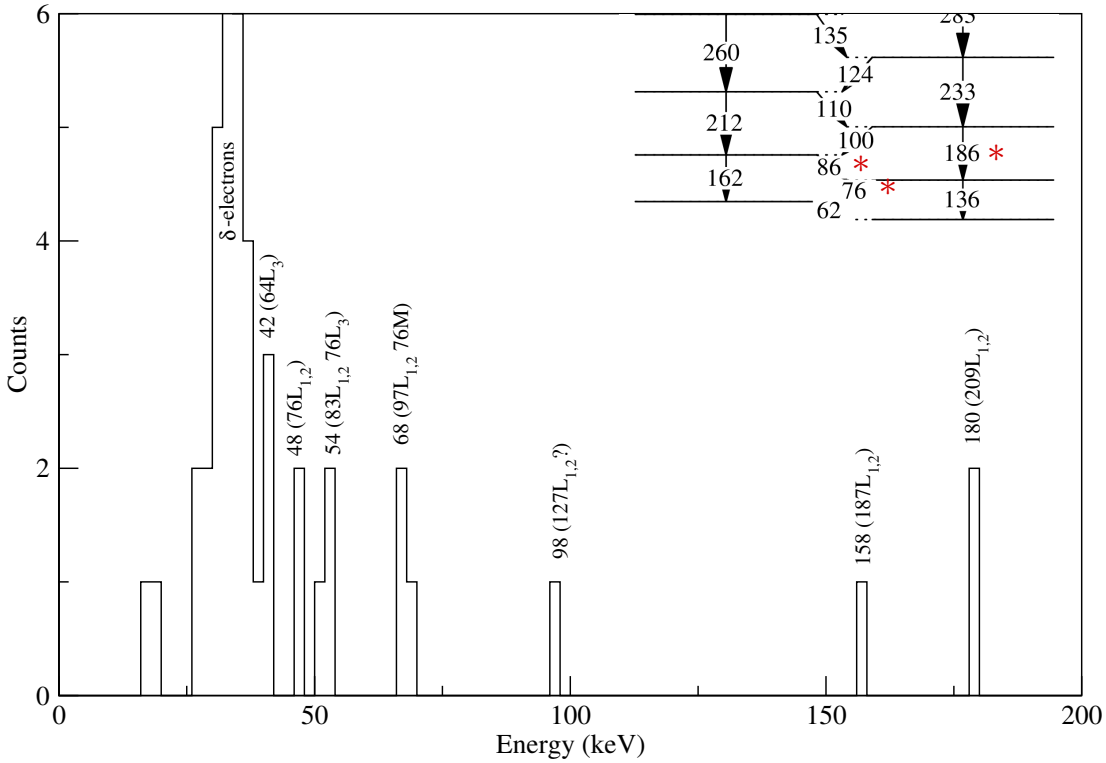

Figure 6.53: *Electrons detected by the silicon detector of* SAGE *in coincidence with the 800 keV γ ray transition.*

Of note is the appearance of yrast band transitions and an intense 209 keV transition which could be part of the structure built on top of the 800 keV transition. Peaks which coincide with the yrast bands transition energies (or in some cases slightly lower energy) are evident. This is in agreement with the study by Lopez-Martens [69] with the proposed structure shown in the Figure 5.11 on page 90. The energies suggest that the band built on top of the 800 keV transition may have similar energies to the yrast bands, and/or it feeds in somewhere near to the lower spin region of the yrast band. This is also supported from the construction of the level scheme in Section 6.2 whereby the 209 keV transition was evident in certain gates but the yrast band stretched E2 was determined to be 212 keV. The 237 keV transition could also be observed in a similar manner and is seen in the focal plane clovers in timing coincidence with the 608 µs isomer. The 800 keV transition is expected to be an M1 transition [69]. Based on the in-beam recoil-tagged prompt data, 56±13 γ ray counts were measured in JUROGAM II at 800 keV. The BRICC ICC for an M1 transition at this energy ($\alpha_K^{M1} = 0.13$ and $\alpha_L^{M1} = 0.03$) and the

SAGE efficiency at the energies for K and L shell electrons ($\varepsilon_{651keV} = 1.5\%$ and $\varepsilon_{771keV} = 1.3\%$). Thus one would expect 3±1 K shell electrons and 0.5±0.1 L shell electrons in the energy region probed. For an E2 transition at 800 keV with BRICC values ($\alpha_K^{E2} = 0.02$ and $\alpha_L^{E2} = 0.01$) then there would be 0.5±0.1 K shell electrons and 0.2±0.1 L shell electrons. Experimentally, no counts were observed in the recoil-tagged SAGE regions of interest. Given statistical limits here, whether one can infer that the 800 keV is mixed M1+E2' or a pure E2 is debatable.

Given the statistics, any tentative construction of a level scheme here would be purely speculative. Both prompt and delayed γ and electron data would give full scope to do this in future studies where experimental conditions may be more favourable. This will hopefully aim to shed more light on the structure of this sideband and the decay path it follows.

Chapter 7

Conclusion and Future Studies

7.1 Summary

Initially the performance of the SAGE spectrometer was tested through the reaction ^{144}Sm(^{36}Ar,p2n)^{177}Au. This allowed for conversion electron measurements on some of the more populated transitions, in particular a number of yrast band transitions. This allowed the confirmation of the multipolarity of the states while demonstrating the scope of the spectrometer.

The heavy transfermium nucleus ^{253}No was studied in-beam through the reaction ^{207}Pb(^{48}Ca, 2n)^{253}No. The recoil-tagging technique was utilised to extract prompt data of interest including γ–electron coincidence matrices for a comprehensive examination of the level scheme. Gamma–electron coincidences allowed for level scheme construction demonstrating two strongly coupled rotational bands with a decay to the bandhead via a 136 keV stretched E2 $\Delta I = 2$ and a 62 keV M1+E2' $\Delta I = 1$ transition. Further transitions where ambiguity over energy assignments was evident required rigorous investigation to confirm assignments. Internal conversion coefficient measurements have demonstrated the E2 and M1+E2' multipolarity of transitions within the bands as expected in such a rotational structure. Measurement of the B(M1+E2')/B(E2) ratio between interband and intraband transitions, confirm the $9/2^-[734]$ Nilsson configuration as the bandhead and groundstate of the two bands, with the single unpaired neutron occupying this orbital in the bandhead (also the α decaying groundstate). Confirmation of this was observed through Monte Carlo simulated data. This is consistent with

the study performed by Herzberg *et al.* [61], and focal plane studies [71],[69], and [74], but not consistent with the in-beam study by Reiter *et al.* [60].

The α decay into excited states in ^{249}Fm energy and half-life was measured to be E_α=8090±36 keV and $T_{1/2}$=101.9±1.1 s, both values consistent with the literature values. The exited single-particle structure in ^{249}Fm was observed following the ^{253}No α-decay to the $9/2^-[734]$ state. Subsequent decays were measured as E1 and M1 transitions to the $7/2^+[624]$ ground state.

The isomeric decay measured was 28.6±2.3 µs, statistically consistent compared to the literature value of 31±4 µs. A weak 162 keV M2 transition was observed and tentatively confirmed to be of M2 nature through X-ray and γ ray measurements.

A longer lived isomer decay was measured to have a half-life of 608±20 µs. It is evident that this potentially populates a non-yrast structure which decays into the yrast bands through a 800 keV transition. Transitions from within states in the non-yrast structure are observed in both the prompt as well as the focal plane spectrometers. Performing prompt γ–e$^-$ coincidence on the 800 keV unveils transitions also determined with focal plane analysis. Given the level of statistics available, it was not justifiable to assign energy or level assignments to this, nor determine at what spin it feeds into the yrast band.

7.1.1 Future Studies

While the structure of the lower lying yrast bands in ^{253}No has now been confirmed through in-beam and decay spectroscopy studies, knowledge of additional structures remains limited. Future studies could focus on exploring the structure of these bands, their nature, and how they decay into the ground state band. Populating the yrast bands to higher spins with the aim of observing how the rotational structure varies with higher spins could also provide further knowledge to compare with other nuclei in the vicinity. All of this is with the overall aim in improving systematics in a region where, currently, limited amounts of experimental data are available. The SAGE spectrometer currently has acquired data on a number of heavy isotopes including ^{251}Md, ^{255}Lr, ^{254}No currently under analysis, with future plans for ^{250}Fm, ^{249}Md, and ^{243,244}Cf scheduled to be studied. Vast advances in experimental capabilities have allowed the

transfermium mid-shell region to be probed and the scope to explore this and hence towards the island of stability is well under way.

Bibliography

[1] C. Weizsäcker, Zeitschrift für Physik **96**, 431 (1935).

[2] M. G. Mayer, Phys. Rev. **78**, 16 (1950).

[3] M. Bender, P.-H. Heenen, and P.-G. Reinhard, Rev. Mod. Phys. **75**, 121 (2003).

[4] P. G. Reinhard, Reports on Progress in Physics **52**, 439 (1989).

[5] S. Ćwiok, J. Dobaczewski, P.-H. Heenen, P. Magierski, and W. Nazarewicz, Nuclear Physics A **611**, 211 (1996).

[6] M. Bender, W. Nazarewicz, and P.-G. Reinhard, Physics Letters B **515**, 42 (2001).

[7] Y. T. Oganessian *et al.*, Phys. Rev. C **74**, 044602 (2006).

[8] D. Rudolph *et al.*, Phys. Rev. Lett. **111**, 112502 (2013).

[9] J. Khuyagbaatar *et al.*, Phys. Rev. Lett. **112**, 172501 (2014).

[10] R.-D. Herzberg and P. Greenlees, Progress in Particle and Nuclear Physics **61**, 674 (2008).

[11] R.-D. Herzberg, Journal of Physics G: Nuclear and Particle Physics **30**, R123 (2004).

[12] J. Hamilton, S. Hofmann, and Y. Oganessian, Annual Review of Nuclear and Particle Science **63**, 383 (2013).

[13] A. Ghiorso, T. Sikkeland, and M. J. Nurmia, Phys. Rev. Lett. **18**, 401 (1967).

[14] R. F. Casten, *Nuclear Structure from a Simple Perspective* (Oxford Science Publications, 2000).

[15] N. Bohr and J. A. Wheeler, Phys. Rev. **56**, 426 (1939).

[16] R.-D. Herzberg, *The Chemistry of The Superheavy Elements: Chapter 2, Nuclear Structure of Superheavy Elements* (Springer, 2014).

[17] A. Bohr and B. R. Mottelson, *Nuclear Structure* (World Scientific, 1998).

[18] E. S. Paul, *Postgraduate Lecture Series: Nuclear Models* (University of Liverpool, 2003).

[19] B. R. Mottelson and S. G. Nilsson, Phys. Rev. **99**, 1615 (1955).

[20] R. B. Firestone, *Table of Isotopes 8th Ed.* (Wiley, 1996).

[21] V. Strutinsky, Nuclear Physics A **95**, 420 (1967).

[22] M. Bender, P. Bonche, T. Duguet, and P.-H. Heenen, Nuclear Physics A **723**, 354 (2003).

[23] A. V. Afanasjev, T. L. Khoo, S. Frauendorf, G. A. Lalazissis, and I. Ahmad, Phys. Rev. C **67**, 024309 (2003).

[24] N. Stone, EPJ Web of Conferences **63**, 01017 (2013).

[25] T. Kibédi and R. Spear, Atomic Data and Nuclear Data Tables **89**, 77 (2005).

[26] E. L. Church and J. Weneser, Phys. Rev. **103**, 1035 (1956).

[27] T. Kibedi, T. Burrows, M. Trzhaskovskaya, P. Davidson, and C. Nestor, BRICC http://bricc.anu.edu.au/index.php.

[28] P. E. Hodgson, *Nuclear heavy-ion reactions* (Oxford : Clarendon Press, 1978).

[29] Y. T. Oganessian and et.al., Phys. Rev. C **64**, 054606 (2001).

[30] R. Bass, *Nuclear Reactions with Heavy Ions* (Springer, 1980).

[31] J. Pakarinen, PhD Thesis, (2007).

[32] P. Papadakis *et al.*, Journal of Physics: Conference Series **312**, 052017 (2011).

[33] J. Pakarinen *et al.*, The European Physical Journal A **50**, 1 (2014).

[34] P. Papadakis, Private Communication, 2012.

[35] P. Butler *et al.*, Nuclear Instruments and Methods in Physics Research Section A: Accelerators, Spectrometers, Detectors and Associated Equipment **381**, 433 (1996).

[36] P. Papadakis, Private Communication, 2014.

[37] J. H. Hamilton and J. Manthuruthil, editors, *Proc. Int. Conf. on Radioactivity in Nuclear Spectroscopy*, 1969.

[38] S. Shepherd *et al.*, Nuclear Instruments and Methods in Physics Research Section A: Accelerators, Spectrometers, Detectors and Associated Equipment **434**, 373 (1999).

[39] C. Beausang *et al.*, Nuclear Instruments and Methods in Physics Research Section A: Accelerators, Spectrometers, Detectors and Associated Equipment **313**, 37 (1992).

[40] P. Nolan, F. Beck, and D. Fossan, Annual Review of Nuclear and Particle Science **44**, 561 (1994).

[41] G. Knoll, *Radiation Detection and Measurement* (Wiley, 2000).

[42] M. Leino *et al.*, Nuclear Instruments and Methods in Physics Research Section B: Beam Interactions with Materials and Atoms **99**, 653 (1995).

[43] N. Bohr, Phys. Rev. **58**, 654 (1940).

[44] W. E. Lamb, Phys. Rev. **58**, 696 (1940).

[45] R. D. Page *et al.*, Nuclear Instruments and Methods in Physics Research Section B: Beam Interactions with Materials and Atoms **204**, 634 (2003).

[46] I. Lazarus *et al.*, Nuclear Science, IEEE Transactions on **48**, 567 (2001).

[47] P. Rahkila, Nuclear Instruments and Methods in Physics Research Section A: Accelerators, Spectrometers, Detectors and Associated Equipment **595**, 637 (2008).

[48] J. Theuerkauf *et al.*, Institude for Nuclear Physics, Köln, (1993).

[49] H. Kankaanpää *et al.*, Nuclear Instruments and Methods in Physics Research Section A: Accelerators, Spectrometers, Detectors and Associated Equipment **534**, 503 (2004).

[50] A. Siivola, Nuclear Physics A **109**, 231 (1968).

[51] F. A. Ali, PhD Thesis.

[52] F. Kondev *et al.*, Physics Letters B **512**, 268 (2001).

[53] F. G. Kondev *et al.*, Phys. Rev. C **61**, 011303 (1999).

[54] K. Heyde and J. L. Wood, Rev. Mod. Phys. **83**, 1467 (2011).

[55] M. Scheck *et al.*, Phys. Rev. C **83**, 037303 (2011).

[56] J. Wood, E. Zganjar, C. D. Coster, and K. Heyde, Nuclear Physics A **651**, 323 (1999).

[57] C. Papanicolopulos *et al.*, Zeitschrift für Physik A Atomic Nuclei **330**, 371 (1988).

[58] V. Berg, Z. Hu, J. Oms, and C. Ekström, Nuclear Physics A **410**, 445 (1983).

[59] D. T. Joss, Private Communication, 2014.

[60] P. Reiter *et al.*, Physical review letters **95**, 032501 (2005).

[61] R.-D. Herzberg *et al.*, The European Physical Journal A **42**, 333 (2009).

[62] R.-D. Herzberg *et al.*, The European Physical Journal A **15**, 203 (2002).

[63] S. Ćwiok, S. Hofmann, and W. Nazarewicz, Nuclear Physics A **573**, 356 (1994).

[64] A. Parkhomenko and A. Sobiczewski, Acta Physica Polonica B **36**, 3115 (2005).

[65] I. Ahmad *et al.*, Physical Review C - Nuclear Physics **68**, 443061 (2003).

[66] S. Tandel *et al.*, Physical Review C - Nuclear Physics **82** (2010).

[67] I. Ahmad, R. K. Sjoblom, and P. R. Fields, Phys. Rev. C **14**, 218 (1976).

[68] M. Asai *et al.*, Phys. Rev. C **83**, 014315 (2011).

[69] A. Lopez-Martens *et al.*, Nuclear Physics A **852**, 15 (2011).

[70] F. P. Heßberger, AIP Conference Proceedings **891** (2007).

[71] F. Hessberger, S. Antalic, D. Ackermann, S. Heinz, and S. Hofmann, GSI Annual Report 2011 **2012-1**, 209 (2012).

[72] C. E. Bemis *et al.*, Phys. Rev. Lett. **31**, 647 (1973).

[73] A. Lopez-Martens *et al.*, The European Physical Journal A **32**, 245 (2007).

[74] S. Antalic *et al.*, The European Physical Journal A **47**, 1 (2011).

[75] S. Moon, PhD Thesis, (2007).

[76] R. D. Herzberg, Private Communication, 2012.

[77] F. Heßberger *et al.*, The European Physical Journal A **48**, 1 (2012).

[78] T. Page, PhD Thesis, (2003).

[79] D. Cox, Private Communication, 2014.

[80] E. Paul, Private Communication, 2012.

[81] F. Dönau, Nuclear Physics A **471**, 469 (1987).

[82] P. Reiter *et al.*, Phys. Rev. Lett. **84**, 3542 (2000).

[83] C. Gray-Jones, PhD Thesis, (2008).

[84] A. Andreyev *et al.*, Nuclear Instruments and Methods in Physics Research Section A: Accelerators, Spectrometers, Detectors and Associated Equipment **533**, 422 (2004).